Dark Matter in Dwarf Galaxies: Observational Tests of the Cold Dark Matter Paradigm on Small Scales

by

Joshua David Simon

B.S. (Stanford University) 1998
M.A. (University of California, Berkeley) 2000

A dissertation submitted in partial satisfaction of the
requirements for the degree of
Doctor of Philosophy

in

Astrophysics

in the

GRADUATE DIVISION
of the
UNIVERSITY OF CALIFORNIA, BERKELEY

Committee in charge:
Professor Leo Blitz, Chair
Professor Chung-Pei Ma
Professor William L. Holzapfel

Spring 2005

The dissertation of Joshua David Simon is approved:

_____

Chair   Date

_____

Date

_____

Date

University of California, Berkeley

Spring 2005

Dark Matter in Dwarf Galaxies: Observational Tests of the Cold Dark Matter Paradigm on Small Scales

Abstract

Dark Matter in Dwarf Galaxies: Observational Tests of the Cold Dark Matter

Paradigm on Small Scales

by

Joshua David Simon

Doctor of Philosophy in Astrophysics

University of California, Berkeley

Professor Leo Blitz, Chair

Over the last decade, several crucial shortcomings of the Cold Dark Matter (CDM) model have been recognized on galaxy-size scales. In this thesis I present new observations addressing two of these problems: the substructure problem and the central density problem. I describe results from our search for a connection between high-velocity clouds (HVCs) and the low-mass dark matter halos seen in CDM simulations that appear to be missing from the real universe. This survey demonstrates that HVCs do not have stellar counterparts similar to other Local Group dwarf galaxies; if HVCs contain any stars at all, their surface brightnesses must be substantially lower than those of any known dwarfs. I also discuss observations of two candidate dark galaxies in the Local Group: Complex H and HVC $127-41-330$. Complex H is a massive, nearby HVC containing $\sim 2 \times 10^7$ M$_\odot$ of H I and less than $\sim 3 \times 10^5$ M$_\odot$ of stars, leaving it with an H I mass to light ratio several times higher than any known galaxy. HVC $127-41-330$ is a smaller HVC that appears to be interacting with the dwarf galaxy LGS 3, placing it at a distance of 700 kpc. The HVC is rotating, with a dynamical mass that makes it dark matter-dominated for any plausible distance. The existence of these two starless objects suggests that the substructure problem is related to the difficulty of forming stars in low-mass dark matter halos. However, many more dark galaxies must be located in order to resolve the substructure problem.

In addition, I present a rotation curve analysis of five nearby dwarf galaxies, based on high-resolution two-dimensional velocity fields in Hα and CO. In contrast to previous studies, most of the galaxies in this sample do not seem to have a strong preference for

pseudo-isothermal density profiles. Instead, these objects exhibit the full range of dark matter density profiles between constant density and NFW halos. One galaxy, NGC 2976, definitively contains a large constant-density core that presents a significant challenge for CDM models. However, for another galaxy, NGC 5963, the derived density profile has a very steep central slope and is well fit by an NFW profile, confirming that some galaxies do contain cuspy profiles like the ones predicted by CDM. This observing program was designed to overcome some of the limitations of the traditional techniques of long-slit Hα spectroscopy and low-resolution H I observations. The results demonstrate that there is a distribution of central density slopes rather than the single universal density profile seen in CDM simulations. Four out of the five observed galaxies show evidence for noncircular motions, which are attributed to the triaxiality of their dark matter halos. These motions constrain the ellipticities of the halos in the planes of the disks to be larger than a few percent.

Professor Leo Blitz
Dissertation Committee Chair

To my parents, and Wendy

Contents

List of Figures

List of Tables

Acknowledgments

As I sit here on the beach of Grand Bay, on the tiny island of Canouan in the far southeastern reaches of the Caribbean (see Figure 0.1), it is (perhaps unsurprisingly) rather difficult to concentrate on my dissertation. Nevertheless, there are many people to whom I owe thanks for their love, support, advice, and assistance over the past seven years, and perhaps this is an appropriate time to acknowledge some of their contributions.

Photo credit: Wendy Simon
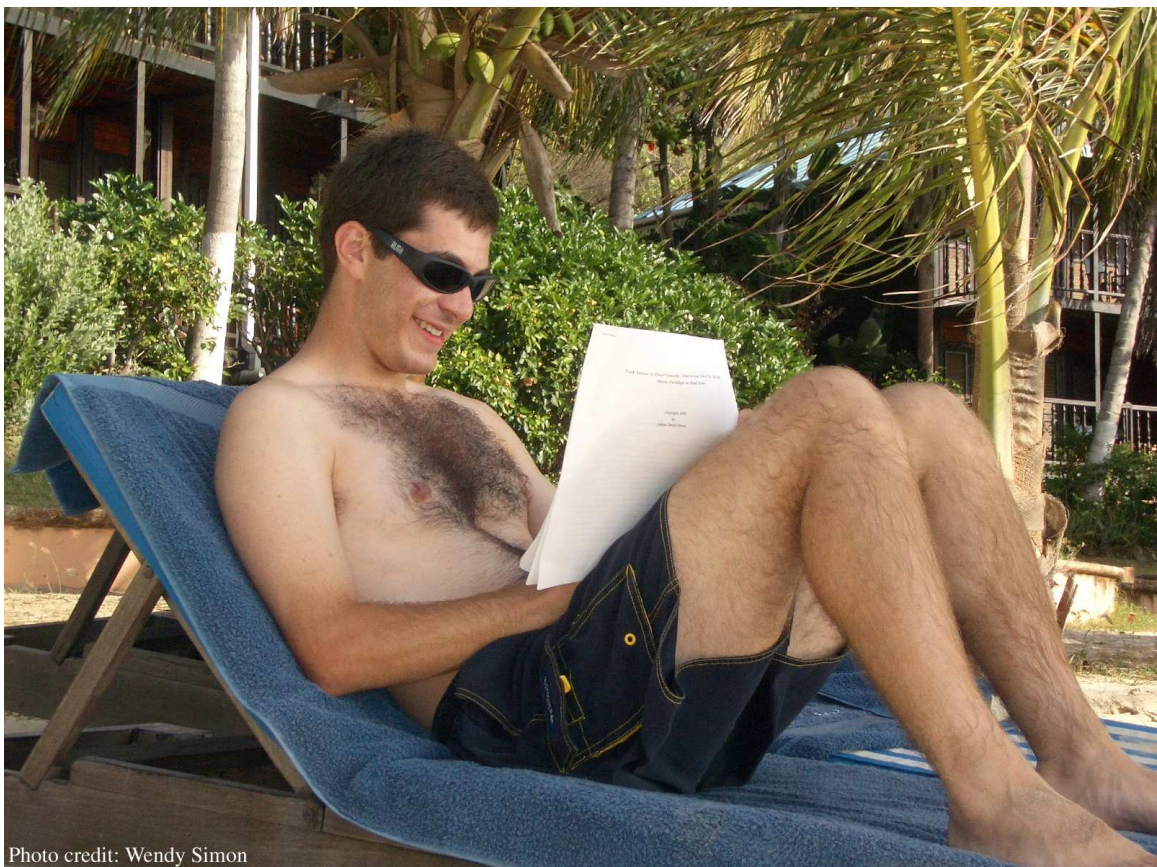
Figure 0.1 — The author hard at work in Canouan.

First and foremost is my new wife Wendy Simon (née Ellis), my nearly constant companion during my time in grad school. Although her continuing insistence that I get home at a reasonable hour may have slightly delayed the completion of this thesis, my life has been made much happier by her presence, encouragement, and love.

I would also like to take this opportunity to express my gratitude to my parents for their love, and of course for their financial support of my undergraduate education. I also thank them for the extraordinary effort they have made each week for the past four years to refrain from asking me how my thesis was going. I hope it has been worth the wait. My uncle, aunt, and cousin, Joel Simon, Sarah Samuels, and Jeremy Simon were a great help to me in my first two months at Berkeley by offering me a place to live during my fruitless search for housing at the height of the dot-com boom. They also welcomed Wendy and me into their home for holidays and provided us with a pleasant change of pace from our one-bedroom apartment by inviting us to house- and dog-sit during many of their vacations. Steve Shih, Ray Salloom, and my other Stanford friends also provided many needed diversions to make sure that my life was not entirely focused on astronomy.

In addition to my friends and family, there are a multitude of astronomers for me to thank. First, I have benefited greatly from my interactions with my advisor, Leo Blitz. Leo allowed me free rein to pursue projects that I found interesting, while also providing important scientific ideas and direction for my thesis. Leo also gave me all the financial support a grad student could want, no questions asked (well, perhaps there were a *few* questions asked . . .). For the second half of this thesis in particular, I have leaned heavily on the broad shoulders of Alberto Bolatto. Alberto's willingness to talk at any time, about any subject, his wide interests, and his ability to always focus on the big picture, have made him an exceptionally valuable surrogate advisor for me. I hope that someday he will be able to forgive me for my refusal to drink with him on any of our multitude of observing runs. Other Berkeley faculty whom I would like to single out include Hy Spinrad, for taking an interest in what I was doing and for reading most (if not all) of my observing proposals, Chung-Pei Ma, for writing me letters of recommendation and for being very accommodating regarding my qualifying exam and my thesis, Bill Holzapfel, also for being willing to sit through my qual and read my thesis, Carl Heiles, for his help with Arecibo data reduction and general advice, and Eliot Quataert, for his gracious assistance with my job applications. I also want to thank my undergraduate advisor, Jeff Willick, for helping me get started in astronomy research and for his efforts to get me into a good grad school. I know that he would be proud if he could see me today.

My officemate for the entirety of my graduate career, Steve Dawson, has been a great friend through it all, from Physics 210 problem sets to this dissertation, and Steve out-did himself as the officiant at my wedding last month. My other classmates, Huei-Ru

Chen, Alison Coil, Chao-Lin Kuo, Dave Sherfesee, and Jon Swift, have also been helpful with all the problem sets our first year and with advice on many topics more recently. Tim Robishaw has spent an inordinate amount of time helping me with all manner of IDL, UNIX, and Latex questions, and has also been a great friend and collaborator. I hope that the incident at Crash Boat Beach involving me, Tim, and our rental car will live on forever in the annals of astronomy adventures. Adam Leroy and Nate McCrady have indulged my frequent need to talk to someone about sports (or maybe it's the other way around), but in either case I am pleased to count them as friends. Adam has also been a frequent lunch companion, and I doubt that I will be able to find a replacement who can match his sense of humor. I am glad to have had Nate and Erik Rosolowsky accompanying me through the job application and thesis writing processes over the past year. My fellow Pioneer High alumnus, Doug Finkbeiner, offered me lots of assistance with programming, observing, and data reduction on my first research project at Berkeley (Chapter 2) and was instrumental in making sure that foursquare on the roof was passed along to a new generation of grad students. And last but not least, I expect great things from my first advisee, Mike Cooper. Finally, to all of my softball, soccer, and basketball teammates on the IM fields, I want to say that I looked forward to every game. We may not have met my goal of bringing home a championship, but we were better than I ever expected and I have lots of great memories.

Chapter 1

Introduction: Cold Dark Matter

The last few years have seen a revolution in cosmology as astronomers have discovered that the universe is filled with not only *dark matter*, but also the even more enigmatic *dark energy* (Riess et al. 1998; Perlmutter et al. 1999; Spergel et al. 2003). The nature of these two dominant components of the universe is currently one of the most fundamental mysteries in physics.

While our understanding of dark energy is still woefully inadequate, recent progress on dark matter has been promising even though the dark matter particle itself remains unidentified. The framework of a fully testable theory of the evolution of a universe dominated by dark matter is now in place, and the model can be confronted with observations. In this thesis, I carry out observational tests of two of the problems that have been identified with the Cold Dark Matter (CDM) model on small physical scales. I begin in this chapter by describing some historical developments of the concept of dark matter. I then discuss the CDM model and its successes and possible failures in predicting the properties of the universe.

1.1 Evidence for Dark Matter

The first hints of the existence of dark matter, or "missing mass", as it was originally known, came relatively early in the history of extragalactic astronomy. In the 1930s, Fritz Zwicky noticed that the galaxies in the Coma cluster are moving much faster than expected based on the amount of luminous matter present (Zwicky 1933, 1937). He therefore argued that the cluster galaxies must have masses of order 100 times larger than one would

calculate for pure stellar systems. Similar results were obtained soon thereafter by Smith (1936) for the Virgo cluster.

During the next four decades, it was generally recognized that Coma and other galaxy clusters must have mass-to-light ratios of up to a few hundred solar masses per solar luminosity (e.g., Mayall 1960; van den Bergh 1960a,b, 1961; Rood et al. 1972), but the nature of the nonluminous mass they contained was completely unknown. Without accurate constraints on both the number of baryons in the universe (Ω_b; Wagoner, Fowler, & Hoyle 1967) and the total mass of the universe (Ω_m), there was no reason to assume that this mass was in the form of anything more exotic than dim stars, brown dwarfs, hot gas, or perhaps black holes.

Beginning in the 1970s, observations by Vera Rubin, Alberto Bosma, and others convincingly demonstrated that the missing mass problem is also present in individual spiral galaxies (Rubin & Ford 1970; Freeman 1970; Einasto, Kaasik, & Saar 1974; Ostriker, Peebles, & Yahil 1974; Roberts & Whitehurst 1975; Roberts 1976; Bosma 1978; Rubin, Thonnard, & Ford 1978, 1980) as well as clusters. These studies showed that spiral galaxies have flat rotation curves extending out to radii of tens of kpc. If the mass distribution of a galaxy is spherically symmetric, Newton's Law of Gravitation (Newton 1687) states that

$$V_{rot}(R)^2 = \frac{GM(R)}{R}, \tag{1.1}$$

where V_{rot} is the rotation velocity as a function of radius, and M is the mass interior to a radius R. A flat rotation curve therefore implies that the mass enclosed increases linearly with radius and that the density declines as R^{-2}. Since the light distribution of spirals tends to decline exponentially with radius (de Vaucouleurs 1959; Freeman 1970), it is clear that these galaxies must contain nonluminous material in their outer regions.[1] These early observations typically revealed at least 10 times more mass than would be expected for a normal stellar population.

Around the same time, elliptical and S0 galaxies (Knapp, Kerr, & Williams 1978; Faber & Gallagher 1979, and references therein), galaxy pairs (Page 1962; Turner 1976; Peterson 1978), and galaxy groups (Gott & Turner 1977; Rood & Dickel 1978; Faber & Gallagher 1979) were likewise found to require large mass-to-light ratios using slightly more

---

[1]Deviations from spherical symmetry (e.g., substantial flattening) may change the exact radial dependence of the mass profile, but not the conclusion that the mass and light have fundamentally different spatial distributions.

complicated arguments. The wide range of observational techniques used in these studies and the variety of types of systems that yielded compatible results left little doubt that dark matter exists. But what is it made of?

Dark matter was originally suspected to be baryonic, possibly consisting of low-mass stars, gas, or stellar remnants. As it gradually became clear that Big Bang Nucleosynthesis constrains Ω_b to be much smaller than 1 (and as the postulated quantities of stars and gas failed to be detected [Hegyi & Olive 1983, 1986]), the theoretical prejudice towards an $\Omega_m = 1$ universe pushed astronomers to consider nonbaryonic possibilities. The most obvious candidate (and the only one known to exist independently of the dark matter problem) is the neutrino (Cowsik & McClelland 1972; Gunn et al. 1978). Neutrinos and other light particles are generically termed "hot dark matter" because of their relativistic velocities at the time at which they decoupled from (froze out of thermal equilibrium with) the photon-baryon fluid in the early universe. Naturally, the alternative is "cold dark matter", elementary particles that are massive enough[2] to have slowed to nonrelativistic velocities by the time they decouple.

Because neutrinos were copiously produced in the early universe, they were considered to be one of the prime nonbaryonic dark matter candidates in the late 1970s and early 1980s (e.g., Szalay & Marx 1976; Schramm & Steigman 1981; Bond & Szalay 1983). It was soon realized that neutrino-dominated universes failed to match a variety of observations, including galaxy clustering (HDM predicts a larger correlation length than is observed [Blumenthal, Pagels, & Primack 1982; White, Frenk, & Davis 1983; White, Davis, & Frenk 1984; Hut & White 1984]), the ages of galaxies (HDM predicts that clusters and superclusters form before galaxies, contrary to observations [Blumenthal et al. 1984]), and the phase-space density in the halos of dwarf spheroidals (Lin & Faber 1983). These results brought the Hot Dark Matter (HDM) model to an early demise. The recent detection of neutrino oscillations (Fukuda et al. 1998), and the resulting conclusion that neutrinos have nonzero rest mass, indicates that neutrinos actually are a form of dark matter; however, their contribution to the density of the universe is negligible.[3]

---

[2]There is one proposed low-mass CDM particle, the axion, which is nonetheless considered to be "cold" because of its exceptionally weak interactions with normal matter (Weinberg 1978; Wilczek 1978; Preskill, Wise, & Wilczek 1983).

[3]Baryonic dark matter also likely exists, as the total amounts of stars and hot gas observed in the local universe add up to only about half of Ω_b (Fukugita, Hogan, & Peebles 1998). These baryons are thought to make up the Warm Hot Intergalactic Medium, a very

Instead, the idea of cold dark matter quickly gained popularity, spurred by the development of cosmological N-body simulations that revealed a close correspondence between structure formation in CDM universes and observations of large scale structure. In §1.2 below, we briefly summarize the development of the CDM theory to its current dominant position over the subsequent 15 years, culminating in the dramatic successes of model fits to cosmic microwave background (CMB) observations.

It is worth pointing out here that dark matter is not the only possible solution to the missing mass problem implied by the kinematics and dynamics of galaxies. In fact, the dark matter hypothesis depends critically on the assumption that the Newtonian laws of gravity are valid over very large distances — distances many orders of magnitude beyond those for which gravity has been probed experimentally. If gravity were to deviate from the behavior extrapolated from smaller scales, the motions of galaxies could be explained without invoking dark matter. Indeed, it is straightforward to construct a model that produces flat rotation curves in galaxies and high velocity dispersions in clusters by slightly altering the law of gravity, as in Mordehai Milgrom's MOdified Newtonian Dynamics (MOND; Milgrom 1983a,b,c). Unfortunately, it has not yet proved possible to generalize MOND or other modifications of gravity into a realistic cosmological theory, preventing a fair comparison with the full set of astronomical observations (Scott et al. 2001). While MOND and similar models are able to explain the original problems that led to the proposal of dark matter, they may run into significant difficulties with the CMB power spectrum, the origin and formation of large-scale structure, gravitational lensing, and other fundamental properties of the universe. Given the totality of the evidence, we conclude that cosmological theories based on cold dark matter provide the best current description of the evolution of the universe.

1.2   The Cold Dark Matter Model

The modern Cold Dark Matter model was first proposed by Peebles (1982), who realized that a massive dark matter particle would eliminate one of the key problems faced by baryon- and HDM-dominated universes: the difficulty in forming galaxies (highly nonlin-

---

diffuse plasma at a temperature of $10^5 - 10^7$ K (making it nearly unobservable with current technology) that outlines the filaments of the cosmic web. Like the neutrinos, this form of dark matter is not dynamically significant.

ear density perturbations) by the present day from the very tiny temperature fluctuations observed in the CMB. Galaxy formation in the CDM model was quickly elaborated by Blumenthal et al. (1984), Bond & Efstathiou (1984), Davis et al. (1985), and Frenk et al. (1985), demonstrating that the model was in impressive (although imperfect) agreement with a wide range of observations. Within just three years of the invention of the model, it was apparent that CDM was at least roughly consistent with the large-scale clustering of galaxies, the approximate mass ranges of galaxies, galaxy scaling relations (such as the Faber-Jackson and Tully-Fisher relations), observational constraints on galaxy formation, the age of the universe, and the amplitude of CMB fluctuations (Blumenthal et al. 1984).

The general outline of the evolution of an $\Omega = 1$ CDM universe goes as follows. At the end of the inflation era, the nearly uniform sea of particles and photons filling the grapefruit-sized universe contained very tiny adiabatic density fluctuations. The distribution of the fluctuations was Gaussian, and their power spectrum was the scale-invariant Harrison-Zeldovich-Peebles spectrum with $P_k \propto k$ (Harrison 1970; Peebles & Yu 1970; Zeldovich 1972). Prior to matter-radiation equality (at $z = 2.4 \times 10^4 \ \Omega h^2$), the fluctuations could grow linearly with the expansion factor a on scales outside the horizon,[4] but on smaller scales (smaller than the Jeans length, which was comparable to the horizon size during the radiation-dominated era) pressure support prevented the fluctuations from growing. This process imprinted a kink onto the primordial power spectrum at the scale of the horizon at matter-radiation equality, such that the power-spectrum on small scales is $P_k \propto k^{-3}$. As the matter-dominated era progressed, the density fluctuations continued to grow linearly with a until late times when the high-density regions began to enter the nonlinear regime ($\delta\rho/\rho \sim 1$). Structure then formed hierarchically, with small-scale objects (low-mass galaxies) collapsing first at relatively high redshift ($z \gtrsim 10$) and galaxy clusters forming quite recently ($z \lesssim 1$). Some of the details of the process of galaxy formation — specifically, whether the predictions of the CDM model are in conflict with the properties of real galaxies — will be the subject of this thesis. For a more thorough treatment of the evolution of the early universe, see a cosmology textbook such as Padmanabhan (1993), Peebles (1993), or Peacock (1999).

As the predictions of the CDM model for galaxy formation were refined, it became clear that it contained several notable shortcomings. Perhaps most glaringly, nearly

---

[4]The term *horizon* refers to the distance that a photon (or other particle traveling at the speed of light) can propagate between the Big Bang and any given later time.

all of the available dynamical evidence pointed to $\Omega_m \approx 0.2$, in conflict with the inflationary expectation of a spatially flat universe. There were also apparent problems with the normalization of the primordial power spectrum (σ_8) and with the shape and amplitude of the galaxy-galaxy correlation function on large scales (e.g., Ostriker 1993, and references therein). By 1992, cosmologists were questioning whether CDM could actually be the correct description of the universe (e.g., Davis et al. 1992).

Just six years later, however, these difficulties all vanished in a single stroke when Riess et al. (1998) and Perlmutter et al. (1999) announced the discovery of the acceleration of the expansion of the universe. The value of the deceleration parameter, $q_0 = \Omega_m/2 - \Omega_\Lambda$, had been widely assumed to be positive, but the supernova measurements clearly showed that $q_0 < 0$, and correspondingly, that the vacuum energy term is nonzero. In combination with CMB observations, these data provide strong evidence that the universe is dominated by dark energy, presumably either in the form of a cosmological constant (Λ) or quintessence (e.g., Lange et al. 2001; Jaffe et al. 2001; Pryke et al. 2002). A Λ-dominated universe straightforwardly accounts for a low matter density and the ages of stars in globular clusters, while still maintaining the theoretically preferred value of $\Omega_{tot} = 1$. The clustering properties of galaxies also naturally matches the predictions of the new ΛCDM model.

On large scales (greater than 1 Mpc), observations are now considered to be in good agreement with the predictions of ΛCDM. The successes are most dramatically exemplified by the CMB observations from the Wilkinson Microwave Anisotropy Probe (WMAP), which yielded a power spectrum that can be fit accurately with what are now standard cosmological parameters (Spergel et al. 2003). There are still a few loose ends to be worked out, such as the presence of very massive galaxies at quite high redshifts, earlier than they would be expected to form in a hierarchical picture (Genzel et al. 2003; Glazebrook et al. 2004). These are not thought to be deal breakers for CDM, though. On smaller scales, however, such as the scales of individual galaxies, there are several potentially serious disagreements between CDM and the observed universe.

1.3 Problems on Small Scales

The so-called small-scale problems with CDM are not necessarily *problems*, per se; rather, they are most accurately described as differences between the observed universe on galaxy-size scales and its appearance in ΛCDM cosmological simulations. For consis-

tency with the literature, though, we will continue to refer to them as "problems." The three problems upon which activity is currently focused were identified thanks to the vast improvements in N-body simulations (both in terms of algorithms and computing power) that took place during the 1990s.

1.3.1   The Central Density Problem

Moore (1994) and Flores & Primack (1994) were the first to recognize the original small-scale problem, which has now become known as the *central density problem* or the *cusp/core problem*: the difference in structure between the dark matter density profiles observed in dwarf galaxies and the centrally concentrated profiles that CDM predicts. In a series of subsequent papers, Navarro, Frenk, & White (1995a, 1996, 1997, hereafter collectively NFW) formalized this problem by pointing out that N-body simulations predict that all CDM dark matter halos should share a universal density profile. The density profile that they defined, now called an NFW profile, is

$$\rho_{NFW}(r) = \frac{\delta_c \rho_{crit}}{(r/r_s)(1 + r/r_s)^2} \ , \tag{1.2}$$

where $\rho_{crit} = 3H^2/8\pi G \sim 10^{-29}$ g cm^{-3}, r_s is the scale radius, and δ_c is the characteristic overdensity associated with the halo (roughly the density at r_s, in units of the critical density). The density of this profile increases as r^{-1} toward the center of the halo, leading to a central density cusp, and declines as r^{-3} at large radii, so that over much of its radial extent the profile approximately follows an r^{-2} power law as required by the roughly flat observed rotation curves of spiral galaxies. The exact power-law index of the profile at small radii (the central slope) has been a continued point of debate since the original NFW result. Moore et al. (1999b) advocated a central power-law slope of -1.5, and other authors have also claimed steeper slopes (Fukushige & Makino 1997, 2001, 2003; Jing & Suto 2000; Ghigna et al. 2000; Klypin et al. 2001; Fukushige, Kawai, & Makino 2004). This argument has been essentially settled in recent papers, with Power et al. (2003) showing that there actually is no well-defined value of the central slope; the power law gets continuously shallower with radius, but on observationally relevant scales (i.e., $\gtrsim 100$ pc) the slope remains close to -1. Finally, Navarro et al. (2004) introduced a new density profile with an additional free parameter that removes the $\sim 10\%$ residuals between the simulated density profiles and the original NFW fit.

Observations, on the contrary, have generally shown that most dwarf galaxies and low-surface brightness (LSB) galaxies have very shallow central density profiles, frequently with central cores of nearly constant density (Moore 1994; Burkert 1995; Blais-Ouellette et al. 1999; Blais-Ouellette, Amram, & Carignan 2001; de Blok et al. 2001a; Borriello & Salucci 2001; de Blok, McGaugh, & Rubin 2001b; de Blok & Bosma 2002; Salucci, Walter, & Borriello 2003; Weldrake, de Blok, & Walter 2003; Simon et al. 2003a; Gentile et al. 2004). Controversy has erupted because of claims that the data used in many of these studies suffer from systematic uncertainties that severely limit their utility in distinguishing between cuspy CDM density profiles and shallow ones (van den Bosch et al. 2000; van den Bosch & Swaters 2001; Swaters et al. 2003a). de Blok, Bosma, & McGaugh (2003) argued that no single systematic problem could account for the difference between the observed and simulated density profiles, but were unable to rule out the possibility that multiple systematics could combine to produce the requisite effect. The analysis of a very large sample of long-slit Hα rotation curves by Spekkens, Giovanelli, & Haynes (2005) seems to have demonstrated conclusively that density profiles accurate enough to distinguish NFW profiles from constant-density cores cannot be derived from long-slit Hα spectroscopy of average quality. While extremely high quality long-slit data might improve the situation somewhat, it appears that two-dimensional velocity fields are required to determine the severity of the central density problem.

Assuming that the disagreement is real and not due to observational problems, theorists have been busily compiling a variety of possible explanations for the central density problem. Some of the proposals that have been advanced include changing the properties of the dark matter by making it self-interacting (Spergel & Steinhardt 2000), introducing feedback from star formation that substantially redistributes mass at the centers of galaxies, or invoking the triaxiality of dark matter halos, which can lead to apparent density profiles that are significantly shallower than the true density profiles along many lines of sight (Hayashi et al. 2005).

It is difficult to determine the relevance of many of these ideas to the real universe without observational input (and further observations are also needed to confirm that the central density problem actually exists), so the immediate hope for improving our understanding of the central density problem rests on high-quality measurements of galaxy density profiles.

1.3.2 The Substructure Problem

The challenge to CDM grew more daunting with the discovery of the *substructure problem*: the dramatic mismatch between the number of low-mass dark matter halos seen in CDM simulations and the number of dwarf galaxies observed in the real universe. It turns out that this problem was initially noted in semianalytic models by Kauffmann, White, & Guiderdoni (1993), but its significance was not fully appreciated until Klypin et al. (1999) and Moore et al. (1999a) independently simulated groups of galaxies similar to the Local Group in a CDM context and examined their properties. They both found that their simulated galaxy groups contained ~ 500 dark matter minihalos with masses greater than $\sim 10^8$ M$_\odot$, in rather serious disagreement with the population of ~ 35 known dwarfs in the Local Group. In the standard ΛCDM model, this prediction seems to be robust; there does not appear to be any way to avoid the presence of this abundance of substructure in galaxy halos. Fundamental changes such as introducing a small-scale cutoff in the primordial power spectrum (Kamionkowski & Liddle 2000) or making the dark matter warm rather than cold (Colín, Avila-Reese, & Valenzuela 2000; Bode, Ostriker, & Turok 2001) can alleviate the problem,. These solutions, however, are generally lacking in motivation from a fundamental physics perspective (e.g., there is no other evidence for a dark matter particle with a low enough mass to be warm) and may also suffer from undesirable side effects such as ruining the good agreement between CDM predictions of the Lyα forest power spectrum and observations. Instead, attention has focused on the efficiency of galaxy formation in low-mass halos. Can dark matter halos of this size acquire and hold on to enough gas to become dwarf galaxies? If so, will gas under these conditions ever become unstable to star formation? How can these processes be reconciled with the formation of *any* very low mass dwarf galaxies, which must be possible since they are observed to exist at the present epoch?

If we accept for the moment the hypothesis that these dark matter minihalos exist, then the question becomes whether or not they are detectable. One possibility is that they could gravitationally lens background sources. Although this effect will not be observable for Local Group halos, it could cause noticeable perturbations to distant gravitational lens systems. It has been known for several years that many gravitational lenses exhibit flux anomalies — while the positions of the lens images can be correctly predicted with simple, smooth lens models, the relative fluxes of the images are generally wrong (Mao & Schneider 1998; Metcalf & Madau 2001; Chiba 2002; Metcalf & Zhao 2002; Dalal & Kochanek 2002;

Kochanek & Dalal 2004). In fact, in some cases it can be shown that no smooth lens model is capable of matching the observed flux ratios. Instead, it appears that the lens galaxies are lumpy, with mass distributions that contain significant substructure at mass scales of $\sim 10^8$ M$_\odot$. What is not yet clear is whether these substructures are luminous or dark (since even galaxies as bright as the Large Magellanic Cloud are difficult to detect at high redshift) and whether the number of subhalos required is consistent with CDM. Preliminary indications are that the lenses may actually contain *more* substructure than CDM predicts (Metcalf et al. 2004).

The lensing results offer significant support for the possibility that numerous dark matter minihalos are present, but given the challenges entailed in obtaining detailed observations of galaxy groups at $z \gtrsim 0.5$ (a typical distance for lens galaxies), it will be difficult to demonstrate the existence of the predicted substructure conclusively with this technique. A promising alternative approach is to search for evidence of the substructure halos in the local universe, where their association (or lack thereof) with luminous objects can be clearly confirmed or ruled out. In particular, many authors have speculated that high-velocity clouds are connected to the substructure problem, and we will examine this hypothesis in detail. If the missing dark matter halos are actually present, that would represent a striking success for the CDM model. If not, one would be forced to conclude that our understanding of halo formation is in doubt. It should be noted, however, that such a failure of CDM would be difficult to prove. Absence of evidence, after all, is not necessarily evidence of absence.

1.3.3   The Angular Momentum Problem

The third of the small-scale problems with CDM stands somewhat apart from the first two in that it is clear that the simulations, rather than the observations, are at fault. The *angular momentum problem* is that simulations of disk galaxies produce disks that are too small and rotating too slowly compared to real galaxies (Navarro et al. 1995b). Somehow, the transfer of the initial angular momentum of a halo from the dark matter to the baryons is not efficient enough in simulations. Because there is no observational work needed to resolve this problem, we will not discuss it any further. Suffice it to say that significant progress is being made in our ability to simulate disk formation, and the most recent simulations suggest that the problem may soon be overcome (Robertson et al. 2004;

Governato et al. 2004).

1.4 Observational Tests of the Small-Scale Problems

In the following chapters of this thesis, we present our work addressing the substructure problem and the central density problem. In Chapters 2, 3, and 4, we investigate the possible existence of large numbers of low-mass dark matter halos in the Local Group, as suggested in §1.3.2. If these objects really are present, the only hope of directly detecting them lies in their association with stars and/or gas. We study the proposed relationship between high-velocity clouds (HVCs) and the missing dwarf galaxies, under the hypothesis that if the missing halos exist they are likely to have acquired some gas, and thus would appear as HVCs (Klypin et al. 1999; Moore et al. 1999a; Blitz et al. 1999). We begin in Chapter 2 by searching for low surface brightness optical counterparts to ~ 250 compact HVCs, which would be expected to exist if HVCs are associated with a large population of faint dwarf galaxies. If HVCs do contain stars, measuring their distances and masses would become straightforward.

In Chapter 3, we consider the case of a particularly intriguing HVC known as Complex H. Previous studies of this cloud suggested that it is very massive ($M_{HI} > 10^7 \ M_\odot$), but its location in the Galactic plane has prevented any optical counterpart from being identified. Outside the Local Group, such massive clouds are nearly always found to be associated with low surface brightness dwarf galaxies, so we use infrared and radio data to search for evidence that Complex H might be a dwarf galaxy as well. In Chapter 4, we employ high-resolution, wide-field H I observations to investigate the nature of another exceptional high-velocity cloud, HVC $127 - 41 - 330$. The maps we obtain allow us to derive unprecedented constraints on the distance and dark matter content of this object.

The following two chapters describe our efforts to resolve the question of whether the central density problem is real, or is only an artifact of observational systematic problems. Our observing campaign involves obtaining high-quality observations of a small sample of well-resolved, well-behaved galaxies, which we use to derive dark matter density profiles. In Chapter 5, we describe in detail how these data and other techniques help us overcome the systematics mentioned in §1.3.1, and we present a case study of one galaxy, NGC 2976. In Chapter 6, we apply the same analysis to a larger sample of five galaxies (incorporating the results of Chapter 5), and discuss our conclusions regarding the central

density problem. We also use the same data to probe the three-dimensional shapes of the dark matter halos of these galaxies in light of the expectation from CDM simulations that halos should be triaxial. In Chapter 7, we summarize the primary results of this thesis and assess the current status of the small-scale problems with the CDM model.

Chapter 2

The Absence of Stars in Compact High-Velocity Clouds

This chapter was previously published in *The Astrophysical Journal* (Simon & Blitz 2002, ApJ, 574, 726).

Abstract

We present the results of our search for faint Local Group dwarf galaxies in compact high-velocity clouds (HVCs). We used digitized Palomar Observatory Sky Survey (POSS) data to examine 1 deg^2 of sky around each of ~ 250 northern hemisphere HVCs. The POSS images were processed to remove foreground stars and large-scale backgrounds, smoothed to enhance arcminute-sized low surface brightness features, and then compared to the original plates. Using this technique, we located 60 candidate dwarf galaxies in the ~ 250 deg^2 that we surveyed. Followup observations of these candidates have revealed several distant clusters of galaxies and a number of possible Galactic cirrus clouds, but no Local Group dwarfs. It appears that many of the low surface brightness features in the sky survey data are plate flaws. The second-generation red POSS plates are sensitive down to surface brightness levels of $26 - 27$ magnitudes arcsecond^{-2}, and our followup images reached 10 σ limiting magnitudes of $R = 21 - 23$ for point sources. Given these limits, all known Local Group galaxies except four of the very diffuse, extended dwarf spheroidals located within 100 kpc of the Milky Way would have been definitively detected had they been in our survey.

Therefore, we can rule out the possibility that these HVCs are associated with normal but faint dwarf galaxies. If compact HVCs do contain stars, they must have surface brightnesses $\gtrsim 1$ mag arcsec^{-2} fainter than most known Local Group galaxies.

2.1   Introduction

The nature of the high-velocity clouds (HVCs) of neutral hydrogen has been a source of controversy since their discovery over 40 years ago and remains so today. It now appears that HVCs do not represent a single phenomenon. Rather, they are an amalgam of several types of objects that were grouped together by the extremely broad observational definition of "HVC": neutral hydrogen that is moving at velocities inconsistent with simple models of Galactic rotation. Some HVCs, notably the Magellanic Stream, are composed of gas that has been either tidally or ram-pressure stripped out of the Magellanic Clouds. Others are very extended clouds close to the Milky Way (distances of a few to a few tens of kpc) whose origin is not clear, although they appear to be extragalactic. Finally, there is a large population of small clouds (in angular size) whose properties have proven very difficult to determine. These were labeled compact HVCs by Braun & Burton (1999, hereafter BB99) and may represent a relatively homogeneous class of objects. We will concentrate on these HVCs for the remainder of this chapter.

One hypothesis that has received significant amounts of attention is that HVCs are clouds of primordial gas in the Local Group (LG), and thus are located at typical distances from the Milky Way (MW) of up to 1 Mpc (Oort 1966, 1970; Verschuur 1969; Kerr & Sullivan 1969). Blitz et al. (1999, hereafter B99) recently proposed a dynamical model based on this idea that simulates the evolution of the Local Group. The model is able to explain the properties of HVCs as the postulated primordial clouds, left over from the formation of the Local Group and currently falling into the LG barycenter. In addition to reproducing observed results of the spatial distribution and kinematics of HVCs, B99 make observational predictions about HVC masses, internal pressures, metallicities, and Hα emission, all of which are being actively investigated.

If the B99 hypothesis is correct, then HVCs must be embedded in $\sim 10^8$ M$_\odot$ dark matter halos in order to be gravitationally bound. The rough correspondence between the numbers and masses of HVCs in this model, and those of the population of low-mass dark matter halos predicted by Cold Dark Matter simulations of galaxy groups (Klypin et al.

1999; Moore et al. 1999a) has led many authors to speculate that the two classes of objects might be related. The search for optical counterparts to HVCs described in this chapter represents an important, but not conclusive, test of this idea.

Other potentially viable theories to explain the HVC puzzle include the Galactic Fountain model (Shapiro & Field 1976; Bregman 1980), the Tidal Debris model, and the new Hot Halo model (Maller & Bullock 2005). According to the Galactic Fountain model, large numbers of supernova explosions in the inner Galaxy expel hot, metal-rich gas from the Milky Way's disk into the halo. These clouds then cool and fall back towards the Galaxy and are seen as HVCs. In contrast, the Tidal Debris model proposes that all HVCs are nearby remnants of the tidal interaction between the Milky Way and the Magellanic Clouds or other, now-disrupted, dwarf galaxies. Maller & Bullock (2005) likewise proposed that HVCs are located relatively close to the Milky Way ($d \lesssim 150$ kpc), but in their model HVCs are cool clouds of gas that have recently condensed out of the massive, hot corona surrounding the Galaxy and are now falling towards us.

The best way to settle the question of the origin of HVCs is to measure their distances, since the four models prefer distances that differ by as much as two orders of magnitude. In this chapter, we describe our search for stars in HVCs, which if present could be used for photometric distance estimates. Despite the large amount of observational effort at 21 cm that has been devoted to HVCs, this work represents the first (and only) systematic, large-scale search for stars.

In §2.2, we will discuss the motivations for this work in more detail. Readers who are already familiar with the recent HVC literature may wish to skip ahead. We will describe our search technique and discuss the datasets used in our analysis in §2.3. §2.4 will briefly present the results of our search of the Palomar Observatory Sky Survey (POSS) data. In §2.5, we will describe our followup observations. The limits we have placed on the stellar content of HVCs and the implications of our results will be discussed in §2.6, and our conclusions will be presented in §2.7.

2.2 Motivations

2.2.1 Are HVCs the Missing Dwarf Galaxies in the Local Group?

Several lines of evidence have recently led to the hypothesis that HVCs are likely to contain stars. First, blind H I surveys of nearby galaxies and groups have found that the low-mass H I clouds they detect are often associated with low-surface brightness (LSB) dwarf galaxies (Banks et al. 1999; Kraan-Korteweg et al. 1999; Pisano & Wilcots 1999; Rosenberg & Schneider 2000; Boyce et al. 2001). This suggests that the LG H I clouds might be similarly associated with currently undiscovered dwarf galaxies. Second, H I has now been detected towards half of the LG dwarf spheroidal (dSph) galaxies and all of the dwarf irregular (dIrr) galaxies (Blitz & Robishaw 2000). In one case, this H I may have been previously classified as an HVC (HVC 561 = Sculptor) by Wakker & van Woerden (1991). The H I around the dSphs appears to be very extended compared to the optical galaxies and is of similar physical size and mass to the HVCs as described by B99. These similarities support the idea that HVCs and H I in dSphs could be related objects.

A further reason to suspect that HVCs might be associated with dwarf galaxies comes from numerical simulations of Cold Dark Matter (CDM) cosmological models. It has become well-known that these simulations produce too much substructure (Klypin et al. 1999; Moore et al. 1999a). In simulated Local Groups, the mass concentrations around MW and M31 analogs contain up to a few hundred small dark matter halos. The real LG is comparatively barren, with only ~ 35 known dwarf galaxies. If CDM is correct and these dark matter minihalos exist, they probably would have accreted some gas, and then could subsequently have formed stars (although see Bullock, Kravtsov, & Weinberg [2000] for one explanation of why star formation might be suppressed in such objects). In any case, it has been suggested by several authors that compact HVCs could be these "missing" dark matter halos (e.g., Klypin et al. 1999; Moore et al. 1999a).

Finally, it is almost certain that the census of Local Group galaxies is not yet complete. In the past several years, at least five new dwarfs have been discovered: And V by Armandroff, Davies, & Jacoby (1998, hereafter A98), And VI by Karachentsev & Karachentseva (1999, hereafter KK99) and Armandroff, Jacoby, & Davies (1999) independently, And VII by KK99, Cetus by Whiting, Hau, & Irwin (1999), and And IX by Zucker et al. (2004). A sixth dSph, Antlia, was first cataloged by Corwin, de Vaucouleurs, & de Vaucouleurs (1985) and Feitzinger & Galinski (1985), and detected in H I by Fouque et al.

(1990), who suspected it to be a Local Group member. Followup photometry confirming this conjecture was not acquired until the galaxy was rediscovered by Whiting, Irwin, & Hau (1997) several years later. An increasing number of proposed Milky Way satellites are also being identified in Sloan Digital Sky Survey and 2MASS data (e.g., Newberg et al. 2002; Rocha-Pinto et al. 2004; Willman et al. 2005a,b). In addition to these recent discoveries, Mateo (1998) noted that there is an apparent deficit of dwarf galaxies at low Galactic latitudes (relative to a uniform distribution on the sky). On this basis, he postulated up to $15 - 20$ LG dwarfs remaining to be discovered at $b \leq 30°$.

2.2.2 Recent HVC Results

Recent observations of HVCs have tended to at least roughly agree with the predictions made by B99. The internal pressures of high-velocity clouds, as determined by ultraviolet absorption line studies, are low in the few clouds that have been observed. This finding is consistent with the HVCs being LG objects (Sembach et al. 1999). The metallicities of HVCs (other than the Magellanic Stream material) have been found to be $0.1 - 0.3$ times solar, also within the range predicted by B99 (Wakker et al. 1999; Murphy et al. 2000; Richter et al. 2001; Gibson et al. 2001; Sembach et al. 2002; Tripp et al. 2003). Some of these measurements are toward the high end of what can be reasonably accommodated by the Blitz et al. model, and if lower metallicity HVCs are not found, this may eventually present a problem for the extragalactic hypothesis. The Galactic Fountain model, though, faces an even bigger challenge, since it predicts solar or higher metallicities for high-velocity gas. It should be noted that all but one of these metallicity determinations are for nearby HVCs that are part of the large complexes. These complexes are believed to be interacting with the Milky Way, and might have been partially enriched as a result. Therefore, these metallicity measurements do not necessarily apply to the presumably more distant and isolated compact clouds, and in fact, may be regarded as upper limits to the metallicities of compact HVCs. A further caveat to the metallicity determinations is that they rely on comparing optical and UV absorption column densities, which probe gas on scales of $\sim 10^{-4}$ arcseconds, with H I observations on an angular scale at least four orders of magnitude larger. The effects of this mismatch are not known.

Hα emission from HVCs has also been observed, but the results of this work are difficult to interpret. A number of researchers have used Fabry-Perot instruments to detect

~ 20 HVCs in Hα, and sometimes also in the nearby N II and S II emission lines (Kutyrev & Reynolds 1989; Tufte, Reynolds, & Haffner 1998; Bland-Hawthorn & Maloney 2002; Weiner, Vogel, & Williams 2002). By comparing the strength of the emission from these clouds with that from gas at known distances (e.g., nearby complexes or the Magellanic Stream), one can estimate the distances to the HVCs. Bland-Hawthorn & Maloney (2002) and Weiner et al. (2002) conclude based on their observations that the HVCs they detect are probably nearby, at distances of tens of kpc. However, their method depends critically on the assumption that HVC ionization is caused primarily by photoionization from the Milky Way's UV field. Although this assumption seems reasonable, it appears to be false for the Magellanic Stream gas (Weiner & Williams 1996). Furthermore, these calculations do not work well for at least one object whose distance is known independently: the Sculptor dwarf spheroidal galaxy. Sculptor is located 80 kpc from the Milky Way, yet it is brighter in Hα than Complexes A, C, and M, which are all an order of magnitude closer. If the HVC distance estimates are normalized to Sculptor instead of Complexes A and M, significantly larger distances (up to ~ 200 kpc) will be derived. In support of the shorter distance scale, Weiner et al. (2002) note that none of the HVCs they observe have fluxes close to their detection limit; every object is at least an 8 σ detection. They argue that the lack of Hα-faint HVCs implies that HVCs are not very far away. As with the metallicity studies cited above, though, many of these observations have been of the HVC complexes that were already known or suspected to be nearby. Until there has been a comprehensive Hα survey of the compact HVCs *and* there is a reliable way to relate HVC Hα fluxes to distances, these observations will not offer strong confirmation or refutation of any HVC models.

2.2.3 A New Technique

Faced with this confused state of affairs, we decided to take a different approach to the HVC problem. The key objects are the ones whose nature is most uncertain: compact HVCs. Since there does not appear to be a simple way to determine their distances directly with current techniques (although see Chapter 4 for a special case), we have attempted an indirect method — searching for stellar counterparts to the HVCs. If we could detect such stars, it would be straightforward to obtain accurate photometric distances to them, and thereby conclusively establish the nature of the high-velocity clouds.

2.3   Search Methodology

2.3.1   POSS Image Processing

The machinery for our search is based loosely on the work of A98 for their similar project (a blind survey for dSph companions of M31). Starting from the outline they provided, we developed an algorithm that processes digitized POSS images[1] from the Space Telescope Science Institute (STScI) to enhance extended LSB objects of the appropriate angular size to be Local Group dwarf galaxies. We adopt similar steps, but in a different order and with significant changes in implementation from A98. Our technique also borrows significantly from the algorithm employed by Schlegel, Finkbeiner, & Davis (1998) to remove point sources from the IRAS all-sky maps. The algorithm is described in detail in the following paragraphs. All of the image processing was done in the IDL environment.

We first attempt to remove the brightest stars from the image. Because these stars have such extensive wings, this task will be incompletely successful, at best. Nevertheless, we can remove enough of the flux that these stars will not dominate the smoothed image, even though they will still be visible. Bright stars are located with a simple count threshold — any pixel with a value of more than 23000 counts was defined to be part of a bright source. This method can succeed because our search largely employed the POSS-II red plates (for $\sim 80\%$ of our targets), which tend to have similar sky background levels ($5000 - 6000$ counts on average) and sensitivities. Having found the brightest stars, we create a circular mask around each one and replace the pixels in the mask with an average of the surrounding pixels.

This process is repeated in order to remove the fainter stars from the image as well. However, because objects other than faint stars can have peak brightnesses as high as or higher than those of the stars, we must use a slightly different technique to detect these stars. We pass a small ($\approx 10''$) median filter over the image, and then subtract the filtered version from the original. Point sources are seriously degraded in flux in the filtered image, and so appear bright in the difference image. Extended sources are only

---

[1]The Digitized Sky Survey was produced at the Space Telescope Science Institute under U.S. Government grant NAG W-2166. The images of these surveys are based on photographic data obtained using the Oschin Schmidt Telescope on Palomar Mountain and the UK Schmidt Telescope. The plates were processed into the present compressed digital form with the permission of these institutions.

minimally affected by the filtering and therefore are largely removed by subtracting the images. Objects brighter than a threshold value of 1000 counts per pixel in the difference image are likely to be foreground stars. The point sources selected with this criterion are masked out and replaced, as described above.

Now that the image is relatively free of stellar light, we must deal with the other major contaminant, the background. Unfortunately, the digitized POSS plates are not flat, especially near the edges, and these background variations significantly hamper a search for LSB galaxies. In order to detect the small increases in surface brightness over a limited area that are associated with dwarf galaxies, the vignetting of the plates and any other large-scale flaws in them must be removed as accurately as possible. We experimented with two-dimensional polynomial fits to the background, but determined that the most reliable means of subtracting just the background (and leaving objects of interest alone) was simply to employ a very wide median filter. The filter must be large enough not to pick up significant signal from dwarf galaxies, or else this procedure could become counterproductive. The largest of the distant dSphs are $\sim 5'$ across, so a filter more than $10'$ wide will be at least four times as large as any dwarf galaxies it encounters. Empirically, this level of filtering seemed to be safe, so we chose a filter width of 600 pixels, corresponding to $10.1'$ on POSS-II and Equatorial Red plates, and $17'$ on POSS-I and SERC-J plates. To deal with the 300 pixel border around the image where the median filter was too close to the edge to function, we simply replicate the last line or column that the median filter did produce outward to the edges of the image.

After removing the background, we treat the bright stars again, because they still tend to be the brightest sources left in the image (although not overwhelmingly so). At every location where a bright star was removed earlier, we check to see if the average brightness is still more than half a standard deviation above the median for the image. If so, we cut out a larger mask around these remnants, and again replace it with an average of the surrounding pixels.

Finally, we smooth the image with a dwarf-galaxy-sized filter in order to further dim the remaining stellar light, and thereby enhance the relative contrast between high- and low-surface brightness objects. We use a Gaussian filter here rather than a median filter because the filter size is such that a median filter runs the risk of smoothing away the entire image. According to Davies et al. (1994), to optimally detect LSB objects the filter should be roughly the same size as the object. At the distances we expect for the HVCs —

300 kpc to 1 Mpc — dwarf galaxies have angular sizes between $1'$ and $6'$. Therefore, we use a 70 pixel ($= 71''$ on POSS-II images and $119''$ on POSS-I images) filter. We choose a filter on the small end of the dwarf galaxy size range because (1) most of the detected objects will be at large distances (due to the greater survey volume there), and (2) we do not want to degrade potential dwarf galaxy signals by smoothing over too large a scale. Since we are not using adaptive filtering here, we are not sensitive to LSB sources of all possible angular sizes. Objects that are smaller than $\approx 30''$ may be missed by our search because of this final filter, and objects larger than $\approx 15'$ could be removed by our background filter.

The free parameters in this algorithm (order of steps, mask and filter sizes, etc.) were tuned by extensive testing on known dwarf spheroidal galaxies, primarily the 7 eponymous companions of Andromeda. In Figure 2.1, we compare processed images of two of the lowest surface brightness LG dSphs with the original POSS-II plates. It is clear that the algorithm works well. Even though the dwarfs are barely visible in the unprocessed POSS-II images, they are the brightest objects in the field of view — dominating the 10th magnitude foreground stars — after smoothing.

2.3.2   HVC Catalogs

We used the catalog of compact high-velocity clouds provided by Braun & Burton (1999) as the basis for the first part of our search. They selected HVCs visually from the Leiden/Dwingeloo Survey of Galactic Neutral Hydrogen (Hartmann & Burton 1997) and from the large HVC catalog compiled by Wakker & van Woerden (1991). BB99 identified a subset of 65 clouds that are both small (less than $2°$ in diameter) and isolated from neighboring emission. They claimed that these objects represent a distinct class of HVCs and are all at Local Group distances. We included the 59 of these HVCs that were located outside the zone of avoidance ($|b| > 5°$) in our sample. BB99 also presented ~ 15 deg^2 H I maps around each of the compact HVCs (see their Figure 1). In many of these moment maps, there are nearby clouds that have comparable intensities. Since it is not entirely clear why these clouds were not included in their catalog, we have chosen 17 of the most prominent of them to use in our analysis as well, for a total of 76 HVCs from BB99.

In addition to these compact HVCs, we also selected targets from the new catalog by Robishaw & Blitz (T. Robishaw, private communication, 2000, hereafter RB00), a complete sample derived from an automated search of the Leiden/Dwingeloo Survey (LDS).
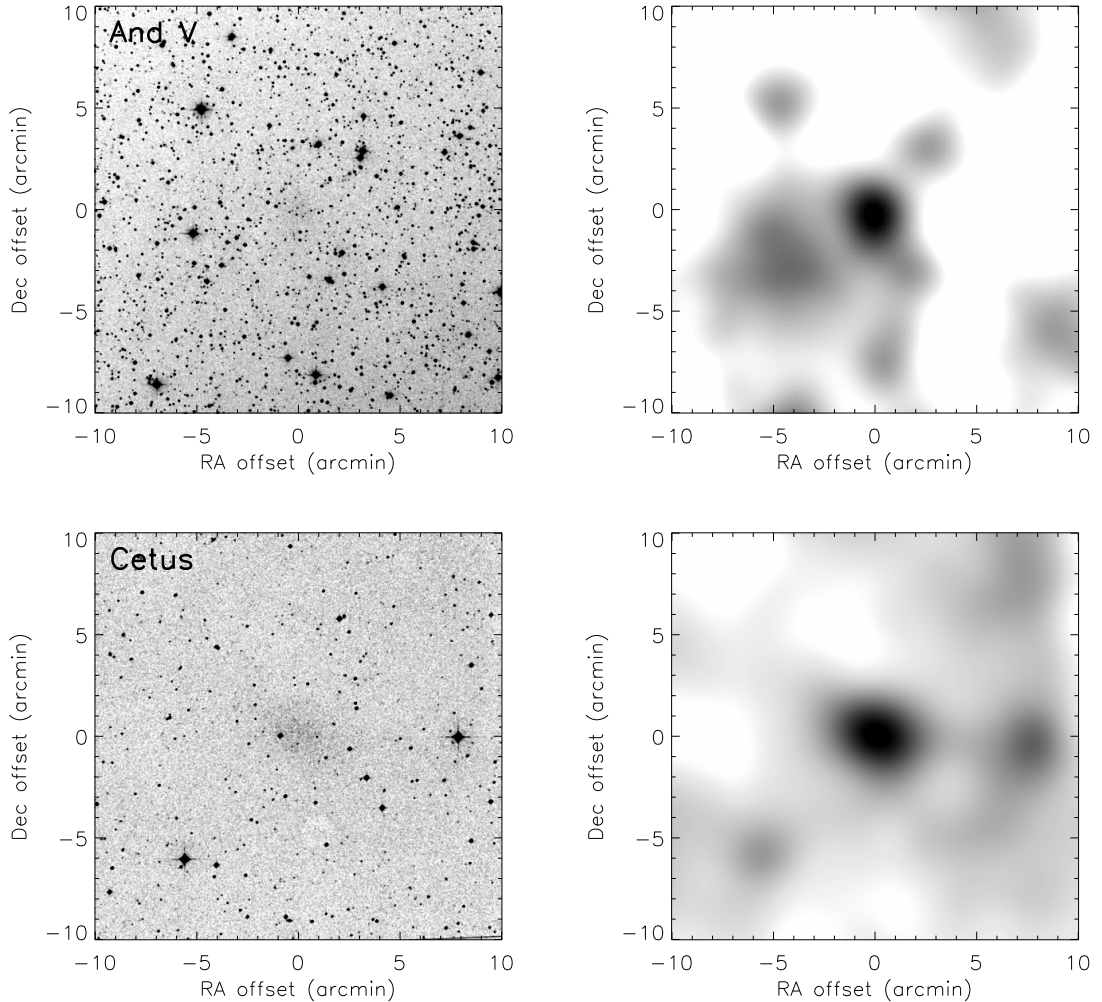
Figure 2.1 — Demonstration of our POSS processing algorithm. On the left are POSS-II red images of two of the lowest surface brightness dwarf spheroidals in the Local Group: And V (top) and Cetus (bottom). The galaxies are just visible as faint smudges at the center of each frame. On the right are the same fields after applying our algorithm. In each case, the dSph has become the brightest object in the image.

Since this catalog is a work in progress, we were forced to take a fairly simplistic approach to defining HVCs. We first selected all H I detections with velocities $|v_{\mathrm{LSR}}| \geq 200$ km s^{-1}. From this list, we grouped the H I detections into clouds by defining as part of a single object all H I within $3°$ in both longitude and latitude, and within 10 km s^{-1} in velocity of the brightest point (the brightest point was also defined as the central position). We then culled this list to eliminate HVCs that could not be observed easily from Lick Observatory

(clouds outside the range $-10° \leq \delta \leq 65°$). This left us with 201 HVCs. It should be noted that, while the final RB00 catalog will be a flux-limited sample down to the sensitivity limit of the LDS, this preliminary version is not. We have certainly missed a number of HVCs by focusing only on the highest velocity clouds. Furthermore, these HVCs are not entirely the compact specimens that we believe are the most distant objects; some of the northernmost Magellanic Stream clouds met the criteria described above, and so have been included. Still, many of these clouds are indeed compact HVCs, and the combination of this list with the catalog of BB99 should include most of the compact HVCs in the northern hemisphere. (Putman et al. [2002] found 179 compact HVCs and 159 slightly more extended clouds in the southern hemisphere in their search of the HIPASS data, and there should be a comparable number in the northern hemisphere.) The positions that we searched are plotted on the sky in Figure 2.2. Finally, we point out that 12 of the BB99 HVCs and one of the secondary clouds were also in the RB00 catalog (the others were excluded by the velocity and declination restrictions). In these cases, we searched around the central positions given by each catalog, so there was necessarily some overlap. Several of the RB00 HVCs were also separated from each other by less than 1°. Taking such occurrences into account, our survey covers 264 unique HVCs and approximately 239 deg^2 of sky. We also searched 54 deg^2 in areas that do not contain an HVC, which can be used for a comparison of results.

2.3.3 Sky Survey Images

STScI has made available digitizations of the following sky surveys that are of use to us:[2] POSS-I[3] (red plate only) for the northern hemisphere; POSS-II[4] (red plate only) for approximately 2/3 of the northern sky; SERC-J[5] plates (blue) for the southern sky;

---

[2]Note that this description refers to the time of the beginning of our search (late 1999); at present, the Digitized Sky Survey (DSS) includes all of the POSS-II red and blue data.

[3]The National Geographic Society - Palomar Observatory Sky Atlas (POSS-I) was made by the California Institute of Technology with grants from the National Geographic Society.

[4]The Second Palomar Observatory Sky Survey (POSS-II) was made by the California Institute of Technology with funds from the National Science Foundation, the National Aeronautics and Space Administration, the National Geographic Society, the Sloan Foundation, the Samuel Oschin Foundation, and the Eastman Kodak Corporation. The Oschin Schmidt Telescope is operated by the California Institute of Technology and Palomar Observatory.

[5]The UK Schmidt Telescope was operated by the Royal Observatory Edinburgh, with funding from the UK Science and Engineering Research Council (later the UK Particle Physics and Astronomy Research Council), until 1988 June, and thereafter by the Anglo-
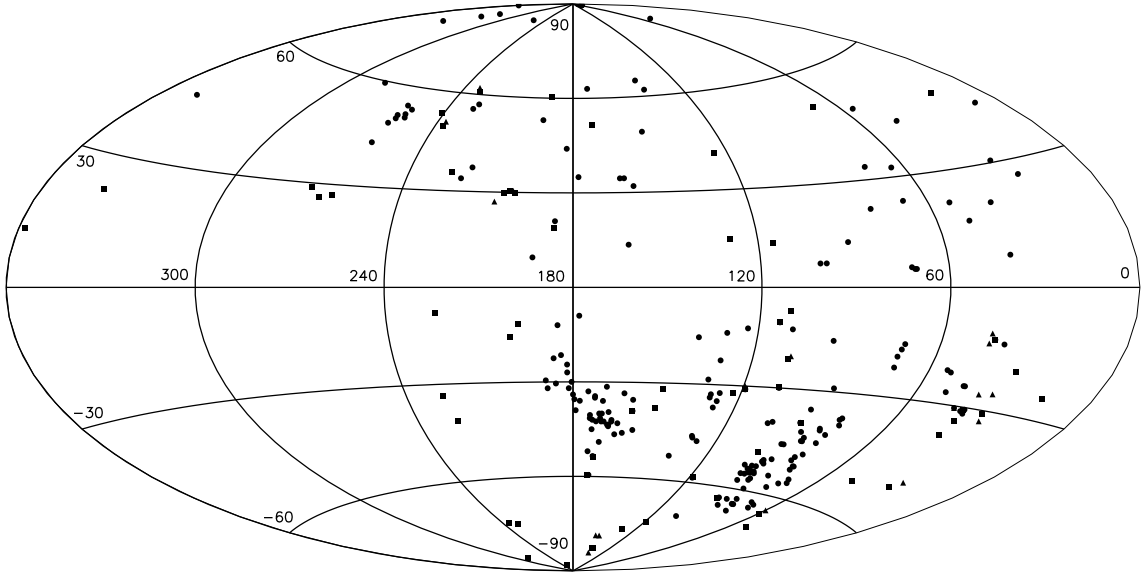
Figure 2.2 — Distribution on the sky of the HVCs we searched. The squares represent HVCs from the BB99 catalog, the circles are HVCs from the catalog of Robishaw & Blitz, and the triangles are secondary clouds selected from BB99. The concentration of HVCs along $\ell = 90°$ between $b = -35°$ and $b = -65°$ shows that both catalogs contain significant numbers of Magellanic Stream clouds.

Second Epoch Survey (red) for a small fraction of the southern hemisphere; and Equatorial Red plates for the region around $\delta = 0°$. This means that at any position we only have access to images of one color, except for a small band around the equator. Furthermore, many positions are only covered by a single plate (especially at $\delta \leq -3°$) from one of these five surveys, making it difficult to distinguish the numerous plate flaws and background variations from real astronomical objects.

By examining the existing data on H I in known dSph galaxies, we determined that in most cases the centroid of the H I distribution is less than $30'$ from the optical galaxy. Of the 10 dSphs found by Blitz & Robishaw (2000) to contain H I gas, 7 meet this criterion, and therefore would have been discovered in our survey if they had not already been known. Extending the search radius to $1°$ would guarantee that we would find virtually all dSphs that are similar to the known ones, but we judged that the 400% increase in area to search

---

Australian Observatory. The blue plates of the southern Sky Atlas and its Equatorial Extension (together known as the SERC-J), as well as the Equatorial Red (ER), and the Second Epoch [red] Survey (SES) were all taken with the UK Schmidt.

that this would require was not worth the $\sim 40\%$ gain in sensitivity. Thus, in our survey for new galaxies, we searched a box $1°$ on a side centered on each HVC in the sample. For the BB99 compact HVCs, we used the POSS-I and SERC-J survey data, because they had the most complete sky coverage. After completing this, a $30'$ wide box around each HVC position was re-examined using POSS-II, SES, or Equatorial Red plates, as available. This process gave us greater sensitivity in the area near the center of each HVC. By the time we reached the RB00 HVCs, most of the POSS-II data were online, so we performed our search of these objects with only the $1°$ POSS-II images (or the best other plate if no POSS-II plate was available).

The search was carried out by processing our downloaded images with the algorithm described above. We compared the processed frames with the originals, blinking back and forth between them. LSB objects showed up as bright spots on the processed images. Every position where such a bright spot was seen and no obvious stellar or galactic counterpart was visible on the unprocessed image was flagged. After this comparison, each flagged region was examined closely by eye on the unprocessed image, using various stretches to best view the LSB feature. Some of these smudges were clearly related to bright Galactic cirrus, other types of nebulae, plate flaws, ghost images, or the wings of bright stars. Such objects were eliminated from consideration. The remaining objects were compared to any other frames of the field in question (POSS-I, or a neighboring POSS-II plate) that were available from STScI. Objects that were visible on a second plate and appeared morphologically like a dwarf galaxy were immediately labeled candidates. Some objects that were not confirmed on additional plates were also added to the candidate list if no other plate was available for comparison, or if their morphology was particularly convincing.

2.4   POSS Search Results

We surveyed one square degree of sky around each of 264 HVCs. Because some of the HVCs were close together, the total area searched was about 239 deg^2. Our survey revealed 60 low-surface brightness objects, for an overall candidate identification rate of 0.25 deg^{-2} of sky searched. Of these, 18 were towards the 59 BB99 compact HVCs (0.31 deg^{-2}) in our sample, and 5 were in the direction of the 17 secondary objects (0.29 deg^{-2}). The remaining 37 were found while examining the 188 HVCs from the RB00 catalog (0.20 deg^{-2}). The positions of these LSB dwarf galaxy candidates are listed in Table 2.1. For

comparison, we also searched (mostly by accident) 54 $\deg^2$ of sky that were not associated with any known high-velocity gas, and found 10 additional LSB features (0.19 $\deg^{-2}$). Without even following up on the candidates, we can see that there is not a large excess of them in the direction of HVCs relative to their abundance in random patches of sky. The somewhat higher smudge detection rates for the BB99 HVCs are not statistically significant.

Table 2.1: The Candidate Dwarf Galaxies Identified in Our Survey

HVC name[a]	α_{J2000}[b]	δ_{J2000}	point source overdensity	nebular counterpart	limiting R_s magnitude of followup image	HVC catalog[c]
104−70−312	00 24 36	−08 09 54	yes	no	22.3	RB
120−30−289[d]	00 38 34	32 43 47	no	no	21.4	BBS
	00 38 40	32 48 22	no	yes	22.7	BBS
118−58−373	00 42 13	04 32 07	yes	no	22.6	BB
124−13−214	00 55 44	50 23 51	no	no	22.6	RB
156−45−303	02 24 40	11 46 50	no	yes	21.3	RB
	02 24 59	11 21 47	no	no	21.4	RB
171−54−235[e]	02 36 08	−00 48 08	yes	no	22.2	BB
158−39−280	02 40 43	16 31 28	no	no	22.1	RB
158−39−285	02 41 41	16 17 15	no	no	22.4	BB
169−43−259	03 01 38	08 14 55	no	no	21.9	RB
169−40−235	03 07 46	10 25 00	no	no	22.1	RB
189−32+202[f]	04 16 23	03 47 29	no	yes	21.5	RB
189−32+248						
182−25−203	04 25 34	13 26 43	no	yes	22.5	RB
162+14−382	06 02 42	51 25 53	no	no	22.9	RB
159+32+268	08 03 13	58 25 30	no	no	23.3	RB
200+30+075	08 24 04	23 38 59	no	yes	23.0	BB
204+30+061	08 26 44	20 15 15	no	no	22.3	BB
237+50+078	10 24 49	06 36 41	yes	no	22.7	BB
237+51+120	10 30 23	07 47 05	no	no	22.6	BBS
261+49+160	11 07 16	−04 54 41	yes	no	22.6	RB
143+65+285	12 00 44	50 06 15	no	no	22.8	RB
	12 02 51	50 22 58	yes	no	23.2	RB
050+81−442	13 29 31	29 13 00	no	no	23.4	RB
347+46−215	14 49 56	−06 42 22	no	no	21.9	RB
347+46+259						

Table 2.1 – Continued

HVC name[a]	α_{J2000}[b]	δ_{J2000}	point source overdensity	nebular counterpart	limiting R_s magnitude of followup image	HVC catalog[c]
070+51−146	15 48 55	43 49 50	no	no	21.9	BB
046+44+201[g]	16 20 30	26 54 03	no	no	22.3	RB
068+24−269	18 14 17	40 53 18	no	yes	23.2	RB
080+22−205	18 44 47	50 31 58	no	yes	23.2	RB
043−13−314	19 55 56	02 43 48	no	yes	22.1	BB
043−13−267						
039−27−310	20 36 19	−07 11 15	no	no	21.9	BBS
046−25−235	20 41 02	−01 16 49	no	no	21.4	RB
031−33−330	20 47 33	−16 20 36	no	no	21.6	BBS
039−31−278	20 51 55	−08 26 19	no	no	21.9	BB
	20 52 21	−08 17 35	no	yes	21.8	BB
040−31−272	20 53 22	−08 25 30	no	no	21.6	RB
043−31−236	20 58 39	−05 41 00	no	no	21.8	RB
072−16−395	21 10 03	24 01 16	no	no	20.2	RB
039−37−238	21 15 21	−11 40 21	no	no	21.8	BB
079−37+213	22 32 37	13 10 41	no	no	22.4	RB
079−37+235						
079−37+252						
080−42−329	22 46 29	10 09 49	no	yes	22.2	RB
083−49−307	23 09 23	05 27 13	no	no	21.1	RB
083−50−325	23 11 24	05 17 13	yes	no	22.2	RB
050−68−201	23 23 12	−19 09 33	no	no	21.1	BB
111−07−466	23 24 53	53 58 00	no	no	22.6	BB
	23 26 30	53 49 12	no	yes	22.8	BB
093−52−312	23 38 57	06 09 19	no	no	21.1	RB
093−52−266						
108−21−395	23 39 46	39 25 39	no	no	20.0	BB
	23 40 37	39 23 25	no	no	21.3	BB
093−55−276	23 43 02	04 28 13	no	no	21.5	RB
080−66−226	23 44 55	09 15 57	no	no	22.1	RB

Table 2.1 – Continued

HVC name[a]	α_{J2000}[b]	δ_{J2000}	point source overdensity	nebular counterpart	limiting R_s magnitude of followup image	HVC catalog[c]
097−53−384	23 48 35	07 07 42	no	yes	21.5	RB
107−30−421	23 48 55	31 28 44	no	yes	22.6	BB
114−11−441	23 49 28	50 57 13	yes	no	22.8	RB
100−49−395	23 50 19	10 48 33	no	no	22.9	RB
	23 50 51	11 27 13	no	no	23.0	RB
097−54−363	23 51 04	05 54 15	no	no	22.4	RB
096−58−273	23 54 18	02 36 42	no	yes	21.5	RB
114−10−440	23 55 04	51 26 45	no	yes	21.1	BB
089−65−312	23 55 35	−06 04 29	no	no	21.5	RB

[a]HVC names are given using the convention of Braun & Burton (1999): 3-digit Galactic longitude, appended with 2-digit Galactic latitude and 3-digit LSR velocity.

[b]The candidate positions should be accurate to $\approx 30''$.

[c]BB refers to HVCs from the BB99 catalog, BBS to secondary clouds selected from BB99's moment maps, and RB to HVCs from the RB00 catalog.

[d]In several cases, we found two LSB objects near one HVC; for these HVCs, the LSB counterparts are listed in order of increasing RA. If we have to refer to them by name, they are called $\ell\ell\ell - bb - vvv$a and $\ell\ell\ell - bb - vvv$b.

[e]Note that BB99 list the wrong declination for this HVC in their Table 1. The actual declination for the given Galactic coordinates is −00 55, not +00 55.

[f]There are multiple HVCs at this position, so the individual components are listed on separate lines. The same is true for five other HVCs in the table.

[g]We observed this HVC in H I with the 305 m Arecibo radio telescope for a separate project and did not detect it, despite the clear signal present at this position in the LDS. We speculate that the LDS "detection" might be interference and that there may not actually be an HVC here.

2.5   Optical Followup Observations

2.5.1   Observing Setup

We obtained followup images of each of the candidate dwarf galaxies from Lick Observatory. We observed with the 1 m Anna L. Nickel Telescope for 12 nights between 1999 July and 2000 April. Conditions during these nights were generally close to photometric, although there were occasional clouds that our observations avoided. The seeing varied from $1''$ to $2''.5$. Our primary detector was CCD5, a 1024×1024 thinned SITe CCD with 24 μm pixels ($5'$ field of view). However, for two nights during which this instrument was unavailable, we used CCD2, an older 2048×2048 L30 464-5 thick phosphor coated CCD with 15 μm pixels ($7'$ field of view).

We also used the 3 m Shane Telescope for deeper followup observations. We observed for 5 nights (2000 April 6–7 and 2000 September 28–30) with the Prime Focus Camera. This instrument utilizes a 2048×2048 SITe CCD with 24 μm pixels to provide a $10'$ field of view. These nights also ranged from photometric to partly cloudy, with variable seeing, but again, our observations were not significantly affected by the clouds.

With both telescopes, we chose to employ a Spinrad R (R_s) filter for most of our observations. We avoided using standard R filters because of the extremely strong Na D lines in the Lick Observatory sky, and we felt that I-band observations would also result in the sky being too bright. The R_s filter is centered at 6850 Å, with a FWHM of approximately 1500 Å(somewhat redder, more symmetrical, and wider than Cousins R), and was designed specifically to suppress the nearby night sky emission lines. R_s magnitudes tend to be similar to Johnson R magnitudes — within 0.1 mag for $-0.8 < V - R < 1.8$ (Djorgovski 1985). On the 1 m telescope, we typically observed each object for 1 hour, and on the 3 m for 15 to 30 minutes. During the course of each night, we observed standard star fields chosen from the Landolt (1992) catalog to obtain photometric calibrations, as described below.

2.5.2 Data Reduction and Analysis

Most of our data reduction was done in IDL, although we used IRAF[6] for some of the photometry. Processing consisted of subtracting off a dark frame (for the 1 m images) or an overscan region (for the 3 m images), flatfielding with a twilight or dome flat, and flatfielding again with a sky flat if necessary. We removed cosmic rays with the QZAP routine. The frames were then shifted and coadded to yield a single image for each object. We obtained 8 to 30 standard star observations per night, which we used to construct a photometric solution of the following form:

$$R_s = m_{\mathrm{instr}} + C + f \times (V - I) + g \times (a - 1), \tag{2.1}$$

where R_s is the apparent Spinrad R magnitude, m_{instr} is the instrumental magnitude, C is the constant offset, f is the color coefficient, $V - I$ is the known or assumed Johnson-Cousins color of the object, g is the tabulated Lick mean extinction coefficient,[7] and a is the airmass. Equation 17 from Djorgovski (1985) was used to convert the Cousins R magnitudes that Landolt (1992) measured for the standard stars into Spinrad R magnitudes. (The diligent reader will note that Djorgovski's Equation 17 actually gives the transformation between *Johnson R* and R_s. This mismatch between the Johnson and Cousins systems could lead to a systematic error of order 0.1 mag, which is not large enough to affect our results. An equally important systematic effect is that the optical path + detector combination we used is quite different from that which Djorgovski calibrated in 1985.)

We used a local-maximum-finding algorithm to detect stars and galaxies in our images. Artificial star tests demonstrated that this algorithm finds essentially all sources that are detected at the 10 σ level or higher. Aperture magnitudes were calculated for each of the detected sources with the DAOPHOT package (Stetson 1987) in IRAF. These magnitudes were converted to R_s using Equation 2.1, and assuming that $V - I = 1.1$ (approximately the correct color for the most luminous red giants). Since the color coefficient was usually of order 0.1, this estimate can be off by several tenths of a magnitude without having any appreciable effect.

After locating the sources and deriving their magnitudes, we checked the coadded

---

[6]IRAF is distributed by the National Optical Astronomy Observatories, which is operated by the Association of Universities for Research in Astronomy, Inc. (AURA) under cooperative agreement with the National Science Foundation.

[7]http://www.ucolick.org/ mountain/mthamilton/techdocs/info/lick-mean-extinct.html

images for overdensities of point sources around the positions of the dwarf galaxy candidates. We traced out a region of interest around each candidate and compared the surface density of sources inside and outside the regions over various magnitude bins. We considered magnitude ranges starting with all the objects brighter than the magnitude limit and fainter than a tip of the red giant branch (TRGB) star at about 100 kpc: $R_s = 16.5$ (since our survey technique is not sensitive to galaxies closer than this distance). We then decreased the bright limit by one magnitude at a time to create successive bins (see Table 2.2 for an example). We used Poisson statistics to quantify the uncertainty in the number of stars expected to lie inside the region based on the background surface density. Overdensities of $3\,\sigma$ or higher were considered significant enough to warrant further investigation.

2.5.3 Results

If there were a resolved dwarf galaxy in the field being examined, one would expect to see an overdensity through all of the magnitude ranges. This overdensity would increase in significance as the bright end of the magnitude bins approached the TRGB of the galaxy, reaching a maximum near the bin where the TRGB was closest to the bright edge of a bin. Visually, a dwarf galaxy should also show an obvious clustering of "undetected" faint stars that do not meet our $10\,\sigma$ limit for photometry, since the red giant branch is more populated at lower luminosities. We searched each image for point source overdensities of at least $3\,\sigma$ in one magnitude bin. Eight of the counterparts met this criterion, with the most significant one having a maximum overdensity of $\sim 11\,\sigma$.

As a comparison, we observed the dwarf spheroidals And III and And V. And III has a total luminosity of $M_V = -10.2$ and a central surface brightness of $\mu_{\rm v} = 24.49$ mag arcsec^{-2}, and given its distance of 760 kpc and the Galactic extinction ($A_R = 0.15$ mag), the TRGB should be located at $R = 21.15$ (Caldwell et al. 1992; Armandroff et al. 1993; Schlegel et al. 1998). And V is a significantly fainter galaxy, with $M_V = -9.1$ and $\mu_{\rm v} = 25.01$ mag arcsec^{-2}, and is slightly farther away and more extincted (810 kpc, $A_R = 0.33$ mag), so it should show a red giant branch starting at $R = 21.48$ (Caldwell 1999; Armandroff et al. 1998; Schlegel et al. 1998). Our results for 3 m observations of And III (15 minutes) and And V (21 minutes) are given in Table 2.2. Based on a comparison between the stellar densities and the background surface density, we detected about 160 stars in And III and 80 in And V. Both galaxies were detected at the $10.9\,\sigma$ level or higher in every

magnitude bin, and the highest overdensities ($\sim 15\ \sigma - 20\ \sigma$) appear in the bins that begin closest to the TRGB magnitudes, matching our expectations. The decreased overdensities seen in the last bin imply that the observations were affected to some degree by crowding or incompleteness at that magnitude level. We also imaged And V for 20 minutes with the 1 m telescope (this exposure was much shorter than any of our observations of dwarf candidates) and detected the galaxy at 4.0 σ in the faintest magnitude bin. This significance level corresponds to 12 stars above the background density over the area of the dwarf galaxy.

Table 2.2.   Detections of Stars in Known Local Group Dwarf Spheroidals

Galaxy	Magnitude Range	Stellar Overdensity	Galaxy	Magnitude Range	Stellar Overdensity
And III	$16.5 - 23.0$	$18.8\ \sigma$	And V	$16.5 - 22.9$	$10.9\ \sigma$
	$17.0 - 23.0$	$18.8\ \sigma$		$16.9 - 22.9$	$10.9\ \sigma$
	$18.0 - 23.0$	$19.3\ \sigma$		$17.9 - 22.9$	$11.3\ \sigma$
	$19.0 - 23.0$	$19.9\ \sigma$		$18.9 - 22.9$	$12.0\ \sigma$
	$20.0 - 23.0$	$20.7\ \sigma$		$19.9 - 22.9$	$12.8\ \sigma$
	$21.0 - 23.0$	$21.8\ \sigma$		$20.9 - 22.9$	$14.6\ \sigma$
	$22.0 - 23.0$	$11.5\ \sigma$		$21.9 - 22.9$	$13.2\ \sigma$

Since we detect known dwarf galaxies very easily with typical 3 m observations, and weakly with much shorter than average 1 m observations, we can be confident that our observations were sufficient to locate any new galaxies similar to the known ones. Because the strongest candidate detections we made are still weaker than And V — one of the least luminous galaxies known — we also know immediately that if there are any dwarf galaxies associated with HVCs, they are fainter than known dwarfs.

In addition to the 8 candidates that showed point source overdensities, we also found that 15 of the dwarf galaxy candidates appeared to contain faint nebular emission in our followup images. We suspect that a number of these are Galactic cirrus clouds. The remaining 37 candidates were not detected in any way during the followup observations, so we are forced to assume that these represent flaws on the Palomar plates that happened to have the appearance of dwarf galaxies.

2.5.4 Comments on Individual Candidates

HVC 104−70−312: At the location of this candidate, we found a 5 σ density enhancement of faint sources, which contains 27 more objects than expected from the background, and peaks in significance around magnitude 19.3. It is higher than 4.5 σ in all but the faintest magnitude bin. The sources appear to be clustered around a bright ($R_s = 18.9$) galaxy near the middle of the region. In our Lick image, it is obvious that most of the sources are within 1$'$ of this galaxy, rather than occupying the full $4' \times 2'$ LSB area identified on the POSS plate. Taking this into account, the overdensity increases in significance to $\sim 9\,\sigma$ (21 more objects than expected). Of the sources brighter than $R_s = 20.4$ (2 magnitudes brighter than the detection limit), 5 out of 9 are classified as galaxies on the basis of their radial profiles (FWHM larger than the point-spread function). For the fainter sources, it rapidly becomes impossible to distinguish stars from galaxies, but at least half of the 16 objects between $R_s = 20.4$ and $R_s = 21.4$ appear to be stars. So there may be a group of $15 - 20$ faint ($R_s \geq 20.4$) stars at this position. There are also ~ 20 objects within 1$'$ of the central galaxy that are visible by eye, but are fainter than our software detection limit. Without further observations, we cannot rule out the possibility that this is an exceedingly dim dwarf galaxy ($M_V \approx -7$), but we suspect that other alternatives (e.g., galaxy cluster, random grouping of foreground stars) are more likely.

HVC 118−58−373: Most of the sources associated with this small (11 objects)

overdensity appear to be stars. The significance stays almost constant (as does the over-abundance by number) down to the $20.6 - 22.6$ bin, where it reaches a maximum of $3.5\ \sigma$. However, even with the fairly deep limiting magnitude of this image, there is no hint of numerous fainter stars in the region below our formal $10\ \sigma$ detection limit, which should of course be present if this were a dwarf galaxy. With so few objects here the statistics are obviously poor, but we argue that this candidate is probably a chance alignment of foreground stars.

HVC 171−54−235: The overdensity is highest ($3.6\ \sigma$) in the largest magnitude range and decreases monotonically thereafter. This behavior is not at all what is expected from a dwarf galaxy. Again, there is no sign of "undetected" ($< 10\ \sigma$) sources. Since the overabundant objects are bright and are not accompanied by more numerous faint counterparts, this candidate is not a dwarf galaxy.

HVC 237+50+078: This candidate has an overdensity of 25 stars, which peaks at a significance level of $3.1\ \sigma$ around magnitude 18. The sources are not very centrally concentrated; rather, many of them are in several small groups of about 6 objects. Of the fraction (about 2/3) that are bright enough to be solidly classified as either stars or galaxies based on their radial profiles, over 60% are galaxies. Thus, the overdensity of *stars* is small, and there is no reason to suspect that this is a dwarf galaxy.

HVC 261+49+160: This object was the first distant galaxy cluster that we accidentally discovered. We noticed a highly significant ($7.8\ \sigma$) clustering of "stars" in our Lick 3 m image. Comparison of the SERC-J and Equatorial Red plates confirmed that these objects have red colors. However, the fact that the brightest of the stars appeared to have slightly extended radial profiles relative to the point-spread function of the Lick image raised suspicions that they were actually marginally resolved distant galaxies. G. Illingworth and V. Tran acquired an image of the cluster with the Low Resolution Imaging Spectrometer (LRIS) (Oke et al. 1995) on the Keck I Telescope[8] that supported this interpretation (see Figure 2.3), so we obtained spectra of the brighter objects with the Hobby-Eberly Telescope.[9] The spectra revealed that the bright central sources in this field

---

[8]The W.M. Keck Observatory is operated as a scientific partnership among the California Institute of Technology, the University of California, and the National Aeronautics and Space Administration. The Observatory was made possible by the generous financial support of the W.M. Keck Foundation.

[9]The Hobby-Eberly Telescope is a joint project of the University of Texas at Austin, Pennsylvania State University, Stanford University, Ludwig-Maximillians-Universität

are compact elliptical galaxies at $z = 0.35$. Thus, we conclude that this is a cluster of galaxies. (We should point out that technically this position was not listed in either of the HVC catalogs we used; it was only examined by mistake. However, there is actually high-velocity H I emission at this position in the LDS that was too weak to be included in the RB00 catalog. This cloud is also listed in the compilation of Wakker & van Woerden [1991], so it really is an HVC.)
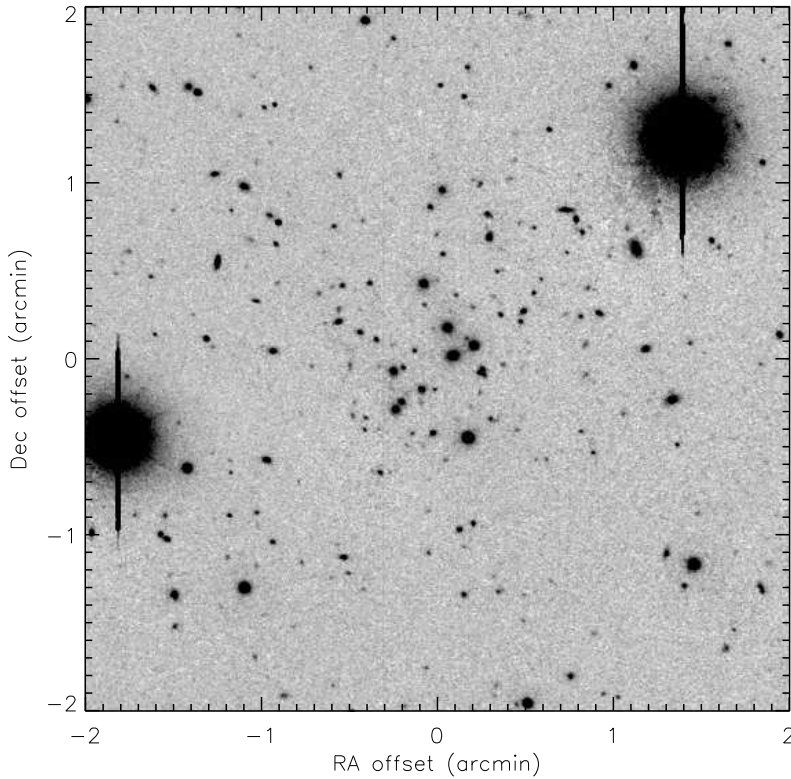
Figure 2.3 — 10-minute Keck/LRIS *I*-band image of the dwarf galaxy candidate 261+49+160, acquired for us by G. Illingworth and V. Tran. The concentration of objects in the center of the frame is a spectroscopically confirmed galaxy cluster at $z = 0.35$.

HVC 143+65+285b: This candidate also appeared in a 3 m image as a small clustering of slightly extended objects (23 more than would be expected from the background surface density). We did not obtain spectra, but *I*-band imaging from the 1 m telescope confirmed that many of these objects have similar colors. The significance of the clustering reaches a maximum of 3.9 σ and begins to fall off around magnitude 19. 64% of the bright

München, and Georg-August-Universität Göttingen.

objects in the region are clearly galaxies, and a 15th magnitude star is also present. These probably combine to explain the source of the LSB emission our algorithm picked up on the POSS plates. We consider this candidate to be a likely galaxy cluster.

HVC 083−50−325: The morphology of this candidate is extremely suggestive of a dwarf galaxy: an elliptical region about $5'$ across with a very strong concentration of faint point sources (Figure 2.4). This was one of the two objects whose overdensities approached those of And III and And V in significance, peaking at $10.8\ \sigma$. However, a number of the brightest objects are clearly galaxies in our Lick R_s image, and a significant fraction of those appear to be interacting. We also obtained V and I images of this field to aid in classifying the sources in the region of enhanced surface density. Taking into consideration the radial profile, morphology, and color of each source, we classified 62% of the identifiable objects as galaxies. Many of the galaxies were concentrated in color-color space around $(V - I, R_s - I) = (2.0, 1.1)$ and also near $(1.5, 0.7)$. Furthermore, an Abell cluster (2545) with a photometric redshift of 0.17 (Gal et al. 2000) is located $20'$ away from this position, increasing the probability that other clusters are in the vicinity. We feel safe in concluding that this candidate is another cluster of galaxies at moderate redshift.

HVC 107−30−421: We found a small ($\sim 1'$), elongated, very faint nebula north of the center of this HVC on the Palomar plates. A deep exposure on the 1 m telescope confirmed the reality of the source, but its extremely low surface brightness ($\mu_{\rm R} \approx 25.3$ mag arcsec^{-2}) made it difficult to classify. A. Bunker, S. Dawson, A. Dey, H. Spinrad, and D. Stern obtained an R-band image for us with Keck/LRIS, which revealed more structure in the object, but definitively did not resolve it into stars (see Figure 2.5). We remain unsure of the nature of this object, but we believe that it is a Galactic nebula. Because no stars were visible in it in the deep, subarcsecond-seeing image from Keck, we are confident that it is not a Local Group dwarf galaxy.

HVC 114−11−441: This candidate has an overdensity of $3.3\ \sigma$ (39 sources) over the magnitude range $16.5 \le R_s \le 22.8$. The significance decreases almost monotonically in the subsequent bins. The Galactic extinction in this direction is $A_R = 0.65$ mag (Schlegel et al. 1998), which makes it unlikely that a dwarf galaxy would be detected here. Since this object is at low Galactic latitude, the slight clustering of stars is probably located in the foreground.
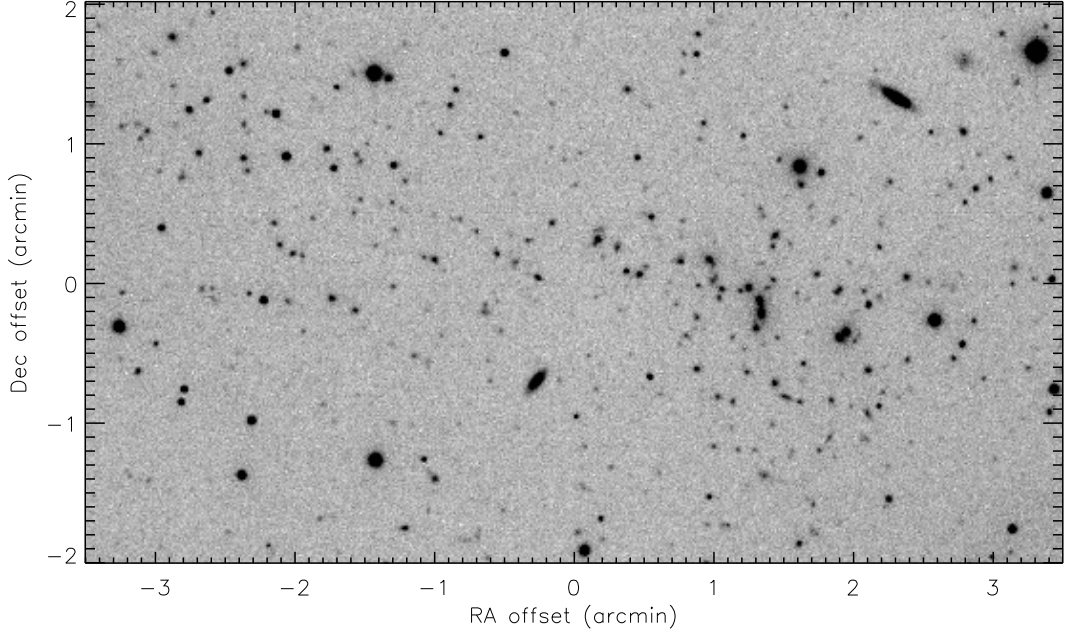
Figure 2.4 — 15-minute R_s image from the Lick 3 m telescope of the candidate $083-50-325$. The main concentration of objects that is described in the text includes several bright, interacting galaxies, and is centered near (RA off, Dec off) = $(1\!\!'\!3, -0\!\!'\!2)$. The overdensity continues less strongly to the northeast, all the way to the upper left corner of the image.

2.6   Discussion

2.6.1   Expected Red Giant Populations

We were unable to find any mention in the literature of the R-band magnitude of the TRGB. However, we can use theoretical studies of stellar evolution to make a reasonable estimate of its location. Girardi et al. (2000, hereafter G00) and Yi et al. (2001, hereafter Y01) both present stellar models that predict TRGB magnitudes of $M_R \approx -3.4$, varying only slightly with age and metallicity within the ranges that interest us. For example, in their [Fe/H] $= -1.7$ models, Y01 find a maximum shift of 0.086 mag in the TRGB magnitude for stars ranging in age between 4 and 15 Gyr. G00 give the maximum shift as 0.020 mag for the same parameters. Likewise, in changing metallicities at a fixed age
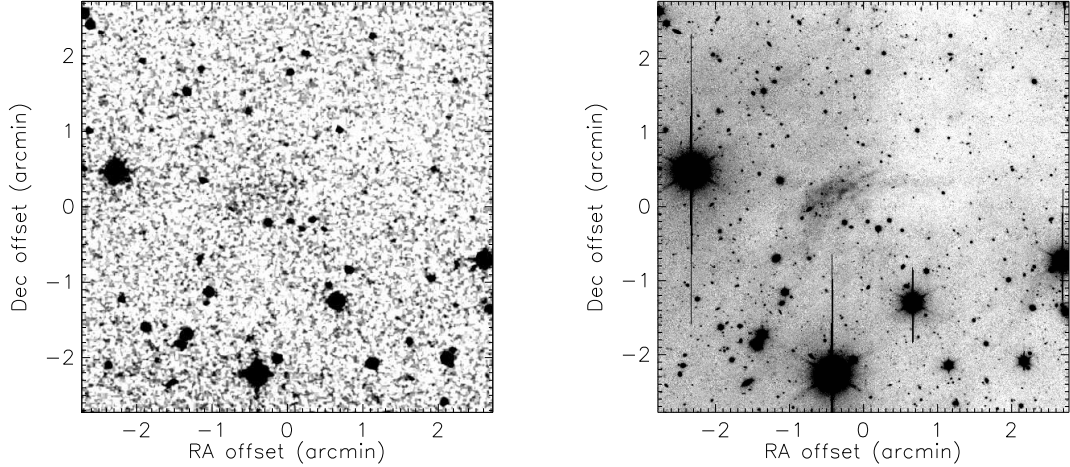
Figure 2.5 — Dwarf galaxy candidate near HVC 107−30−421. On the left is a POSS-II red image showing an LSB smudge just to the left of the field center. The R-band Keck/LRIS image of the same field, obtained by A. Bunker and collaborators, is on the right. Note that even objects with surface brightnesses as low as $\mu_{\rm R} = 25.3$ mag arcsec^{-2} are visible by eye (with difficulty) on raw POSS-II images.

(10 Gyr), the TRGB magnitude varies by only 0.144 and 0.068 mag, according to Y01 and G00, respectively (over most of the range covered by known dwarf spheroidals, $-2.3 \leq$ [Fe/H] ≤ -1.3). Given what is known about the TRGB in V and I (Lee, Freedman, & Madore 1993), these values seem reasonable, but we can compare them with observations as a further test. One of the few published datasets involving R-band observations of a large, homogeneous population of red giants is the study of the Fornax dSph by Stetson, Hesser, & Smecker-Hane (1998). Using their data, and an assumed distance modulus for Fornax of 20.70 mag (Beauchamp et al. 1995; Saviane, Held, & Bertelli 2000), we derive a TRGB magnitude of $M_R = -3.3$. Fornax has a high metallicity for a dSph of [Fe/H] $= -1.0$ (Saviane et al. 2000), so we should not be surprised that it has a slightly fainter tip magnitude than the models give. We conclude that $M_R = -3.4$ is the best guess for the TRGB magnitude in a typical Local Group dwarf spheroidal.

We noted in §2.5.3 that our observations of dSph companions of Andromeda detected ~ 100 stars in each galaxy. Other recent studies of distant Local Group dwarfs have measured similar or larger numbers of stars within one magnitude of the TRGB: ~ 100 such stars in And VI (Armandroff et al. 1999), ~ 200 stars in And VI and ~ 650 stars in

And VII (Grebel & Guhathakurta 1999), 156 stars (including some AGB contamination) in Phoenix (Held, Saviane, & Momany 1999), and 77 stars in Tucana (Saviane, Held, & Piotto 1996). Since typical background surface densities in our images are ~ 8 stars arcmin^{-2} (varying strongly with Galactic latitude) and these densities are a factor of a few higher, such objects are easily detected. Their absence in our survey indicates that HVCs do not contain dwarf galaxies with typical parameters ($M_V \lesssim -9$, $\mu_{\rm V} \lesssim 25.0$ mag arcsec^{-2}).

2.6.2 Distance and Surface Brightness Limits

Our followup observations of dwarf galaxy candidates reached 10 σ limiting R_s magnitudes between 20.0 and 23.4, with a median value of 22.2. We can convert these limiting magnitudes into a minimum distance at which a dwarf galaxy would have to lie in order to have escaped detection. If we assume that these observations must probe 1 magnitude below the TRGB in order to detect a dwarf galaxy, then the limiting distance is

$$d_{lim} = 10^{\frac{m_{lim}+7.4}{5}} \text{ pc}. \qquad (2.2)$$

For the minimum, median, and maximum limiting magnitudes we achieved, this distance corresponds to 302 kpc, 832 kpc, and 1445 kpc, respectively. These distance limits are quite conservative, because we have insisted that stars be detected at 10 σ (even though they can be visually identified in images at significantly fainter levels), and because objects as bright as the known dSphs can easily be located on images that reach less than a magnitude below the TRGB. Therefore, we can state with confidence that none of the candidate dwarf galaxies are actually dwarfs within $100 - 300$ kpc of the Milky Way, and all but two would have to be several times farther away to have been missed.

The depth of the POSS-II portion of our search is more difficult to assess. The Palomar data are not of uniform sensitivity: exposure times vary by up to a factor of two from plate to plate, and on a single plate there is significant vignetting within $\sim 1°$ of the edges. Furthermore, different parts of the sky are covered by different photographic surveys. Distant LG galaxies ($\gtrsim 200$ kpc) are not resolved and appear in the Palomar data as smudges with higher surface brightnesses than the surrounding areas. Because all of the distant dSphs (except And IX; see below) are easily visible by eye on the Palomar plates, we know that the POSS sensitivity range goes at least as faint as $\mu_{\rm V} = 25.0$ mag arcsec^{-2}. Using the stellar evolution models discussed in §2.6.1 again, we estimate that these galaxies

should have colors around $V - R = 0.5$. Thus, the R-band sensitivity of the Palomar images (since we used the red plates wherever possible) is better than $\mu_R = 24.5$ mag arcsec^{-2}.

A few dwarf spheroidals are known to have surface brightnesses lower than these levels. Some of the Milky Way companions at $d < 100$ kpc have $25.3 \leq \mu_V \leq 26.2$ mag arcsec^{-2} (i.e., Carina, Draco, Sextans, Ursa Minor, and Sagittarius). Out of these, Carina and Draco are visible by eye in POSS-II images, and the others are detectable via star counts. Since galaxies this close are resolved into individual stars on POSS plates, it is not entirely clear how to consider them with regard to a limiting surface brightness. Two of the recently discovered objects also present interesting tests of the sensitivity of the POSS-II data and our algorithm. SDSSJ1049+5103, an exceptionally faint object thought to be either the lowest-mass dSph or an unusually diffuse globular cluster (Willman et al. 2005a), can be detected with our algorithm despite an estimated surface brightness of $\mu_V = 27$ mag arcsec^{-2} (B. Willman 2005, private communication) and an absolute magnitude of $M_V = -3$. And IX, which has the lowest surface brightness ($\mu_V = 26.8$ mag arcsec^{-2}) and luminosity ($M_V = -8.3$) of any confirmed dwarf galaxy (Zucker et al. 2004), is only marginally visible in the raw POSS-II data (and probably could not have been discovered by eye, unlike almost all of the brighter galaxies), but stands out more clearly after processing. In summary, all LG galaxies with $\mu_V < 25.5$ mag arcsec^{-2} are visible, and one of the three galaxies with $\mu_V = 25.5$ mag arcsec^{-2} can also be seen visually. Thus, the naked-eye sensitivity of the red POSS-II plates is likely to be around $\mu_V = 25.5$ mag arcsec^{-2} on average (although the sensitivity of the best quality plates is almost certainly a magnitude deeper), or $\mu_R = 25.0$ mag arcsec^{-2}. Our processing routine should improve these values by $1 - 1.5$ magnitudes, as indicated by our detections of the faintest known dwarfs. So, we estimate that our survey is able to find galaxies down to $\mu_V = 26.5$ mag arcsec^{-2}, or $\mu_R = 26.0$ mag arcsec^{-2}. (It is worth noting that foreground Galactic extinction prevents us from quite reaching these limits; the median A_R for HVCs in our sample is 0.18 magnitudes [Schlegel et al. 1998].)

2.6.3 Implications

The fact that our survey did not detect *any* new dwarf galaxies toward the ~ 250 HVCs that we examined rules out the hypothesis that HVCs are the gaseous components of normal, but faint, Local Group dwarf galaxies. If these HVCs do contain stars, they

must have central surface brightnesses $\mu_{\rm V} \gtrsim 26$ mag arcsec^{-2}. They are also likely to have absolute magnitudes $M_V \gtrsim -9$, although a very extended stellar counterpart with an extremely low surface brightness could yield a higher total luminosity while still escaping detection. Even though it is conceivable that a few objects could have been missed because of our survey design, on the whole it seems clear that HVCs are starless systems.

Known LG dwarf galaxies do have surface brightnesses as faint as $\mu_{\rm V} = 26.8$ mag arcsec^{-2} (see Figure 2.6), but all of these galaxies except for a handful of the very extended MW satellites can be found with our techniques. Since all of the distant dwarfs are visible in the POSS-II data and would be relatively easily detected by both our POSS processing algorithm and our followup imaging campaign, we are confident that any objects similar to known dwarf spheroidals would have been discovered in our survey if they were present. Lower surface brightness stellar counterparts could still be present, but the fact that no such systems (with or without H I components) are known argues against this possibility. We believe that the most likely explanation for our findings is that HVCs simply do not contain stars.

This result does not lead to the anticipated outcome of our survey: a means of discriminating between HVC models. In the Galactic Fountain, Tidal Debris, and Hot Halo models, stars would not be expected to form in HVCs, in agreement with our finding. However, although the Local Group model certainly allows for stars in HVCs, and we would argue suggests that stellar counterparts are likely, it does not require them. So while a positive result in our search would have strongly supported the Local Group model, the inverse is not necessarily the case. As mentioned earlier, Bullock et al. (2000) and others have proposed ideas explaining how small dark matter halos scattered throughout the Local Group could contain some neutral gas without having formed stars. The absence of stars may be an important clue to the nature of HVCs, but by itself, it does not allow us to solve the puzzle.

2.6.4 Compatibility with Previous and Subsequent Work

There have been no other comprehensive and quantitative searches for evidence of stars in HVCs. Ivezić & Christodoulou (1997) examined IRAS data towards the large HVC complexes in an effort to locate any star formation that might be occurring, but only came up with one possible young star in positional coincidence with high-velocity H I. BB99
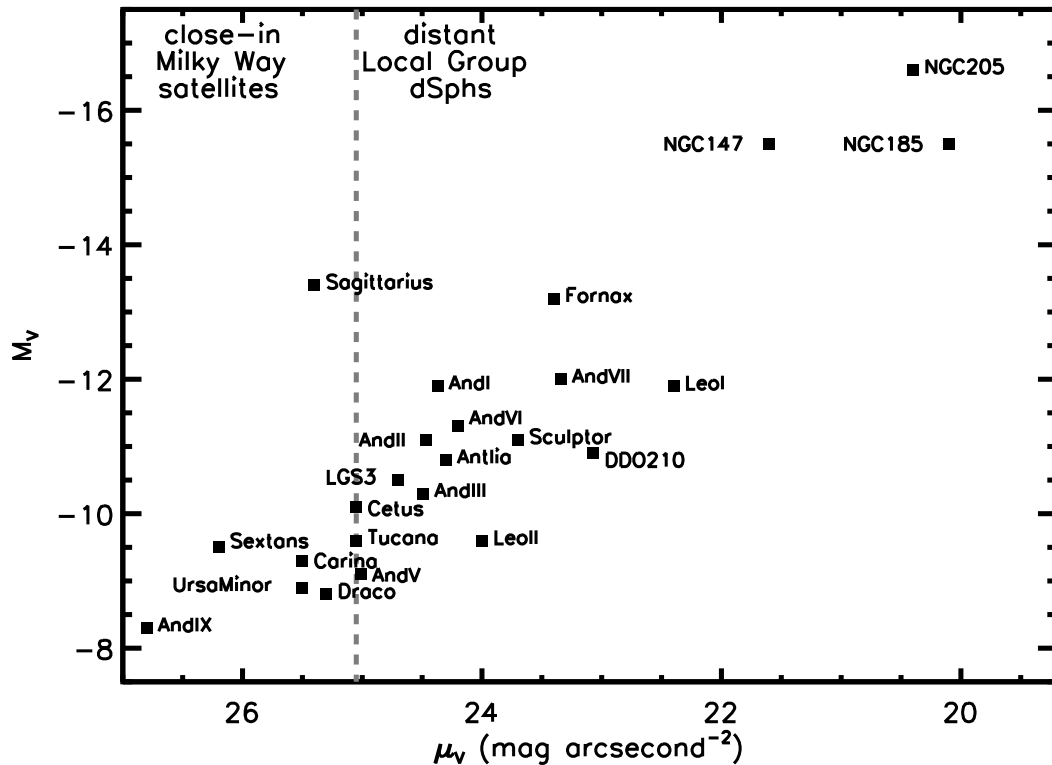
Figure 2.6 — Relationship between luminosity and surface brightness for spheroidal galaxies, dwarf spheroidals, and the so-called transitional (dSph/dIrr) galaxies in the Local Group (Pegasus and Phoenix are not included in the figure because they lack published surface photometry data). The only known dwarfs with $\mu_V > 25.05$ mag arcsec^{-2} (to the left of the dashed line) are the Milky Way satellites within 100 kpc and And IX. All but one of the M31 companions and isolated dwarfs in the LG have higher surface brightnesses. The data used to make this plot were taken from tables compiled by Mateo (1998) and van den Bergh (1999, 2000) (see references therein for the original sources), except for the surface photometry for DDO 210, which was adapted from Lee et al. (1999), and the data for And IX, which were obtained by Zucker et al. (2004).

searched DSS images in the direction of each of their compact HVCs, but found no clear optical counterparts. After our survey was carried out, Willman et al. (2002) searched for resolved stellar counterparts to HVCs that lie in the Sloan Digital Sky Survey area and likewise failed to detected any stars. Davies et al. (2002), Hopp, Schulte-Ladbeck, & Kerp (2003), and Siegel et al. (2005) also each used deep imaging of $3-5$ HVCs to search unsuccessfully for very low-luminosity stellar counterparts. And in Chapter 3 we use infrared and millimeter-wave observations to search for a stellar counterpart to Complex H,

with null results. Thus, the result of this work is entirely compatible with the data existing in the literature, and it seems safe to conclude that there are no stars in HVCs.

2.7 Conclusions

We have surveyed 1 deg^2 of sky around each of 264 high-velocity clouds in search of new Local Group dwarf galaxies. We processed digital POSS-I and POSS-II images with an algorithm to enhance low-surface brightness features. Tests with known dwarfs confirmed that objects as faint as $\mu_{\rm V} = 26.8$ mag arcsec^{-2} are detectable with this technique. We then examined the images and found 60 faint smudges that we classified as possible LG dwarfs. Using the 1 m and 3 m telescopes at Lick Observatory, we imaged each of these candidates to a typical limiting stellar magnitude of $R_s = 22.2$. Examination of the data revealed several $\geq 3~\sigma$ density enhancements of faint sources in the areas selected from the POSS plates, but none of these appear to be LG dwarf galaxies. Typical faint LG dwarf spheroidal galaxies would have been detected at the $\gtrsim 10~\sigma$ level, with ~ 100 stars brighter than the detection limit. Therefore, we conclude that there are no undiscovered normal dwarf galaxies within a 30$'$ radius of any of these HVCs, provided that the HVCs are located at least 100 kpc from the Milky Way; dwarf galaxies at a smaller distance might be too diffuse to detect in this manner.

There were both observational and theoretical grounds for suspecting that compact HVCs might harbor faint LSB dwarf galaxies. It is well-known that the highly successful Cold Dark Matter theory predicts large numbers of small dark matter halos, which have not yet been detected observationally. Klypin et al. (1999) and others have pointed out that HVCs are numerous enough (and massive enough, in the Local Group picture) to comprise the set of missing halos. From the observational side, Blitz & Robishaw (2000) noted that there are similarities between the H I components of LG dwarfs and the properties of HVCs, if they are located at typical distances from the Milky Way of ~ 700 kpc. Furthermore, blind H I surveys of nearby groups of galaxies often find that the H I clouds they detect are associated with LSB dwarfs.

The implications of our observation that LG H I clouds lack such stellar counterparts are unclear, both for HVC models and for the substructure problem. While this finding does not rule out the Local Group hypothesis for the spatial distribution of the HVCs, it also does not provide any supporting evidence. We are still unable to constrain

HVC distances, but we have placed significant limits on their stellar content. Regardless of the location of the HVCs, as long as they are at least 100 kpc away they either lack stars entirely, or they have lower surface brightnesses and luminosities than other stellar systems in the Local Group.

Chapter 3

The Cosmological Significance of High-Velocity Cloud Complex H

Abstract

We have used new and archival infrared and radio observations to search for a dwarf galaxy associated with the high-velocity cloud (HVC) known as Complex H. Complex H is a massive ($M_{\mathrm{H\ I}} \gtrsim 10^7$ M$_\odot$) and probably nearby ($d = 27$ kpc) HVC whose location in the Galactic plane has hampered previous investigations of its stellar content. Virtually all similar H I clouds in other galaxy groups are associated with low surface brightness dwarf galaxies. We selected mid-infrared sources observed by the MSX satellite in the direction of Complex H that appeared likely to be star-forming regions and observed them at the wavelength of the CO ($J = 1 \rightarrow 0$) rotational transition in order to determine their velocities. 59 of the 60 observed sources show emission at Milky Way velocities, and we detected no emission at velocities consistent with that of Complex H. We use these observations to set upper limits on the ongoing star formation rate in the HVC of $\lesssim 3 \times 10^{-4}$ M$_\odot$ yr^{-1}. We also searched the 2MASS database for evidence of any dwarf-galaxy-like stellar population in the direction of the HVC and found no trace of a distant red giant population. Given the lack of evidence for either current star formation or an evolved population, we conclude that Complex H cannot be a dwarf galaxy with properties similar to those of known dwarfs. Complex H is therefore one of the most massive known H I clouds that does not contain any stars. If Complex H is self-gravitating, then this object is one

of the first dark galaxies to be discovered. These findings may offer observational support for the idea that the Cold Dark Matter substructure problem is related to the difficulty of forming stars in low-mass dark matter halos; alternatively, Complex H could be an example of a cold accretion flow onto the Milky Way.

3.1   Introduction

What determines whether a low-mass gas cloud or dark matter halo becomes a dwarf galaxy or fails to undergo any star formation, remaining dark for billions of years? The answer to this question may underlie the substructure problem in Cold Dark Matter (CDM) cosmologies — the dramatic mismatch between the number of dark matter minihalos produced in numerical simulations and the number of dwarf galaxies observed in the Local Group (Klypin et al. 1999; Moore et al. 1999a). Many possible explanations for why low-mass halos might not form stars have been proposed (e.g., Efstathiou 1992; Scannapieco, Ferrara, & Broadhurst 2000; Bullock, Kravtsov, & Weinberg 2000; Scannapieco, Thacker, & Davis 2001; Somerville 2002; Verde, Oh, & Jimenez 2002; Dekel & Woo 2003; Kravtsov, Gnedin, & Klypin 2004), but the existence of very low-mass dwarfs today suggests that this problem is not yet fully understood. One approach to improving our understanding of the formation of dwarf galaxies is to study extreme objects in order to determine what makes them unique. In this chapter we investigate the nature of Complex H, an unusually massive high-velocity cloud (HVC) located in the Galactic plane.

Complex H is centered on HVC $131+1-200$, which was first discovered by Hulsbosch (1971) and Dieter (1971). Wakker & van Woerden (1991) noted that this HVC seems to be associated in position and velocity with a large number of other clouds, and named the grouping Complex H after Hulsbosch. The complex subtends 478 deg^2 (Wakker & van Woerden 1991) and extends in velocity all the way from $v_{\mathrm{LSR}} = -230$ km s^{-1} down to $v_{\mathrm{LSR}} \approx -120$ km s^{-1} where it begins to blend into Milky Way emission. The H I column density at the center of the cloud is $\gtrsim 2 \times 10^{20}$ cm^{-2}, and the column is at least 2.0×10^{19} cm^{-2} for most of the central 25 deg^2. Complex H has an integrated H I mass of $\approx 2.7 \times 10^4\ d_{\mathrm{kpc}}^2$ M$_\odot$, where d_{kpc} is the distance to Complex H in kiloparsecs (Wakker et al. 1998, hereafter W98). Ivezić & Christodoulou (1997) used IRAS data to search for star formation in Complex H and found one candidate young stellar object, but this source is likely to be a foreground Milky Way object.
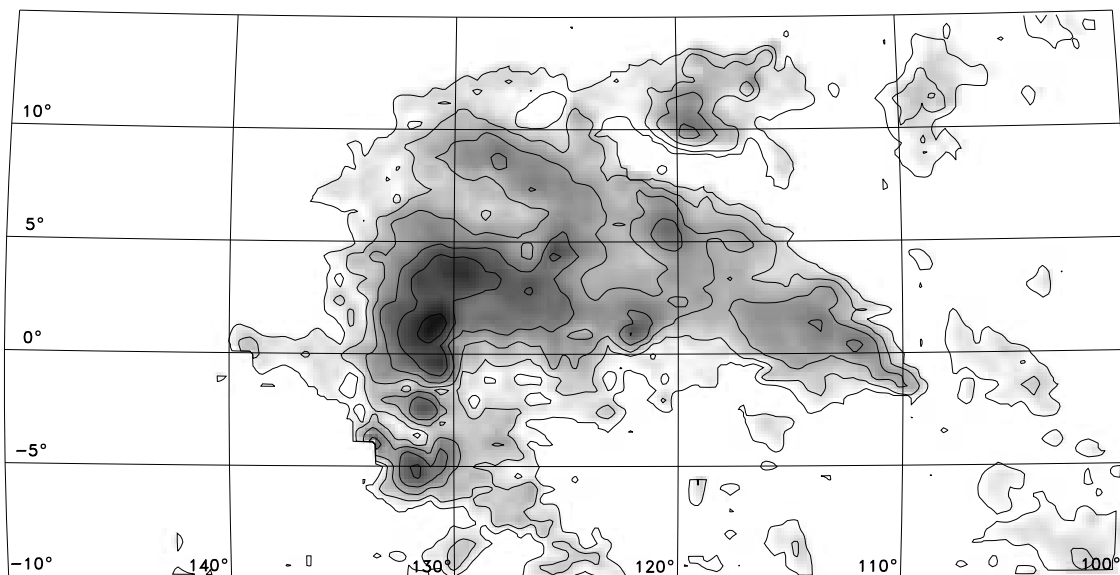
Figure 3.1 — H I map of Complex H in Galactic coordinates from the Leiden/Dwingeloo Survey of Galactic Neutral Hydrogen (Hartmann & Burton 1997). The image shows the integrated intensity for velocities between -230 km s^{-1} and -150 km s^{-1}. The contours are spaced logarithmically and correspond to column densities of 4.6×10^{18} cm^{-2}, 9.2×10^{18} cm^{-2}, 1.8×10^{19} cm^{-2}, 3.7×10^{19} cm^{-2}, 7.3×10^{19} cm^{-2}, and 1.5×10^{20} cm^{-2}. The Dwingeloo telescope has a beam size of $36'$ and the survey was carried out with a grid spacing of $30'$.

W98 examined ultraviolet spectra of 17 OB stars for interstellar absorption lines of Mg II, C II, and O I in the direction of Complex H. They detected no absorption near the velocity of Complex H and concluded that even for substantially subsolar abundances, the HVC must be located beyond the furthest of the stars they studied. They placed a firm lower limit of 3.4 kpc on the distance to Complex H. Since the distances of some of the OB stars are rather uncertain, the actual minimum distance could be as large as 6.5 kpc. Blitz et al. (1999) additionally pointed out that the velocity of Complex H is too large for it to be in circular rotation around the Galaxy at any distance. They further argued that the lack of any observational evidence for an interaction between Complex H and the interstellar medium of the Milky Way strongly implies that the HVC must be located beyond the edge of the disk of the Galaxy, at least ~ 20 kpc away from the Sun. Since Complex H has velocities of up to 100 km s^{-1} with respect to the nearest Galactic gas, strong shocks and X-ray and radio emission would be produced if it were located within the H I disk of the Milky Way.

Lockman (2003) further noticed that the velocity gradient across the cloud in the b (Galactic latitude) direction can be used to derive its vertical motion relative to the Galaxy. Using H I maps from the Green Bank Telescope, he constructed a model of Complex H and argued that the HVC is in an inclined, retrograde orbit around the Milky Way and is beginning to suffer tidal stripping of its outer layers. These calculations place Complex H 33 ± 9 kpc from the Galactic center and 27 ± 9 kpc from the Sun. More general distance constraints can be derived by considering the aforementioned lack of interaction between Complex H and the Milky Way, and the total mass of the cloud. The Milky Way disk gas extends out to a minimum Galactocentric distance of 27 kpc at the position of Complex H (Blitz et al. 1999), placing a firm lower limit of 21 kpc on the distance between the HVC and the Sun if the cloud lies just beyond the edge of the disk. At distances of more than 100 kpc, Complex H would be the fourth most massive object in the Local Group, which seems unlikely since no counterpart at other wavelengths has been detected. The full range of plausible distances is therefore $21 - 100$ kpc, corresponding to H I masses of $1.2 \times 10^7 - 2.7 \times 10^8$ M$_\odot$.

Because starless extragalactic gas clouds as large as Complex H are not seen in other groups of galaxies (with only one exception [Minchin et al. 2005]), it seems reasonable to suppose that Complex H is the H I component of a previously undiscovered dwarf galaxy. At the distance of 27 kpc preferred by Lockman (2003), Complex H would have an H I

mass, total mass (assuming that it is gravitationally bound), and physical extent that are consistent with those of other Local Group galaxies.

Before we proceed, the issue of the total mass of Complex H deserves some comment. If the HVC is actually a dwarf galaxy, a baryon fraction of 0.04 (typical for dwarf galaxies) would imply a total mass of $\sim 5 \times 10^8$ M$_\odot$. In a ΛCDM cosmology, such a dark matter halo should have a peak circular velocity of at least ~ 30 km s^{-1}. Neither the velocity gradient across the cloud (which in the Lockman model is attributable to the orbital velocity of the HVC rather than its internal motions) nor the velocity dispersion of the gas is nearly this large, so the kinematics of the cloud do not require a total mass this high. Nevertheless, if the H I extent of the cloud is smaller than the scale radius of the dark matter halo, the observed kinematics would not be expected to reflect the full gravitational potential of the halo.

We now consider the possibilities for confirming or refuting the presence of a dwarf galaxy in Complex H. The V-band extinction in the direction of the center of the HVC is estimated to be 4 magnitudes (Schlegel, Finkbeiner, & Davis 1998), although the calculated extinction near the Galactic plane is subject to significant uncertainties. The combination of heavy extinction and severe crowding makes an optical detection of a distant group of stars very difficult (although not impossible, as was illustrated by the detection of the Sagittarius dwarf spheroidal behind the Galactic center by Ibata, Gilmore, & Irwin 1995). Instead, we shall search for evidence of a dwarf galaxy at longer wavelengths where both the extinction and the crowding are less severe or nonexistent. Specifically, we use mid-infrared observations from the Midcourse Space Experiment (MSX) satellite to identify star-forming regions that could be associated with Complex H. We then employ millimeter-wave CO observations to determine the nature and location of these objects. These data should reveal the presence of massive stars in Complex H if any star formation has taken place in the last $\sim 10^7$ years. Other Local Group dwarf irregulars that have comparable H I masses to Complex H, such as Sextans B and IC 1613, are actively forming stars. In addition, we use the Two Micron All Sky Survey (2MASS) near-infrared database to search for stars in the putative dwarf galaxy, taking advantage of the order of magnitude decrease in extinction between V-band and K-band.

In the following section, we discuss the MSX dataset, present our new CO observations, and describe the results of our search for star formation. In §3.3 we describe our analysis of the 2MASS data and in §3.4 we consider the interpretation of our findings. Our

conclusions are summarized in §3.5.

3.2 Search for Recent Star Formation in Complex H

3.2.1 MSX Data

The MSX satellite (Mill et al. 1994) was a US Department of Defense mission, undertaken by the Ballistic Missile Defense Organization. Launched in 1996, the infrared instrument on board consisted of a 35-cm off-axis telescope with detectors in six mid-infrared bands (two very narrow near 4 μm, and four broad at roughly 8, 12, 15, and 21 μm). All sensors had pixels of 18.3″. The primary infrared product was a survey of the entire Galactic plane within $-5° < b < 5°$ and about 19″ (FWHM) resolution (Price et al. 2001). The MSX Point Source Catalog version 2.3 (PSC2.3) contains six-color infrared photometry for over 4.3×10^5 sources in the Galactic plane (Egan et al. 2003)

3.2.2 Target Selection

If Complex H is indeed the gaseous counterpart of a dwarf galaxy, the galaxy could be either a dwarf irregular (dIrr) or a dwarf spheroidal (dSph), but its gas content would be rather large for a dSph (Blitz & Robishaw 2000). A dwarf irregular galaxy would likely contain star–forming regions, which ought to be bright enough in the infrared to be detected by MSX. The 19″ resolution of the MSX data corresponds to a physical size of $0.092d_{\mathrm{kpc}}$ pc, where d_{kpc} is the distance to Complex H in kiloparsecs. A typical H II region of diameter 50 pc would subtend an angle of 6′.4 at the nominal distance of 27 kpc to Complex H, and would thus be resolved easily by MSX. Ultracompact H II regions (less than 2 pc in diameter), however, would show up as point sources at distances of greater than ~ 20 kpc. Therefore, we consider both point sources and extended sources in our search for evidence of star formation in the HVC.

As a first step, we searched the PSC2.3 for evidence of an enhanced density of infrared point sources near the center of Complex H. The distribution of these sources in the plane of the Galaxy is displayed in Figure 3.2. Although there are a few overdensities close to the expected location, further investigation reveals that the string of sources from $\ell \approx 132° - 138°$ is associated with the Milky Way star forming complex W3/W4/W5 (e.g., Carpenter, Heyer, & Snell 2000) and the cluster at $\ell = 126.7°$, $b = -0.8°$ is the H II region

Sharpless 187 (Sharpless 1959; Joncas, Durand, & Roger 1992). It is also worth noting that the average density on the sky of point sources around $\ell = 131°$, $b = 1°$ (the core of the HVC) is very close to the global average value for the outer Galactic plane of about 20 deg^{-2}.

We then examined the area in question in more detail. The region of highest H I column density in the HVC is roughly bounded by $127° < \ell < 133°$ and $-1° < b < 5°$, so for simplicity we will assume that any star formation that has taken place in Complex H occurred in this area. The MSX band A (8 μm) deep mosaic image of this region is shown in Figure 3.3, along with H I data from the Leiden/Dwingeloo Survey (Hartmann & Burton 1997). The MSX image was cut from a $10° \times 10°$ product with $36''$ pixels and $72''$ resolution, which has a 3 σ sensitivity limit for low surface brightness diffuse emission that varies across the image from $2-9 \times 10^{-7}$ W m^{-2} sr^{-1}, and is sensitive to point sources with flux densities down to ≈ 100 mJy. By comparison, an unobscured OB main sequence star at a distance of 27 kpc has a flux density of $\lesssim 5$ mJy (OB supergiants can be a factor of $2-3$ brighter) so, if the putative dwarf galaxy has a low dust content, only rich OB associations in Complex H would be detectable. Nevertheless, a single OB star still embedded in a molecular cloud and therefore reradiating most of its energy in the infrared could be detected. Therefore, it is likely that recent massive star formation regions in Complex H would be visible in the MSX data.

We selected 43 of the brightest extended sources for follow-up observations based on a mosaic constructed of high-resolution ($6''$ pixels, $19''$ resolution) MSX images covering the region displayed in Figure 3.3. It is clear from a casual inspection of the figure that the brightest infrared sources in this part of the sky are concentrated well away from the H I peak of Complex H. We therefore added 10 bright point sources located near the core of the HVC to our target list. Finally, we included seven IRAS sources (many of which were expected to be Galactic star-forming regions) from the compilation of Fich & Terebey (1996) in order to make sure that they were actually Milky Way objects and to confirm that our observing strategy could detect star-forming regions.

3.2.3 CO Observations

We observed our targets with the NRAO/UASO 12 m reflector on the days of 2000 May 5 – 9. At the wavelength of the CO ($J = 1 \rightarrow 0$) line, the telescope has a
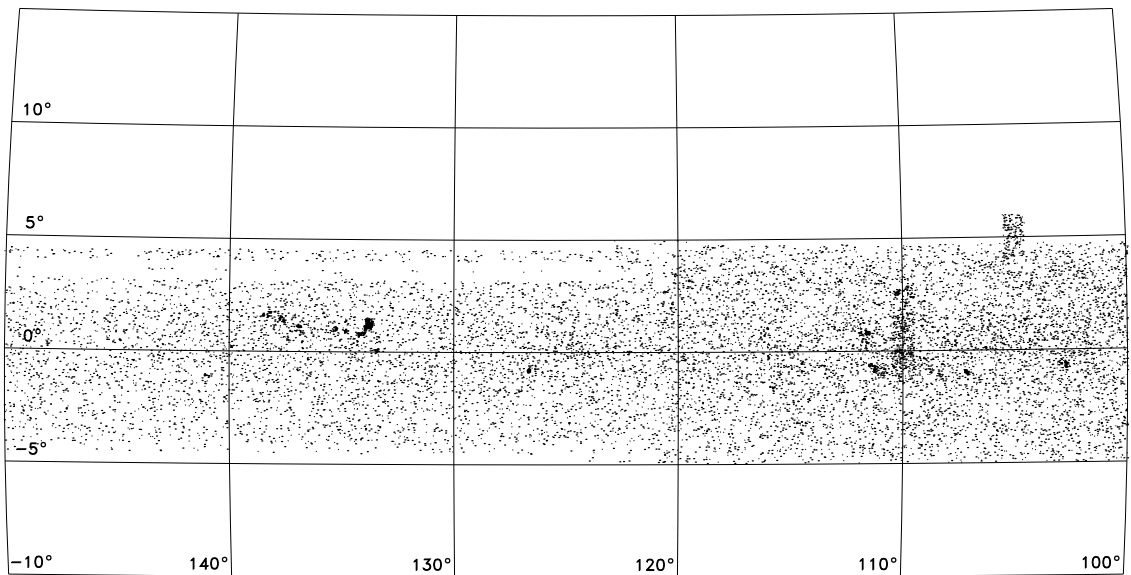
Figure 3.2 — MSX point sources in the outer Galaxy. All sources listed in the Point Source Catalog (Egan et al. 2003) are plotted. Overdensities near the position of Complex H ($\ell = 131°, b = 1°$; see Figure 3.1) are visible, but they can all be identified with nearby Milky Way H II regions.
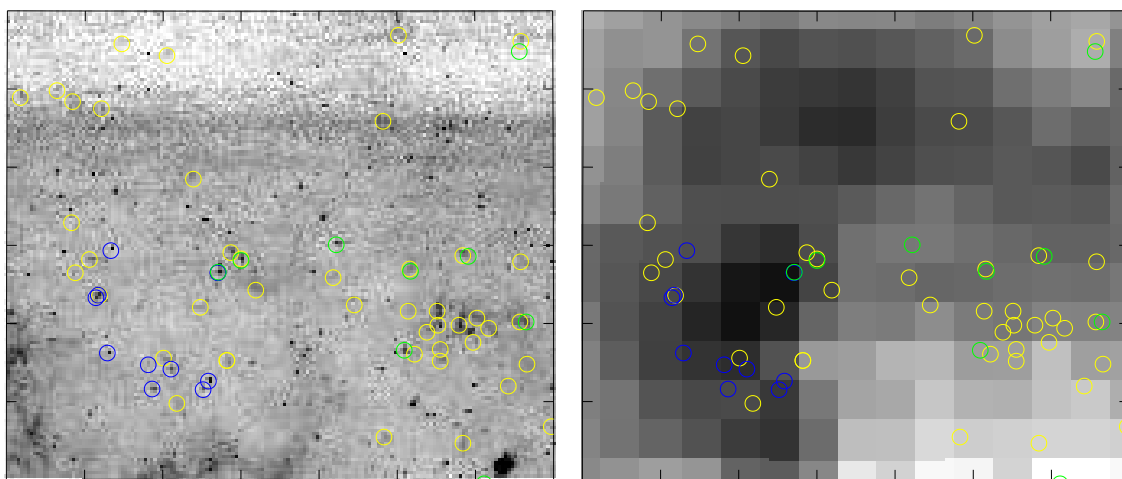
Figure 3.3 — (a) MSX 8 μm deep mosaic image of the center of Complex H. The displayed region spans Galactic longitudes from 126° (right edge of the image) to 133° (left edge) and Galactic latitudes from −1° to 5°. The sources we selected for followup observations are circled. Yellow circles represent MSX extended sources, blue circles represent MSX point sources, and green circles represent IRAS sources from Fich & Terebey (1996). (b) H I image of the center of Complex H from the Leiden/Dwingeloo Survey. The angular coverage is the same as in panel (a). The infrared targets are overplotted as in panel (a). It is clear that the location of the H I peak of the HVC lies near a minimum of the infrared emission, suggesting that the MSX sources are not associated with Complex H.

beam width of $55''$. We used the millimeter autocorrelator with a 300 MHz bandwidth and 0.2541 km s^{-1} resolution and two polarizations. System temperatures were between 300 and 500 K for most of our observations, and reached as high as 1000 K for a few scans as the HVC approached the horizon. Typical integration times were $8 - 12$ minutes per position, for a total observing time of $40 - 60$ minutes on each source. We observed in relative position–switching mode with beam throws of a few arcminutes and used the online vane calibration to set the antenna temperature scale. The telescope pointing and focus were checked approximately every six hours, or after sunrise and sunset. The data were reduced in COMB by subtracting a linear baseline from each spectrum and then combining the two polarizations. For the extended sources, we observed a five point cross pattern around each source, with the spacing of the points chosen to be slightly less than the radius of the source. For the point sources, we only observed a single position since the beam size of the 12 m telescope is larger than the resolution of the MSX data.

3.2.4   Millimeter Search Results

We observed the 60 targets shown in Figure 3.3 and examined the spectra for emission or absorption (emission in the off position) features in the velocity range -300 km s$^{-1} <$ $V_{LSR} < 100$ km s^{-1}. Milky Way objects should appear with velocities $V_{LSR} > -120$ km s^{-1}, and we expect Complex H emission to lie between -230 km s^{-1} and -170 km s^{-1} if any is present (velocities as high as -120 km s^{-1} are also possible, but less likely). We detected Milky Way CO lines in either emission or absorption toward all 43 of the MSX extended sources, nine out of the ten MSX point sources, and all seven of the Fich & Terebey H II regions, indicating that at least 59 of our 60 targets are almost certainly Milky Way starforming regions. The only object that we did not detect, MSX6C G131.1875+00.4726, may be a Milky Way infrared source of some kind that does not contain any CO, or it could be that the molecular gas is simply offset enough from the infrared position that it lies outside the beam of the 12 m. We did not find any emission lines at velocities below -102 km s^{-1},[1] so there is no evidence that any of these targets are associated with Complex H.

In Table 3.1 we list the results of our CO observations for each source. Columns (1) and (2) contain the Galactic coordinates of the targets, column (3) contains the ve-

---

[1]Several spectra showed apparently significant features at lower velocities, but repeat observations failed to confirm the reality of these lines.

locity centroids of the detected lines, column (4) contains the peak observed brightness temperatures (again, note that negative observed temperatures indicate the the emission was located in the off position), column (5) contains the integrated intensity of the line, and column (6) describes how the targets were selected. For many lines of sight multiple emission components were detected, so we include all lines with an integrated intensity that is significant at the $5\,\sigma$ level or higher in this table. Note, however, that we frequently omit lines at local velocities (-10 km s$^{-1} \lesssim V_{LSR} \lesssim 5$ km s^{-1}) when other components with more negative velocities are also detected along the same line of sight. Our compilation is therefore incomplete at these velocities, but this local material is not relevant for our purposes. The distribution of velocities that we find for the Milky Way clouds we detect is plotted in Figure 3.4. Distinct peaks in the distribution appear at velocities of -10 km s^{-1} (local material), -55 km s^{-1} (Perseus spiral arm), and -80 km s^{-1} (outer spiral arm).

Table 3.1: Milky Way CO Lines Detected Toward Mid-Infrared Sources

ℓ (1)	b (2)	V_{LSR} (km s^{-1}) (3)	T_b (K) (4)	I_{CO} (K km s^{-1}) (5)	Source (6)
126.03	-0.32	-47.0	5.84	8.16	MSXE
126.34	0.48	1.9	4.89	5.35	MSXE
		-4.6	1.49	1.89	
		-12.8	3.61	10.66	
		-45.3	1.65	2.23	
126.41	4.61	3.8	2.15	2.78	MSXE
		-6.5	0.97	2.01	
		-9.8	0.51	0.50	
126.42	1.79	-11.5	0.52	0.41	MSXE
		-46.2	0.41	0.59	
126.43	1.02	1.4	-0.65	-1.30	MSXE
		-67.2	0.95	1.10	
126.58	0.20	-11.9	2.99	5.15	MSXE
		-13.1	-2.85	-6.56	
		-52.9	1.10	1.15	
126.83	0.94	-10.5	2.42	3.95	MSXE
		-36.3	1.65	1.99	
		-54.0	-0.83	-1.03	
126.98	1.07	-37.0	2.11	3.28	MSXE
		-53.9	1.02	1.59	
127.03	0.76	-41.9	12.02	19.70	MSXE

Table 3.1 – Continued

ℓ (1)	b (2)	V_{LSR} (km s^{-1}) (3)	T_b (K) (4)	I_{CO} (K km s^{-1}) (5)	Source (6)
		−51.0	0.40	0.77	
127.16	−0.53	−13.3	−2.46	−2.12	MSXE
		−44.5	5.96	12.74	
		−53.8	1.28	1.45	
		−56.1	−3.35	−3.49	
127.16	1.87	−1.1	2.11	5.45	MSXE
127.21	0.98	−43.0	9.04	22.61	MSXE
		−52.1	2.98	3.37	
127.45	0.67	9.4	1.80	5.93	MSXE
		−52.5	1.74	2.69	
127.45	0.52	−34.4	3.73	4.60	MSXE
		−50.4	1.47	3.13	
127.48	0.98	−39.7	8.56	8.99	MSXE
127.49	1.16	−36.0	0.51	0.57	MSXE
		−52.1	0.61	1.31	
		−58.2	0.37	0.80	
127.62	0.89	−41.5	7.08	8.04	MSXE
		−51.7	1.28	1.61	
127.78	0.61	8.1	1.22	2.41	MSXE
127.84	1.70	−55.4	2.08	2.40	MSXE
127.86	1.16	−59.8	2.57	6.34	MSXE
		−53.8	1.68	2.95	
127.98	4.69	−8.7	2.93	4.41	MSXE
128.17	−0.45	−12.7	2.51	4.67	MSXE
		−41.7	3.67	5.48	
128.18	3.59	−8.9	2.31	2.11	MSXE
128.55	1.24	−51.1	1.71	3.36	MSXE
		−52.9	1.06	0.87	
128.82	1.59	−7.8	1.57	1.67	MSXE
		−10.0	1.27	1.58	
		−55.7	2.65	4.02	
		−82.2	1.71	2.60	
129.81	1.43	−38.4	1.86	4.15	MSXE
		−55.0	1.21	1.51	
		−77.0	0.61	0.69	
		−82.2	0.82	0.88	
130.00	1.83	−47.2	3.71	3.76	MSXE
		−81.0	1.00	1.46	
130.13	1.91	2.4	1.10	1.86	MSXE
130.18	0.53	−10.9	2.38	2.76	MSXE
		−12.6	1.21	1.18	

Table 3.1 – Continued

ℓ (1)	b (2)	V_{LSR} (km s^{-1}) (3)	T_b (K) (4)	I_{CO} (K km s^{-1}) (5)	Source (6)
		-45.6	0.86	1.10	
130.52	1.21	-66.0	0.57	0.83	MSXE
130.61	2.85	-7.4	-1.73	-2.33	MSXE
130.82	-0.02	-17.1	4.32	5.54	MSXE
		-33.0	3.38	4.07	
130.95	4.43	-14.1	1.78	2.87	MSXE
130.99	0.56	-30.8	1.91	3.18	MSXE
131.53	4.58	-33.1	6.67	11.48	MSXE
131.79	3.75	-8.2	-1.49	-1.50	MSXE
		-8.0	0.80	0.38	
		-40.7	-0.66	-1.21	
131.81	1.36	-57.4	1.22	1.69	MSXE
		-79.0	3.11	4.68	
131.94	1.82	-45.6	1.22	2.02	MSXE
		-69.9	0.89	1.60	
132.12	1.65	-75.0	0.43	0.88	MSXE
		-101.7	0.37	0.39	
132.16	3.84	-41.2	2.30	4.03	MSXE
132.17	2.29	-7.7	2.69	3.50	MSXE
		-73.7	0.67	0.75	
132.36	3.98	-41.1	1.80	2.65	MSXE
132.83	3.89	-1.5	1.24	1.48	MSXE
		-7.9	-1.06	-1.24	
		-9.6	3.05	2.71	
131.666	1.934	-41.2	0.44	0.44	MSXP
		-79.1	0.46	0.72	
131.856	1.331	-56.1	0.49	0.72	MSXP
		-78.7	8.38	23.94	
131.826	1.364	-56.3	0.38	0.43	MSXP
		-78.5	3.14	4.48	
130.294	1.654	-3.3	0.51	0.66	MSXP
		-54.5	6.04	9.95	
131.709	0.624	-2.7	2.21	6.50	MSXP
131.186	0.474	$\cdots$	$\cdots$	$\cdots$	MSXP
131.136	0.164	-5.0	2.00	4.10	MSXP
		-19.0	0.30	0.86	
130.416	0.266	-9.1	0.69	0.44	MSXP
		-11.5	-4.65	-11.81	
130.896	0.419	-58.9	2.20	5.48	MSXP
130.484	0.156	-11.5	-1.20	-1.91	MSXP
		-88.7	0.40	0.87	

Table 3.1 – Continued

ℓ (1)	b (2)	V_{LSR} (km s^{-1}) (3)	T_b (K) (4)	I_{CO} (K km s^{-1}) (5)	Source (6)
130.294	1.654	−54.5	6.49	10.34	MSXP
126.43	4.48	2.2	3.82	6.25	FT96
		−10.2	2.23	5.69	
127.09	1.86	−0.4	2.66	3.63	FT96
		−2.9	1.38	1.53	
		−8.1	1.00	0.64	
127.83	1.67	−7.3	1.17	1.81	FT96
		−57.7	4.38	4.23	
		−87.3	−1.30	−1.98	
127.91	0.66	−63.4	6.55	19.10	FT96
128.78	2.01	−82.0	10.47	30.76	FT96
130.00	1.81	−43.5	0.59	0.86	FT96
		−47.2	2.89	2.96	
		−81.5	0.52	1.22	
130.29	1.66	−10.8	0.55	0.79	FT96
		−43.0	0.77	1.26	
		−54.5	3.45	6.05	

Over the velocity range in which Complex H emission is most likely (-230 km s^{-1} < V_{LSR} < -170 km s^{-1}), our spectra reach a typical rms of 0.05 K for extended sources and 0.13 K for point sources (because of the shorter integration times). Assuming a distance of 27 kpc and a linewidth of 6 channels (1.52 km s^{-1}), similar to the linewidths of the Galactic lines we detected, we translate these rms values to 3 σ upper limits on the total molecular mass associated with each source of $24 - 130$ M$_\odot$, with a median upper limit of 47 M$_\odot$. These masses correspond to typical molecular cores in Galactic star forming regions, but are much smaller than the masses of giant molecular clouds. These mass limits also assume that the Milky Way value of X_{CO}, the CO-H$_2$ conversion factor, is appropriate for Complex H. Recent analyses of X_{CO} in other galaxies suggest that it has at most a weak dependence on metallicity (Walter et al. 2001, 2002; Bolatto et al. 2003; Rosolowsky et al. 2003), which would validate our assumption.

In addition to searching for localized CO emission in Complex H, we can also combine all of our spectra to search for a very faint, diffuse component. Our spectra of 60 sources span 7° of longitude and 6° of latitude, covering a total area of approximately 0.05
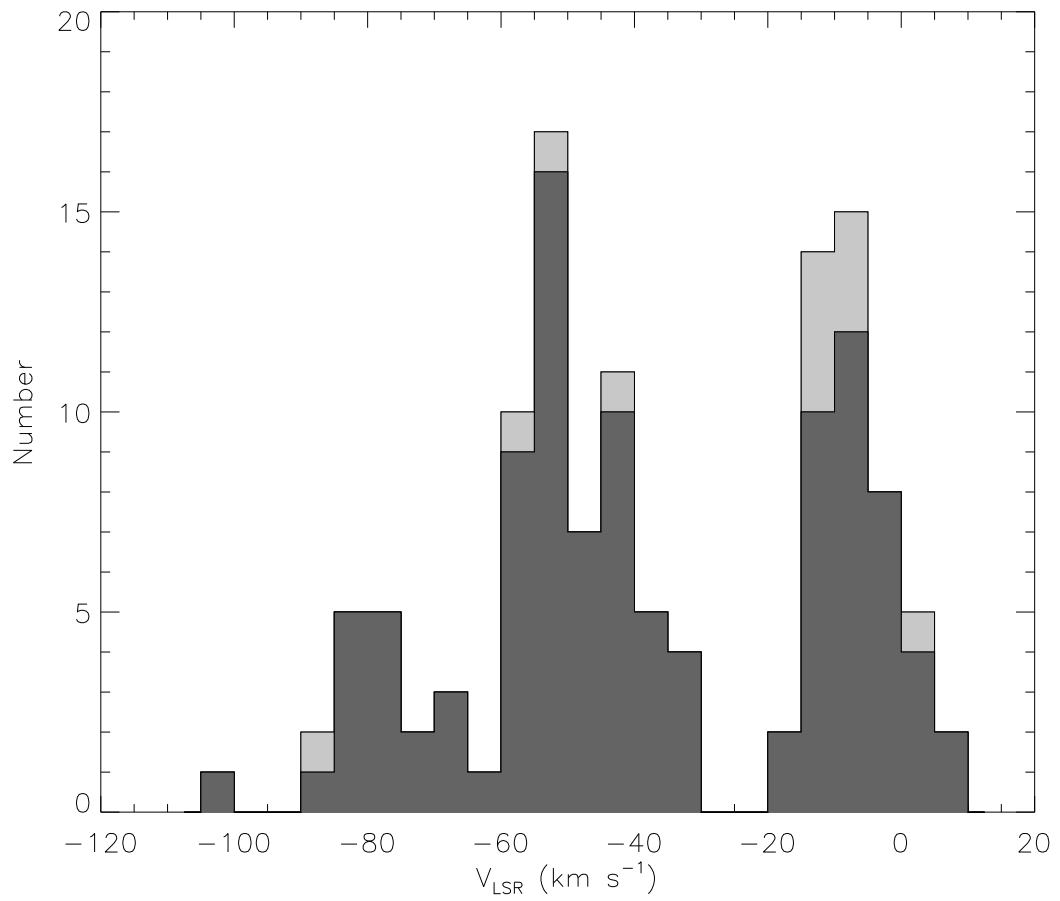
Figure 3.4 — Velocity histogram of the Milky Way CO lines we detected. Emission lines are shown in dark gray and absorption lines (which actually represent emission in the reference position) are shown in light gray.

deg^2 ($\sim 10^4$ pc^2 at a distance of 27 kpc) with a net integration time of 125 ks. The average spectrum over all of our observed positions has an rms noise level of 5 mK, which (again assuming the Galactic value of X_{CO} and a linewidth of 1.52 km s^{-1}) yields a 3 σ upper limit of ~ 1000 M$_\odot$ on the diffuse molecular content of the HVC.

3.2.5   Limits on the Star Formation Rate in Complex H

If we interpret these results as implying that there are currently no OB associations in Complex H, then the flux limits in §3.2.2 suggest that fewer than 25 OB stars are present (for an average OB star flux at 8 μm of 4 mJy). Given a total lifetime of an OB star of $\sim 10^7$ yr and a typical mass of 20 M$_\odot$, we calculate that the rate of formation of massive stars in Complex H is less than 5×10^{-5} M$_\odot$ yr^{-1}. Our observations do not place any direct constraints on the *total* star formation rate in Complex H, since low-mass stars do not produce detectable amounts of mid-infrared emission. However, if we assume a Salpeter initial mass function (Salpeter 1955) with upper and lower mass limits of 200 M$_\odot$ and 0.1 M$_\odot$, respectively, we can translate the high-mass star formation rate we derived into an upper limit on the total star formation rate of 3.2×10^{-4} M$_\odot$ yr^{-1}. Using a Kroupa initial mass function (Kroupa 2001), which turns over at the low-mass end, instead of the Salpeter form reduces the limiting total star formation rate slightly to 2.1×10^{-4} M$_\odot$ yr^{-1}. Under the more stringent assumption that our observations rule out the presence of *any* O or B stars in Complex H, the upper limit on the star formation rate is a factor of 25 lower at 1.3×10^{-5} M$_\odot$ yr^{-1} (for a Salpeter IMF) or 8.4×10^{-6} M$_\odot$ yr^{-1} (for a Kroupa IMF).

By comparison, known Local Group dIrrs have star formation rates ranging from 1×10^{-4} M$_\odot$ yr^{-1} for the Sagittarius dwarf irregular galaxy, with an absolute magnitude of $M_V = -12.3$, up to nearly 1 M$_\odot$ yr^{-1} for IC 10, with an absolute magnitude of $M_V = -15.7$ (Mateo 1998, and references therein).

3.3   Search for a Distant Stellar Population Behind the Milky Way

Dwarf galaxies, whether they contain significant amounts of gas or not, usually have a substantial fraction of their stellar mass locked up in an old, metal-poor stellar population. Therefore, even though Complex H lacks appreciable amounts of massive star

formation, we must also search for an evolved stellar population associated with the HVC. The most luminous stars in such a population are on the red giant branch (RGB) and the asymptotic giant branch (AGB). These stars can be easily recognized by their characteristic distribution in optical and near-infrared color-magnitude diagrams (CMDs). In the case of Complex H, optical data are largely useless because of the very high foreground density of Milky Way stars combined with several magnitudes of extinction. Near-infrared observations, in contrast, offer several strong advantages: much less extinction, lower foreground levels (since most stellar spectra peak at shorter wavelengths), and the enhanced brightness of RGB and AGB stars relative to other types of stars. In this section, we describe our use of 2MASS data to search for evidence of an ancient stellar population in Complex H.

3.3.1   2MASS Data

The 2MASS project surveyed the entire sky in three near–infrared bands (J, H, and K_S). 2MASS images have typical seeing of about $3''$, and the data are complete down to 10 σ limiting magnitudes of $J = 15.8$, $H = 15.1$, and $K_S = 14.3$ (2MASS Explanatory Supplement.[2]) In the near–infrared, the red giant branch extends up to $K_S \approx -6.2$ at a color of $J - K_S \approx 1$ (Nikolaev & Weinberg 2000), so a population of evolved stars is visible in the 2MASS dataset out to a distance modulus of $m - M \approx 20$ ($d = 100$ kpc). The 2MASS Point Source Catalog (Cutri et al. 2003) includes photometry and astrometry for $\sim 4.7 \times 10^8$ objects.

3.3.2   Search Technique

Using the 2MASS Point Source Catalog, we can construct color–magnitude diagrams (CMDs) of the center of Complex H. By comparing these CMDs to those of nearby regions (e.g., at the same Galactic latitude but $\sim 10°$ away in longitude), it is straightforward to search for a population of evolved stars behind the Milky Way. If the population is relatively massive (comparable to Sagittarius, for example), the RGB will be visually obvious in the CMD without even attempting to enhance the signal by statistically removing foreground stars. In Figure 3.5 we show the K_S, $J - K_S$ CMD for 1 deg^2 centered on the peak of the HI distribution of Complex H ($\ell = 131°, b = 1°$). The two strong plumes of stars extending upward around $J - K_S = 0.4$ and $J - K_S = 0.8$ correspond to foreground

---

[2]http://www.ipac.caltech.edu/2mass/releases/allsky/doc/explsup.html

main sequence stars and red clump stars, respectively. The Milky Way red giant branch is visible just redward of the red clump stars at brighter magnitudes ($J - K_S \gtrsim 0.4$, $K_S \lesssim 10$). A red giant population associated with Complex H would appear as a prominent sequence of stars extending up and to the right from the right side of the foreground giant branch (e.g., Cole 2001). There is no sign of a distinct stellar population at any distance greater than ~ 20 kpc.

The signature of a less luminous stellar population (more like Draco or Ursa Minor) may be easier to detect using the luminosity functions instead of the CMDs. We therefore also examined the K_S-band stellar luminosity function of this field, both by itself and in comparison to the control field at $\ell = 140°, b = 1°$. A distant red giant branch causes a sudden increase in the slope of the luminosity function (either differential or cumulative) when the magnitude of the tip of the red giant branch (TRGB) is reached. The sensitivity of this method can be enhanced by dividing the luminosity function into color bins (since red giants, AGB stars, etc. have particular colors for a given combination of age and metallicity). For color ranges covering the RGB, and carbon stars and long period variables, we detect no difference between the luminosity functions of the core of Complex H and the control field.

3.3.3 Detection Limits

In order to determine what limits these nondetections place on the stellar content of Complex H, we used a Monte Carlo code to sample stars of various ages and metallicities from the Padua isochrone set (Girardi et al. 2000). We selected a sample with a metallicity of $z = 0.004$ and star formation from $5 - 12$ Gyr ago, similar to the stellar populations of the Fornax and Sagittarius dSphs. This model produces a giant branch very similar to that of Sagittarius. We then overlaid the model population onto a field near Complex H and used Poisson statistics to estimate the likelihood that the on-field CMD was similar to the off-field CMD plus the model (normalized to the same number of stars). Figure 3.6 shows the 1, 2, and 3 σ detection limits, behind the Complex H field, for that Fornax- or Sagittarius-like population as a function of distance. The locations of a few other dwarf spheroidals with intermediate-age populations are also plotted in the figure. At the distance of Complex H, a population with a mass of 2.5×10^5 M$_\odot$ in stars would be marginally detected in the 2MASS data. Sgr itself, as the most luminous of these galaxies around the Milky Way, would be
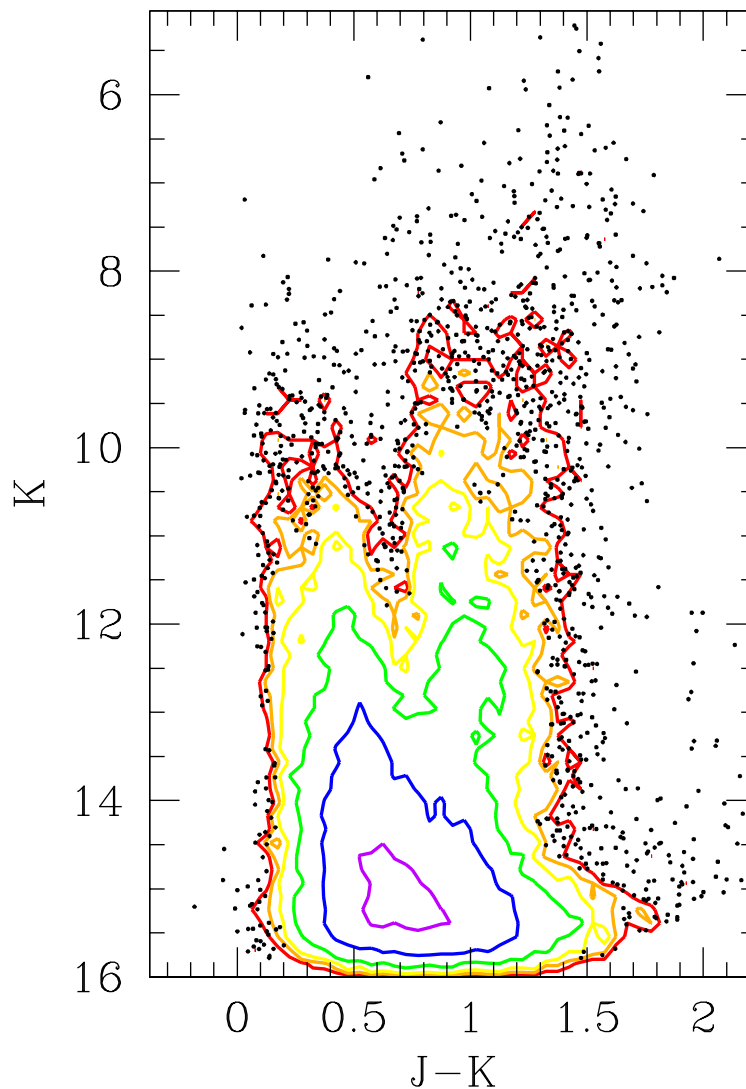
Figure 3.5 — 2MASS Hess/color-magnitude diagram of the center of Complex H. The stellar density in the CMD is contoured with levels of 4, 8, 16, 40, 120, 360 stars per 0.01 mag^2. Individual stars are plotted for areas below the second contour. The feature on the blue side of the diagram extending from $J - K_{\mathrm{S}} = 0.8$ at the faint end to $J - K_{\mathrm{S}} = 0.2$ at $K_{\mathrm{S}} = 9$ is the Milky Way disk main sequence spanning a wide range of ages and distances. On the red side of the diagram, the disk red clump (also spanning a wide range of ages and distances) extends from $J - K_{\mathrm{S}} = 1.0$ at $K_{\mathrm{S}} > 12$ to $J - K_{\mathrm{S}} = 0.7$ at $K_{\mathrm{S}} = 7$. There is no excess population of RGB or AGB stars associated with the HVC.

detected at the 70 σ level at the position of Complex H. A very faint dwarf spheroidal such as Carina ($M_* \approx 3 \times 10^5$ $M_\odot$), however, is down in the noise because its luminosity is a factor of ~ 40 lower. Based on these results, it is clear that any old population with a metallicity of [Fe/H] ≈ -0.7 that is present must have a mass of less than $2 - 3 \times 10^5$ $M_\odot$. Because of the metallicity dependence of color of the RGB, a more metal-poor population is easier to hide down in the Galactic plane; the bluer giant branch is more concealed by the foreground screen of Milky Way red giants and red clump stars. For a purely old population with [Fe/H] ≈ -2, the detection limits are about twice as high as those shown in Figure 3.6 ($4 - 6 \times 10^5$ $M_\odot$). We are therefore unable to rule out the presence of a galaxy such as Ursa Minor, Draco, Sextans, or Sculptor at the location of Complex H; at best, these objects could be detected at ~ 3 σ in the 2MASS data because of the bright foregrounds. The known dwarf galaxies with these kinds of stellar masses and stellar populations, however, have H I masses $\ll 10^7$ $M_\odot$.

It is possible to construct larger stellar populations that are undetectable with 2MASS by using only relatively young stars. Populations younger than ~ 1 Gyr avoid the RGB phase transition, so the brightest easily identifiable stars in the near-infrared CMD are the core-helium burning stars. The detection limits then become $\gtrsim 10$ times higher than those plotted in Figure 3.6, and stellar masses of $\sim 3 \times 10^6$ $M_\odot$ are possible. Even younger populations (e.g., $300 - 700$ Myr) could contain even more mass (up to 10^7 $M_\odot$) and still not be visible. However, a galaxy containing this many young stars and only a very small fraction of old stars ($< 10\%$ to avoid the limits derived above) would be very unusual. If star formation at any appreciable level had continued as recently as a few tens of Myr ago, we should have discovered the remnants of that activity in §3.2.

Our conclusion is that we can rule out any moderate to large dwarf spheroidals associated with Complex H, but extremely low-mass dSphs such as Draco can hide down in the Galactic foreground at the limits of detectability. We can also construct pathological populations (unlike those of known dwarf galaxies) that have significant stellar masses, but not enough old stars to be seen in 2MASS. However, there are no known dwarf irregular galaxies that contain as much gas as Complex H does and would not be detectable in 2MASS at a distance of 27 kpc.
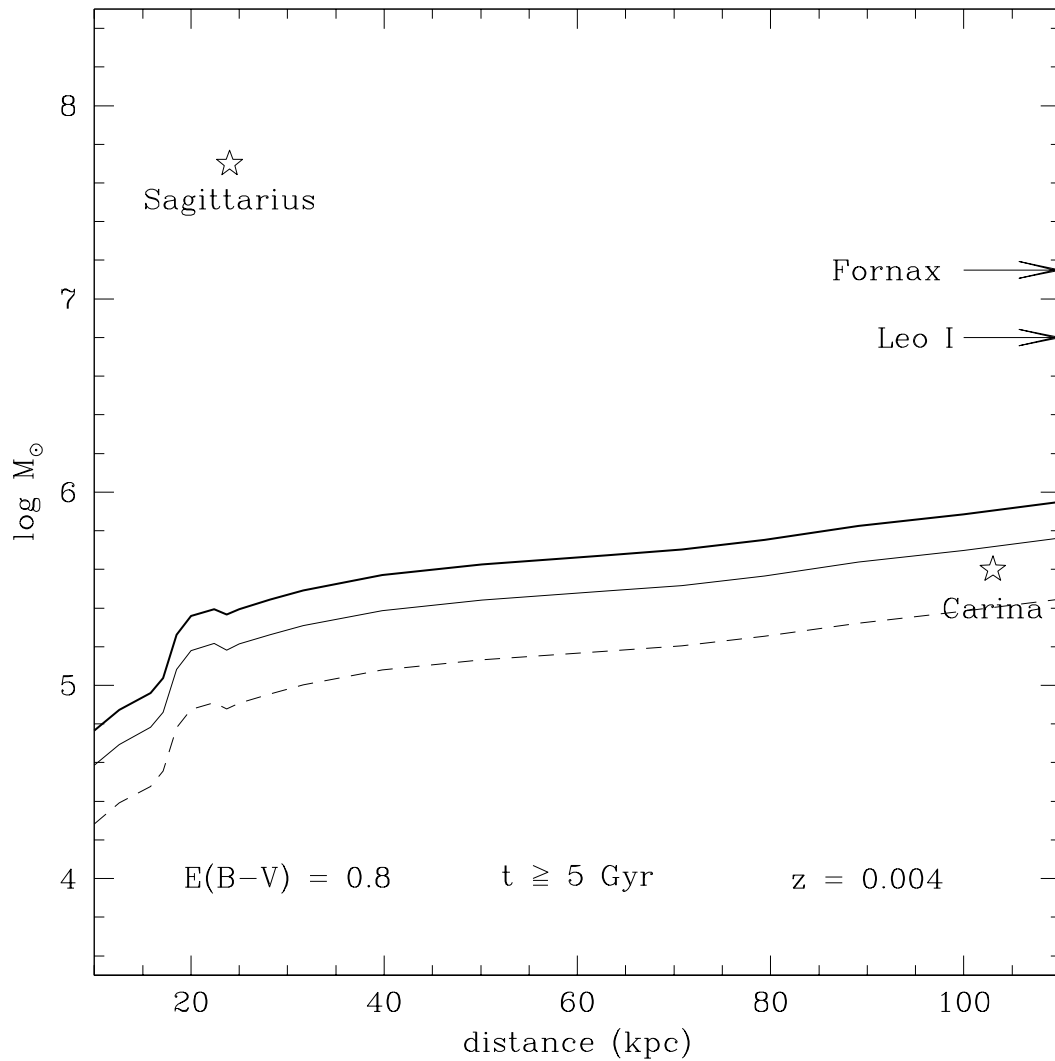
Figure 3.6 — Detection limits for a mixed old and intermediate age stellar population at the position of Complex H. The dashed, thin solid, and thick solid lines represent 1 σ, 2 σ, and 3 σ detection limits. A dwarf the size of Sagittarius, Fornax, or Leo I would be strongly detected at any distance. Much less massive objects comparable to Carina would probably not be detected at 105 kpc (the actual distance of Carina), but would be a 3 σ detection at the probable distance of 27 kpc to Complex H.

3.4 Discussion

3.4.1 What Is Complex H?

W98 presented six plausible explanations of the origin of Complex H, ranging from the neutral edge of a superbubble in the outer Galaxy to a massive, distant intergalactic cloud in the Local Group. Given the distance limits discussed in §3.1, the remaining possibilities are (1) Complex H was produced by a Galactic fountain, (2) Complex H is an infalling extragalactic cloud, and (3) Complex H is a nearby dwarf galaxy. A Galactic fountain origin for Complex H cannot be ruled out entirely without absorption-line measurements, but the low metallicities of other HVCs (e.g., Lu et al. 1994a,b; Wakker et al. 1999; Wakker 2001; Richter et al. 2001; Sembach et al. 2002; Tripp et al. 2003) and its large mass and distance suggest that this possibility is unlikely.

Complex H does not appear to host either significant amounts of recent star formation or a substantial old stellar population, making it difficult to distinguish between the latter two possibilities. If Complex H is associated with a dwarf galaxy, it must be a rather faint dwarf to have escaped detection. The combination of a low total luminosity, small numbers of evolved stars, low levels of ongoing star formation, and a large gas mass would make this dwarf galaxy unique in the Local Group.

On the other hand, if Complex H is *not* a dwarf galaxy, we would be forced to conclude by default that it is an infalling extragalactic cloud that is in the process of being accreted by the Milky Way. In this case, we must understand why Complex H has failed to form any stars despite the $\gtrsim 10^7$ M$_\odot$ of H I that it contains. What makes Complex H different from other gas clouds of similar masses? Did it only acquire its gas recently, not allowing time for star formation? Is its internal pressure too low for molecular clouds to form (Blitz & Rosolowsky 2004)? Higher resolution H I observations of Complex H support the latter possibility, indicating peak H I column densities of $\sim 2.5 \times 10^{20}$ cm^{-2} and number densities of a few particles per cm^3 (Wakker & Schwarz 1991; Wakker, Vijfschaft, & Schwarz 1991; Lockman 2003). However, these measurements do not address the more fundamental issue of *why* the pressure and density in such a large cloud of gas are so low.

The key question that must be answered to resolve this issue is whether Complex H is surrounded by a dark matter halo, and therefore represents CDM substructure, or whether it is a cold accretion flow such as those recently suggested by Birnboim & Dekel (2003), Keres et al. (2004), and Dekel & Birnboim (2004). The argument for Complex H being a

dark galaxy relies on the CDM prediction of large numbers of low-mass dark matter halos, its large H I mass, and its almost unprecedented H I-to-stellar mass ratio. Since the predicted subhalos are likely to exist (see §3.4.3), and the most massive subhalos should have retained or accreted some gas, Complex H seems to have many of the expected properties of one of these objects. The only hole in this case is the kinematics of the cloud. As described in §3.1, a cloud as massive as Complex H should have a rotation velocity of ~ 30 km s^{-1}, implying a velocity gradient as large as 60 km s^{-1}, or a velocity dispersion of similar magnitude. The observed gradient across the HVC is closer to 20 km s^{-1}, and the velocity dispersion is about 12 km s^{-1}, much smaller than expected. These values can still be compatible with a large total mass for Complex H if (1) we are seeing the rotation close to face-on, and therefore underestimating its amplitude, or (2) the H I is confined to the central regions of the dark matter halo, so that the kinematics do not reveal the full mass of the cloud. It is worth noting that other Local Group dwarfs with similar H I masses to Complex H (e.g., Sextans B and IC 1613) also have fairly low rotation amplitudes (~ 10 km s^{-1}) and velocity dispersions.

Because this interpretation requires somewhat special circumstances, the alternative possibility that Complex H represents an instance of "cold mode" gas accretion onto the Milky Way (as opposed to the standard "hot mode", in which gas is shock heated to very high temperatures and ionized at large radii before accreting onto a galaxy and later cooling) must be considered as well. Complex H would be the first observed example of this process, which has heretofore only been seen in hydrodynamic simulations. This would constitute strong evidence that cold accretion actually does play an important role in galaxy formation in the real universe. In addition to the kinematics, another piece of evidence in support of this idea is that Complex H is located relatively close on the sky to M31, which corresponds to the direction along the filament from which the Local Group formed. However, there are also problematic aspects to this picture, notably that Complex H cannot be gravitationally bound without large amounts of dark matter, and therefore would necessarily be a transient object that formed recently, and also that similar objects have not been detected around other galaxies even though surveys with sufficient sensitivity to detect Complex H analogs have been carried out. More detailed observations of the kinematics of Complex H may help to determine which of these possibilities is correct, but the more basic problem that the behavior of gas clouds in the Local Group is not yet understood (Sternberg, McKee, & Wolfire 2002) also must be addressed.

3.4.2 Implications for the Nature of HVCs

Complex H now joins an increasingly long list of other high-velocity clouds that appear not to contain stars (Simon & Blitz 2002; Davies et al. 2002; Willman et al. 2002; Hopp, Schulte-Ladbeck, & Kerp 2003; Siegel et al. 2005). The hypothesis that HVCs are the H I counterparts of normal low-surface brightness dwarf galaxies can therefore safely be put to rest. It remains possible, of course, that HVCs could host stellar populations whose surface brightness is significantly lower than that of any currently known galaxy, but more likely, HVCs simply do not contain any stars.

A number of competing models to explain the origins of HVCs have been proposed in recent years: (1) HVCs are distant ($d \gtrsim 500$ kpc), massive clouds that are the left-over building blocks of the Local Group (Blitz et al. 1999), (2) HVCs are small, nearby ($d \lesssim 50$ kpc) clouds that represent tidal debris from destroyed dwarf galaxies, and (3) HVCs are low-mass clouds at intermediate distances ($d \lesssim 150$ kpc) that are cooling and condensing out of the halo of hot gas that surrounds the Milky Way (Maller & Bullock 2005). Only in the first model would HVCs be expected to be associated with dwarf galaxies. The absence of stars in HVCs, however, is not necessarily evidence against this model because of the many possible mechanisms for suppressing star formation in low-mass objects (see §3.1). Our results therefore do not provide us with significant new leverage on the nature of HVCs. Still, it may be worth noting that Complex H is cooler ($T \sim 50$ K; Wakker et al. 1991) and possibly more massive than the clouds expected in the Maller & Bullock (2005) model.

3.4.3 Implications for the Substructure Problem

According to ΛCDM numerical simulations, the Local Group should contain up to ~ 500 low-mass dark matter halos (Klypin et al. 1999; Moore et al. 1999a). Observationally, there are less than 40 known Local Group dwarf galaxies (e.g., Mateo 1998; van den Bergh 2000). Possible explanations for this mismatch are: (1) the simulations are overpredicting the amount of substructure that should be present, (2) there are many faint Local Group dwarfs that have not yet been discovered, or (3) ~ 90 % of low-mass halos never form stars. There are only a few ways to alter the predictions of the simulations, such as changing the initial power spectrum of density fluctuations (Kamionkowski & Liddle 2000) or imbuing the dark matter particles with new properties (e.g., a nonzero self-interaction cross-section

[Spergel & Steinhardt 2000] or annihilation rate [e.g., Kaplinghat et al. 2000]). Because there is little theoretical or observational motivation for these ideas at present, much of the attention has focused on the other two potential solutions of the substructure problem.

Recent observational work has cast doubt on the idea that hundreds of undiscovered dwarf galaxies could exist in the Local Group. Our results, along with the optical studies of other HVCs cited above (§3.4.2), show that HVCs do not contain dwarf galaxy-like stellar populations. The most straightforward interpretation of these findings is that there are no stars in HVCs; if any stars have formed, the process must have been extremely inefficient. We therefore argue that the substructure problem likely originates in the difficulty that low-mass dark matter halos experience in becoming dwarf galaxies. A number of theoretical ideas support the plausibility of this hypothesis. For example, the heating of the intergalactic medium that occurred during the epoch of reionization may have prevented low-mass halos from holding on to their gas (Bullock et al. 2000). Simple photoionization caused by the ultraviolet background can also prevent these halos from forming stars (Somerville 2002). Tidal stripping may have removed most of the mass from dwarf galaxies relatively early in the history of the universe (Kravtsov et al. 2004). Alternatively, the supernova-driven winds produced by the formation of massive galaxies at high redshift could have blown out the interstellar medium of their satellite galaxies (Scannapieco et al. 2000, 2001).

Observations are also beginning to provide evidence in favor of this picture as well. Flux anomalies in multiply-imaged quasars appear to require that the lensing galaxies contain significant substructure (Mao & Schneider 1998; Chiba 2002; Metcalf & Zhao 2002; Dalal & Kochanek 2002; Kochanek & Dalal 2004). It is not yet clear whether these substructures are luminous or dark, but their abundance is roughly consistent with ΛCDM predictions. In the nearby universe, Robishaw, Simon, & Blitz (2002) recently identified a mysterious object that may be the first of the posited dark galaxies to be discovered in the Local Group. This object is a high-velocity cloud (HVC $127-41-330$) that is apparently interacting with the Local Group dwarf galaxy LGS 3 and therefore is located at a distance of ~ 700 kpc from the Milky Way. The velocity field of this HVC indicates that it is rotating, and the inferred total mass is at least four times as large as the H I mass. A preliminary search for stars in HVC $127-41-330$ did not yield any evidence for a stellar component (Robishaw et al. 2002), leading us to conclude that this object has all of the expected characteristics of one of the missing dark matter halos from CDM simulations (Si-

mon, Robishaw, & Blitz 2003b). It is worth noting, however, that several extremely faint and low surface brightness objects have recently been discovered in the Sloan Digital Sky Survey, suggesting that the census of luminous dwarfs in the Local Group may not yet be complete (Zucker et al. 2004; Willman et al. 2005a,b).

3.4.4 Starless Gas Clouds in the Local Group

Do dark galaxies actually exist? Blind H I surveys covering large areas of sky and smaller targeted surveys of nearby galaxy groups have turned up small numbers of low-mass H I clouds, but deep optical imaging almost invariably reveals that these objects are associated with dwarf galaxies. The only exception is the object recently announced by Minchin et al. (2005), VirgoHI21. This 10^8 M$_\odot$ cloud in the Virgo cluster has no optical counterpart down to a surface brightness limit of $\mu_B = 27.5$ mag arcsec^{-2}, which would make it the lowest surface brightness galaxy known if it does turn out to contain any stars. VirgoHI21 is currently the only such starless cloud outside the Local Group, and therefore by default represents the closest extragalactic analog to Complex H, despite its large mass and location in a cluster environment. Minchin et al. (2005) suggest that previous H I surveys have not reached low enough column density limits to detect other similar objects, so more sensitive H I surveys may yet reveal a larger population of starless H I clouds.

Based on a thermal instability model of gas clouds embedded in dark matter halos, Taylor & Webster (2005) conclude that objects with H I masses comparable to Complex H are likely ($> 50\%$ probability) to form stars. However, the minimum self-regulating star formation rate that they predict for a 10^7 M$_\odot$ cloud is $\sim 10^{-6}$ M$_\odot$ yr^{-1}, significantly below the level that we would be able to detect; this model therefore does not require Complex H to be completely starless.

If Complex H and HVC $127-41-330$ indeed lack any stellar component, then these clouds, along with Wright's Cloud (Wright 1974, 1979) and Davies' Cloud (Davies 1975), may be the most massive examples of a population of starless clouds of gas in the Local Group. It is tempting to associate these objects with some of the dark matter substructures predicted by CDM, but further kinematical studies will be necessary to determine whether Complex H, Wright's Cloud, and Davies' Cloud are in fact dark matter–dominated. The association of these objects with dark matter halos would provide strong evidence that the CDM substructure predictions are correct and that many more low-mass halos do exist

in the Local Group, although the lower-mass halos may contain much less neutral gas (or none at all), making them more difficult to detect. Future multiwavelength investigations of these massive H I clouds to ascertain how they are distinct from similar-sized clouds that formed dwarf galaxies will help to illuminate the process of galaxy formation at both high and low redshift.

3.5   Conclusions

We have sought infrared and radio evidence of a dwarf galaxy associated with the massive, nearby HVC Complex H. Lockman (2003) showed that Complex H is most likely located slightly beyond the edge of the Milky Way disk at a distance of 27 ± 9 kpc from the Sun, consistent with the nondetection of high-velocity absorption lines in the spectra of distant OB stars (Wakker et al. 1998). Mid-infrared observations from the MSX satellite reveal many star-forming regions in the Galactic plane near the position of Complex H. We used CO observations to measure the velocities of 59 such sources and determined that they are clearly Milky Way objects. Only one of the sources was not detected in CO and therefore has an unknown origin, but it is plausible that our observations happened to miss the Milky Way CO cloud near this line of sight. Under the assumptions that Complex H lies at the distance of 27 kpc suggested by Lockman (2003), and that the Galactic CO-H_2 conversion factor applies to HVCs, we placed $3\,\sigma$ upper limits of $24 - 130$ M$_\odot$ on the amount of molecular gas that could be present in Complex H at the position of each of these targets. These limits allow us to rule out the possibility that any of the infrared sources are associated with typical star-forming molecular cores or giant molecular clouds in Complex H. We also derived an upper limit of ~ 1000 M$_\odot$ on the mass of diffuse molecular gas that Complex H could contain. Assuming that there are no massive stars currently present in Complex H, as these observations suggest, we placed upper limits on the star formation rate in the HVC of 3.2×10^{-4} M$_\odot$ yr^{-1} M$_\odot$ yr^{-1} for a Salpeter initial mass function and 2.1×10^{-4} M$_\odot$ yr^{-1} M$_\odot$ yr^{-1} for a Kroupa initial mass function. If the actual star formation rate in the HVC is close to these limits, Complex H would rank near the bottom of the list of Local Group dwarf irregulars in star formation despite its large reservoir of atomic gas.

We also used 2MASS data to constrain the possible size of intermediate and old stellar populations within Complex H. Near-infrared color-magnitude diagrams of the core of the HVC do not contain any excess RGB or AGB stars compared to nearby control fields.

The K_s-band luminosity function at the position of Complex H also reveals no evidence for an extragalactic population of stars. We derived upper limits on the evolved stellar content of the HVC by using Monte Carlo techniques to create model dwarf galaxy CMDs based on the stellar isochrones of Girardi et al. (2000). We then added these CMDs to the control field CMDs near Complex H. In this manner, we determined that a dSph-like population with a stellar mass of $\gtrsim 3 \times 10^5$ M$_\odot$ would be detectable in the 2MASS dataset. Very metal-poor populations ([Fe/H] ≈ -2) and young stars ($\lesssim 1$ Gyr) are more difficult to detect in the near-infrared, so the upper limits for those populations are somewhat higher.

While we cannot entirely rule out the existence of a dwarf galaxy associated with Complex H, these results demonstrate that the galaxy must have an exceptionally low luminosity if it exists. There are no known dwarfs that have the required characteristics of a large gas mass, very low current rates of star formation, and a very small intermediate and old stellar population. If Complex H does contain any stars, it almost certainly has the largest $M_{\rm H\,I}/L_B$ and one of the smallest populations of evolved stars in the Local Group.

We presented arguments that Complex H is either a dark galaxy in the Local Group, or an example of a cold accretion flow onto the Milky Way. In either case, this HVC is a unique object whose existence has important implications for our understanding of galaxy formation, and further observations and modeling will be needed to determine the true nature of Complex H. If Complex H is a dark galaxy, and the Cold Dark Matter prediction of hundreds of low-mass dark matter halos in the Local Group is correct, then our results provide observational evidence that these halos may be unable to form stars. Some of the most massive subhalos, such as Complex H and the dark matter–dominated HVC described by Robishaw et al. (2002) may have accumulated enough gas to be detected as high-velocity clouds, but the bulk of the population could remain entirely dark.

Chapter 4

21 cm Imaging of LGS 3 and an Apparently Interacting High-Velocity Cloud

This chapter is a modified version of a paper that was previously published in *The Astrophysical Journal Letters* (Robishaw, Simon, & Blitz 2002, ApJ, 580, L129). It also incorporates some material from an article published in the proceedings of *Satellites and Tidal Streams* (Simon, Robishaw, & Blitz 2003, ASP Conf. Ser. 327, 32).

Abstract

We present a $93' \times 93'$ map of the area near the Local Group dwarf galaxy LGS 3, centered on an H I cloud $30'$ away from the galaxy. Previous authors associated this cloud with LGS 3 but relied on observations made with a $36'$ beam. Our high-resolution ($3'.4$), wide-field Arecibo observations of the region reveal that the H I cloud is distinct from the galaxy and suggest an interaction between the two. We point out faint emission features in the map that may be gas that has been tidally removed from the H I cloud by LGS 3. We also derive the rotation curve of the cloud and find that it is in solid-body rotation out to a radius of $10'$, beyond which the rotation velocity begins to decline. Assuming a spherical geometry for the cloud, the implied dynamical mass is $2.8 \times 10^7 \, (d/1 \text{ Mpc}) \, M_\odot$, where d is the distance in Mpc. The observed H I mass is $5.5 \times 10^6 \, (d/1 \text{ Mpc})^2 \, M_\odot$, indicating that

the cloud is dark matter-dominated unless its distance is at least 1.9 Mpc. We propose that the cloud is a high-velocity cloud that is undergoing a tidal interaction with LGS 3 and therefore is located roughly 700 kpc away from the Milky Way. The cloud then contains a total mass of $\sim 2.0 \times 10^7$ $M_\odot$, 82% of which consists of dark matter.

4.1   Introduction

As described in the previous two chapters, despite numerous reasons to suspect a connection between high-velocity clouds and the substructure problem, physical evidence supporting this hypothesis has proved elusive. HVCs are definitively not associated with normal low-luminosity dwarf galaxies and appear likely not to contain any stars at all. Robust HVC distances therefore cannot be obtained from optical observations, although there is some hope for Hα distance estimates. Consequently, we must turn to alternate techniques for determining the distances and dark matter content of HVCs. In this chapter, we present the special case of one high-velocity cloud whose position, morphology, and kinematics allow us to constrain these critical parameters.

4.1.1   HVC 127−41−330

Defying years of intensive study, HVC distances and masses remain almost completely unknown. We attack this problem by using the upgraded Arecibo telescope to completely map a large area (2.4 deg^2) around the Local Group dwarf galaxy LGS 3 and a newly identified HVC. If the HVC and the dwarf galaxy are interacting, as we will argue, then this system presents a unique opportunity to constrain the distance and mass of an HVC, and to determine whether HVCs are related to the missing dark matter halos in the Local Group.

The H I cloud next to LGS 3 appears to have been first detected by Hulsbosch in 1982 using the Dwingeloo 25 m telescope (Christian & Tully 1983). The original H I observations of LGS 3 by Thuan & Martin (1979), made using Arecibo, did not detect the cloud because they were directed at the optical position of the galaxy rather than 30′ away. According to Christian & Tully (1983), Hulsbosch reported that LGS 3 lies on the edge of a large cloud of gas (called HVC 127−41−330 by them) that contains a significant velocity gradient. However, with the 36′ resolution of his Dwingeloo observations, Hulsbosch was apparently unable to draw any firm conclusions about the nature of this

object. Over the next 17 years the situation remained murky as few observers paid attention to this part of the sky. The sole reference to the cloud during this period was in the HVC survey of Hulsbosch & Wakker (1988), who listed the cloud in three entries of their HVC catalog, at $(\ell, b, v_{\mathrm{LSR}}) = (127°, -41°, -331)$, $(128°, -41°, -329)$, and $(127°, -42°, -352)$. They considered all of these detections to be part of LGS 3, which is located at $(\ell, b, v_{\mathrm{LSR}}) = (126°75, -40°89, -287)$.

Five years ago the cloud was rediscovered by Blitz & Robishaw (2000) during their search for gas associated with Local Group dwarf spheroidals in the Leiden/Dwingeloo Survey (LDS) of Galactic Neutral Hydrogen (Hartmann & Burton 1997). Blitz & Robishaw (2000) pointed out that the cloud is not only substantially larger in area and H I mass (if at the same distance as the galaxy) than the gas known to be associated with LGS 3 itself (Thuan & Martin 1979; Young & Lo 1997), but is also offset in both position ($\sim 30'$) and velocity (-50 km s^{-1}) from the dwarf galaxy. They speculated that the cloud might have been ram-pressure stripped out of LGS 3 by hot gas in the halo of M31. They noted, however, that the velocity of the cloud should be less negative than the velocity of LGS 3 ($v_{\mathrm{LSR}} = -287$ km s^{-1}), which it is not ($v_{\mathrm{HVC}} \approx -330$ km s^{-1}). Like Hulsbosch, their ability to consider other possible origins for the cloud was limited by the low angular resolution of the Dwingeloo data.

In order to ascertain the true physical situation involving this object, we included LGS 3 in our Arecibo H I survey of high-velocity clouds. The Arecibo data offer significantly improved sensitivity and an order of magnitude increase in angular resolution compared to previous observations.

In §4.2, we describe our observations and discuss the data reduction. Our analysis of the data is presented along with our map of the HVC and its rotation curve in §4.3. In §4.4, we discuss our results and evidence for a possible interaction between the HVC and LGS 3.

4.2 Observations and Data Reduction

The observations were conducted over five nights in 2000 November using the upgraded Arecibo telescope.[1] We employed the L-band narrow receiver and the 9-level,

[1]The Arecibo Observatory is part of the National Astronomy and Ionosphere Center, which is operated by Cornell University under a cooperative agreement with the National

dual-polarization correlator configuration to yield spectra with a velocity resolution of 0.644 km s^{-1}. At the frequency of H I observations, the telescope has a half-power beam width of 3$.'$4, a main beam efficiency of 0.48, and a gain of 7.2 K/Jy (Heiles 2000).

The data we present in this chapter include 3 nights of on-the-fly (OTF) maps, Nyquist sampled in right ascension and declination, and 2 nights of drift scans. The OTF maps cover a 93$'$ × 93$'$ region and the drift scans add sensitivity in a 40$'$ × 40$'$ area between and including the HVC and LGS 3. The total integration time was ∼22 s beam^{-1} for most of the map and ∼92 s beam^{-1} in the area covered by the drift scans. We reached rms sensitivity levels at the full velocity resolution of 75 mK beam^{-1} and 34 mK beam^{-1} in those regions, respectively.

Each night we observed a single off-source position, which we used to remove the bandpass shape for all of the spectra from that night. Gain calibration was provided by the injection of a known signal into the correlator once per strip. We fitted and removed a linear baseline from each spectrum. We developed a new algorithm to remove spectral standing waves that were present in the data. The drift scans were resampled to match the sampling of the OTF maps, and we then coadded each night's observations to form a single data cube. The reduction will be described in more detail in a future paper presenting the results of our survey of 27 HVCs and Local Group dwarf galaxies.

4.3   Results

Our map (Figure 4.1) reveals considerable detail that was not apparent in previous observations. The H I associated with LGS 3 is visible in the upper right (northwest) as the small red blob at $(\alpha, \delta)_{2000} = (01^h03^m54^s, +21°53')$. The emission is marginally resolved spatially and has an intensity-weighted mean LSR velocity of −287 km s^{-1}. We measure an integrated H I flux of 2.3 ± 0.5 Jy km s^{-1}, in agreement with the value of 2.7 ± 0.2 Jy kms measured by Young & Lo (1997) with the VLA. For a distance of 700 kpc,[2] the H I mass

---

Science Foundation.

[2]Three previous authors have measured distances to LGS 3 of very close to 800 kpc: 810 kpc (Lee 1995); 770 kpc (Aparicio, Gallart, & Bertelli 1997); 830 kpc (Mould 1997). However, in a recent paper based on HST data, Miller et al. (2001) derived a distance of 620 ± 20 kpc. Our own analysis of the HST photometry, using the techniques of Méndez et al. (2002), indicates that the small number of stars in LGS 3 makes Tip of the Red Giant Branch distance measurements unusually uncertain. The true distance uncertainty is likely

of LGS 3 is 2.6×10^5 M$_\odot$. The extended emission seen previously (Christian & Tully 1983; Hulsbosch & Wakker 1988; Blitz & Robishaw 2000) is now resolved into a large, double-lobed H I cloud in the center of the map with a systemic velocity of -331.3 ± 1.0 km s^{-1}, an integrated flux of 24 ± 8 Jy km s^{-1}, and a mean linewidth of 24 km s^{-1}. This cloud is completely separate from LGS 3, located $30'$ away with a velocity difference of -45 km s^{-1}. If the cloud is at the distance of LGS 3, it contains 10 times as much H I, making it unlikely that it originated in LGS 3. Therefore, this cloud qualifies as an HVC.

Although LGS 3 and the HVC may not share a common origin, their apparent proximity in position and velocity demands that we investigate the possibility of an inter-action between them. In this vein, we note that to the east of the HVC, at $(\alpha, \delta)_{2000} = (01^h08^m56^s, +21°53')$, a faint vertical strip of H I extends for $\sim 20'$ along the edge of the map. A similar feature is also visible running horizontally in the southwest part of the map at $(\alpha, \delta)_{2000} = (01^h05^m00^s, +21°13')$. The symmetrical placement of this gas relative to the line connecting LGS 3 and the HVC is suggestive of a tidal interaction, with the two faint clouds representing leading and trailing tidal arms. We consider this idea further in §4.4.

The most striking feature of the HVC is the velocity gradient across it. We ex-amined the gradient by averaging spectra perpendicular to the major axis. We fitted a Gaussian profile to the averaged spectrum at each point along the major axis to create a rotation curve, which is displayed in Figure 4.2a. The rotation curve increases roughly linearly over its central $20'$ and then turns over. The turnover and the overall symmetry of the rotation curve suggest that the HVC is a single, rotating, gravitationally-bound object, and is not composed of two physically distinct clouds that happen to coincide along the line of sight. In order to measure a symmetric rotation curve from two separate clouds, they would have to: have the same extent; have the same large aspect ratio; be aligned along their major axes; have their velocity fields vary with radius in just such a way as to mimic the appearance of a single rotating cloud. We consider this, although not impossible, rather unlikely. We further point out that if the HVC were composed of two overlapping clouds, then the linewidths would be largest at the center of the HVC. Since we observe exactly the opposite, we conclude that the HVC must be a single cloud.

The next question is whether we can be certain that the velocity gradient is due to rotation, despite the appearance of the velocity field as similar to that of a rotating

closer to 100 kpc, so we adopt an intermediate distance of 700 kpc for all calculations.
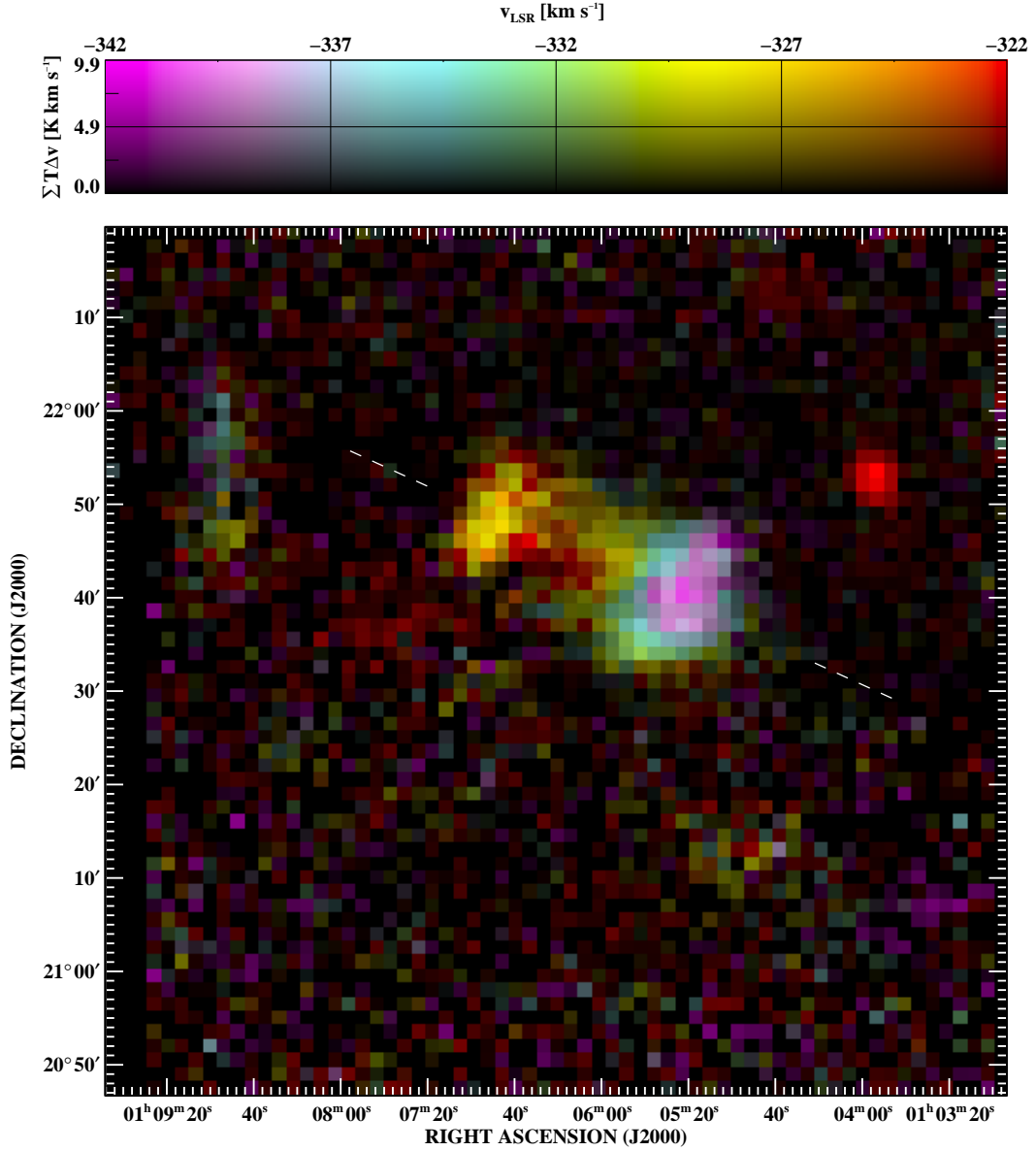
Figure 4.1 — High-resolution H I map of HVC and LGS 3. This color-intensity (velocity-column density) image consists of ~10 hr of on-source integration time acquired over the course of 5 nights. The pixel size is 1′.5, or slightly less than half of a beamwidth. Visible in the map are the Local Group dwarf galaxy LGS 3 (the bright red object at $(\alpha, \delta)_{2000} = (01^h 03^m 54^s, +21°53')$ in the upper right), a compact HVC (the large double-lobed cloud in the center) with a 14 km s^{-1} gradient across it, and two faint features (to the left and lower right of the HVC) that we believe are remnants of a tidal interaction between LGS 3 and the HVC. The dashed white line shows the major axis of the HVC.
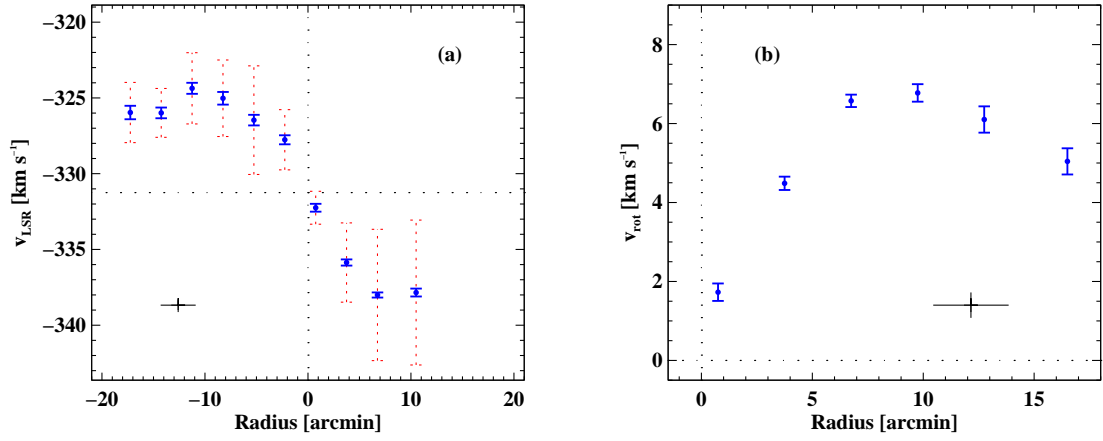
Figure 4.2 — (a) The rotation curve along the major axis of the HVC. The point of maximum symmetry is shown by the dotted lines and occurs at $(\alpha, \delta)_{2000} = (01^{\rm h}05^{\rm m}49^{\rm s}, +21°42')$ with a systemic velocity of -331.3 ± 1.0 km s^{-1}. Blue error bars represent the $1\,\sigma$ uncertainty in the velocity of the fitted Gaussian; red dotted error bars represent the rms of the velocity field perpendicular to the major axis. Removing this rotation curve from the velocity field yields a residual field with an rms of 3 km s^{-1}. (b) The rotation curve folded about the point of maximum symmetry. After a solid-body rise out to a radius of $10'$, the rotation curve begins to decrease. The error bars are the $1\,\sigma$ uncertainties of the weighted average of the Gaussian fits. The crosses indicate the velocity and spatial resolution of our measurements.

disk. If the gradient is *not* due to rotation, the only alternative is shear. A simple timing calculation shows that this explanation is unlikely. The cloud currently has a radius of about 3 kpc (d/1 Mpc), where d is the distance of the HVC in Mpc. The velocity gradient is 14 km s^{-1}, which would correspond to an expansion velocity of 7 km s^{-1}. At that expansion rate, the time for the cloud to reach its current size is 4×10^8 (d/1 Mpc) yr. In this scenario, distances of less than 100 kpc are highly implausible — the HVC would have to be extraordinarily young, and even then the nearest possible progenitors, the Magellanic Clouds, are too far away for the HVC to have reached its present position at any reasonable velocity. At 700 kpc, the lifetime of the cloud is still uncomfortably shorter than a Hubble time, and the lack of a credible progenitor object is equally severe. We conclude that the velocity gradient is probably due to rotation.

We can therefore use the rotation curve to compare the dynamical mass of the HVC to its luminous mass, which we assume consists only of H I and a cosmic abundance of He, such that $M_{\mathrm{lum}} = 1.3 M_{\mathrm{H\,I}}$. The dynamical mass ($M_{\mathrm{dyn}}$) is the mass required to account for the rotational velocity of the HVC at the last measured point, assuming a spherical mass distribution (see Figure 4.2b). The H I mass scales as the square of the distance to the HVC, $M_{\mathrm{H\,I}} = 5.5 \times 10^6 (d/1~\mathrm{Mpc})^2~\mathrm{M_\odot}$, which is $2.7 \times 10^6~\mathrm{M_\odot}$ for a distance of 700 kpc. The dynamical mass, however, scales linearly with distance, $M_{\mathrm{dyn}} = 2.8 \times 10^7 (d/1~\mathrm{Mpc})~\mathrm{M_\odot}$, yielding $2.0 \times 10^7~\mathrm{M_\odot}$ at 700 kpc. (Note that we assume that the rotation is seen edge-on; if this is not the case, then the actual dynamical mass will be larger by a factor of $1/\sin^2 i$.) Therefore, if the HVC is indeed self-gravitating, as is suggested by its rotation curve, and it is located at the distance of LGS 3, *it must be composed mostly of dark matter* (82%). Furthermore, if the cloud is assumed to be any closer than LGS 3 (and is self-gravitating), its dynamical-mass-to-luminous-mass ratio ($M_{\mathrm{dyn}}/M_{\mathrm{lum}}$) must be even larger; if the cloud is further than LGS 3, it remains dark-matter dominated out to a distance of 1.9 Mpc. Since the darkest known galaxy-sized objects have $M_{\mathrm{dyn}}/M_{\mathrm{lum}} \lesssim 100$ (see Mateo 1998, and references therein), we can place a firm lower limit on the distance to the HVC of 39 kpc.

If the velocity gradient across the cloud does indicate rotation, there is only one way to avoid the conclusion that the HVC is composed primarily of dark matter, which is to invoke the presence of large amounts of ionized gas. Current photoionization models of gas clouds embedded in dark matter halos in the Local Group environment suggest that low column density clouds like this HVC should be largely ionized (Sternberg, McKee, & Wolfire 2002). However, these models have difficulty accounting for extended neutral

structures at column densities of $\sim 10^{18}$ cm^{-2} such as the tidal tails that we observe more than $30'$ away from the center of the HVC, so the models may still be missing some essential ingredients. Resolving the relative contributions of neutral and ionized gas to the mass of HVC $127-41-330$ will require sensitive, wide-field Hα observations.

4.3.1 New Arecibo Observations

In August 2002, we used another Arecibo observing run to make a new, more sensitive map of LGS 3 and the HVC. This map, displayed in Figure 4.3, confirms all of the features seen in our original data. The tidal tails are now visible in detail, and their connection to the main body of the HVC is evident. The tails are somewhat more extended than could be seen in the first map, and additional observations over a wider field have revealed that the southwest tail continues on beyond the edge of the map shown in Figure 4.3. The new data are fully consistent with the scenario proposed by Robishaw et al. (2002) of a tidal interaction between the HVC and LGS 3.

4.4 Discussion

Is the HVC indeed interacting with LGS 3? We can approach this question by considering the likelihood that these two objects are completely unrelated. Putman et al. (2002) found that compact HVCs cover $\lesssim 1\%$ of the southern sky. de Heij, Braun, & Burton (2002) used an automated analysis of the LDS to measure a similar covering fraction for $\delta \gtrsim -30°$. There are indications in the de Heij et al. (2002) catalog of a factor of ~ 2 overdensity of compact HVCs within $20°$ of LGS 3, which is not surprising because M31 and the Local Group barycenter are located in the same direction as LGS 3.

We estimate the probability of a spatial coincidence between a dwarf galaxy and a compact HVC by considering the number of compact HVCs and dwarf galaxies near LGS 3. For example, within $20°$ of LGS 3 there are 5 dwarf spheroidal galaxies and 14 compact HVCs from the de Heij et al. (2002) catalog. The HVC discussed in this chapter is located $\sim 30'$ away from LGS 3, so we begin with a circle of radius $30'$ around each of the nearby dwarfs. Now, the probability that at least one of the compact HVCs lies within one of these circles is $p \approx N_{\mathrm{CHVC}} \Omega_{\mathrm{dwarfs}} / \Omega_{20}$, where N_{CHVC} is the number of compact HVCs contained in the region, Ω_{dwarfs} is the solid angle subtended by the circles around the five dwarf galaxies, and Ω_{20} is the solid angle subtended by the region within $20°$ of LGS 3. This
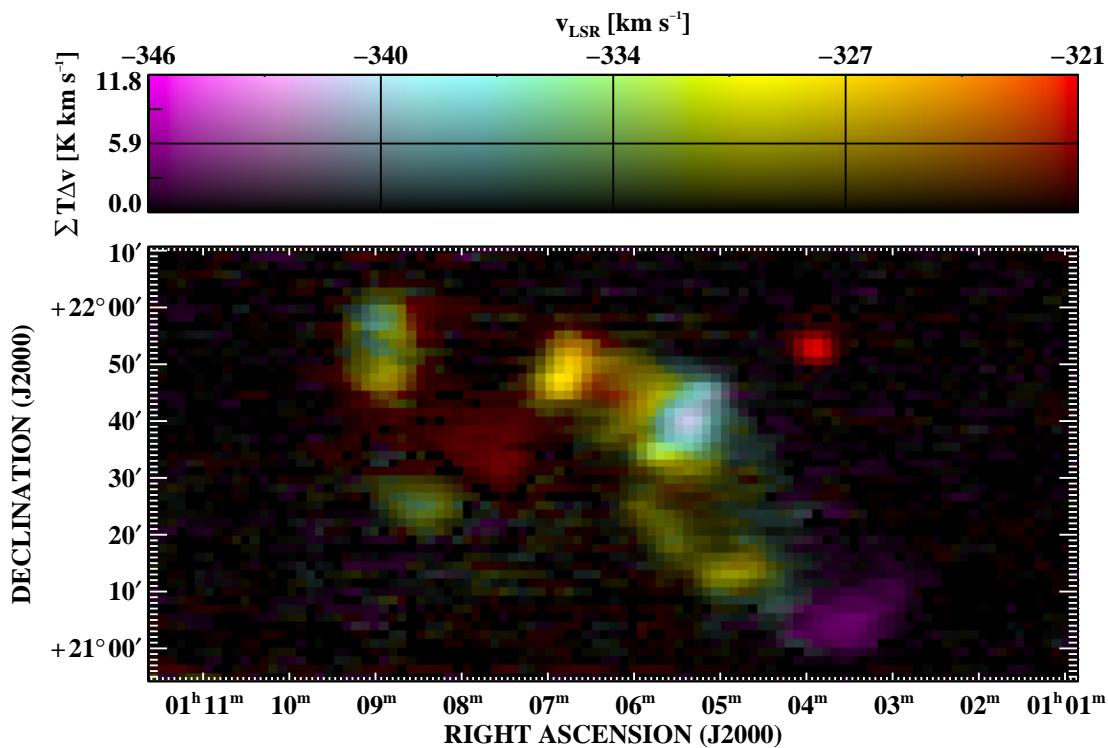
Figure 4.3 — High-sensitivity, wide-field H I map of the region containing the HVC and LGS 3. Colors represent velocity, and intensity represents column density. The faint features to the east and southwest of the HVC that were barely visible in our original data (Figure 4.1) now stand out clearly. Both are (mostly) spatially continuous structures that connect to the main body of the HVC, supporting our interpretation of them as tidal tails that are being torn off of the HVC by LGS 3.

probability is 4.4%. If we increase the region under consideration to within $60°$ of LGS 3, there are 10 dwarf spheroidals (including the small dwarf irregulars WLM and Pegasus) and 46 compact HVCs, and the probability of a chance coincidence is 3.5%. Given such an angular coincidence, the probability of the velocities also matching within 50 km s^{-1} is $\sim 20\%$, for a joint probability of less than 1%. Since these values are not quite negligibly small, we cannot dismiss the possibility of a chance superposition entirely. Nevertheless, we conclude the HVC is probably at the same distance as LGS 3.

Another piece of evidence that the HVC is a self-gravitating, distant cloud, rather than an unbound, nearby object associated with the Milky Way, is its extremely large velocity with respect to the Galactic Standard of Rest (GSR) of $v_{\mathrm{GSR}} = -200$ km s^{-1}. An object originally associated with the Galaxy (e.g., in a Galactic fountain) would have difficulty acquiring such a high velocity. This velocity also renders a distance beyond the Local Group implausible.

Could this object be another dwarf galaxy interacting with LGS 3, rather than an HVC? Simon & Blitz (2002) searched the compact HVCs in the northern hemisphere and concluded that they do not contain stellar counterparts similar to the known Local Group dwarf galaxies. There is no obvious counterpart to this HVC on the Second Palomar Observatory Sky Survey[3] plates either (see Figure 4.4). We used the techniques of Simon & Blitz (2002) to search more carefully and found a very faint low-surface brightness feature nearby. However, follow-up imaging with the Lick 3 m telescope revealed that there is no distant stellar population here. Therefore this cloud, like all other compact HVCs, appears to be a pure gas cloud.

Based on our data, we suggest that the faint features to the east and south of the HVC are remnants of a tidal interaction between the HVC and LGS 3. We now consider the consequences of such a situation. The total mass of LGS 3 (derived from its central velocity dispersion) is 1.3×10^7 M$_\odot$ (Mateo 1998). Hence, its tidal field becomes comparable to the surface gravity of the HVC if the HVC orbit has a minimum approach of $\sim$4 kpc. If the faint features are tidal in origin, the orbit of the HVC is strongly constrained. Since the gravity of LGS 3 is not enough to bind the system—the escape velocity of LGS 3 is

---

[3]The Second Palomar Observatory Sky Survey (POSS-II) was made by the California Institute of Technology with funds from the National Science Foundation, the National Geographic Society, the Sloan Foundation, the Samuel Oschin Foundation, and the Eastman Kodak Corporation.
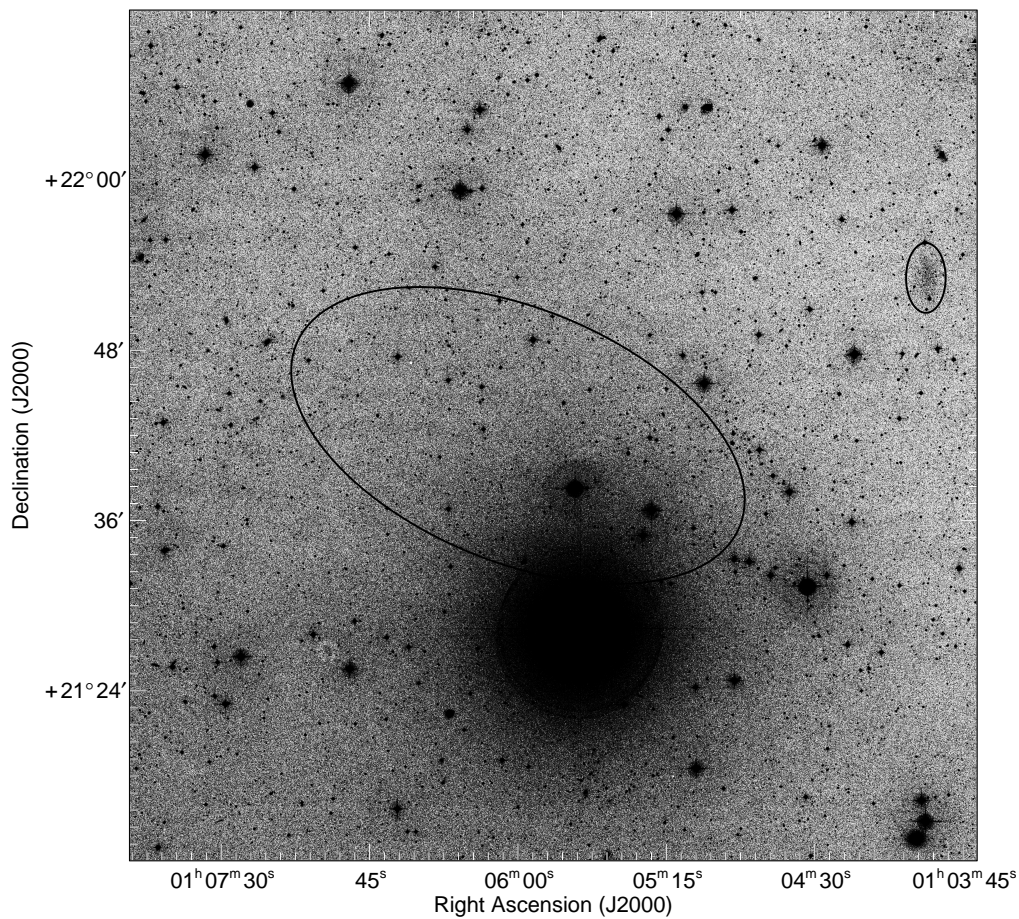
Figure 4.4 — $1° \times 1°$ POSS-II red image of the region around LGS 3 and HVC $127-41-330$. The approximate boundaries of LGS 3 (in the upper right part of the image) and the HVC (in the center of the image) are outlined with ellipses. Although LGS 3 has a very low surface brightness of $\mu_{\rm v} = 24.7$ mag arcsec^{-2}(Lee 1995), it is still easily visible on the plate. Despite the unfortunate presence of a fifth magnitude foreground star just south of the HVC, it is clear that the HVC is not associated with a dwarf galaxy with a surface brightness comparable to that of LGS 3.

$\sim$19 km s^{-1}, while the relative velocity between LGS 3 and the HVC is $\gtrsim$50 km s^{-1}—the encounter between them must be a one-time event. The existence of the tidal tails implies that they have already made their closest approach. Given their relative velocity and their projected separation of 5.8 kpc, such an approach would have taken place $\sim$10^8 years ago. It may be worth noting that this time approximately coincides with the end of the star formation activity in LGS 3 (Miller et al. 2001). The primary caveat involved with these calculations is that the mass of LGS 3 is only measured from the velocity dispersion of 4 of its stars, indicating that there are very large uncertainties on these numbers (Cook et al. 1999). Future spectroscopy of a larger sample of stars in LGS 3 would be very useful for determining its total mass and mass distribution.

4.5   Conclusions

We have presented high-resolution H $\textsc{i}$ observations of a 2.4 deg^2 area including the Local Group dwarf galaxy LGS 3 and a previously unresolved cloud of gas adjacent to the galaxy. Our data show that the H $\textsc{i}$ cloud is 30$'$ away from the galaxy, with a velocity difference of -45 km s^{-1}, and that they do not appear to be connected. If they are at the same distance, the cloud contains 10 times as much H $\textsc{i}$ and twice as much total mass as LGS 3. Optical imaging of the cloud revealed no stellar counterparts. We therefore argue that the cloud is an HVC, and should not be considered part of the H $\textsc{i}$ component of LGS 3. However, the H $\textsc{i}$ morphology does suggest that an interaction is occurring.

We propose that the faint, thin strips of gas on either side of the HVC are tidal arms produced by a close encounter with LGS 3. We note that the probability of a line-of-sight coincidence between the two objects, if they are at different distances, is $\sim$4%. We therefore suggest that the most likely interpretation of this system is that LGS 3 and the HVC are at the same distance and have recently undergone a tidal interaction.

We also examine the rotation curve of the HVC, which exhibits a linear increase with radius out to 10$'$ and then begins to decrease. Under the assumption that the HVC is self-gravitating, which is supported by the rotation curve's symmetry and turnover at large radii, we use the dynamical mass and the H $\textsc{i}$ mass to derive a lower distance limit for the HVC. For $M_{\mathrm{dyn}}/M_{\mathrm{lum}}$ to be $\lesssim$ 100, the HVC must be at least 39 kpc away if it is self-gravitating. The extremely negative v_{GSR} of the HVC constrains it to be within the Local Group. This HVC is thus unique in that there is evidence that it is both dark

matter-dominated and physically associated with an object at a known distance.

Given these findings, what can we conclude about the nature of this HVC? We have presented several arguments that it is probably located hundreds of kiloparsecs away, most likely at 700 kpc. The HVC appears to be undergoing a tidal interaction with LGS 3, which is stripping away a substantial portion of its neutral gas. Assuming that our distance estimate is correct, the HVC has a total mass of 2×10^7 M$_\odot$ and and H I mass of 2.7×10^6 M$_\odot$. If the HVC is in the Local Group it is dark matter-dominated, regardless of its exact distance. And, it does not contain any stars. This set of properties is exactly what is expected of the missing dark matter satellites that are predicted by CDM simulations. We propose that this HVC is the first observed representative of this population of missing objects.

Chapter 5

High-Resolution Measurements of the Dark Matter Halo of NGC 2976: Evidence for a Shallow Density Profile

This chapter was previously published in *The Astrophysical Journal* (Simon, Bolatto, Leroy, & Blitz 2003, ApJ, 596, 957).

Abstract

We have obtained two-dimensional velocity fields of the dwarf spiral galaxy NGC 2976 in Hα and CO. The high spatial (~ 75 pc) and spectral (13 km s^{-1} and 2 km s^{-1}, respectively) resolution of these observations, along with our multicolor optical and near-infrared imaging, allow us to measure the shape of the density profile of the dark matter halo with good precision. We find that the total (baryonic plus dark matter) mass distribution of NGC 2976 follows a $\rho_{\mathrm{TOT}} \propto r^{-0.27 \pm 0.09}$ power law out to a radius of 1.8 kpc, assuming that the observed radial motions provide no support. The density profile attributed to the dark halo is even shallower, consistent with a nearly constant density of dark matter over the entire observed region. A maximal disk fit yields an upper limit to the K-band stellar mass-to-light ratio (M_*/L_K) of $0.09^{+0.15}_{-0.08}$ M$_\odot$/L$_{\odot,K}$ (including systematic uncertainties), with

the caveat that for $M_*/L_K > 0.19$ $\mathrm{M_\odot/L_{\odot,K}}$ the dark matter density increases with radius, which is unphysical. Assuming 0.10 $\mathrm{M_\odot/L_{\odot,K}} \lesssim M_*/L_K \leq 0.19$ $\mathrm{M_\odot/L_{\odot,K}}$, the dark matter density profile lies between $\rho_{\mathrm{DM}} \propto r^{-0.17}$ and $\rho_{\mathrm{DM}} \propto r^{-0.01}$. Therefore, independent of any assumptions about the stellar disk or the functional form of the density profile, NGC 2976 does not contain a cuspy dark matter halo. We also investigate some of the systematic effects that can hamper rotation curve studies, and show that (1) long-slit rotation curves are far more vulnerable to systematic errors than two-dimensional velocity fields, (2) NGC 2976 contains radial motions that are as large as 90% of the rotational velocities at small radii, and (3) the Hα and CO velocity fields of NGC 2976 agree within their uncertainties, with a typical scatter between the two velocities of 5.3 km s^{-1} at any position in the galaxy.

5.1 Introduction

The apparent disagreement between the observed dark matter density profiles of dwarf and low-surface brightness (LSB) galaxies and the density profiles predicted by numerical Cold Dark Matter (CDM) simulations has been widely discussed by both theorists and observers over the past several years (e.g., Flores & Primack 1994; Burkert 1995; Navarro, Frenk, & White 1996; Moore et al. 1999b). However, there remains a disturbing lack of consensus in the observational community on the actual shape of the observed dark matter density profiles. Many authors claim that only constant-density cores are allowed by the observations (de Blok et al. 2001a; Borriello & Salucci 2001; de Blok, McGaugh, & Rubin 2001b; de Blok & Bosma 2002; Salucci, Walter, & Borriello 2003; Weldrake, de Blok, & Walter 2003). On the other hand, van den Bosch et al. (2000), van den Bosch & Swaters (2001), and Swaters et al. (2003a, hereafter SMVB) argue that most existing rotation curves are also consistent with NFW-like ($\rho \propto r^{-1}$) central density cusps. Even the very highest resolution ($\lesssim 100$ pc) studies do not seem to be converging on a single result; Blais-Ouellette, Amram, & Carignan (2001) found $\rho \propto r^{-0.3}$ in NGC 3109 and $\rho \propto r^{-0.5}$ in IC 2574 (ignoring the stellar disk contributions to the rotation curves), Bolatto et al. (2002) showed that NGC 4605 has a density profile $\rho \propto r^{-0.65}$, and Weldrake et al. (2003) determined that NGC 6822 contains an essentially constant-density halo.

The recent study by SMVB shows that, in large part, the lack of consensus among observers reflects ambiguities in the data themselves. For the parameters of typical dwarf/LSB galaxy observations (~ 50 km s^{-1} velocity resolution and $\sim 1''$ seeing for

long-slit Hα observations, and ~ 2 km s^{-1} velocity resolution and $\sim 15''$ angular resolution for H I interferometry), they find that *most galaxies show central density profiles that are consistent with any shape between r^0 and r^{-1}.*

We address this problem with a new study that combines a number of techniques to overcome the observational challenges. Our program includes (1) two-dimensional velocity fields obtained at optical (Hα), millimeter (CO), and centimeter (H I) wavelengths, (2) high angular resolution ($\sim 5''$), (3) high spectral resolution ($\lesssim 10$ km s^{-1}), (4) multicolor optical and near-infrared photometry, and (5) nearby dwarf galaxies as targets. Observing completely independent tracers of the velocity field at two or three different wavelengths reduces our vulnerability to the systematic problems that can affect a single tracer. For example, Hα velocity fields can be distorted by extinction, or by large-scale flows that are associated with star formation, while existing H I data generally suffer from beam smearing. Two-dimensional velocity fields also represent a major improvement over the traditional long-slit spectra, making the effect of positioning errors negligible and allowing us to account for simple noncircular motions. High angular resolution is important because the central cores described in the literature have typical radii of ~ 1 kpc, which corresponds to an angular size of 20.6 $(d/10$ Mpc$)^{-1}$ arcseconds. In order to resolve this size scale and minimize the impact of beam smearing on our conclusions, an angular resolution element several times smaller is required. High spectral resolution is also beneficial because it results in more accurate rotation curves. Finally, our multicolor photometry plays a crucial role in allowing us to more realistically model the rotational contribution from stellar disks instead of simply guessing an appropriate mass-to-light ratio and assuming an exponential disk.

Target selection also has important effects on the strength of the conclusions we will be able to draw. We focus on very nearby objects ($d < 10$ Mpc) in order to maximize our physical resolution. Dwarf and LSB galaxies are the preferred targets for this type of study because they are presumed to be the most dark matter-dominated galaxies. (Note that in this chapter when we refer to dwarf galaxies, we mean high-mass dwarf irregulars and low-mass spiral galaxies, not dwarf spheroidals or ellipticals.) LSB galaxies, though, tend to be relatively distant and are necessarily quite faint, so they are difficult to observe with sufficient resolution and sensitivity. Dwarf galaxies, in comparison, are both bright and plentiful in the nearby universe. Dwarfs are traditionally presumed to be dark matter-dominated at all radii (Carignan & Freeman 1988; Carignan & Beaulieu 1989; Jobin & Carignan 1990; Martimbeau, Carignan, & Roy 1994). However, the observations upon

which this assumption is based were made at low angular resolution. Higher resolution observations of the inner regions of dwarf galaxies show, as we discuss later, that stars can dominate the kinematics of dwarf galaxies in their inner kpc (e.g., Broeils 1992; Swaters 1999; Blais-Ouellette et al. 1999; Bolatto et al. 2002). Comparable data for LSB galaxies are scarce (although see Swaters, Madore, & Trewhella 2000; Swaters et al. 2003b), but it is possible that reliance on low-resolution observations (e.g., de Blok & McGaugh 1997) could have caused an overstatement of the case for dark matter domination in these galaxies as well. Future studies of LSB galaxies, featuring two-dimensional Hα spectroscopy and/or $\leq$ 100 pc resolution H I observations, if feasible, are desirable both to investigate this question and to clarify the severity of the cusp/core problem.

In a previous paper, we reported on a rotation curve study of the dwarf spiral galaxy NGC 4605 (Bolatto et al. 2002). In this chapter, we present a similar, but improved, study of a second nearby dwarf galaxy, NGC 2976. As before, we use high-resolution CO interferometry to study the inner velocity field of the galaxy, but we have also acquired high-resolution two-dimensional Hα data (instead of long-slit observations) to supplement the CO and extend the velocity field out to larger radii. In addition, we have obtained multicolor optical imaging of this galaxy, which, combined with archival Two Micron All Sky Survey (2MASS) near-infrared images, enables us to accurately model the stellar disk. We also take this opportunity to present a detailed introduction to the analysis techniques that we will apply to a larger sample of galaxies in Chapter 6.

In the following section, we describe NGC 2976 and our observations and data reduction. In §5.3, we model the stellar and gaseous disks. In §5.4, we derive the rotation curve of the galaxy and the density profile of its dark matter halo. The analysis routines that we use are presented in more detail in Appendix A, and some useful formulas are given in Appendix B. We discuss our results and their implications in §5.5. In §5.6, we describe some systematic uncertainties that can affect rotation curve studies, and test the robustness of our results against them. We present our conclusions in §5.7.

5.2 Target, Observations, and Data Reduction

5.2.1 Properties of NGC 2976

NGC 2976 is a regular Sc dwarf galaxy located in the M81 group. Karachentsev et al. (2002) measured a distance of 3.56 ± 0.38 Mpc using the Tip of the Red Giant Branch (TRGB) method, and the Tully-Fisher distance is 3.33 ± 0.50 Mpc (M. Pierce 100', private communication). We adopt a distance of 3.45 Mpc, which sets the conversion between physical and angular scales to 16.7 pc arcsec^{-1}. NGC 2976 has absolute magnitudes of $M_B = -17.0$ and $M_K = -20.2$, a heliocentric velocity of -0.8 ± 1.8 km s^{-1}, an inclination-corrected H I linewidth of $W_{20} = 165$ km s^{-1}, and a total mass of 3.5×10^9 M$_\odot$, so it is somewhat less luminous and less massive than the Large Magellanic Cloud. The low systemic velocity is not a problem for our observations because the galaxy is located at high Galactic latitude, where there is little Milky Way CO emission, and no Galactic Hα emission is visible. In optical and near-infrared images it is clear that NGC 2976 is a bulgeless, unbarred, pure disk system (see Figure 5.1), which makes it an ideal galaxy for mass modeling.

5.2.2 Hα Observations and Reductions

Our Hα observations were obtained on the nights of 2002 March 20–21 at the 3.5 m WIYN telescope with the DensePak instrument. DensePak is an array of 94 $2''.8$-diameter fibers, fixed in a $30'' \times 45''$ rectangle with a fiber-to-fiber spacing of $4''$ (Barden, Sawyer, & Honeycutt 1998). Five of the fibers are broken and four are sky fibers, placed at fixed positions outside the main array. Thus, there are 85 data fibers covering almost the whole instrument footprint (see Figure 5.2). The fibers feed into the Bench Spectrograph, which we used in its echelle mode to yield 13 km s^{-1} velocity resolution over a 180 Å range centered on Hα. The detector was a 2048^2 SITe T2KC CCD.

We observed the galaxy at 13 positions to cover most of its optical extent (see Figures 5.3 and 5.4a). The galaxy was not visible on the guide camera at the telescope, so we acquired the target by offsetting from a nearby bright star. Each subsequent position on the galaxy was observed by making a blind offset from the previous position. Integration times at each position were between 20 and 70 minutes, with just a single 20-minute exposure at most positions. Consecutive exposures at the same position were reduced separately and
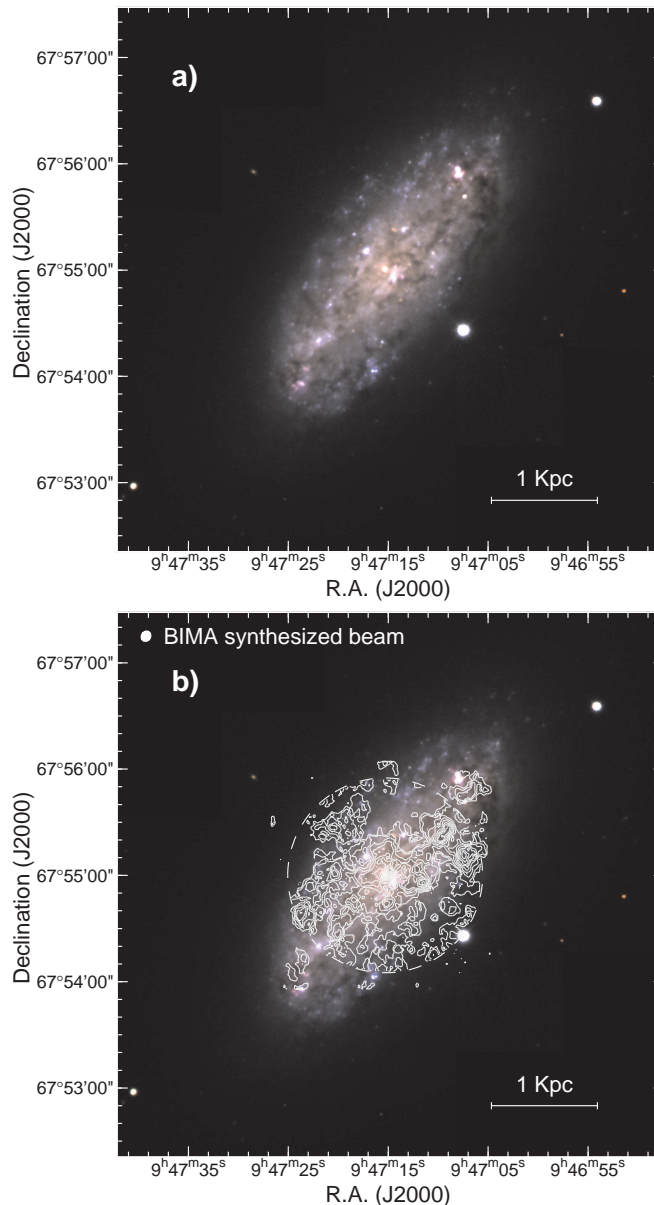
Figure 5.1 — (*a*) BVR composite image of NGC 2976 from the 1.8 m telescope at Lowell Observatory. Exposure times were 10 minutes in B and 5 minutes in V and R. Note the distinct lack of a bulge, a bar, or any spiral structure. (*b*) BVR composite image of NGC 2976 with integrated intensity CO contours overlaid. Note how well the CO traces out the optical dust lanes. The dashed circle shows the extent of the BIMA primary beam. The contour levels are 0.35, 0.70, 1.4, 2.1, and 2.8 Jy km s^{-1} inside the primary beam, and a single contour at 1.4 Jy km s^{-1} is shown outside the primary beam. For these observations, 0.35 Jy km s^{-1} corresponds to a molecular hydrogen column density of 2×10^{20} cm^{-2} (assuming that the Galactic CO-H$_2$ conversion factor is valid in NGC 2976). The BIMA synthesized beam ($5''.2 \times 6''.0$) is shown in the upper left corner.
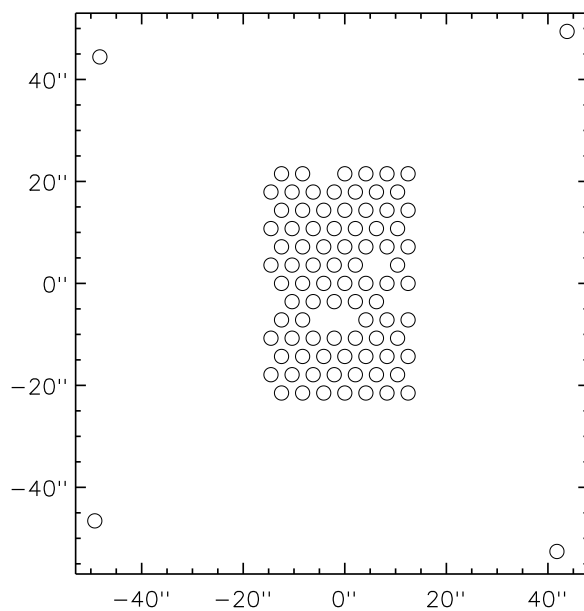
Figure 5.2 — DensePak fiber layout. The four outlying fibers are the sky fibers. Since they are located only about $1'$ from the main array, in some cases the sky spectra were contaminated by emission from the target galaxy.

then coadded. Two of the fields were observed on both nights, and one field was observed twice on the same night, but five hours apart. In these three cases, instead of assuming that the positions observed were the same for the later observations as they were for the earlier ones, we analyzed the frames entirely independently. We therefore had 16 observations of NGC 2976, yielding a total of 1360 spectra, of which 1087 contained Hα emission at a level of 3 σ or higher. Based on comparison with adjacent fibers that contained brighter emission at similar velocities, we also judged that 9 spectra containing emission at a significance level between 2.2 σ and 3 σ represented real signal. The median detection level in the 1096 spectra that contained emission was 27 σ in integrated intensity, or 12 σ at the peak of the line.

The DensePak data were reduced in IRAF,[1] using the HYDRA package. We subtracted a bias frame, removed cosmic rays, interpolated over bad columns, and then extracted the spectra with the task DOHYDRA. The trace and response function for each fiber and the relative transmission efficiencies were derived from a set of flat field images, and wavelength calibration was provided by spectra of a CuAr lamp. Night-sky emission line wavelengths from Osterbrock et al. (1996) and observations of a radial velocity standard star were used to check the wavelength scale. After extraction and wavelength calibration, we averaged together the four sky fibers, leaving out any sky spectra that were contaminated by emission lines from the target galaxy. We then removed a linear baseline, performed a Gaussian fit to the averaged sky emission near Hα, and subtracted the fit from all of the data fibers. Some spectra contained noticeable residuals at the wavelength of the sky Hα line after this subtraction. Sky residuals are easily distinguishable from real signals because they are unresolved and always located in the same four pixels. If the residual overlapped with and was comparable in strength to the Hα emission from NGC 2976, the spectrum was discarded (29 spectra were thrown out because of this consideration). This only occurred in places where the galaxy velocities were about -17 km s^{-1} (see Figure 5.4). Individual frames of the same field were then averaged together (except for the cases noted above), weighted by exposure time if it was clear, or signal-to-noise ratio if there were clouds during the exposure. Velocities were calculated for each fiber by fitting a Gaussian to the observed Hα emission. Typical linewidths are 34 km s^{-1}, and the median uncertainties on

---

[1] IRAF is distributed by the National Optical Astronomy Observatories, which is operated by the Association of Universities for Research in Astronomy, Inc. (AURA) under cooperative agreement with the National Science Foundation.
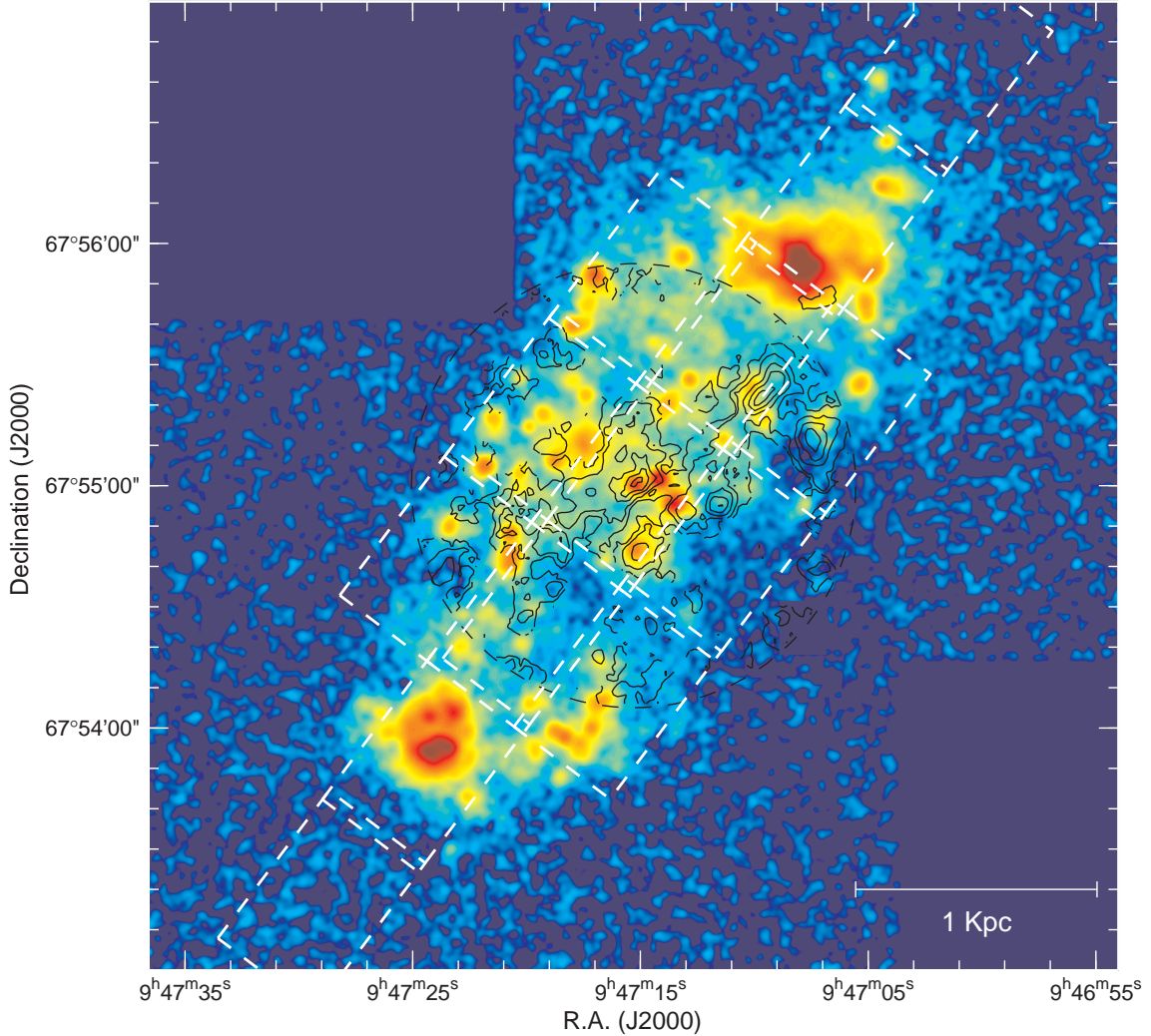
Figure 5.3 — Continuum-subtracted Hα image of NGC 2976. This $4' \times 4'$ image consists of two 1200 s exposures on the Lowell 1.8 m telescope that have been combined to cover the whole galaxy. The images were taken through a 32 Å-wide filter, and the continuum was removed by appropriately scaling and subtracting images taken through a narrow-band filter centered at 6441 Å. The black contours represent integrated CO intensity, as in Figure 5.1b. The white dashed rectangles overlaid on the image show the intended locations of our DensePak pointings (these have not been corrected for pointing errors; see Section 5.2.2 and Figure 5.4a), with one row or column of fibers overlapping between every pair of adjacent pointings. The artifacts at $(\alpha, \delta) = (09^h 46^m 54^s, 67°56'35'')$ and $(\alpha, \delta) = (09^h 47^m 07^s, 67°54'26'')$ are caused by masking out residuals from bright stars.
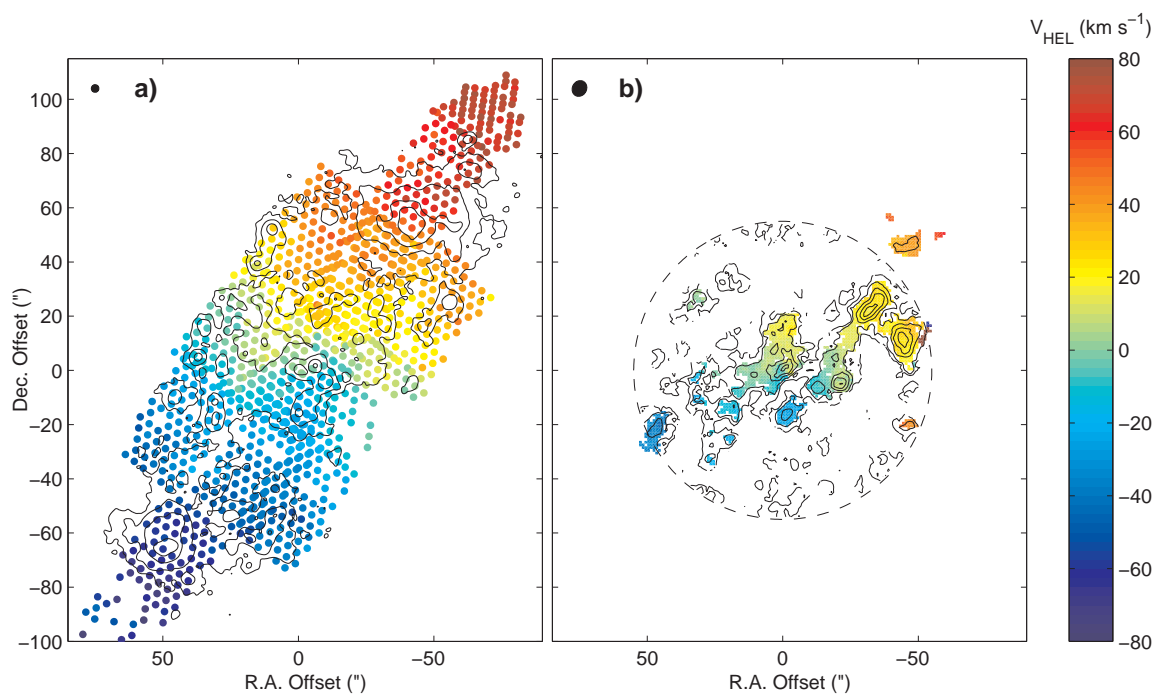
Figure 5.4 — (*a*) Hα velocity field from DensePak observations. The contours represent Hα intensity from the image displayed in Figure 5.3. (*b*) CO velocity field from BIMA observations. The contours represent integrated CO intensity, as in Figure 5.1*b*. The angular resolution of each dataset is shown in the upper left corners.

the Gaussian fit centroids are 0.77 km s^{-1}; some fits have uncertainties as small as 0.04 km s^{-1}, and a few are as large as 23 km s^{-1}.

It was obvious from comparing frames that were taken several hours apart or on different nights that the telescope positioning accuracy for our observing procedure was only $\approx 5''$. We therefore designed an algorithm to determine the absolute positions that were observed based on our Hα image of NGC 2976, which is displayed in Figure 5.3. We sampled the Hα image with simulated "fibers" of the same size and location as the DensePak fibers, and added up the flux in each simulated fiber. By cross-correlating this set of photometric fluxes with the observed spectroscopic fluxes (integrated over the Hα line), we could measure the similarity between them. We repeated this process at a grid of positions around the expected pointing center and searched for the highest value of the cross-correlation function. We estimate that the accuracy of the positions derived with this method is $1''$. The algorithm failed for one field, because only 15 of its fibers contained detectable signal, and very little emission was visible at that location in the image. For this field we assumed that the offset from the expected position was the same as the one we measured for the preceding exposure. Since this field is located $\sim 2'$ from the center of the galaxy, an error of a few arcseconds in its position is unlikely to be important. For the other 15 fields, the algorithm gave a smooth, well-defined peak with a cross-correlation coefficient between 0.81 and 0.996. We verified the results of the cross-correlation by finding the location of the minimum rms difference between the photometric and spectroscopic fluxes. This position was always within $1''$ of the cross-correlation maximum. Fourteen of these 15 fields are located within $6\rlap{.}''9$ of their expected positions, and the other differs by $11\rlap{.}''3$.

5.2.3 CO Observations and Reductions

Our ^{12}CO ($J = 1 \rightarrow 0$) observations were acquired using the B, C, and D configurations of the 10-element BIMA array (Welch et al. 1996) between April 2001 and March 2002. The total integration time was ~ 80 hours, much of which was in the most extended (B) configuration. The BIMA primary beam has a half-power diameter of $\sim 100''$, and we found CO emission spanning this entire width, including a cloud outside the primary beam at $r = 70''$ (see Figure 5.1b). For our observations, the spectrometer was configured with 2 km s^{-1} wide channels and a 260 km s^{-1} bandpass. The individual tracks were calibrated, combined, imaged, and deconvolved using the CLEAN algorithm within the MIRIAD pack-

age. The tracks were then combined with natural weighting to create a $5''\!.2 \times 6''\!.0$ (87×100 pc) synthesized beam with a position angle (PA) of $-31°$. The rms noise of the individual planes of the datacube is 24 mJy beam^{-1} in each 2 km s^{-1} channel. An integrated intensity contour map is displayed in Figure 5.1b, and a first moment map produced from a masked version of the datacube is shown in Figure 5.4b. Because the signal in a single channel was relatively weak, we used the first moments to represent the velocity at each position instead of attempting to fit Gaussians to the line emission. Typical uncertainties in the line velocities are 3 km s^{-1}, and typical linewidths are $10-15$ km s^{-1} across most of the galaxy, although some lines are as wide as 35 km s^{-1} near the center.

5.2.4   Optical and Near-IR Imaging and Reductions

We observed NGC 2976 with B, V, R, and I filters at the 1.8 m Perkins Telescope at Lowell Observatory on the photometric night of 2002 February 11. The detector was a 2048^2 Loral CCD with 15 μm pixels and a $3'\!.2$ field of view, and the seeing was $\approx 1''\!.4$. We used exposure times of 600 s in B and 300 s in V, R, and I and observed three overlapping positions to cover the full extent of the galaxy. A three-color composite of these images is displayed in Figure 5.1a. To extend our set of images to the near-infrared, we used the 2MASS JHK_s Atlas images of NGC 2976. The 2MASS images are $8'\!.5 \times 17'$ and have $1''$ pixels, adequately sampling the $\approx 3''$ seeing.

The optical data reduction, done in IDL, consisted of the following steps: overscan subtraction, dark subtraction, flatfielding, and cosmic ray removal. Several bad columns were fixed by adding or subtracting a constant so that their median values matched those of the surrounding columns; except for the constant offset, the fluxes in these columns do not appear to be systematically affected. The three images in each filter were then shifted and coadded. We observed several Landolt (1992) standard fields for photometric calibration, which was done with the IRAF implementation of DAOPHOT (Stetson 1987). With the new standard stars in these fields identified by Stetson (2000) in addition to the original Landolt ones (we used Stetson's magnitudes for all of the stars), we had 34–38 standard star measurements per filter. Our photometric solutions were derived from a least-squares fit to the following formula:

$$m = m_{\mathrm{instr}} + C + f(V - I) + g(a - 1) \; , \tag{5.1}$$

where m is the apparent magnitude, m_{instr} is the instrumental magnitude ($25-2.5\log\text{flux}+$ $2.5\log$ integration time), C is a constant that sets the instrumental zero point, f is the color coefficient, $V-I$ is the color of the object, and g is the extinction coefficient. Our observations did not span a large enough range of airmass to determine the extinction coefficient directly, so we used previously derived values. Reasonable ranges for the coefficients are $0.2 < g_B < 0.4$ mag airmass^{-1}, $0.1 < g_V < 0.3$ mag airmass^{-1}, $0.05 < g_R < 0.15$ mag airmass^{-1}, and $0.02 < g_I < 0.12$ mag airmass^{-1} (P. Massey 2002, private communication). For B and V, we used values of 0.27 mag airmass^{-1} and 0.15 mag airmass^{-1}, which were the mean values of ~ 15 measurements made between 1997 and 1999 at the same telescope (D. Hunter 2002, private communication). Lacking comparable measurements in R and I, we used the standard Lick Observatory values of 0.11 mag airmass^{-1} and 0.08 mag airmass^{-1}, respectively. These fall within the reasonable ranges for both filters, and the Hunter B and V measurements are very close to the Lick values. Since all of our images were taken at airmasses close to 1.2, these assumptions are unlikely to cause significant errors.

In order to double-check our photometric solutions, we obtained the V- and I-band Keck[2] images that Méndez (2002) acquired for the purpose of measuring the TRGB distance to NGC 2976. These images were taken with the Low-Resolution Imaging Spectrometer (Oke et al. 1995), and cover a $5' \times 7'$ field. Exposure times were 300 s in I and 400 s in V.

5.2.5 Surface Brightness Profiles

We used the IRAF routine ELLIPSE in the STSDAS package to perform surface photometry on the images. The routine fits elliptical isophotes to a galaxy image at specified radii, and allows the position angle (PA), ellipticity, and center to change with radius. There is no evidence that the PA changes with radius, so we used the average value of $143°$, identical to the cataloged PA of the galaxy (de Vaucouleurs et al. 1991, hereafter RC3). The ellipticity ϵ, which is related to the inclination angle via the formula $\cos^2 i = [(1-\epsilon)^2 - (1-\epsilon_{max})^2]/[1-(1-\epsilon_{max})^2]$, where $\epsilon \equiv 1 - b/a$, a and b are the major and minor axis lengths, and $\epsilon_{max} = 0.8$, varies from ~ 0.4 to ~ 0.7 in the inner part of the galaxy before converging to a constant value of 0.49 for $r > 114''$. Galaxies often display such behavior,

and it is not generally interpreted as a changing inclination angle with radius. Accordingly, we use an ellipticity of 0.49 for the whole galaxy. The corresponding inclination angle is $61°4$, the same as the RC3 inclination of $61°5$ within the uncertainties. The center of the isophotal fits changed incoherently with radius before converging for $r > 120''$. The isophotal center was within a few arcseconds of the visually obvious nucleus at $(\alpha_{2000}, \delta_{2000}) = (09^h 47^m 15.3^s, 67°55^m 00.4^s)$, so we used the nucleus as the fit center. The coordinates of the nucleus coincide with the cataloged galaxy positions within their uncertainties (Cotton, Condon, & Arbizzani 1999; Falco et al. 1999). We then ran ELLIPSE again with all of the parameters fixed to produce the final surface brightness profiles. We fit ellipses every $2''$ out to a radius of $172''$, where the ellipses began to run off the edge of the image.

We also ran ELLIPSE on the Keck images with the same parameters. This revealed some systematic differences between the Lowell and Keck photometry: although the profile shapes were quite similar in the two datasets, the Lowell V magnitudes are 0.1 mag brighter than the Keck V magnitudes, and the Lowell I magnitudes are 0.1 mag fainter than the Keck I magnitudes. The cause of this discrepancy is not clear, and it is worrisome because a 0.2 mag change in the galaxy color is significant. However, as we will show in §5.3.1, the measured Lowell colors all predict stellar mass-to-light ratios that are consistent with one another, while the Keck $V - I$ color predicts a noticeably higher mass-to-light ratio that is inconsistent with the other determinations. An additional piece of evidence in favor of the Lowell magnitudes is that the tabulated $B - V$ color in, e.g., the RC3 is close to our measured value, so we conclude that it is safe to assume that our Lowell photometry is accurate. Since the LRIS field of view is larger than that of the Lowell CCD, we also used the Keck images to verify that the light profile does not change shape at larger radii, and to measure the fraction of the total flux that we missed due to the limited extent of the Lowell mosaic. We estimate that $\sim 96\%$ of the galaxy's light is contained within the $r = 172''$ ellipse out to which we measured, so our integrated magnitude measurements should probably be revised upwards by 4% (0.04 mag).

The measured surface brightness profiles are corrected by applying the Schlegel, Finkbeiner, & Davis (1998) Galactic extinction estimates in each band. To account for extinction within NGC 2976, we used an inclination-based approach, as described by Sakai et al. (2000). Sakai et al. (2000) give internal extinction coefficients for all of the bands we use except J, so to determine the J-band correction we interpolated their results from the other bands and found that $A_J = 0.8 A_I$. For our best-fit axial ratio of 1.96, we estimate

that the internal extinction in magnitudes in the seven bands is (from B to K_s): 0.23, 0.20, 0.18, 0.13, 0.11, 0.07, and 0.03.

The surface brightness profiles, displayed in Figure 5.5, are qualitatively similar in all of the filters. NGC 2976 clearly contains three components: a nucleus, an exponential inner disk, and an exponential outer disk. Since the nucleus is not resolved in any of our images, we used the HST/NICMOS images acquired by Böker et al. (1999) to estimate that its radius is less than $0\rlap{.}''36$ (6 pc). It seems to be too reddened to reliably derive a mass-to-light ratio from its colors. The nuclear luminosity is 6×10^6 $L_{\odot,K}$, so the rotation velocity due to the nucleus is $39(M_{nuc}/L_K)^{1/2}(r/1'')^{-1/2}$ km s^{-1}, where M_{nuc}/L_K is the stellar mass-to-light ratio of the nucleus in solar units. If we assume that the mass-to-light ratio is the same as the maximum allowable value for the disk (see §5.4.2), the nucleus becomes dynamically insignificant outside $10''$. Because the nucleus is probably a large cluster of young stars (judging by its compactness, luminosity, and Hα emission), its actual mass-to-light ratio is likely much lower. Parameters for the disk of NGC 2976 in each band are listed in Table 5.1. The presence of an outer exponential disk, with a surface brightness that declines more quickly than would be expected from extrapolating the inner disk, has been seen in other spiral galaxies (Näslund & Jörsäter 1997; Pohlen 2002; Pohlen et al. 2002, hereafter PDLA). The ratio of the inner scale length to the outer scale length is 2.1, consistent with the value of 2.0 ± 0.2 measured by PDLA for four other galaxies. In fact, NGC 2976 only differs from the galaxies PDLA observed in that the break between the inner and outer disks occurs close-in, at 1 inner disk scale length instead of ~ 4 scale lengths. NGC 2976 is an order of magnitude less luminous than the galaxies in the PDLA sample, suggesting that the break radius might be a function of luminosity.
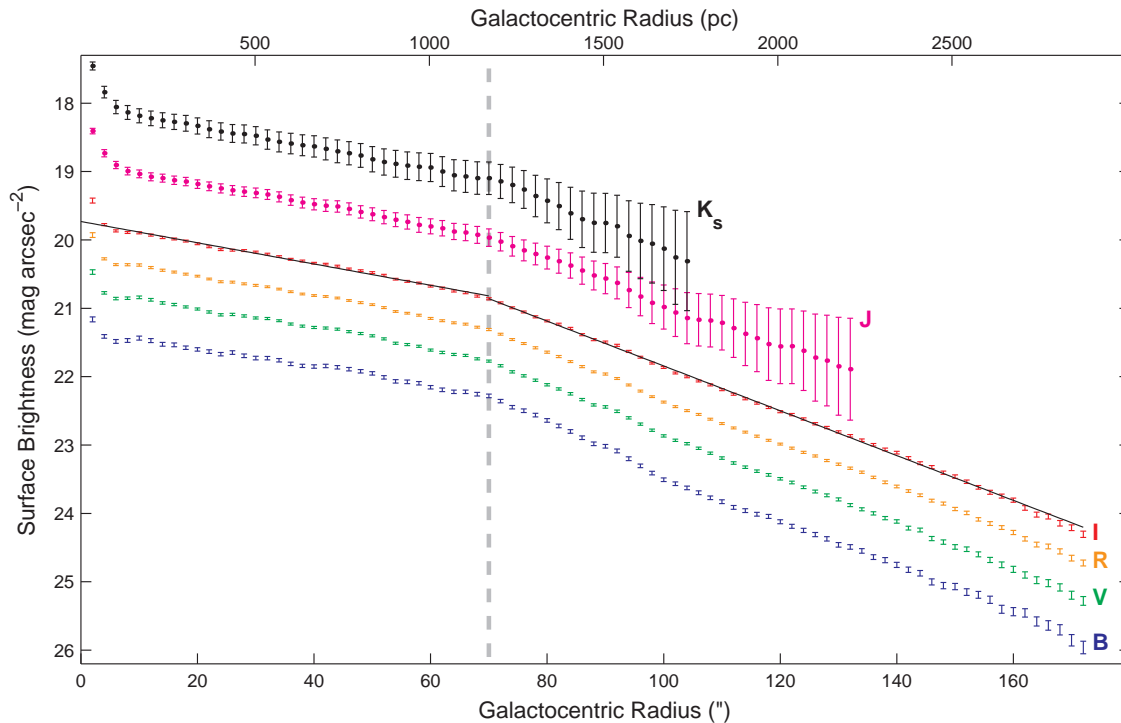
Figure 5.5 — Optical and near-infrared surface brightness profiles of NGC 2976. For the J and K_s profiles we plot data points and error bars, but we omit the points for B, V, R, and I because they would obscure the error bars. The J and K_s data can be traced further out, but we do not plot the data beyond where the uncertainties reach a factor of 2 (0.75 mag). The H-band profile has also been left off for clarity; the error bars for H and K_s overlap at most radii. In each color, the nucleus, exponential inner disk, and exponential outer disk are all visible. In the optical filters, there is a transition region between the inner and outer disks where the colors are bluer than the disk values. Exponential fits to the I-band profile are shown by the solid black lines. The vertical dashed line at a radius of $70''$ emphasizes the breakpoint between the inner and outer disks. For central surface brightnesses and disk scale lengths, see Table 5.1.

Table 5.1.   NGC 2976 Surface Brightness Profiles

Filter	Integrated Magnitude[a,b]	Central Surface Brightness μ_0 [mag arcsec^{-2}][c,b]	Inner Disk Scale Length[c] [″]	Outer Disk Scale Length[d] [″]	$\mu_{\rm sky}$ [mag arcsec^{-2}]
B	10.71	21.31 ± 0.01	79.3 ± 1.5	34.1 ± 0.4	22.10
V	10.14	20.69 ± 0.01	72.8 ± 0.8	33.6 ± 0.2	21.28
R	9.66	20.21 ± 0.01	71.2 ± 0.7	34.4 ± 0.2	20.71
I	9.19	19.73 ± 0.01	69.8 ± 0.7	33.1 ± 0.1	19.68
J	8.29	18.88 ± 0.03	71.8 ± 4.0	34.3 ± 2.9	16.01
H	7.71	18.24 ± 0.04	70.2 ± 5.5	31.1 ± 3.9	13.98
K_s	7.48	18.03 ± 0.06	69.6 ± 7.2	31.5 ± 5.0	13.47

[a]These magnitudes are measured within an elliptical aperture with a semimajor axis of $172''$ on our Lowell and 2MASS images. The galaxy does extend to somewhat larger radii on the Keck images, so we have certainly underestimated the flux here. The Keck data suggest that the Lowell magnitudes should be made $\sim 4\%$ brighter, although if the galaxy is more extended even than those images reveal, the true correction could be slightly larger.

[b]We have applied Galactic extinction corrections to these data. Internal extinction corrections have *not* been applied, but our adopted values for the internal extinction are given in the text (§5.2.5) if the reader wishes to use them.

[c]Central surface brightnesses and inner scale lengths were calculated from the light distribution between $10''$ and $70''$.

[d]Outer scale lengths were calculated from the light distribution outside $100''$ for B, V, and R (where there was a visible transition region between the inner and outer disks), and outside $70''$ for the near-infrared bands (where there was no transition region).

5.3 Baryonic Components of NGC 2976

Because our images of NGC 2976 do not reveal a bulge or a bar, and its nucleus is dynamically unimportant, the only relevant reservoirs of baryons to consider are the stellar and gaseous disks.

5.3.1 The Stellar Disk

There are two common approaches to studying the importance of the stellar contribution to a galaxy rotation curve: (1) compare multicolor surface photometry of the galaxy with the predictions of stellar population synthesis models to obtain an estimate of the stellar mass-to-light ratio (M_*/L) that is independent of the galaxy kinematics, or (2) leave M_*/L as a free parameter while simultaneously fitting a scaled stellar disk and a dark matter halo to the observed rotation curve. The second technique has a very significant drawback: χ^2 is insensitive to changes in M_*/L during rotation curve fits (McGaugh & de Blok 1998; Swaters 1999; Bolatto et al. 2002), so the fit with the lowest value of χ^2 does not necessarily convey any information about the value of M_*/L. As an illustration of this effect, the best fit often turns out to be $M_*/L = 0$, even though that is clearly not correct. We would therefore like to have an independent constraint on the mass-to-light ratio so that we do not have to leave it as a free parameter. For this reason, and because we have $BVRIJHK_s$ photometry available, we choose the first method.

Population Synthesis Constraints On M_*/L

One way to estimate a stellar mass-to-light ratio from photometry alone is to use the semi-empirical relationships derived by Bell & de Jong (2001). Bell & de Jong (2001) showed that the colors of spiral galaxies are strongly correlated with the mass-to-light ratios of their stellar populations. With our multicolor photometry, we can construct the entire array of colors for which they give formulas, and then calculate the expected mass-to-light ratios, which are listed in Table 5.2. The average predicted values from the six tabulated inner disk colors are 0.48 ± 0.02 M$_\odot$/L$_{\odot,K}$ in K_s band,[3] and 1.07 ± 0.07 M$_\odot$/L$_{\odot,R}$ in R

---

[3] We will mostly use the K-band stellar disk for the remainder of the chapter for the following reasons: (1) K-band light is the best tracer of the stellar *mass* distribution and the least skewed by luminous young stars from recent star formation, and (2) K band is the least affected by extinction.

band. That all of the colors predict consistent mass-to-light ratios is an indication that the predictions have some validity for this galaxy. It must be noted, however, that the Bell & de Jong (2001) mass-to-light ratios are derived assuming that galaxies have maximal disks. If the average galaxy has a disk that is a factor f $(0 \leq f \leq 1)$ less than maximal, then the predicted mass-to-light ratios from their calculations must also be scaled by the same factor f. A further uncertainty in this analysis is the initial mass function (IMF), which may not follow the assumed scaled Salpeter form, particularly at low masses.

An alternative method to measure M_*/L_K photometrically is to compare the observed colors directly to the outputs of publicly available stellar population synthesis models. We used the Starburst99 population synthesis models (Leitherer et al. 1999) to attempt to constrain M_*/L_K in this way. For a given star formation history (constant star formation rate or instantaneous burst of star formation), Starburst99 predicts colors and luminosities as a function of time. This allows us to search systematically for the population age that matches the observed set of colors most closely. The two best Starburst99 models are (1) a population with a small (10%) young component that has been forming stars continously, and the remaining stars in an old $(t \gtrsim 3$ Gyr$)$ population that formed in an instantaneous burst, and (2) a very young $(\sim 10^7$ yr old$)$ starburst. However, the mass-to-light ratios of these models seem rather implausible: $M_*/L_K > 2$ for model (1) and $M_*/L_K \approx 0.02$ for model (2). Neither of these values is compatible with observed values of M_*/L_K in the few other galaxies for which measurements are available (e.g., Olling & Merrifield 2001; Vallejo, Braine, & Baudry 2002) or with the predictions of Bell & de Jong (2001). We also tried the online population synthesis code described by Worthey (1994), which predicts colors and mass-to-light ratios for an arbitrary combination of input stellar ages and metallicities. It is more difficult to do a comprehensive search through the likely parameter space with this technique, but we did find that a mixture of 70% of an old (but metal-rich) population and 30% of a young population $(t = 1.1$ Gyr$)$ comes close to reproducing the observed colors (assuming a Miller-Scalo IMF), yielding a mass-to-light ratio of 0.31 $M_\odot/L_{\odot,K}$.

We conclude that it is not possible to uniquely determine the M_*/L_K for NGC 2976 by comparing the galaxy colors with the predictions of current population synthesis models. From this information alone, NGC 2976 could contain either a very young starburst, or a normal, mixed stellar population with a low to moderate (0.3 to 0.5) M_*/L_K. There are three reasons for discounting the starburst possibility in NGC 2976. First, the colors of the outer disk of NGC 2976, where our observations show no evidence for widespread star

Table 5.2.   Stellar Mass-to-Light Ratio Predictions

Color	Mean Inner Disk Color[a,b]	Predicted M_*/L_K[c] $[\mathrm{M}_\odot/\mathrm{L}_{\odot,K}]$	Predicted M_*/L_R $[\mathrm{M}_\odot/\mathrm{L}_{\odot,R}]$	Mean Outer Disk Color[b,d]
$B - V$	0.53	0.45	0.97	0.60
$B - R$	0.98	0.46	1.03	1.10
$V - I$	0.87	0.47	1.04	0.93
$V - J$	1.72	0.49	1.11	1.85
$V - H$	2.31	0.50	1.16	2.33
$V - K_s$	2.48	0.49	1.13	2.53

[a]Calculated for $10'' \leq r \leq 70''$.

[b]Note that these colors have been corrected for Galactic extinction and internal extinction. The Galactic extinction is taken from Schlegel et al. (1998) and the internal extinction corrections are given in the text.

[c]We use the predictions for the formation epoch with bursts of star formation model, assuming a scaled Salpeter initial mass function, as described in Bell & de Jong (2001).

[d]Calculated for $100'' \leq r \leq 172''$.

formation, are very similar to the inner disk colors, particularly in the near-infrared where extinction is less important (as shown in Table 5.2). It is unlikely that the galaxy contains a starburst and an old population that coincidentally have the same observed colors. Second, the starburst would have to be unusually young (in which case our observations of it at this particular time are rather fortuitous), and also quite strong, dominating not only the light output from the galaxy, but also containing a significant fraction of its total stellar mass (otherwise the mass-to-light ratio would begin to run into the kinematic limit; see §5.4.2). And finally, the visual appearance of the galaxy is not suggestive of a vigorous starburst. The more likely alternative is that NGC 2976 has a substantial old component to its stellar population, driving M_*/L_K toward the values of a few tenths that are seen in other galaxies.

Rotation Velocities Due to a Thin Disk

In order to compare the stellar rotation velocities to the observed rotation curve, we calculate the rotation velocities for material confined to a thin disk. Because the disk of NGC 2976 is not a pure exponential, its rotation curve must be calculated numerically. We perform the calculation with the routine CCDPOT, which is based on a derivation given by Binney & Tremaine (1987), in the NEMO package (Teuben 1995). This rotation curve is similar to that from the fitted exponential disk out to the breakpoint between the inner and outer disks, where it briefly exceeds the exponential disk rotation curve, and then begins to decline more quickly (as expected, since the surface density at large radii is lower than in the single exponential case). Our calculations assume an infinitely thin disk for simplicity; allowing the disk to have some thickness leaves the shape of the rotation curve almost unchanged, but lowers its amplitude, thus raising the allowed M_*/L_K (Swaters 1999; Peng et al. 2002). For a scale height equal to 1/6 of the disk scale length, the rotation curve is lowered by about 10% (Peng et al. 2002), so that the allowed M_*/L_K may be 20% higher than in the infinitely thin case (since $v_{rot} \propto \sqrt{M_*/L_K}$).

5.3.2 The Gas Disk

The atomic and molecular gas disks of NGC 2976 do not contribute appreciably to its measured rotation curve. Although it is rich in CO for a dwarf galaxy, the measured total flux of ~ 45 Jy km s^{-1} over the central 750 pc (Young et al. 1995) implies only $\sim 10^7$ M$_\odot$ of molecular gas (including helium), if the Galactic CO-H$_2$ conversion factor

is valid in NGC 2976. The total molecular mass might be somewhat larger, because the BIMA observations did not cover the large H II regions at either end of the inner disk, which are likely associated with molecular clouds. Nevertheless, the molecular material is not dynamically significant globally or locally, regardless of how it is distributed. The atomic gas mass is much larger, at 1.5×10^8 M$_\odot$ (Appleton, Davies, & Stephenson 1981; Stil & Israel 2002a). We adapt the H I surface density distribution from the data presented by Stil & Israel (2002a). The stellar, atomic, and molecular surface densities are plotted in Figure 5.6. Even with a low M_*/L_K, the stars are clearly the dominant reservoir of baryons in NGC 2976. It is noteworthy that the H I and stellar scale lengths in the outer galaxy appear nearly identical, and the surface densities are comparable as well. We calculate the rotation curves of the gaseous components directly from their surface density profiles (again assuming zero thickness) using the same method as for the stars.

5.4   Rotation Curve and Dark Matter Halo of NGC 2976

Now that we have a handle on the behavior of the stellar and gas disks of the galaxy, we can move on to our primary goal of constraining the structure of the dark matter halo. First, we convert our two-dimensional velocity field into a one-dimensional rotation curve. This is accomplished by fitting tilted-ring models to the velocity field using three complementary techniques. The algorithms are mentioned briefly below, and more detailed descriptions are given in Appendix A. ROTCUR breaks the velocity field into rings and fits for the PA, inclination, center, systemic velocity, and rotation velocity in each ring. RINGFIT also divides the galaxy into rings, and it fits for the rotation velocity, the radial velocity (in the plane of the galaxy), and the systemic velocity in each ring. RINGFIT thus has the desirable feature that a simple form of noncircular motions are included in the fit. The third algorithm, ROTCURSHAPE, fits the entire velocity field with a single PA, inclination, center, and systemic velocity, and also assumes a functional form for the rotation curve and solves for the parameters of that function. Fit results are similar for all three procedures, although fitting for radial velocities in addition to rotation does make the rotation curve somewhat shallower (see §5.6.2).
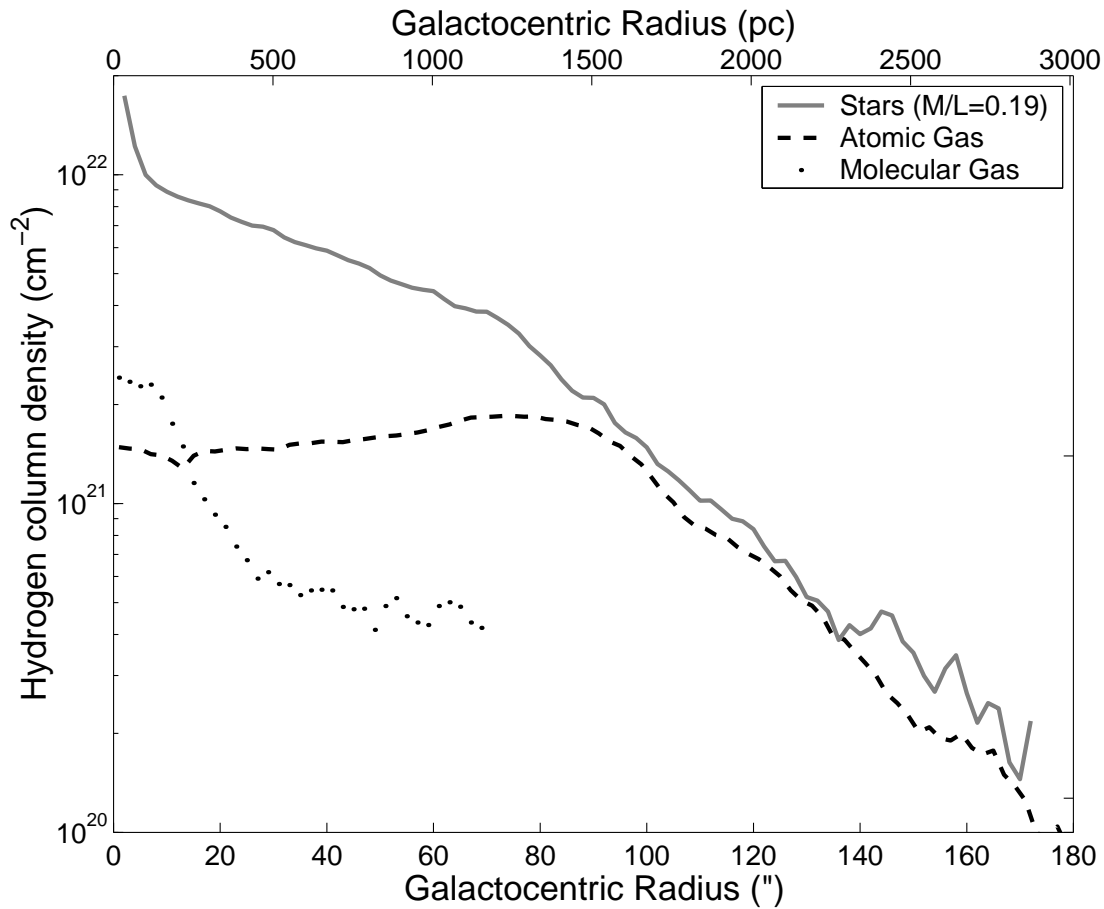
Figure 5.6 — Surface densities of stars and gas in NGC 2976. The H I and H$_2$ surface densities do not include helium, so the stellar surface densities are divided by a factor of 1.3 to match. Of the baryonic components, the stars dominate the inner disk, but the H I is almost as important in the outer disk. The molecular gas surface density outside 40″ is quite uncertain.

5.4.1 Rotation Curve of NGC 2976

It is apparent from the data (Figure 5.4) that the velocity field near the center of the galaxy cannot be adequately described by rotation alone. There are two choices for how to proceed: (1) use additional Fourier terms to describe the velocity field, or (2) allow for changes in the position angle of the galaxy with radius. The second possibility, which is difficult to reconcile with the photometry, is discussed in §5.5.5; for now, we will use Fourier analysis to provide an accurate description of the velocity field. The next Fourier term beyond pure rotation ($\cos\theta$, where θ is the angle from the major axis in the plane of the galaxy; see Appendix A) is pure radial motions ($\sin\theta$). We have investigated the decomposition of the velocity field using higher order terms, and found that they are much smaller than the rotation and radial components and are consistent with noise. Therefore, we leave those terms out of our subsequent analysis.

Our final rotation curve was derived with RINGFIT, so that we could account for the radial motions that are present in the velocity field. We first fit the Hα and CO velocity fields separately to verify that they agree with each other, as displayed in Figure 5.7a. At small radii ($r < 40''$), it is evident that the derived rotation curves and radial motions do agree, although they begin to diverge somewhat at $r > 40''$. However, the CO ring fits at these radii are based on only one or two independent measurements, so the apparent difference between the CO and Hα velocity fields is not significant. Therefore, we combine the two datasets and fit again, weighting each data point by the inverse square of its statistical uncertainty. The fits for rings at $r < 40''$ are displayed in Figure 5.8, where it is apparent that the velocity maxima do not lie along the major axis. This indicates the presence of radial motions, which could not have been measured with long-slit observations or ROTCUR fitting. The rotation curve from these fits is plotted in Figure 5.7b, and the significance of the radial velocities is again apparent. The estimated systematic uncertainties (the derivation of which is described in §5.6.2) are shown by the shaded gray areas surrounding each curve.

The residual velocity field after subtracting this best-fit model is displayed in Figure 5.9. Although individual residuals are occasionally as large as 30 km s^{-1}, the rms of the residual field is 6.4 km s^{-1}, and there are no obvious systematic trends. The velocity variations in the residual map are much larger than the uncertainties in the observed velocities, and the value of 6.4 km s^{-1} is consistent with the random velocities of gas observed in other galaxies; the residuals therefore likely represent real small-scale structure in the velocity
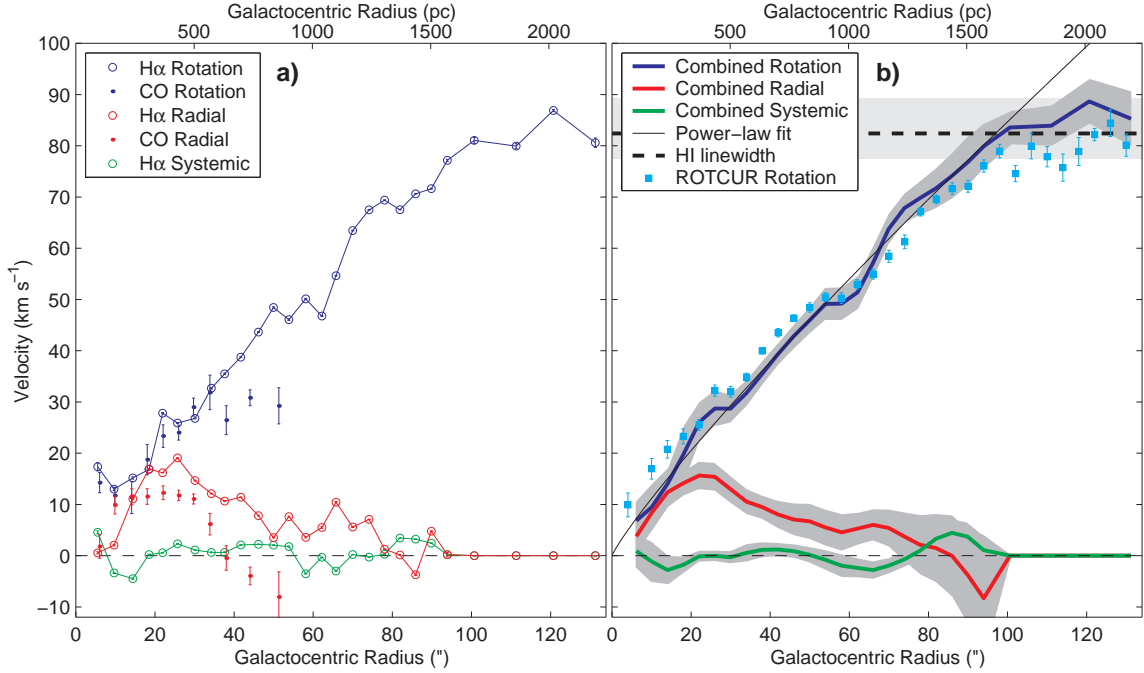
Figure 5.7 — (a) Hα and CO velocity field decompositions from RINGFIT. The blue points represent rotation velocities, the red points represent radial velocities, and the green points are systemic velocities. Open symbols are from the Hα velocity field, and filled symbols are CO data. The rotational and radial velocities of the CO and Hα are consistent with each other. Because the number of independent CO data points is small, we reduced the number of degrees of freedom in the fit by fixing the systemic velocities. The error bars are only statistical errors, which substantially underestimate the true uncertainties. (b) Combined velocity field decompositions from RINGFIT. To create this rotation curve, we combined the Hα and CO data into a single velocity field. We then ran a Monte Carlo simulation in which the velocity field is fit many times, assuming a PA, inclination, and center position that are drawn randomly from the Gaussian distributions $PA = -37° \pm 5°$, $i = 61°.5 \pm 3°$, and center = nucleus $\pm 2''$. The curves show the mean results from 1000 realizations of the simulation, and the shading that follows the curves represents 1 σ systematic uncertainties in each of the plotted quantities. The thin black line is a power-law fit to the rotation curve, corresponding to a density profile of $\rho_{\rm TOT} \propto r^{-0.27}$. The cyan points are the ROTCUR rotation curve, showing the difference that arises if the radial velocities are not included in the fit. Note that although we have plotted the radial motions as positive velocities, whether they represent inflow or outflow cannot be determined without knowing which side of the galaxy is the near side.
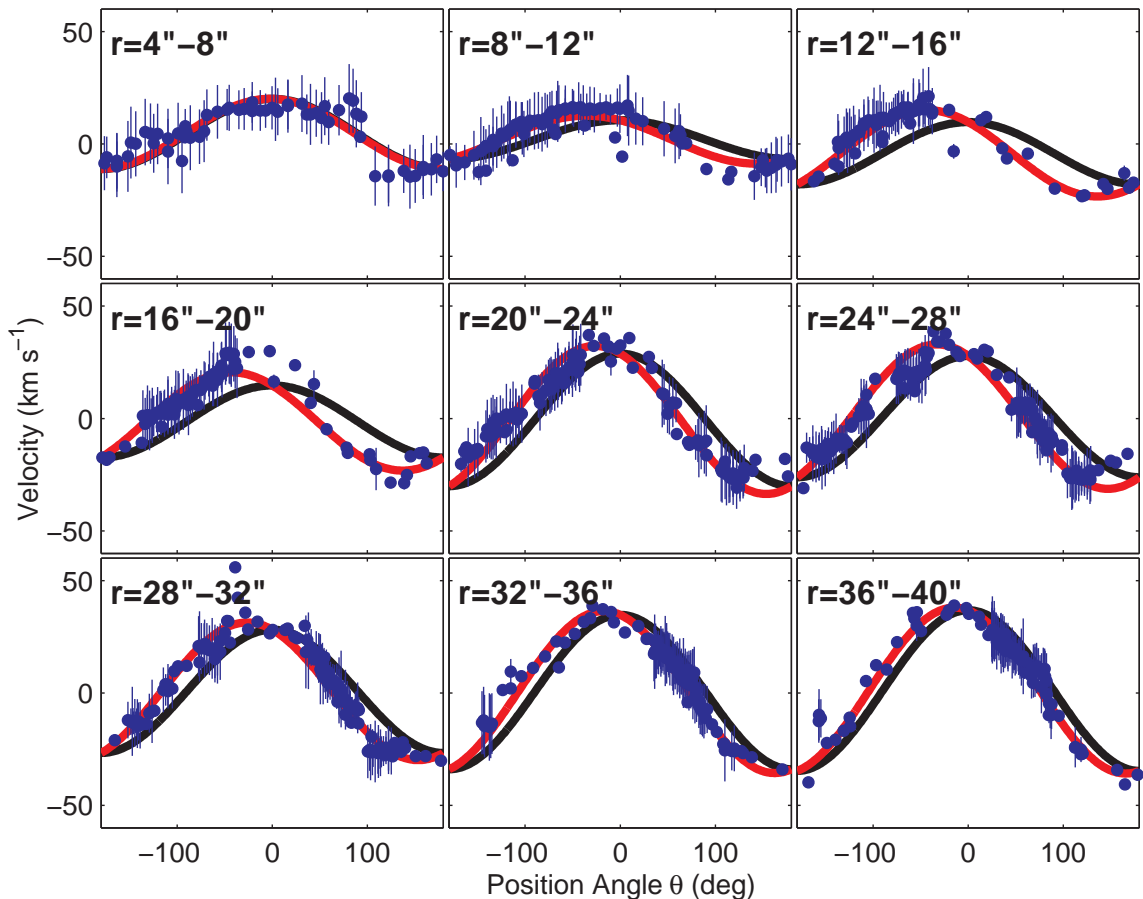
Figure 5.8 — Fits to the velocity field using RINGFIT. The observed velocities are plotted as a function of angle θ in the plane of the galaxy, where $\theta = 0$ is the major axis. Data points with small error bars are from the Hα velocity field (and are all independent), and data points with large error bars are from the CO velocity field (and are not all independent; the error bars have been increased to account for this). The black curves show the rotational component of the fits $(\cos\theta)$, and the red curves show the fits including both rotation and radial motions $(\sin\theta)$. The displacement of the velocity maxima from $\theta = 0$ illustrates the need for radial motions in the fits. At radii beyond $40''$, radial motions are not needed to obtain good fits to the data.

field. The rotation velocities and radial velocities with their associated uncertainties, and the stellar and gas rotation curves, are all listed in Table 5.3. In order to incorporate more accurately the uncertainties in the rotation curve, the values listed in Table 5.3 and plotted in Figure 5.7b are the mean values obtained from a Monte Carlo study rather than directly from the data (see §5.6.2).
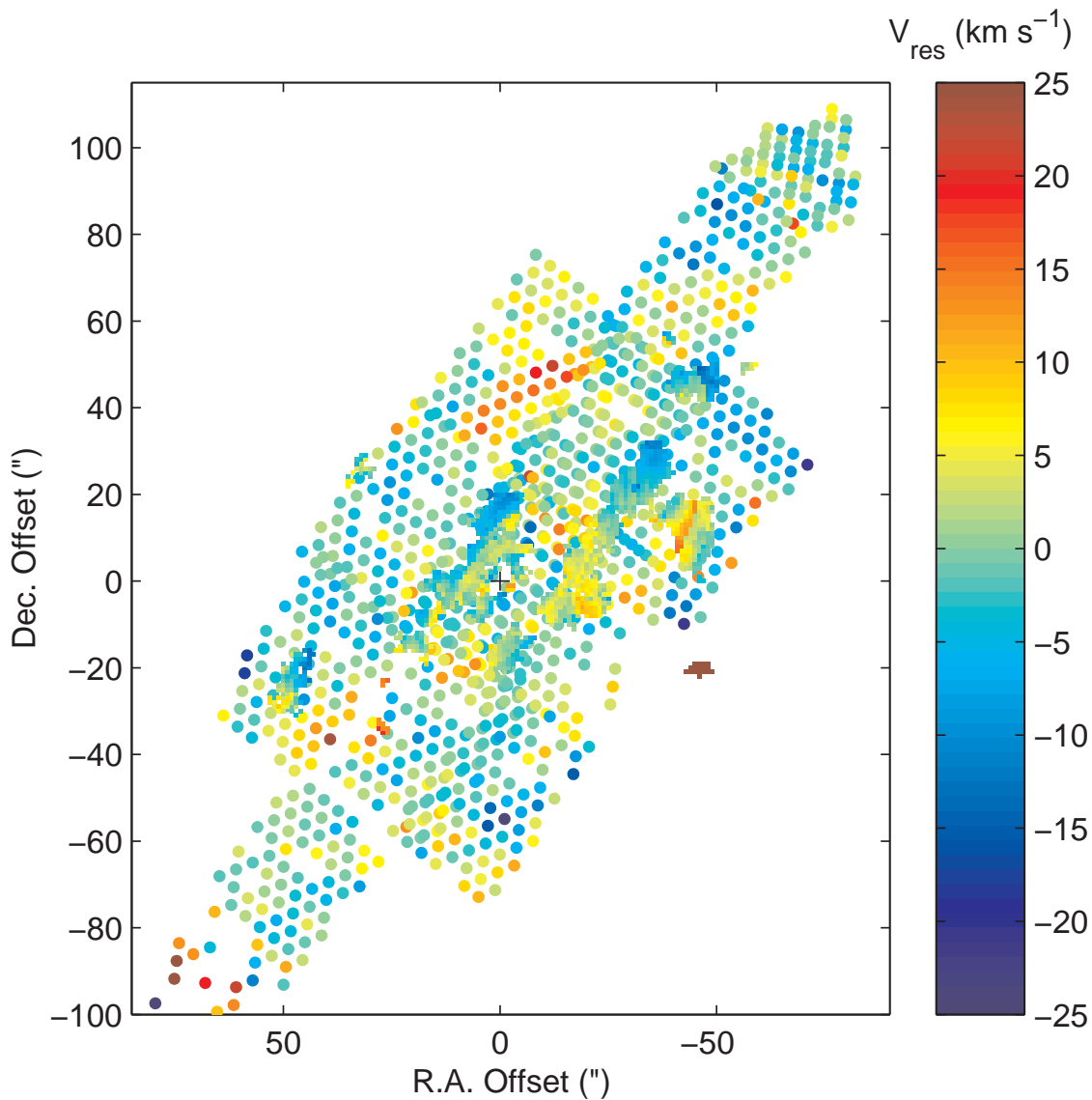
Figure 5.9 — Residual velocity field after subtracting RINGFIT model from the combined Hα and CO velocity fields. Hα data are shown by the circles, and the CO data are shown by the closely-packed square pixels. The rms of the residuals is 6.4 km s^{-1}; 5.5 km s^{-1} if the small patch of probably spurious CO emission southwest of the galaxy at (R.A. offset, Dec. Offset) = ($-45''$, $-20''$) is excluded.

Table 5.3: Rotation Curve Data

Radius[a]	v_{rot}[b]	v_{rad}[b,c]	v_{sys}[b,c]	$v_{*,rot}$[d]	$v_{\mathrm{HI},rot}$[e]	$v_{\mathrm{H_2},rot}$[f]	Δv_{drift}[g]
[$''$]	[km s^{-1}]	[km s^{-1}]	[km s^{-1}]	[km s^{-1}]	[km s^{-1}]	[km s^{-1}]	[km s^{-1}]
6.2	$6.8 \pm 0.4 \pm 3.6$	$3.8 \pm 0.2 \pm 3.3$	$-0.1 \pm 0.1 \pm 3.1$	20.6 ± 0.5	0.9	2.4	4.7
10.0	$9.5 \pm 0.3 \pm 4.3$	$8.4 \pm 0.1 \pm 3.8$	$-2.1 \pm 0.1 \pm 4.0$	23.8 ± 0.6	1.5	4.1	4.4
14.0	$14.0 \pm 0.2 \pm 3.1$	$12.4 \pm 0.1 \pm 2.8$	$-3.8 \pm 0.1 \pm 2.7$	27.9 ± 0.7	2.1	5.0	3.1
18.1	$19.8 \pm 0.1 \pm 5.5$	$14.2 \pm 0.1 \pm 2.4$	$-2.8 \pm 0.1 \pm 1.6$	33.4 ± 0.8	2.5	5.0	1.9
22.1	$26.1 \pm 0.1 \pm 3.9$	$15.7 \pm 0.1 \pm 2.7$	$-1.1 \pm 0.1 \pm 1.1$	38.1 ± 0.8	2.8	5.1	1.0
26.0	$28.7 \pm 0.1 \pm 3.5$	$15.4 \pm 0.1 \pm 2.7$	$-1.0 \pm 0.1 \pm 1.0$	41.2 ± 0.7	3.4	5.0	0.4
30.0	$28.7 \pm 0.1 \pm 2.7$	$13.0 \pm 0.1 \pm 2.6$	$-1.3 \pm 0.1 \pm 1.2$	46.8 ± 0.7	3.8	4.9	-0.1
34.0	$31.7 \pm 0.1 \pm 2.5$	$10.6 \pm 0.1 \pm 2.4$	$-0.5 \pm 0.1 \pm 1.7$	50.0 ± 0.6	4.2	4.8	-0.5
38.0	$35.5 \pm 0.1 \pm 2.3$	$9.5 \pm 0.1 \pm 2.3$	$0.1 \pm 0.1 \pm 1.5$	52.9 ± 0.5	5.0	4.7	-0.8
42.0	$39.4 \pm 0.1 \pm 2.1$	$8.0 \pm 0.1 \pm 2.7$	$0.2 \pm 0.1 \pm 1.3$	57.0 ± 0.4	5.9	5.1	-1.1
46.0	$42.9 \pm 0.1 \pm 2.3$	$7.1 \pm 0.1 \pm 3.1$	$-0.1 \pm 0.1 \pm 1.3$	60.5 ± 0.2	6.4	4.9	-1.3
50.0	$46.0 \pm 0.1 \pm 2.6$	$6.7 \pm 0.1 \pm 3.4$	$-0.8 \pm 0.1 \pm 1.5$	64.0 ± 0.1	7.2	4.6	-1.5
54.0	$49.1 \pm 0.1 \pm 3.1$	$5.5 \pm 0.1 \pm 3.5$	$-1.8 \pm 0.1 \pm 1.9$	65.6 ± 0.1	7.9	5.2	-1.5
58.1	$49.2 \pm 0.1 \pm 3.2$	$4.6 \pm 0.1 \pm 3.6$	$-3.0 \pm 0.1 \pm 2.2$	67.9 ± 0.3	8.6	5.0	-1.5
62.1	$51.4 \pm 0.1 \pm 3.2$	$5.3 \pm 0.1 \pm 3.1$	$-3.4 \pm 0.1 \pm 1.8$	71.9 ± 0.4	9.6	5.1	-1.3
66.0	$57.2 \pm 0.1 \pm 3.1$	$6.0 \pm 0.1 \pm 3.0$	$-3.8 \pm 0.1 \pm 1.7$	73.2 ± 0.6	11.1	5.9	-0.8
69.9	$63.8 \pm 0.1 \pm 2.9$	$5.4 \pm 0.1 \pm 3.6$	$-3.0 \pm 0.1 \pm 1.5$	76.3 ± 0.8	13.2	5.9	-0.3
73.9	$67.8 \pm 0.1 \pm 2.8$	$3.7 \pm 0.1 \pm 4.7$	$-1.7 \pm 0.1 \pm 1.4$	80.7 ± 1.0	15.0	6.0	0.4
77.9	$69.8 \pm 0.1 \pm 3.3$	$2.1 \pm 0.1 \pm 5.8$	$0.0 \pm 0.1 \pm 1.7$	83.5 ± 1.2	16.7	6.2	1.1
81.9	$71.7 \pm 0.1 \pm 3.9$	$1.5 \pm 0.1 \pm 6.6$	$2.3 \pm 0.1 \pm 2.2$	84.9 ± 1.4	18.5	6.4	1.9
85.9	$74.1 \pm 0.1 \pm 4.4$	$0.0 \pm 0.2 \pm 7.9$	$3.5 \pm 0.1 \pm 2.7$	84.5 ± 1.6	20.2	6.5	2.7
89.9	$76.7 \pm 0.1 \pm 4.8$	$-3.8 \pm 0.3 \pm 9.1$	$2.7 \pm 0.1 \pm 2.8$	83.5 ± 1.8	22.1	6.7	3.4
94.0	$79.9 \pm 0.2 \pm 4.4$	$-8.3 \pm 0.4 \pm 12.4$	$0.1 \pm 0.1 \pm 2.8$	85.4 ± 2.0	23.6	6.9	4.1
100.6	$83.6 \pm 0.6 \pm 3.3$	0	0	84.5 ± 2.3	25.7	7.1	5.0
111.1	$83.9 \pm 0.6 \pm 3.9$	0	0	81.2 ± 2.8	25.1	7.5	5.7

Table 5.3 – Continued

Radius[a]	v_{rot}[b]	v_{rad}[b,c]	v_{sys}[b,c]	$v_{*,rot}$[d]	$v_{\mathrm{HI},rot}$[e]	$v_{\mathrm{CO},rot}$[f]	Δv_{drift}[g]
["]	[km s^{-1}]	[km s^{-1}]	[km s^{-1}]	[km s^{-1}]	[km s^{-1}]	[km s^{-1}]	[km s^{-1}]
120.7	$88.7 \pm 0.6 \pm 4.4$	0	0	80.8 ± 3.3	25.3	7.8	4.6
131.2	$85.3 \pm 0.8 \pm 5.3$	0	0	77.6 ± 3.8	25.4	8.1	3.2

[a]To convert to pc, multiply by 16.7.

[b]Fitted velocities are given as value $\pm$ statistical error $\pm$ systematic error.

[c]Radial velocities and systemic velocities were fixed at zero for the outer four rings, where a lack of velocity field information away from the major axis limited our ability to constrain them.

[d]Stellar velocities are given for the case of $M_*/L_K = 1.0$ $\mathrm{M}_\odot/\mathrm{L}_{\odot,K}$. To get the stellar velocities for a different stellar mass-to-light ratio, multiply the tabulated values by $\sqrt{M_*/L_K}$. The listed uncertainties include only statistical errors.

[e]The uncertainties on the H I rotation velocities are not known because we do not have access to the original data, but are probably about 10–20%.

[f]The uncertainties on the H_2 rotation velocities are quite high because the CO-H_2 conversion factor is not known accurately. Since the H_2 rotation velocities are so small, this uncertainty is unimportant.

[g]This column gives the asymmetric drift correction to the rotation curve (see §5.6.2). To correct for asymmetric drift, add the values in this column to the observed rotation velocities in column 2.

The rotation curve of NGC 2976 is well-described by a power law from the center of the galaxy out to a radius of almost 2 kpc, as displayed in Figure 5.10a. The residuals after subtracting the fit from the rotation curve are shown in the bottom panel. The rotation curve only begins to deviate systematically from power-law behavior at $r \approx 110''$ (1.84 kpc). The *total* (baryonic plus dark matter) density profile corresponding to the rotation curve is $\rho_{\mathrm{TOT}} = 1.6(r/1 \mathrm{\ pc})^{-0.27\pm0.09} \mathrm{\ M}_\odot \mathrm{\ pc}^{-3}$ (see Appendix B, Equations B.2 and B.3, for the conversion between power laws in velocity and density). This density profile is the mean of the fits to 1000 Monte Carlo rotation curves, which represents a more accurate estimate of the uncertainties than the fit to the single rotation curve shown in Figure 5.7b. In the following subsection, we show that the density profile of the *dark matter halo alone* follows a shallower power law.

A key assumption underlying the derivation of this density profile is that the orbits are circular, and therefore that the gravitational and centrifugal forces are in equilibrium. This assumption is not likely to be correct in detail, but an inversion of the velocity field (including noncircular motions) to obtain the underlying nonaxisymmetric potential is beyond the scope of this chapter. Nevertheless, we note that the radial motions are comparable in magnitude to the rotation only for the inner four points of the rotation curve (the central 300 pc of the galaxy). At larger radii the rotation clearly dominates, and the orbits are nearly circular. If we fit the rotation curve using only points between 300 pc and 1.8 kpc — where the radial motions are probably unimportant — the derived density profile is almost identical to the one described in the previous paragraph. This suggests that a more complete analysis of the effect of noncircular motions on the inversion from a rotation curve to a density profile should not have a large impact on the derived slope of the density profile.

5.4.2 Limits on the Dark Matter Halo

To reveal the shape of the density profile of the dark matter halo, we first remove the rotational velocities contributed by the baryonic components of the galaxy from the observed rotation curve. The rotation curve of the dark matter halo is defined by

$$v_{halo}^2 = v_{rot}^2 - v_{*,rot}^2 - v_{\mathrm{HI},rot}^2 - v_{\mathrm{H}_2,rot}^2. \qquad (5.2)$$

We determine the lower limit to the dark matter density profile slope by maximizing the rotation curve contribution from the stellar disk. The maximum possible stellar rotation
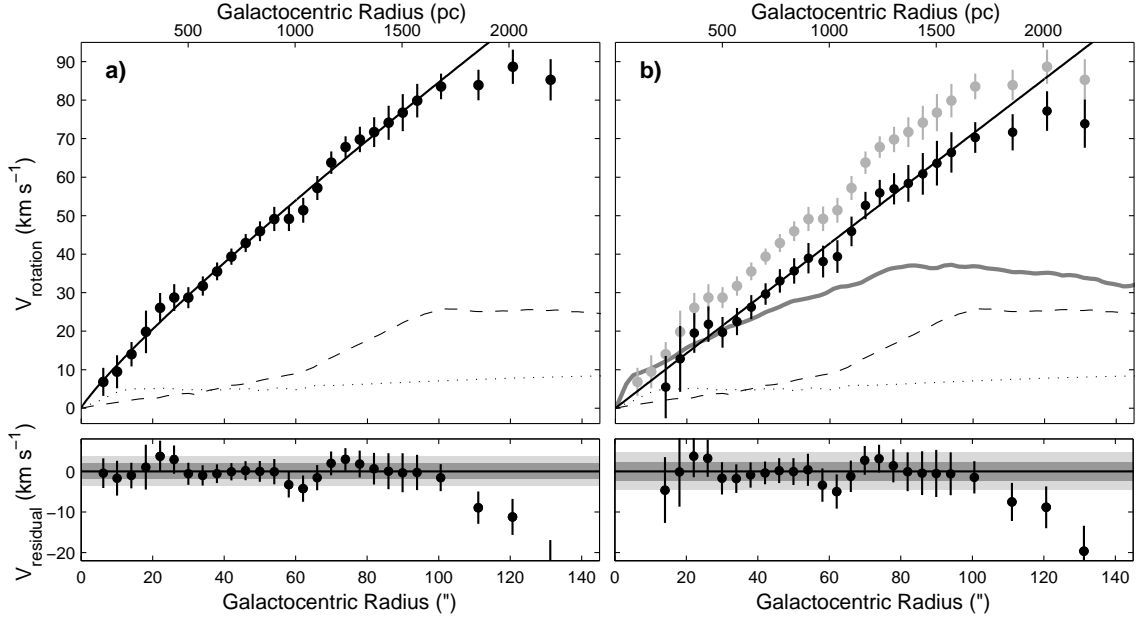
Figure 5.10 — (*a*) Minimum disk rotation curve of NGC 2976. Here we assume that the dark matter is dynamically dominant over the baryons at all radii, so that the observed rotation velocities (black circles) are attributable entirely to the dark matter halo. This represents the cuspiest possible shape for the dark matter halo. The plotted error bars are combined statistical and systematic uncertainties. The rotation velocities due to H I and H_2 are plotted as dashed and dotted curves, respectively. A power law fit to the rotation curve is shown by the solid black curve. The corresponding density profile is $\rho \propto r^{-0.27}$. Residuals from the fit are displayed in the lower panel, and 1 σ and 2 σ departures from the fit are represented by the shaded regions. (*b*) Maximum disk rotation curve of NGC 2976. In this case, we scale up the stellar disk (solid gray curve) as high as the observed rotation velocities (gray circles) allow. The stellar disk shown here has a mass-to-light ratio of 0.19 $M_\odot/L_{\odot,K}$. This is the most massive stellar disk that can be present without making the dark matter density increase with radius, which is probably not physically realistic. After subtracting the rotation velocities due to the stars, the rotation velocities due to the H I (dashed curve), and the rotation velocities due to the H_2 (dotted curve) in quadrature from the observed rotation curve, the dark matter rotation velocities are displayed as black circles. The two missing data points near the center of the galaxy had $v_{rot} < v_*$, yielding imaginary v_{halo}. The solid black curve is a power law fit to the halo velocities (for $14'' < r < 105''$) which corresponds to a density profile of $\rho_{\mathrm{DM}} \propto r^{-0.01}$. The halo residuals after the power law fit are displayed in the bottom panel.

curve is set by scaling up the mass-to-light ratio of the stellar disk until the criterion

$$v_{*,rot}^2 < v_{rot}^2 - v_{\mathrm{HI},rot}^2 - v_{\mathrm{H_2},rot}^2 \tag{5.3}$$

is no longer met at every point of the rotation curve. This requirement sets maximum disk mass-to-light ratios of $M_*/L_K = 0.09^{+0.15}_{-0.08}$ $\mathrm{M_\odot/L_{\odot,K}}$ and $M_*/L_R = 0.53^{+0.56}_{-0.46}$ $\mathrm{M_\odot/L_{\odot,R}}$, where the uncertainties are calculated by replacing v_{rot} with $v_{rot} \pm \delta v_{rot}$ in Equation 5.3.

We now use Equation 5.2 to obtain the rotation curve due to the dark halo. Under the assumption that the density profile can be described with a power law, $\rho_{\mathrm{DM}} \propto r^{-\alpha_{\mathrm{DM}}}$, we perform a linear fit to determine α_{DM} as a function of M_*/L_K. The fit extends out to a radius of $105''$, and we ignore points that have imaginary halo rotation velocities. A power law provides a good fit to the halo rotation curve for any mass-to-light ratio. The results of these fits are plotted in Figure 5.11. For $M_*/L_K > 0.19$ $\mathrm{M_\odot/L_{\odot,K}}$, $\alpha_{\mathrm{DM}} < 0$ and the density of the dark matter halo is *increasing* with radius. Because such a dark matter configuration is probably unphysical, we consider 0.19 $\mathrm{M_\odot/L_{\odot,K}}$ to be a firm upper limit to the stellar disk mass-to-light ratio, with the corresponding *lower limit* to α_{DM} of 0. The dark matter density profile for this maximal disk is

$$\rho_{\mathrm{DM}} = 0.1 \left(\frac{r}{1 \text{ pc}} \right)^{-0.01 \pm 0.13} \mathrm{M_\odot} \text{ pc}^{-3}. \tag{5.4}$$

As we argued in §5.3.1, the only way that the stellar mass-to-light ratio can be lower than this value is if the galaxy contains a young starburst, so Equation 5.4 represents the most likely shape for the dark matter halo. Note that even though the kinematic value of M_*/L_K we derive is rather low, there are two effects that we have not accounted for that tend to raise it: the finite thickness of the stellar disk (§5.3.1), and asymmetric drift (§5.6.2). Including these effects raises the maximum disk M_*/L_K close to the range that is predicted from the photometry.

The slope of the total density profile of the galaxy represents the absolute *upper limit* for the slope of the dark matter density profile, so $\alpha_{\mathrm{DM}} \leq 0.27 \pm 0.09$. In practice, because the galaxy contains stars and gas, the actual upper limit must be lower. If NGC 2976 is not undergoing a strong and very young starburst, its stellar mass-to-light ratio must be at least 0.10 $\mathrm{M_\odot/L_{\odot,K}}$.

Therefore, we conclude that the dark matter density profile is bracketed by $\rho_{\mathrm{DM}} \propto r^{-0.17 \pm 0.09}$ and $\rho_{\mathrm{DM}} \propto r^0$ (see Figure 5.11). Due to the extremely low value of the maximal
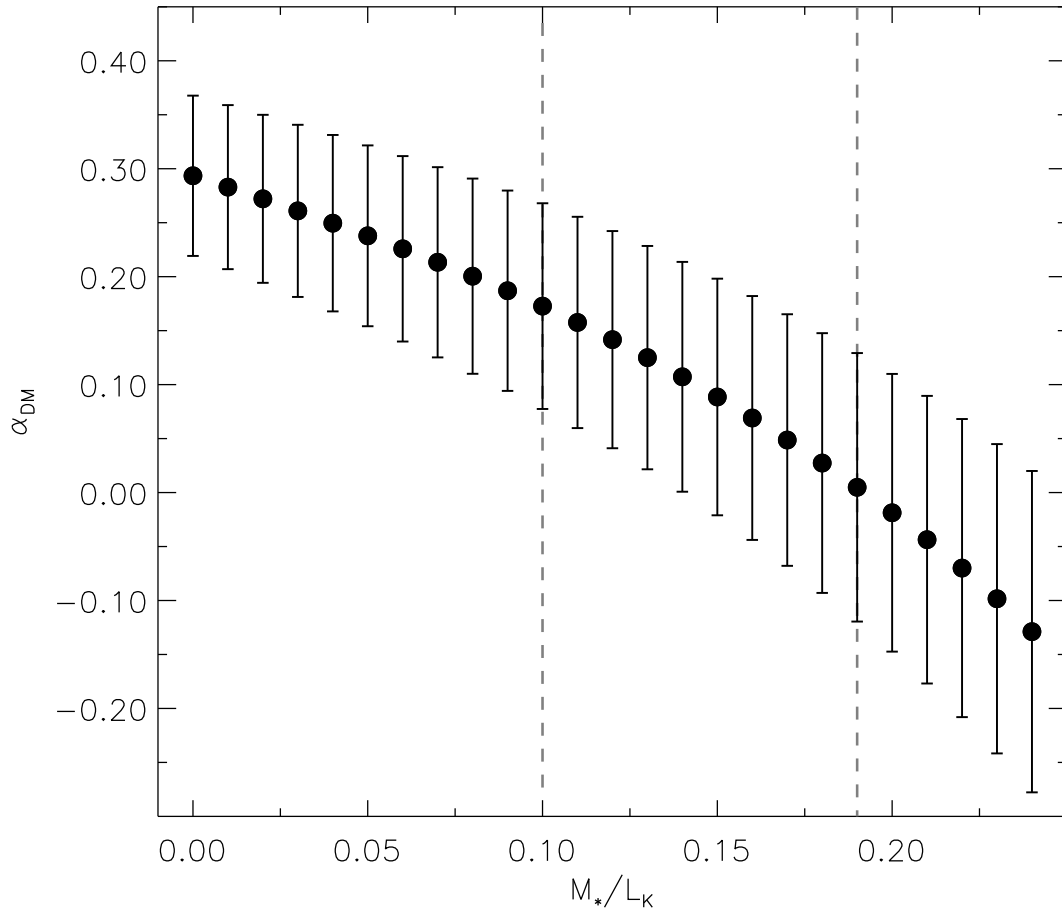
Figure 5.11 — Dark matter density profile slope α_{DM} as a function of the assumed K_s-band stellar mass-to-light ratio. The error bars represent the formal uncertainty in the value of α_{DM} from the power law fit. The dashed gray lines show the upper and lower limits to the mass-to-light ratio that we consider reasonable based on the combination of the stellar population models and the kinematics. Note that for small values of M_*/L_K the dark matter density profile is slightly steeper than the total density profile. This unusual effect is caused by the steep increase in the H I rotation curve at $r > 60''$.

disk mass-to-light ratio, the galaxy must contain an essentially maximal disk. We adopt the $M_*/L_K = 0.19$ $M_\odot/L_{\odot,K}$ disk and $\alpha_{\mathrm{DM}} = 0.01$ halo, which are shown in Figure 5.10b, as our preferred solution for the rest of the chapter. This disk dominates the gravitational potential of the galaxy out to a radius of $35''$ (550 pc). The total mass of NGC 2976 out to the edge of the observed velocity field at 2.2 kpc is 3.5×10^9 $M_\odot$, of which 5% is contributed by the gas, and up to 14% (for $M_*/L_K = 0.19$ $M_\odot/L_{\odot,K}$) is contributed by the stars.

5.5   Discussion

5.5.1   Comparison to Cold Dark Matter Simulations

In the previous section, we derived the dark matter density profile of NGC 2976, and determined that it cannot have a slope steeper than $\alpha_{\mathrm{DM}} = \alpha_{\mathrm{TOT}} = 0.27 \pm 0.09$. Even in this minimum disk case an NFW halo in NGC 2976 is ruled out.

Does the Density Profile of NGC 2976 Conflict With CDM?

The shallow central density profile of NGC 2976 does not necessarily imply a problem with CDM. One alternative possibility is that the simulations and the observations may not be directly comparable, or that the simulations may not incorporate all of the relevant physics. Our observations have only probed the very inner portion of the galaxy's potential, whereas the numerical simulations are better at revealing the density structure at large radii. The highest-resolution simulations can reach radii as small as 0.5% of the virial radius (Power et al. 2003). An NFW halo comparable in size to NGC 2976 would have a virial radius of ~ 80 kpc, so a simulation resolution element would be 400 pc in the best case. There would then be ~ 5 resolution elements within the observed region of the galaxy, which might not be enough to accurately determine the slope of the density profile over those radii. It is therefore plausible that higher-resolution simulations could help to resolve the apparent conflict between the observational and theoretical results. It is also worth noting that only a few of the CDM simulations reported in the literature to date have explored galaxies as small as NGC 2976. However, the results of these studies indicate that, if anything, dwarf galaxies have steeper density profiles than larger galaxies and galaxy clusters (Navarro et al. 2004; Colín et al. 2004, although see Ricotti 2003). Finally, we point out that the current dataset just reaches what appears to be the peak of

the rotation curve; it would be extremely interesting to trace the rotation curve farther out as it presumably flattens and turns over. We are in the process of using recently-obtained VLA H I observations to carry out this study.

Beyond numerical effects, though, there are more important reasons to suspect that the simulations may not correspond well to the observations. One potentially significant problem with current simulations is that they neglect the effects of the baryons on the dark matter halo. As we have shown, the central region of NGC 2976 is dominated by the stellar disk. It is possible that the formation of a massive disk at the center of a cuspy spherical halo could destroy the central cusp (Weinberg & Katz 2002, although see Gnedin & Zhao 2002).

An additional possibility for accounting for the very shallow central density profile within the context of CDM is suggested by the recent work of Stoehr et al. (2002) and Hayashi et al. (2003). These authors find in their simulations that dark matter satellite halos orbiting in the potential of a more massive neighbor are subject to tidal stripping. The stripped satellites end up with density profiles that are much shallower than their original NFW profiles. If NGC 2976 can be identified with one of the few most massive dark matter satellites of M81, this mechanism provides a natural way to explain its nearly constant-density dark matter halo without modifying the CDM model. However, Kazantzidis et al. (2004b) argued that Stoehr et al. (2002) and Hayashi et al. (2003) were incorrect, and satellite density profiles are not altered by tidal stripping even in cases of very significant mass loss.

We conclude that the solution to the central density problem does not currently require fundamental changes to CDM. There are a number of simpler explanations that may remedy the discrepancy between observations and simulations. More complete simulations can help to clarify the situation, as can more carefully targeted high-resolution observations (for example, studies of a few isolated galaxies could confirm or refute the possibility that density profiles are being modified by tidal stripping).

NFW and Pseudo-isothermal Fits for NGC 2976

Up to this point, we have used power law fits to describe the rotation curve and density profile, giving us a straightforward measurement of the central slope.[4] This method

---

[4]Note that in general a power law is not a good representation of the expected CDM density profile form, which has a logarithmic slope that varies from ~ -1 to -3. Our

has two advantages over the traditional approach of fitting the rotation curve with various observationally or theoretically motivated functional forms to see which one best matches the data. First, it is model-independent. Second, some functional forms (NFW, for example) require that the data cover a certain range of radii in order to constrain the fit parameters. An NFW rotation curve reaches its maximum at $2.16r_s$ and then turns over. If the velocity data do not extend beyond the turnover radius, the scale radius (and hence the concentration parameter) of the halo cannot be reliably measured.

Although we argue that the power-law approach may be more useful, we recognize that performing NFW and pseudo-isothermal fits to our data will facilitate comparisons to previous work. Accordingly, we have used the ROTCURSHAPE routine (Appendix A.3) to attempt to find best-fitting parameters for the velocity field of NGC 2976, assuming each of those functional forms for the rotation curve. An isothermal halo with a constant-density core provides a reasonable fit to the data, with a core radius of $67''$ (1.12 kpc) and an asymptotic velocity of 130 km s^{-1}. This fit is comparable in quality to the power law fit. For an NFW rotation curve, ROTCURSHAPE cannot obtain a satisfactory fit for any value of the concentration. We also attempted to fit the NFW form just to the rotation curve (not the full velocity field) with various nonlinear least-squares techniques. Because we know that the rotation curve of NGC 2976 is shallower than an NFW rotation curve, we fixed the concentration parameter at an artificially low value ($c = 9.2$, ~ 2 σ lower than expected; Bullock et al. [2001]) for these fits, and only solved for v_{200} and r_{200}. We found that neither v_{200} nor r_{200} are significantly constrained by the rotation curve of NGC 2976. The best NFW fits have a reduced χ^2 value of 6.2 (compare to a reduced χ^2 of 1.3 for a power law fit), and the NFW rotation curve only passes within 1 σ (combined statistical and systematic uncertainties) of 2 out of the 27 points in the rotation curve. The remainder of the fitted points are up to 4.1 σ away from the data points, showing that an NFW rotation curve is very strongly excluded for this galaxy. Note that both the pseudo-isothermal and NFW fits described here were performed on the total mass distribution of the galaxy, not just the contribution from the dark matter halo. Removing the stellar and gas disk velocities first would make the NFW fit worse.

Although our velocity field does not extend beyond the turnover of the rotation curve and NFW fits to the rotation curve are unconstrained, there is another way to estimate

measurements, however, are all within the characteristic radius of the halo of NGC 2976, where the density profile predicted by CDM is close to a power law.

the NFW concentration parameter, and the effective concentration parameters for other dark halo models from the data. Alam, Bullock, & Weinberg (2002) defined the parameters $R_{V/2}$ (the radius at which the rotation curve has risen to half of its maximum value) and $\Delta_{V/2}$ (the mean density within $R_{V/2}$, in units of the critical density) in order to make it easier to compare rotation curve observations with theoretical predictions. For the minimum disk case in NGC 2976, $V_{max} = 86$ km s^{-1}, $R_{V/2} = 768$ pc and $\Delta_{V/2} = 1.3 \times 10^6$. Using the formulae given by Alam et al. (2002), we calculate concentrations of 19.9, 4.4, 55.1, and 246.0 for an NFW profile, a Moore profile, a Burkert profile, and an isothermal+core profile, respectively. For our preferred solution, after accounting for the stellar and gas disks, the dark matter halo parameters are $V_{max} = 74$ km s^{-1}, $R_{V/2} = 902$ pc and $\Delta_{V/2} = 7.0 \times 10^5$, reducing the concentrations to 15.6, 3.3, 43.7, and 180.1.

The Alam et al. (2002) analysis is designed to study the *value* of the central density of the dark matter halo (which is also a potential point of disagreement between observations and simulations). With or without accounting for the baryonic contribution to the rotation curve, the central density of the dark matter halo of NGC 2976 (parameterized by Alam et al.'s definition of $\Delta_{V/2}$) is consistent with ΛCDM simulations, even though the shape of the density profile is not.

5.5.2 Comparison to NGC 4605

NFW suggested, and most subsequent authors have agreed, that relaxed CDM halos should all have the same shape independent of mass or merger history.[5] NGC 2976 is superficially rather similar to the first galaxy we studied, NGC 4605, so it is reasonable to compare the two. Our observations of NGC 4605 showed that its dark matter halo has a density profile with $\alpha_{\rm DM} = 0.65$ (Bolatto et al. 2002). At first glance, this result does not appear to seriously conflict with our findings for NGC 2976. However, the NGC 4605 density profile was for a maximal disk, and therefore represents a *lower limit* on $\alpha_{\rm DM}$. We argued that the maximum disk solution was the most likely for NGC 4605 because the mass-to-light ratio could not realistically be much smaller than its maximum value of 0.25 M$_\odot$/L$_{\odot,K}$ in that galaxy, and because it leads to a simpler density structure for the halo (a single power law rather than two).

---

[5]Provided that they have not recently undergone a major merger. There is no kinematic or photometric evidence to suggest that either of the galaxies discussed here was recently involved in a merger.

For NGC 2976, by contrast, we set an *upper limit* of $\alpha_{\mathrm{DM}} = 0.27$ for the minimum disk case, and we prefer lower values of α_{DM} because a minimum disk is not physically realistic. For solutions in the range that we believe is reasonable ($0 \leq \alpha_{\mathrm{DM}} \leq 0.17$), the dark matter density profile slope disagrees with that of NGC 4605 by up to 5 σ, even though the disks of these two galaxies are quite similar. Although we have only examined two galaxies so far, their incompatible dark matter density profiles suggest that the cosmic scatter in halo properties may be large.

5.5.3 Are All Dwarf Galaxies Dark Matter-Dominated?

It is generally assumed that, with the possible exception of tidal dwarfs (Barnes & Hernquist 1992), all dwarf galaxies are dynamically dominated by dark matter (Carignan & Freeman 1988; Carignan & Beaulieu 1989; Jobin & Carignan 1990; Martimbeau et al. 1994). While this assumption is likely true for the outer parts of dwarfs (radii larger than ~ 2 times the disk scale length), the observational evidence is more ambiguous close to their centers. One of the main sources of this problem is that dwarf rotation curves are traditionally observed in H I, with angular resolution as low as $30''$. The rotation curves therefore often contain only two or three data points at radii where the stellar and gas disks are dynamically important. To make matters worse, these inner data points are the most likely to be affected by beam smearing and other systematic problems. We suggest that higher resolution observations of dwarf galaxies may show that their central regions are often dominated by luminous material.

In the case of NGC 2976, the baryonic mass dominates the central 220 pc of the galaxy even for the lower limit to M_*/L_K of 0.10 $\mathrm{M}_\odot/\mathrm{L}_{\odot,K}$. For our preferred solution of a maximal disk ($M_*/L_K = 0.19$ $\mathrm{M}_\odot/\mathrm{L}_{\odot,K}$), the disk dominates out to a radius of 550 pc. Consequently, the stellar disk has a significant impact on the derived density profile of the dark matter halo: slopes ranging from $\alpha_{\mathrm{DM}} = 0.29$ to $\alpha_{\mathrm{DM}} = -0.13$ are possible depending on the choice of M_*/L_K (see Figure 5.11).

That stars contribute to the dynamics of a dwarf galaxy is not unique to NGC 2976; similar conclusions were reached for NGC 1560 by Broeils (1992), for NGC 5585 by Blais-Ouellette et al. (1999), and for NGC 4605 by Bolatto et al. (2002). In addition, this result is also in agreement with the work of, e.g., Persic, Salucci, & Stel (1996, hereafter PSS), who showed that the fraction of dark mass in spiral galaxies is a strong inverse function

of luminosity. PSS found that in galaxies with luminosities comparable to NGC 2976 ($M_I = -18.5$), dark matter can be detected gravitationally beginning at $10 - 15\%$ of the optical radius (which is located at 2.8 kpc for NGC 2976), or about 350 pc. This is entirely consistent with our mass modeling (see Figure 5.10b). The average $M_I = -18.5$ rotation curve constructed by PSS has dark matter dominating the rotation curve at radii beyond $0.2R_{opt}$ (560 pc), also consistent with our preferred solution. Thus, even though it may seem counterintuitive, the PSS results support our conclusion that luminous matter is sometimes an important contributor to the inner rotation curves of dwarf galaxies.

5.5.4   Are the Kinematics of NGC 2976 Affected By M81?

NGC 2976 does not appear to be participating in the dramatic tidal interaction currently taking place between M81, M82, and NGC 3077 (Yun, Ho, & Lo 1994); however, it has likely interacted with M81 in the past. Appleton et al. (1981) discovered a faint H I streamer stretching from M81 to NGC 2976. Boyce et al. (2001) used HIJASS data to show that this gas comprises a single tidal bridge that smoothly connects the two galaxies (see their Figure 2a). The bridge contains somewhat more H I than NGC 2976 itself (2.1×10^8 M$_\odot$ and 1.5×10^8 M$_\odot$, respectively). Unfortunately, the HIJASS observations lack the angular resolution to see the details of the connection between the bridge and NGC 2976, and the presence of Galactic H I further complicates the situation. Yun, Ho, & Lo (2000) suggested that the bridge is a remnant of an interaction that took place only between M81 and NGC 2976 before the current M81/M82/NGC 3077 event. Nevertheless, the optical galaxy (Figure 5.1) and the inner H I disk (Stil & Israel 2002a,b) both appear regular, symmetric, and undisturbed. Assuming that M81 has a total mass of $\sim 10^{12}$ M$_\odot$ (Karachentsev et al. 2002), its tidal field only becomes comparable to the gravity of NGC 2976 (at a radius of 2 kpc) if the galaxies approach within 20 kpc of each other. Since M81 is currently at a projected distance of 79 kpc, the present-day kinematics of NGC 2976 are probably unaffected by the interaction.

5.5.5   Possible Origins of Noncircular Motions

In Figure 5.4a it is clear that the velocity field of NGC 2976 is distorted compared to a purely rotating disk. The velocity gradient near the center of the galaxy is not directed along the photometric major axis, but is offset by up to $\sim 40°$ (see Figure 5.8). This twisting

of the isovelocity contours means that the kinematics of NGC 2976 cannot be described by the simplest model: a constant PA and only rotational motions. We have shown that the velocity field *can* be adequately described by adding radial motions in the plane of the galaxy to the model. If there are systematic trends remaining after this model has been subtracted from the data, they are only present at the level of a few km s^{-1} (see Figure 5.9). However, a purely rotational velocity field with a kinematic PA that declines monotonically from $\sim 6°$ near the center of the galaxy to $-37°$ at a radius of $90''$, and remains constant at $-37°$ for larger radii can also fit the data. This model is the one produced by ROTCUR if the kinematic PA is left as a free parameter (see Appendix A.1). The total density profile obtained under these assumptions is $\rho_{\mathrm{TOT}} \propto r^{-0.56}$. Since the photometric PA of the galaxy is quite stable, varying only a few degrees from its average value beyond a radius of $30''$ (at smaller radii, local bright spots dominate the isophotal fitting), this model requires a physical mechanism that could cause the behavior of the photometric and kinematic PAs to deviate strongly from one another. It is unclear what such a mechanism could be, and why it would make the kinematic PA change so rapidly. Because this model lacks an observational motivation, while radial (or other noncircular) motions are expected to occur naturally for a variety of reasons (see below), we prefer the radial motion interpretation of the velocity field.

There are a number of possible sources of the radial motions. The galaxy could contain a stellar bar, although there is no sign of a bar in any of our images, even at 2.2 μm. Further evidence against the presence of a bar is the lack of measurable higher order terms in our harmonic decomposition of the velocity field. The velocity field of a barred galaxy should contain a nonzero $\sin 3\theta$ term (Schoenmakers, Franx, & de Zeeuw 1997; Wong 2000). An alternative to a bar is the possibility that the dark halo is triaxial rather than spherical, as we have assumed. It is expected that CDM halos should be at least moderately triaxial (Dubinski & Carlberg 1991; Warren et al. 1992; Cole & Lacey 1996), and the potential of a triaxial halo is certainly not axisymmetric, so the velocity field of a galaxy embedded in a triaxial halo would exhibit noncircular motions. Hayashi et al. (2005) have simulated a highly idealized version of a disk in a triaxial halo, and found that not only are there radial motions in the velocity field, but that along certain lines of sight the density profile an observer would derive from the velocity field appears to contain a constant-density core, even though the intrinsic density profile of the halo is an NFW profile. Even more strikingly, the dependence of the radial motions on radius (when the disk is viewed along these lines

of sight) is identical to the behavior of the radial motions that we observed in NGC 2976 (see Figure 5.12). Future simulations of a gaseous disk in a triaxial halo with more realistic assumptions would be quite interesting, but this early result along strongly suggests that the radial motions in NGC 2976 — and perhaps the appearance of a shallow density profile as well — are caused by triaxiality. Other potential causes of the radial motions include a disk that has nonzero ellipticity, and outflows associated with star formation.

5.6 Systematics

In this section, we study in detail the systematic uncertainties in our analysis, and also some systematic problems that afflict rotation curve studies in general. We emphasize that systematic effects are the dominant source of uncertainties in our analysis. Some of the details contained in this section are therefore crucial to understanding the reliability of our conclusions. The general reader may wish to use the summary in the following paragraph and the subsection headings to select the portions in which he or she is interested.

We begin in §5.6.1 by mentioning the importance of considering systematic problems, and our efforts to account for these problems in the design of our survey. Section 5.6.2 continues with a description of our tests for systematic errors caused by the rotation curve fitting. In §5.6.3 we demonstrate that the Hα and CO velocity fields of NGC 2976 are consistent with each other, not just globally, but on a point-to-point basis. In §5.6.4 we use our velocity field to simulate long-slit observations of NGC 2976, and compare the derived long-slit density profiles to the one we extract from the two-dimensional velocity data. Section 5.6.5 examines the problem of offsets between the kinematic center of a galaxy and the position of the slit during spectroscopic observations, and §5.6.6 briefly discusses the difficulties that barred galaxies present for density profile studies.

5.6.1 The Problem of Systematics

It is well-known, although not often discussed, that there are a number of serious systematic uncertainties that can cause an observed rotation curve (and the associated density profile) to differ significantly from the true one. Worse, nearly all of these effects work in the same direction to cause density profiles to appear systematically shallower than they actually are. Fortunately, the most severe of these problems can be minimized or avoided by using two-dimensional velocity fields and by making velocity measurements at
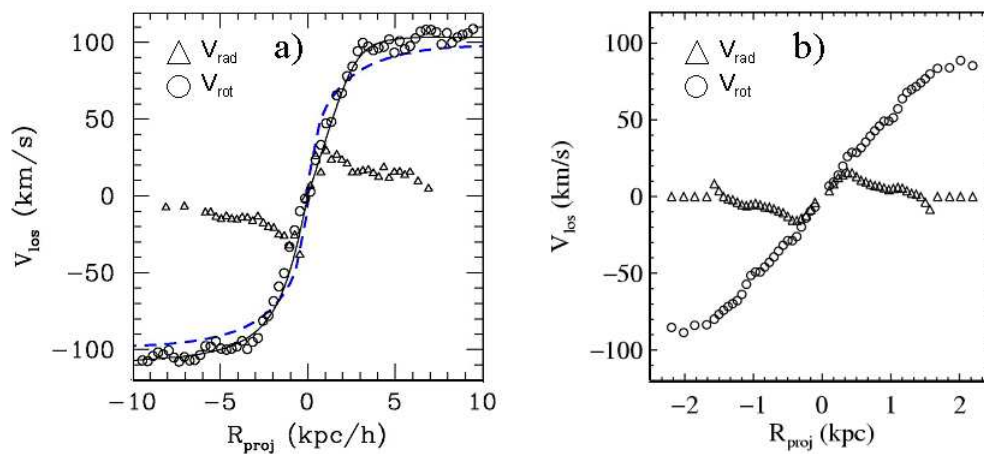
Figure 5.12 — *(a)* Rotation curve (circles) and radial velocity curve (triangles) of a disk in a triaxial halo simulated by Hayashi et al. (2005). Along the line of sight from which these motions are viewed, the apparent density profile of this halo has a constant-density core, even though the actual density profile is cuspy. *(b)* Rotation curve (circles) and radial velocity curve (triangles) of NGC 2976. The remarkable similarity between the radial velocity curves and the derived density profiles for this simulated disk and NGC 2976 strongly suggest that the radial motions in NGC 2976 are caused by the triaxiality of its dark matter halo. If this is indeed the case, NGC 2976 may actually have a steeper density profile that appears shallow because of our viewing angle.

very high precision (Blais-Ouellette et al. 1999; van den Bosch & Swaters 2001; Bolatto et al. 2002; Swaters et al. 2003a). SMVB model several of these effects in detail and determine how severely observational results may be affected in various situations. One of the key systematics to investigate is the location of the dynamical center of the galaxy with respect to the assumed center. Other systematic errors that might potentially cause problems for rotation curve studies include extinction (for Hα observations), beam smearing (for H I observations), noncircular motions (which could be caused by a bar, an intrinsically elliptical disk, a triaxial halo, or outflows associated with vigorous star formation), incorrect PAs, inclinations, and systemic velocities, asymmetric drift, and using observations made at low velocity resolution to study galaxies with small rotation amplitudes. We designed our study so as to avoid some of these problems, and to be able to account for the others, as described in the introduction; a few key points are mentioned below. We know that extinction does not affect our results because our CO and Hα velocity fields agree near the center of the galaxy, where extinction should be most important. Since we have two-dimensional information, we can explicitly account for radial motions, as discussed in §5.4, §5.6.2, and Appendix A. Our velocity resolution is ~ 10 times smaller than the maximum rotation velocity of NGC 2976 (and the precision of our velocity measurements is another order of magnitude smaller), so we are unlikely to be missing significant features in the velocity field due to insufficient resolution.

5.6.2   Rotation Curve Fitting Systematics

Due to the high precision of our velocity measurements, the statistical error bars on both the rotation curve and the radial velocity curve are negligible (less than 1 km s^{-1} everywhere). Therefore, the limiting factors on the accuracy of the rotation curve are the systematic uncertainties associated with our fit, which is a normal state of affairs for rotation curve and density profile observations.

Algorithmic Differences

The most straightforward check for systematic problems is to compare the rotation curves produced by different algorithms. Recall that neither ROTCUR nor ROTCURSHAPE allow the user to fit for the $\sin\theta$ term (radial motions) in Eq. A.2, and RINGFIT and ROTCURSHAPE both require that the PA, inclination, and center position not vary with

radius. Using a set of input parameters that are compatible with all three algorithms (PA$= -37°$, $i = 61°\!.5$, $\cos\theta$ weighting, and no radial motions) and considering radii less than $105''$, the algorithms all produce essentially identical results. We conclude that none of the assumptions that are built in to the fitting algorithms affect the results.

The only significant difference that appears between the algorithms stems from the inclusion of radial velocities in the fit. Earlier, we noted that it is obvious from inspection of the velocity field (Figure 5.4) that noncircular motions are present in NGC 2976: for example, the velocity fits in individual rings for $r < 40''$ show that the observed velocity maximum is systematically offset from the photometric major axis (Figure 5.8). Neglecting the $\sin\theta$ term and fitting only for rotation increases the exponent of the density profile from $\alpha_{\mathrm{TOT}} = 0.27$ to $\alpha_{\mathrm{TOT}} = 0.42$ (for $0 < r < 105''$).

If radial motions are ignored, however, an accurate description of the velocity field requires that the kinematic PA changes with radius. When either the kinematic PA or the inclination varies with radius, ROTCUR yields $\alpha_{\mathrm{TOT}} \approx 0.56$. If we allow both parameters to change with radius, tying the inclination to the photometric axis ratio and fitting for the kinematic PA, we obtain total density exponents as high as $\alpha_{\mathrm{TOT}} = 0.7$. Thus, by exchanging radial motions for geometric degrees of freedom it is possible to push α_{TOT} to higher values. However, we regard these models as contrived and lacking physical motivation, and therefore less appealing than simply including radial motions.

Uncertainty in Center Position

Assessing the uncertainties on the rotation velocities requires that we first know the uncertainties on each of the parameters that are used to calculate the rotation velocities: the center, PA, inclination, and systemic velocity. We begin by considering the center position of NGC 2976.

The galaxy nucleus is located within $3''$ of previously published estimates of the galaxy's position. The astrometric precision on the photometric location of the nucleus is $0''\!.2$. However, the velocity field is only aligned with the images to about $1''$, and the resolution of the velocity field is $4''$, which limits the degree to which we can verify that the nucleus and the kinematic center of the galaxy coincide. To determine the position and uncertainty of the kinematic center, we used a bootstrap resampling technique. By running RINGFIT on 200 bootstrap samples of the velocity field, we measured a kinematic center

of $(\alpha_{2000}, \delta_{2000}) = (09^h47^m15.5^s, 67°55^m00.2^s)$, with an uncertainty of $2''$ in both α and δ. Thus, there is no evidence for an offset between the kinematic and photometric centers of NGC 2976.

Uncertainty in Position Angle

We used the same bootstrap method to measure the kinematic PA[6] and its uncertainty. The kinematic PA is well-determined at $\mathrm{PA}_{kin} = -36° \pm 5°$ and agrees with the photometric PA.

Uncertainty in Inclination Angle

Since the photometric inclination of NGC 2976 is relatively high, an error in the inclination angle does not significantly change the rotation velocities. Furthermore, because changing the inclination by a small amount is approximately equivalent to scaling the rotation curve by a constant, the exponent of the power law fit should not be affected. The reader may recall that if the ellipticity is left as a free parameter during the surface brightness profile fitting (§5.2.5), ELLIPSE calculates inclinations that vary smoothly between $55°$ and $77°$ across the galaxy. As mentioned before, this behavior is not interpreted as an actual change of the inclination angle with radius. Nevertheless, if we force ROTCUR to use this function for the inclination, the density profile slope for the total mass distribution increases to $\alpha_{\mathrm{TOT}} \approx 0.56$, as discussed in §5.6.2.

Uncertainty in Systemic Velocity

If the systemic velocities are left as a free parameter in the velocity field fits, they have a scatter of 1.8 km s^{-1} from ring to ring. It is possible that these variations are real, although they are only marginally significant when the systematic uncertainties are taken into account. The alternative approach is to fix v_{sys} at its average value and then fit again with only v_{rot} and v_{rad} as free parameters. The results of the fit with v_{sys} fixed are nearly identical to the previous results. None of the radial or rotational velocities are changed by more than 1 σ, the density profile exponent for the total mass distribution increases by less

---

[6]The kinematic PA is distinct from the photometric PA in that it is defined as the angle between north and the *receding side* of the galaxy's major axis, so that it has a range of $-180°$ to $180°$ (where positive angles are east of north).

than 1 σ (to $\alpha_{\mathrm{TOT}} = 0.34 \pm 0.09$), and the maximum allowed mass-to-light ratio increases to 0.24 $\mathrm{M}_\odot/\mathrm{L}_{\odot,K}$.

Uncertainties in Rotation Velocities and Radial Velocities

Using the measured uncertainties in the center position and PA, and assuming an uncertainty of $3°$ for the inclination angle, we calculated the resulting uncertainties on the rotation velocities and the radial velocities with a Monte Carlo technique. We generated 1000 random centers, PAs, and inclinations, assuming a Gaussian distribution for each of the parameters, and ran RINGFIT with each set of parameters. The standard deviation of the 1000 rotation velocities in each ring was defined to be the systematic error of that rotation velocity, and the systematic errors in the radial velocities and systemic velocities were calculated in the same way. The systematic errors on the rotation curve range from 2.1 km s^{-1} to 5.5 km s^{-1}, as listed in Table 5.3. Power law fits to the 1000 Monte Carlo rotation curves yield a mean slope of the total density profile of $\alpha_{\mathrm{TOT}} = 0.27 \pm 0.09$.

Asymmetric Drift Correction

We have also calculated the asymmetric drift correction to the rotation curve, as defined by, e.g., Côté, Carignan, & Freeman (2000). We derived the velocity dispersion σ as a function of radius from the Hα data, and the surface density Σ by adding the H I and H$_2$ column densities. We then fit polynomials to $\sigma(r)$ and $\Sigma(r)$ and calculated the derivatives $d\sigma/d\ln r$ and $d\ln\Sigma/d\ln r$ analytically. There are significant uncertainties that factor into this calculation, including (1) we have not included the ionized gas surface density (although its contribution is expected to be small), (2) the H$_2$ surface density is uncertain due to our imprecise knowledge of the CO-H$_2$ conversion factor, (3) our velocity field extends to radii that are smaller than the resolution of the H I data, so that the calculated asymmetric drift may be incorrect for the inner few points of the rotation curve where the correction is most important, and (4) some of the Hα velocity dispersion is probably due to flows associated with star formation. Because we view the derived corrections as rather uncertain, we have not corrected the observed rotation curve for asymmetric drift. However, the corrections are listed in Table 5.3 if the reader wishes to apply them. Their effects are to increase the maximum disk mass-to-light ratio, and to make the rotation curve slightly more linear, but the overall conclusions of the chapter do not change.

Conclusions From Analysis of Rotation Curve Systematics

We have shown that the only ways to significantly change the derived slope of the density profile of NGC 2976 are to (1) assume the stellar mass-to-light ratio is zero, (2) ignore the radial component of the velocity field, or (3) allow the kinematic PA and/or inclination to change with radius. Assuming that the observed velocities are due entirely to rotation raises α_{TOT} by ~ 0.15, and allowing the PA and inclination to change with radius raises α_{TOT} by up to an additional ~ 0.25. Accounting for the contribution of the maximum stellar disk, however, limits the dark matter density profile exponent to $0.26 \leq \alpha_{\mathrm{DM}} \leq 0.4$ in these circumstances.

Because inspection of the velocity field and the fits clearly reveals the presence of radial motions, neglecting the radial component is not justified. Changes in the PA with radius are not supported by the photometry, and changes in the inclination with radius are difficult to understand physically. Therefore, we argue that these solutions, despite being mathematically viable, are contrived and not motivated by the data.

We conclude that the galaxy contains substantial radial motions, and that the density profile results are not significantly affected by the most obvious sources of systematic errors. We caution that the robustness against systematics that we find is specific to this dataset, and may not be true in general. Because the rotation curve of NGC 2976 increases with radius so slowly, errors in any of the geometric parameters of the galaxy are diminished in importance. A galaxy with a more rapidly rising rotation curve would probably be more severely affected. Assuming that the radial motions provide no support, the dark matter density profile slope is in the range $0 \leq \alpha_{\mathrm{DM}} \leq 0.27$, with a 2 σ upper limit of $\alpha_{\mathrm{DM}} \leq 0.45$, where systematic errors have been included in the uncertainty on α_{DM}. NGC 2976 thus violates the prediction of universal central density cusps by CDM simulations.

5.6.3 Comparing Velocities Derived From Different Tracers

Some recent studies in the literature have shown that, beam smearing questions aside, there do not appear to be systematic offsets between H I and Hα rotation velocities (e.g., McGaugh, Rubin, & de Blok 2001; Marchesini et al. 2002). With a handful of exceptions, though, these studies employed long-slit Hα data, so the comparisons essentially took place only along the major axis. In addition, the spatial and velocity resolution of the H I and Hα data were often quite different.

In this chapter, we have presented for the first time the data necessary for a two-dimensional comparison across a dwarf galaxy of the CO and Hα velocity fields. The angular resolution of the two datasets is similar ($6''$ and $4''$, respectively), and although the CO velocity resolution is better by a factor of ~ 6, the higher signal-to-noise at Hα compensates such that the velocities can be measured with comparable precision. We use the following technique to compare the velocity fields. At the position of each Hα fiber, we compute a weighted average of the velocities of all of the pixels in the CO map that fall within the radius of the fiber. CO pixels that do not contain any emission are not used in computing the average, and of course, Hα fibers that do not coincide with any molecular emission are not used either. This process yields a unique one-to-one mapping between the two velocity fields. The rms difference between $v_{\mathrm{H}\alpha}$ and v_{CO} is 5.3 km s^{-1}, with the comparison being made at 173 points. Similar studies in the Milky Way found that the dispersion between the velocities of molecular clouds and the associated Hα-emitting gas was 4–6 km s^{-1} (Fich, Treffers, & Blitz 1982; Fich, Dahl, & Treffers 1990), so much of the scatter we observe in NGC 2976 may be intrinsic to the process of H II region formation rather than caused by observational uncertainties. We plot the Hα velocities against the CO velocities in Figure 5.13. There is a weak systematic trend visible in the residuals, with $v_{\mathrm{CO}} > v_{\mathrm{H}\alpha}$ near the center of the galaxy and $v_{\mathrm{CO}} < v_{\mathrm{H}\alpha}$ on the northwest side of the galaxy. The amplitude of this trend is only a few km s^{-1}, so it does not affect our rotation curve. The origin of the trend is not clear, but we suggest that it could be a result of the spatial distribution of the gas. For example, where the ionized gas is largely in front of the molecular clouds, the expansion of H II regions away from nearby molecular clouds would make $v_{\mathrm{H}\alpha} > v_{\mathrm{CO}}$. This effect should appear preferentially where Hα emission is bright. Conversely, where the molecular clouds are in front, one would expect that $v_{\mathrm{H}\alpha} < v_{\mathrm{CO}}$. These areas should have faint Hα emission due to extinction within the molecular clouds. The Hα distribution in NGC 2976 appears to be qualitatively consistent with this interpretation; the Hα is brighter in the northwest, where the Hα velocities are larger, and there is an Hα hole to the southeast, where some of the CO velocities are higher. In any case, we conclude that the Hα and CO velocity fields agree, with a scatter of 5.3 km s^{-1}, and thus that both species should be accurate tracers of the gravitational potential of NGC 2976.
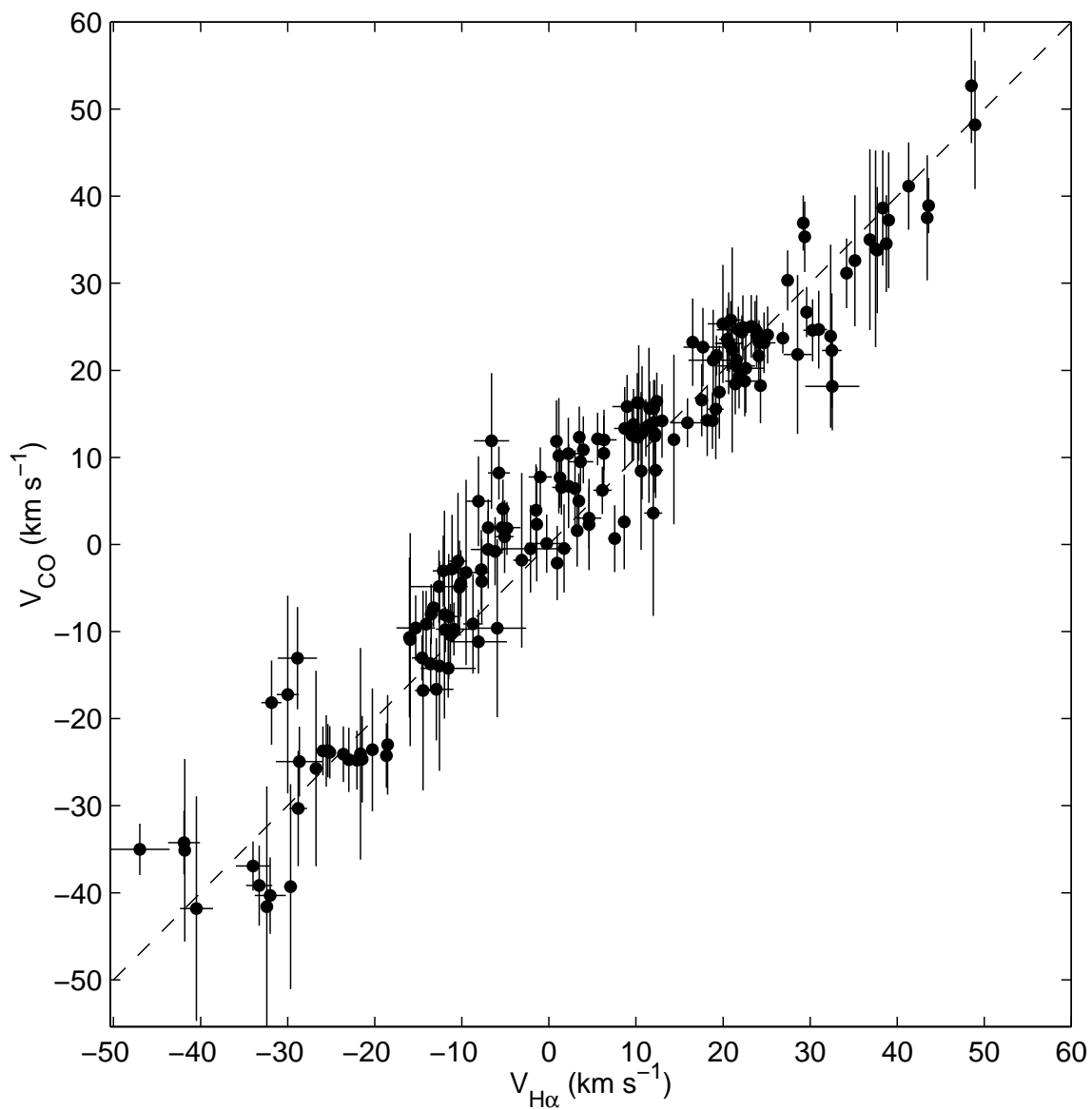
Figure 5.13 — Point-by-point comparison of Hα and CO velocities. Although the line $v_{\mathrm{H}\alpha}$ = v_{CO} provides a very good description of the data, with remarkably small scatter, there are still small systematic trends visible near the center of the galaxy and at positive velocities.

5.6.4 Simulated Long-slit Observations of NGC 2976

Our Hα dataset is well suited for studying the systematic problems associated with deriving rotation curves from long-slit spectroscopy. It is straightforward to recreate what would be seen by an observer taking long-slit spectra of NGC 2976. We begin by selecting all of the fibers within 1$''$ of a given cut parallel to the major axis of the galaxy. This creates an unevenly-sampled rotation curve, which we smooth by averaging the points into 4$''$-wide bins. We then proceed exactly as we would have if we had obtained these rotation velocities from a long-slit spectrograph. We find the center of the rotation curve by folding it about various points to determine the position of maximum symmetry. Three criteria are used to judge the degree of symmetry: the correlation coefficient of the two sides, the rms difference in velocity between points at the same radius on opposite sides, and the appearance of the rotation curve. These criteria are combined in a necessarily somewhat subjective manner, but since we know the true center in this case from our two-dimensional velocity field, we have verified that the chosen center never differs from the actual one by more than 12$''$ (200 pc). We fold the rotation curve about the chosen center and average the two sides together, weighting each point by the inverse square of its uncertainty. Finally, we fit a power law to the resulting rotation curve, ignoring any points near the center that have negative rotation velocities. We repeat this process with offsets from the major axis of up to 14$''$ (230 pc). The indices, α_{TOT}, of the power law fits in density for each rotation curve are displayed in Figure 5.14.

The naive expectation from this experiment is that slits placed off of the major axis will make the density profile appear to be shallower than it actually is, and that this effect should become more severe with increasing distance from the major axis. The actual results do not show this trend very clearly. The positive slit offsets (corresponding to the northeast side of the galaxy) appear to agree with the expected behavior; for large slit offsets the slopes are on average shallower than the value that should be derived ($\alpha_{\mathrm{TOT}} = 0.42$, since we are neglecting radial motions). Offsets on the other side of the galaxy, though, do not follow a systematic trend. The derived slopes for negative offsets are similar to the actual slope. Note that when the rotation curve is folded about the correct central position (instead of the one that gives the most symmetric appearance), the slopes are systematically shallower than when other central positions are used. We speculate that this systematic effect is not very strong in NGC 2976 because this galaxy has a relatively shallow central velocity
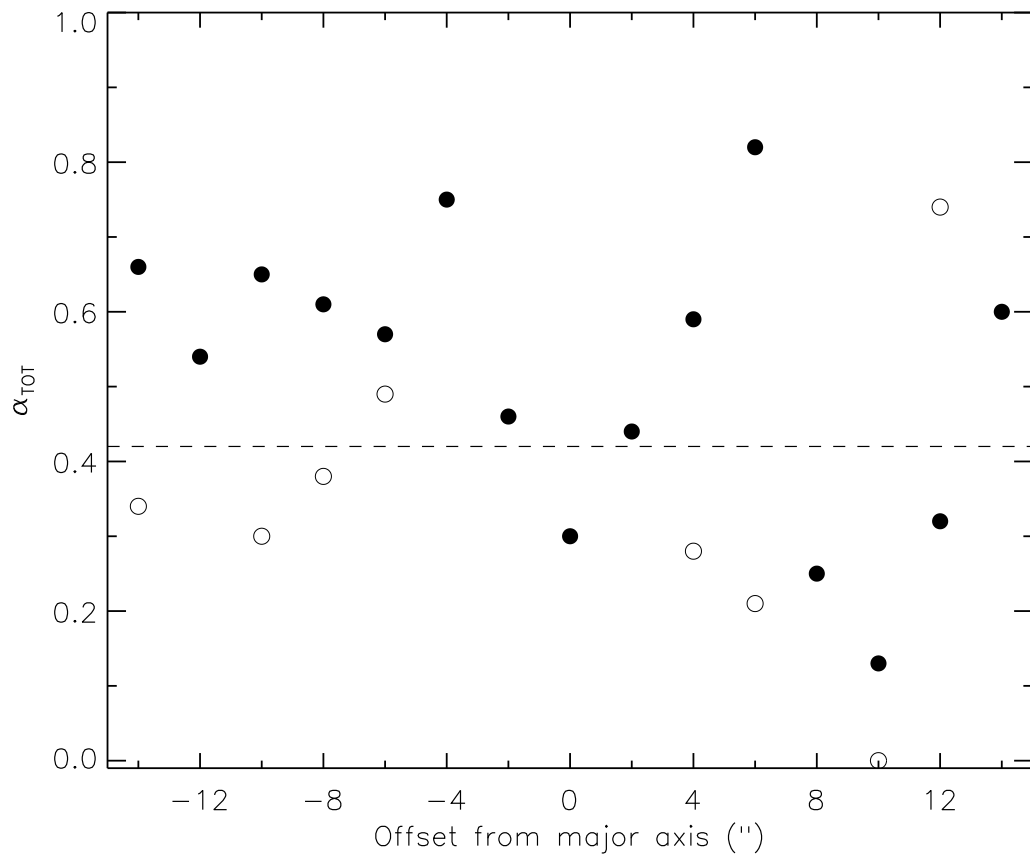
Figure 5.14 — Density profile slopes derived from simulated long-slit observations of NGC 2976. The filled circles indicate the derived value of the density profile slope α_{TOT} for each offset from the major axis. The dashed line shows the value of α_{TOT} from our analysis of the full velocity field (without radial motions, since they cannot be accounted for in long-slit observations). The open circles represent the slopes that would have been derived had the correct (closest to the actual center) folding point been selected for each of the slits. For some slits, the value of α_{TOT} is quite sensitive to the choice of the folding point. Note that the open symbol at (10,0.0) should actually be located at $\alpha_{\mathrm{TOT}} = -0.21$, except that we do not allow negative values of α_{TOT} because they are unphysical.

gradient. Other galaxies with steeper rotation curves might be affected more severely. A possible explanation for the difference between the two sides of the galaxy is that the Hα distribution is rather asymmetric; to the northeast of the major axis are a number of bright point sources, while the emission on the southwest side is faint and diffuse. In addition to coherent systematic errors, this exercise shows that attempting to derive a density profile from a single velocity cut through a galaxy is also a noisy process. Depending on the position of the slit, one could estimate a density profile between $\rho_{\mathrm{TOT}} \propto r^{-0.13}$ and $\rho_{\mathrm{TOT}} \propto r^{-0.82}$ for this galaxy. Only with observations along many slits, or full two-dimensional velocity data, can one be confident that the rotation curve and density profile of a galaxy accurately reflect its gravitational potential.

5.6.5 Positioning Errors and Slit Offsets

There are several factors that can play a role in positioning errors. First is the pointing and guiding of the telescope used to acquire the data. McGaugh et al. (2001) and de Blok & Bosma (2002) report that observations of LSB galaxies with different telescopes and instruments by independent observers result in essentially identical rotation curves. On this basis, they conclude that pointing errors do not impact their results. Telescope pointing and guiding are thus unlikely to cause problems for long-slit observations, although they can be an issue for two-dimensional observations like ours, where the galaxy may not be visible on the guiding camera while observing it (see §5.2.2 for our solution to this problem). Quite independent of the telescope pointing, though, is the question of whether the center of a given galaxy is where it is reported to be. Even when the photometric center is known accurately, galaxies can have dynamical centers that differ from the photometric ones by hundreds of parsecs (Puche, Carignan, & Wainscoat 1991; Helfer & Blitz 1995; Matthews & Gallagher 2002). Because of these two additional problems, a demonstration that pointing errors are minimal does not suffice to prove that rotation curves are systematically unaffected by offsets between their assumed and actual centers.

One example in the literature of a galaxy in which a poorly-determined center may have caused erroneous conclusions about its density profile is NGC 2552, often referred to by its alternate name of UGC 4325. The rotation curve of this dwarf LSB galaxy has been discussed in a number of recent papers (de Blok et al. 2001a; van den Bosch & Swaters 2001; de Blok & Bosma 2002; Marchesini et al. 2002; Swaters et al. 2003a; de Blok, Bosma,

& McGaugh 2003). All of these authors find density profiles with $\alpha \approx 0.3$, where α is the central slope of the density profile (see §5.4.2 or Equation B.2). With six independent analyses reaching the same conclusion, it would seem that the density profile of this galaxy is well-determined. However, closer inspection reveals a potentially important discrepancy between these studies: they assume widely varying central positions for the galaxy (see Table 5.4). Two papers (van den Bosch & Swaters 2001; Swaters et al. 2003a) measure the galaxy's center from their own photometry, while the other four make no reference to the assumed center. It is reasonable to suppose that they used the coordinates given by one of the standard databases, such as the NASA/IPAC Extragalactic Database[7] or the SIMBAD Database.[8] These different positions span a range of $11''$, or 550 pc at the distance of NGC 2552.

The reason for the uncertainty in the galaxy center is clear from inspection of a Digitized Sky Survey image: NGC 2552 is a lopsided galaxy, with a low surface brightness outer disk that is off center relative to the brighter inner disk. However, there has recently been an accurate determination of the actual position of the galaxy; Böker et al. (2003) used HST imaging to show that NGC 2552 contains a nuclear star cluster, and that this nucleus is also the center of the inner isophotes. Because galaxies can display offsets between their nuclei and their dynamical centers, it is possible that the nucleus is not located at the dynamical center of NGC 2552, but in the absence of two-dimensional kinematic information it represents the best guess. As can be seen in Table 5.4, the previously-used positions are up to $9''$ (450 pc) away from the nucleus. Based on the results of SMVB and our discussion in §5.6.4, we suggest that density profiles derived from the long-slit observations cited above could have been significantly over or underestimated. de Blok et al. (2003) argue that this is not the case because the three slit positions they used to observe NGC 2552 (one through their assumed center, and the other two $5''$ away on either side) result in similar density profiles. However, one of the three slopes that they measure ($\alpha = 0.32, \ -0.16, \ 0.30$) differs from the others by $3\,\sigma$, showing that slit offsets can cause density profiles different from the true one to be derived. Also, if none of the three slits went through the actual center of the galaxy, then further observations may be needed to ensure that the measured density profile is correct. Given this degree of confusion over the position of a relatively nearby ($d = 10$ Mpc) and high-surface brightness (for a galaxy classified as LSB; $\mu_R = 21.6$ mag

[7]http://nedwww.ipac.caltech.edu/
[8]http://simbad.u-strasbg.fr/

arcsec^{-2}) galaxy, it is certainly not obvious that the centers of fainter and more distant galaxies are well-determined in the literature.

5.6.6 Barred And Highly Inclined Galaxies

Two other common attributes of galaxies that can cause systematic errors deserve mention here: bars and high inclination angles. SMVB already discussed the problems associated with galaxies that are seen edge-on or nearly so and demonstrated that observations of such galaxies must be analyzed with extreme care. Equally problematic, though, are galaxies that contain bars. Barred galaxies certainly have noncircular motions out to the end of the bar, so one-dimensional velocity data will be systematically affected. Density profiles of barred galaxies derived from long-slit data are therefore not trustworthy at radii less than the bar semimajor axis. SMVB include five barred galaxies in their sample, and unsurprisingly find that these objects have shallower central density slopes than their other targets. The kinematics of barred galaxies are interesting in their own right; there are suggestions that the presence of a bar can affect the evolution of dark matter density cusps (Weinberg & Katz 2002), and with two-dimensional velocity fields it is possible to use barred galaxies to study dark matter density profiles (Weiner, Sellwood, & Williams 2001a; Weiner et al. 2001b). However, long-slit observations of barred galaxies may not be a reliable way to attack the density profile question.

5.7 Conclusions

We have used two-dimensional velocity fields, sampled at high spatial resolution and high spectral resolution in CO and Hα to study the density profile of NGC 2976 and the parameters of its stellar disk and dark matter halo. We obtained rotation curves from the two-dimensional data using tilted-ring models derived with three independent and complementary algorithms. Our tilted-ring fitting shows that there are significant radial (i.e., noncircular) motions in the inner 20$''$ (300 pc) of the galaxy. Accounting for these motions yields a total density profile of $\rho_{\mathrm{TOT}} \propto r^{-0.27 \pm 0.09}$. There is a narrow range of possible stellar mass-to-light ratios for NGC 2976, and the corresponding dark matter halo density profiles range from $\rho_{\mathrm{DM}} \propto r^{-0.17 \pm 0.08}$ to $\rho_{\mathrm{DM}} \propto r^{-0.01 \pm 0.13}$ (constant density). A key assumption that we make in the inversion of the rotation curve to obtain the density profile is that the gravitational and centrifugal forces are in equilibrium (or equivalently,

that the radial motions provide no support). The density profile obtained by excluding measurements inside the $20''$ radius is identical to that computed when including them, substantiating this assumption.

We found that in our preferred model, the maximum mass-to-light ratio of the stellar disk of NGC 2976 is $M_*/L_K = 0.09^{+0.15}_{-0.08}$ $M_\odot/L_{\odot,K}$. If $M_*/L_K > 0.19$ $M_\odot/L_{\odot,K}$, the dark matter halo has the unphysical property that its density increases with radius. Accounting for the thickness of the stellar disk and the asymmetric drift correction to the rotation curve brings this kinematic value of M_*/L_K into line with photometric estimates. Comparison with stellar population synthesis models (Worthey 1994; Leitherer et al. 1999; Bell & de Jong 2001) suggests that the mass-to-light ratio is unlikely to be less than 0.10 $M_\odot/L_{\odot,K}$, so the stellar disk — and hence the dark matter halo — are tightly constrained. We investigated many of the likely systematic effects on the rotation curve and found that none of them can bring the density profile close to $\rho_{\mathrm{DM}} \propto r^{-1}$. We therefore rule out an NFW or Moore et al. (1999b) density profile in the center of this galaxy at high confidence regardless of the stellar contribution.

In addition, we investigated the most extreme models of the galaxy that are allowed by the data. Density profile slopes as high as $\alpha_{\mathrm{DM}} \sim 0.7$ can be obtained, *but only when all three of the following are true:* (1) the mass-to-light ratio of the matter in the disk is zero, (2) the observed velocities are attributed entirely to rotation, despite the observed radial motions, and (3) the kinematic PA and inclination both change with radius in the manner described in §5.5.5 and §5.6.2. Retaining requirements (2) and (3), but assuming a maximal stellar disk, reduces α_{DM} to $\lesssim 0.4$. We consider these models to be quite unlikely, and inconsistent with the complementary data we have presented for this galaxy.

We also discussed whether a universal dark matter halo shape is consistent with our observations. In a similar study of the slightly more massive galaxy NGC 4605, Bolatto et al. (2002) found a lower limit to the dark matter density profile slope of $\alpha_{\mathrm{DM}} = 0.65$. Since the upper limit for NGC 2976 is $\alpha_{\mathrm{DM}} = 0.27$, the density profiles of the halos of these galaxies are different from one another. If the disk of NGC 4605 is submaximal, or the disk of NGC 2976 is not minimal (which is likely), the inconsistency becomes more severe. In addition, we note that both of these dwarf galaxies are dynamically dominated by luminous matter at small radii.

Finally, we considered the impact of some of the known systematic uncertainties that afflict rotation curve studies, following up on the recent work of SMVB and de Blok

et al. (2003). We found that *systematic errors can cause the density profiles inferred from long-slit observations to differ significantly from the true density profiles.* We also illustrated the difficulties that can arise in determining the positions of galaxy centers without adequate two-dimensional kinematic and photometric information. These problems — as well as the disk-halo degeneracy — can be largely overcome by using high-resolution two-dimensional velocity fields, as we have shown in this chapter.

Although previous studies have found that central density cusps cannot be ruled out in many dwarf and LSB galaxies, we have demonstrated that a cusp is not present in NGC 2976; the dark matter halo of this galaxy is nearly constant density out to the edge of the observed Hα emission at a radius of 2.2 kpc.

Table 5.4.　Central Positions for NGC 2552

Method of Determining Center	α (J2000.0)	δ (J2000.0)	Distance From Nucleus ['']	Reference
nucleus[a]	$08^h19^m20.4^s$	$50°00'33''$	0.0	1
outer isophotes[b]	$08^h19^m20.4^s$	$50°00'36''$	2.7	2
outer isophotes[c]	$08^h19^m19.7^s$	$50°00'32''$	6.8	3
NED	$08^h19^m20.1^s$	$50°00'25''$	8.5	4
SIMBAD	$08^h19^m19.6^s$	$50°00'28''$	9.2	5

[a]This position is also the center of the inner isophotes.

[b]Measured by Swaters (1999) from their photometry.

[c]Measured by Swaters & Balcells (2002) from their photometry.

References. — 1, Böker, Stanek, & van der Marel (2003); 2, van den Bosch & Swaters (2001); 3, Swaters et al. (2003a); 4, Falco et al. (1999); 5, Nilson (1973).

Chapter 6

High-Resolution Measurements of the Halos of Four Low-Mass Galaxies: Deviations from a Universal Density Profile

This chapter was previously published in *The Astrophysical Journal* (Simon, Bolatto, Leroy, Blitz, & Gates 2005, ApJ, 621, 757).

Abstract

We derive rotation curves for four nearby, low-mass spiral galaxies and use them to constrain the shapes of their dark matter density profiles. This analysis is based on high-resolution two-dimensional Hα velocity fields of NGC 4605, NGC 5949, NGC 5963, and NGC 6689 and CO velocity fields of NGC 4605 and NGC 5963. In combination with our previous study of NGC 2976, the full sample of five galaxies contains density profiles that span the range from $\alpha_{\mathrm{DM}} = 0$ to $\alpha_{\mathrm{DM}} = 1.20$, where α_{DM} is the power law index describing the central density profile. The scatter in α_{DM} from galaxy to galaxy is 0.44, three times as large as in Cold Dark Matter (CDM) simulations, and the mean density profile slope is $\alpha_{\mathrm{DM}} = 0.73$, shallower than that predicted by the simulations. These results call into question the hypothesis that all galaxies share a universal dark matter density profile. We

show that one of the galaxies in our sample, NGC 5963, has a cuspy density profile that closely resembles those seen in CDM simulations, demonstrating that while galaxies with the steep central density cusps predicted by CDM do exist, they are in the minority. In spite of these differences between observations and simulations, the relatively cuspy density profiles we find do not suggest that this problem represents a crisis for CDM. Improving the resolution of the simulations and incorporating additional physics may resolve the remaining discrepancies. We also find that four of the galaxies contain detectable radial motions in the plane of the galaxy. We investigate the hypothesis that these motions are caused by a triaxial dark matter halo, and place lower limits on the ellipticity of the orbits in the plane of the disk of 0.043-0.175.

6.1   Introduction

Over the last several years, one of the most persistent problems confronting the Cold Dark Matter (CDM) model has been the dichotomy between observed galaxy density profiles and those seen in cosmological simulations. The simulations generate dark matter halos with central density cusps of $\rho \propto r^{-1}$ or steeper (e.g., Navarro et al. 1996; Moore et al. 1999b). Observations of dwarf and low surface-brightness (LSB) galaxies, though, have usually shown that density profiles with shallow central cores, where the density is nearly constant with radius, fit the data better than cuspy profiles (Moore 1994; Burkert 1995; Blais-Ouellette et al. 1999, 2001; de Blok et al. 2001a; Borriello & Salucci 2001; de Blok et al. 2001b; de Blok & Bosma 2002; Salucci et al. 2003; Weldrake et al. 2003; Simon et al. 2003a; Gentile et al. 2004). This disparity is important because density profiles represent some of the strongest available constraints on the CDM simulations at small spatial scales.

Because most observational errors tend to make density profiles seem shallower than they actually are, whether this disagreement is real or only apparent has been a point of contention. Recently, van den Bosch et al. (2000) and van den Bosch & Swaters (2001) put forth the argument that most existing rotation curves have neither the spatial resolution nor the velocity resolution necessary to test the simulations adequately. Swaters et al. (2003a) extended this argument with simulations showing that even high-resolution data may be subject to numerous systematic effects that can make density profiles appear artificially shallow. However, de Blok & Bosma (2002) and de Blok et al. (2003) use observations and simulations to reach the opposite conclusion: that systematic uncertainties do not

significantly affect most observed rotation curves. In an attempt to resolve this debate, we began an effort to measure the density profiles of a sample of nearby low-mass galaxies at very high spatial and velocity resolution, using improved techniques to minimize the importance of systematic uncertainties.

In two previous papers, we reported on our results for the dwarf spiral galaxies NGC 4605 (Bolatto et al. 2002) and NGC 2976 (Simon et al. 2003a, hereafter Chapter 5). We found that NGC 2976 contains a nearly constant density core, while NGC 4605 has a density profile that is intermediate between the usually observed constant density cores and the cusps predicted by simulations. In this chapter, we present similar analyses of three more nearby galaxies, NGC 5949, NGC 5963, and NGC 6689. Since our earlier study of NGC 4605 did not include a two-dimensional Hα velocity field, which prevented us from confirming the existence of the radial motions suggested by the CO data, we also update that work with an Hα velocity field, additional CO mapping, and new optical imaging. As before, we use high-resolution two-dimensional velocity fields to constrain the overall mass distribution, and optical and near-infrared imaging to model and remove the baryonic contribution to the rotation curve.

In the following section, we describe our observations and data reduction. We briefly explain our methods of modeling stellar disks and constructing tilted-ring models of the velocity fields, and we refer the reader to Chapter 5 for additional details. In §6.3, we present the results of our rotation curve analysis and fit the rotation curves with various functional forms. In §6.4, we discuss the most important implications of this work. We consider the effect of relaxing the assumption that dark matter halos are spherical on the derived density profiles in §6.5, and we present our conclusions in §6.6.

6.2 Observations, Data Reduction, and Methodology

The primary objective of this study is to derive very accurate rotation curves (and hence density profiles) of low-mass,[1] dark matter-dominated spiral galaxies. We use two-dimensional velocity fields to measure the rotation curves in order to avoid the systematic

---

[1]We refrain from using the term *dwarf galaxy* here to avoid confusion caused by the range of definitions of the term in the literature. We instead refer to our targets as *low-mass* galaxies, by which we mean that they are significantly less massive than giant galaxies such as the Milky Way and thus can be expected to be dark matter-dominated.

problems associated with long-slit spectroscopy (Swaters et al. 2003a; Simon et al. 2003a). Where possible, we obtain velocity fields at multiple wavelengths (e.g., Hα and CO) as a further guard against systematic errors. Modeling and removing the stellar disk is an important step in the derivation of the dark matter density profile, so we use multicolor imaging to obtain the best available estimate of the stellar mass-to-light ratio.

Our target galaxies were originally selected from the CO survey of nearby dwarf galaxies by Leroy et al. (2005) in the hope that we could map the CO emission in the centers of the galaxies with the BIMA interferometer. Only three galaxies in the survey (NGC 2976, NGC 4605, and NGC 5963) contained enough CO to produce useful interferometer maps, so for the purposes of this work we also included two additional galaxies that are similar in mass (with rotation velocities of approximately 100 km s^{-1}), distance (approximately 10 Mpc), inclination, and luminosity to the CO-rich dwarfs.

6.2.1 Target Galaxies and Observations

The properties of NGC 4605 are described by Bolatto et al. (2002). This late type galaxy has an absolute magnitude of $M_B = -17.7$, and it is located 4.26 ± 0.64 Mpc away (M. Pierce 2001, private communication). While NGC 4605 is classified as a barred galaxy (SBc), detailed images do not reveal evidence for the presence of a bar.

NGC 5949 is an Sbc galaxy of similar luminosity ($M_B = -18.2$) at a larger distance. Since this galaxy was included in the Spiral Field I-band (SFI) Tully-Fisher survey, we can use the observed parameters given by Haynes et al. (1999a,b), corrected for Galactic and internal extinction and for turbulent broadening of the H I line, and the Tully-Fisher Relation determined by Giovanelli et al. (1997) to calculate a distance of 14.0 ± 2.4 Mpc.

NGC 5963 is an Sc galaxy associated with the NGC 5866 group (Fouque et al. 1992). The nearest large galaxy in the group is NGC 5907, at a projected distance of 430 kpc, so it is unlikely that NGC 5963 is currently interacting with its neighbors. It has a heliocentric recession velocity of 654 ± 3.1 km s^{-1}. There are no photometric distance determinations for this galaxy in the literature, so it is reasonable to assume that it lies at the distance of 13 Mpc implied by the Hubble flow[2] after correcting for the motion of the Local Group towards Virgo. The uncertainty on this distance is probably of order 3 Mpc.

[2]We use the *Hubble Space Telescope* Key Project value of $H_0 = 72$ km s^{-1} Mpc^{-1} (Freedman et al. 2001) for the Hubble constant.

At 13 Mpc, NGC 5963 has an absolute magnitude of $M_B = -17.8$.

NGC 6689 (also called NGC 6690) is listed as an SBcd galaxy in NED and an SBc in LEDA, but it is classified as an unbarred Sc galaxy in the UGC (Nilson 1973), and an Sd in the Third Reference Catalog of Bright Galaxies (de Vaucouleurs et al. 1991). No bar is evident in any of our optical or near-infrared images. We conclude that the conflicting classifications are due to the relatively high inclination of the galaxy, and that NGC 6689 does not contain a bar. The galaxy is rather similar to the others (but more inclined), with a distance of 11 Mpc (again using the Virgocentric-flow-corrected velocity) and an absolute magnitude of $M_B = -17.6$.

Hα Observations and Reductions

Our Hα observations were obtained on 2002 March 20–21, 2002 May 25–28, and 2003 April 15 at the 3.5 m WIYN telescope with the DensePak fiber array. See Barden et al. (1998) and Chapter 5 for details about the instrument and spectrograph setup, respectively.

We observed the galaxies at five to eleven positions, depending on the spatial extent of their Hα emission. These observations resulted in 350–650 independent velocity measurements for each galaxy. Exposure times ranged from 10 minutes to 60 minutes per position. The angular resolution of these data is $4''$, and the velocity resolution is 13 km s^{-1}.

The DensePak data were reduced as described in Chapter 5. The only significant change in the data reduction resulted from the replacement of the CuAr comparison lamp with a ThAr lamp in 2002 May. The very bright Th lines near the wavelength of Hα allowed us to improve the accuracy of the wavelength solution by about a factor of two (to ~ 0.2 km s^{-1}).

CO Observations and Reductions

Our ^{12}CO ($J = 1 \rightarrow 0$) observations of NGC 4605 and NGC 5963 were acquired using the B, C, and D configurations of the 10-element BIMA array (Welch et al. 1996) between April 2001 and March 2002. The total integration time for each galaxy was ~ 80 hours, much of which was in the most extended (B) configuration. The CO emission in NGC 4605 extends beyond the BIMA primary beam diameter of $\sim 100''$, so we constructed a mosaic of observations made at several positions along the major axis of the galaxy. (The CO observations of the central field used in this chapter are the same as those of Bolatto

et al. 2002, and the other major axis fields are from the new mosaic.) Because of the greater distance of NGC 5963, the CO emission in that galaxy is much more compact and fits easily inside the primary beam. Observational setup and data reduction were identical to that described in Chapter 5. Beam sizes and sensitivities were $5\rlap{.}''8 \times 5\rlap{.}''1$ (120×105 pc) and 24 mJy beam^{-1} for the NGC 4605 central field and $15\rlap{.}''1 \times 13\rlap{.}''4$ (312×277 pc) and 70 mJy beam^{-1} for the outlying fields of the mosaic. For NGC 5963, the beam size was $5\rlap{.}''8 \times 5\rlap{.}''3$ (370×331 pc), and the sensitivity was 31 mJy beam^{-1}. We detected CO in NGC 5949 and NGC 6689 with observations at the UASO 12 m telescope (Leroy et al. 2005), but the emission was not bright enough to map with BIMA.

Optical and Near-Infrared Imaging and Reductions

We observed NGC 4605 and NGC 5963 with B, V, R, and I filters at the 1.8 m Perkins Telescope at Lowell Observatory on 2002 February 11. NGC 5963 was also observed with much longer exposure times in B and R with the 1 m Nickel Telescope at Lick Observatory on 2003 June 23–24 in order to probe farther out into the LSB disk of the galaxy. NGC 5949 was imaged in B, V, R, and I at the Nickel on 2003 September 11, and NGC 6689 was observed in Sloan r' and i' bands with the Mosaic camera on the 4 m Mayall Telescope at Kitt Peak on 2003 October 20. All imaging took place under photometric conditions. Reduction and photometric calibration of these images followed the description of Chapter 5. To extend our set of images to the near-infrared, we used the 2MASS J, H, and K_s Atlas images of each galaxy. Three-color optical images of all four galaxies are displayed in Figure 6.1.

6.2.2 Isophotal fits and Stellar Disk Rotation Curves

We used the optical/near-IR images of these galaxies to place reasonable limits on the contributions of their stellar disks to their rotation curves. We extracted surface brightness profiles from the images with the IRAF task ELLIPSE, as described in Chapter 5. For each image of each galaxy, we ran ELLIPSE allowing the center position, position angle (PA), and ellipticity of the isophotes to vary with radius. We then defined the isophotal center of the galaxy in that band to be the weighted average of the ellipse centers. ELLIPSE was then run again with the center fixed, and we measured the weighted averages of the PA
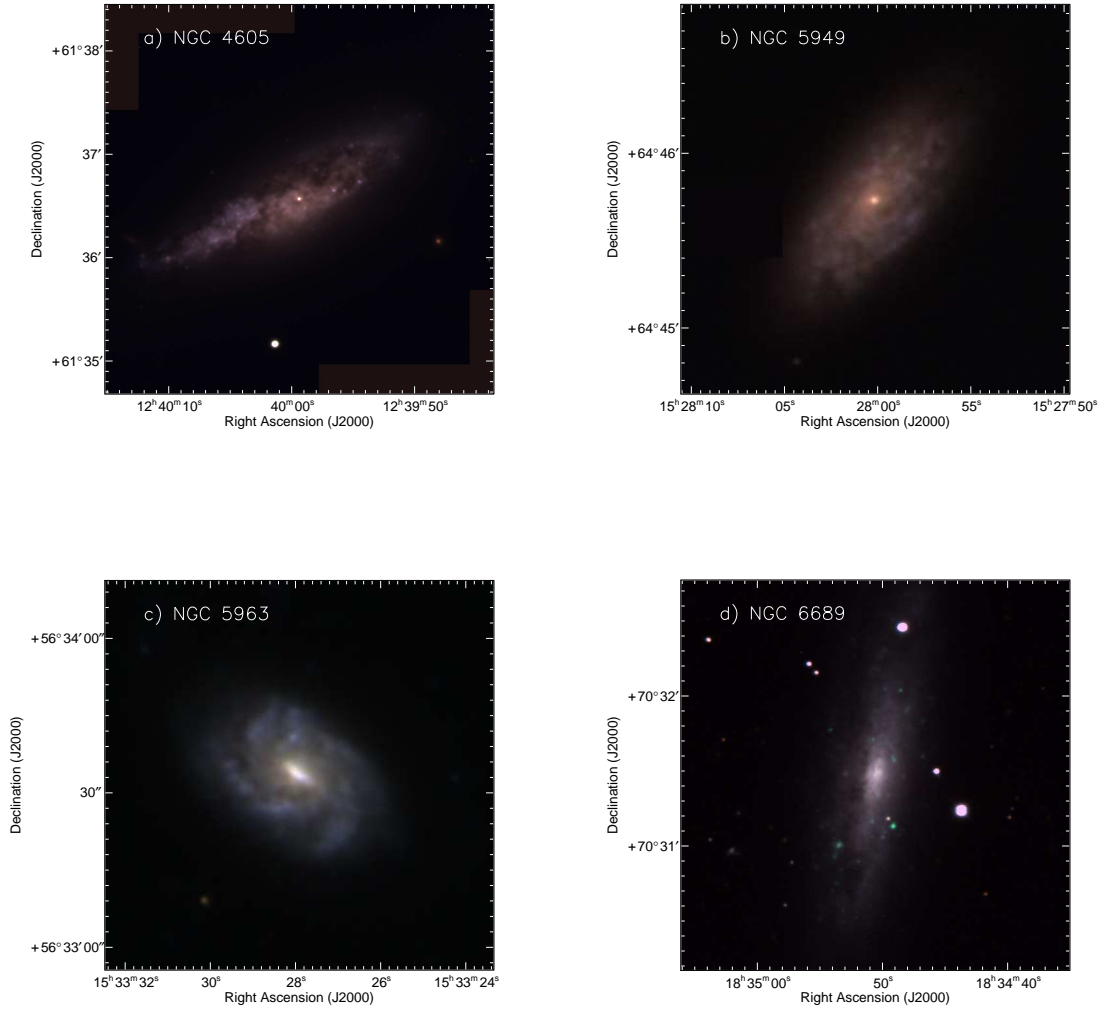
Figure 6.1 — Three-color images of our four target galaxies. Each image uses the asinh scaling recommended by Lupton et al. (2004) to retain an optimal combination of color and intensity information. (a) BVR image of NGC 4605 from Lowell Observatory. The southeast $\frac{2}{3}$ of the galaxy is clearly brighter than the remainder. (b) BVR image of NGC 5949 from Lick Observatory. The blacked-out rectangle on the east side of the galaxy is where a large dust grain on the window of the CCD dewar was not completely removed by flat-fielding. We masked out the affected area for the photometric analysis. (c) BVR image of NGC 5963 from Lowell Observatory. (d) $r'\mathrm{H}\alpha i'$ image of NGC 6689 from Kitt Peak National Observatory.

and ellipticity. We then averaged the isophotal centers,[3] position angles, and ellipticities for each galaxy in every available band to define fiducial values. In cases where a trend as a function of wavelength was noticed for any of the parameters, values for the redder bands were given preference to minimize the importance of extinction. Finally, we ran ELLIPSE one more time with all three parameters fixed in order to determine the final surface brightness profiles, which are shown in Figure 6.2. The measured isophotal parameters for each galaxy are listed in Table 6.1. Discussion of the various surface brightness profiles can be found in §6.3.5.

Bell & de Jong (2001) showed that the color and stellar mass-to-light ratio (M_*/L) of a galaxy are correlated. In order to obtain an estimate of the mass-to-light ratios of our targets, we used the observed colors and the updated color-M/L relations given by Bell et al. (2003) to compute expected R-band mass-to-light ratios. For NGC 6689, since we do not have any optical observations in the Johnson-Cousins system, we instead used the relations Bell et al. (2003) defined for the Sloan magnitude system. Measured colors and mass-to-light ratios are given in Table 6.2. Two apparent flaws in the Bell et al. (2003) models are evident from our calculations: (1) the $B - V$ and $B - R$ colors do not predict consistent R band mass-to-light ratios, and (2) the predicted K band mass-to-light ratios appear to be significantly too high.

Stellar rotation curves were calculated via numerical integration of the stellar surface mass densities (derived from the observed surface brightness profiles) using the NEMO software package (Teuben 1995). The primary assumption required by the NEMO implementation of this method is that the disks are infinitesimally thin. Removing this assumption leaves the shape of the stellar rotation curve unchanged but modestly lowers its amplitude.

6.2.3 Velocity Field Fitting

The velocity fields of the four galaxies are shown in Figure 6.3. The circles represent fiber-based Hα measurements, and the filled-in regions show CO measurements. In general, the velocity fields appear quite regular, with only NGC 4605 showing any sign that its kinematic and photometric minor axes might not be aligned.

---

[3]For the two galaxies with visually obvious nuclei (NGC 4605 and NGC 5949), we found that the isophotal centers were located quite close to the nuclei. In these cases, we fixed the ellipse centers on the nuclei instead of the formal isophotal centers.
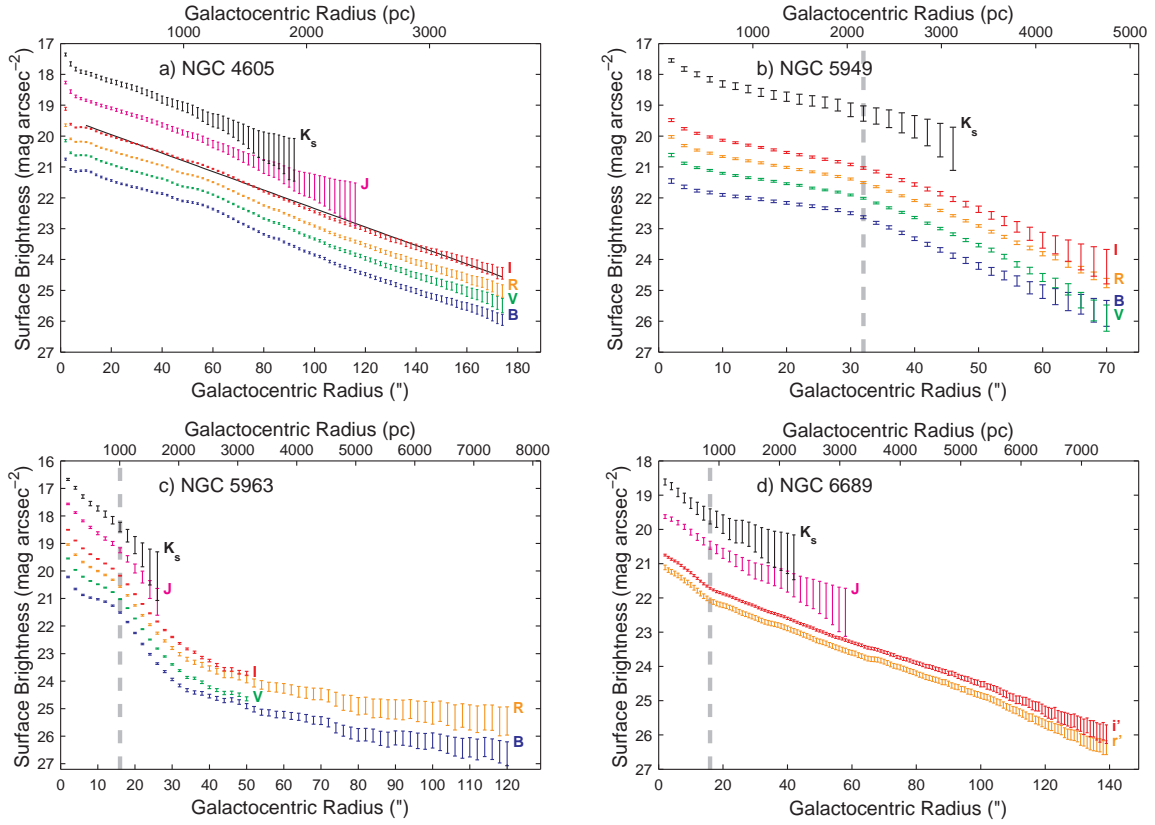
Figure 6.2 — (*a*) Optical and near-infrared surface brightness profiles of NGC 4605. In each band, the nucleus and exponential disk are visible. The black solid line represents an exponential fit to the *I*-band profile; the maximum deviation from the data is 0.13 magnitudes. (*b*) Optical and near-infrared surface brightness profiles of NGC 5949. In each band, the nucleus, exponential inner disk, and exponential outer disk are all visible. (*c*) Optical and near-infrared surface brightness profiles of NGC 5963. (*d*) Optical and near-infrared surface brightness profiles of NGC 6689. For all galaxies, the *J* and K_s data can be traced farther out, but we do not plot the data beyond where the uncertainties reach a factor of two (0.75 mag). The *H*-band profiles of each galaxy have been omitted for clarity; the error bars for *H* and K_s overlap at most radii. The vertical dashed lines in panels *(b)*, *(c)*, and *(d)* emphasize breakpoints in the profiles. The galaxies are generally well described by exponential disks, except for NGC 5963, which has an unusual and difficult to characterize surface brightness profile. We speculate that this galaxy may have evolved a dense, bulgelike central region through secular processes (a pseudobulge).

Table 6.1.   Measured Isophotal Parameters of Target Galaxies

Galaxy	α (J2000.0)	δ (J2000.0)	PA	ellipticity	inclination
NGC 4605	$12^h39^m59{.}^s27$	$61°36'33{.}''3$	$119°$	0.630	$71.5°$
NGC 5949	$15^h28^m00{.}^s69$	$64°45'47{.}''7$	$144°$	0.535	$64.6°$
NGC 5963	$15^h33^m27{.}^s90$	$56°33'35{.}''0$	$54°$	0.320	$48.4°$
NGC 6689	$18^h34^m50{.}^s18$	$70°31'27{.}''1$	$170°$	0.690	$76.0°$
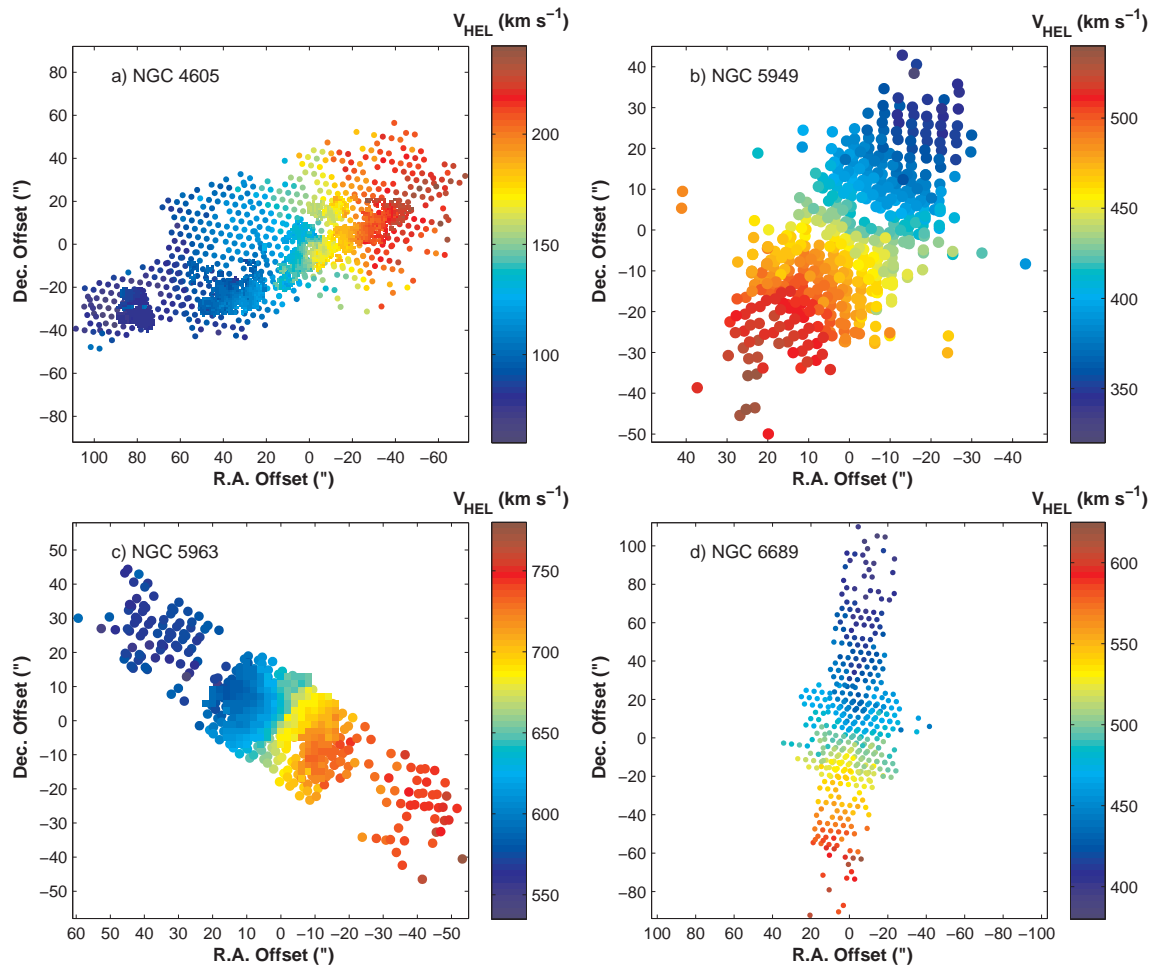
Figure 6.3 — Velocity fields of the four galaxies discussed in this chapter. (*a*) Combined Hα (circles) and CO (filled-in) velocity field of NGC 4605. (*b*) Hα velocity field of NGC 5949. (*c*) Combined Hα and CO velocity field of NGC 5963. (*d*) Hα velocity field of NGC 6689.

Table 6.2. Stellar Mass-to-Light Ratios

	Mean Inner Disk Color[a]	M_*/L_R $[\mathrm{M}_\odot/\mathrm{L}_{\odot,R}]$	M_*/L_K $[\mathrm{M}_\odot/\mathrm{L}_{\odot,K}]$
NGC 4605			
Predictions from $B-V$ color[b]	0.45[c]	0.94	0.72
Predictions from $B-R$ color[b]	0.82[c]	1.09	0.71
Observed maximum disk values		1.36	0.37
NGC 5949			
Predictions from $B-V$ color[b]	0.63[d]	1.48	0.76
Predictions from $B-R$ color[b]	1.14[d]	1.80	0.78
Observed maximum disk values		2.07	0.49
NGC 5963			
Predictions from $B-V$ color[b]	0.51[e]	1.09	0.73
Predictions from $B-R$ color[b]	0.97[e]	1.38	0.74
Observed maximum disk values		2.09	0.61
NGC 6689			
Predictions from $r'-i'$ color[b]	0.22[f]	1.96[g]	0.78
Observed maximum disk values		3.14	1.07

[a]These colors have been corrected for Galactic extinction and internal extinction. The Galactic extinction corrections were taken from Schlegel, Finkbeiner, & Davis (1998) and the internal extinction corrections were derived with the method of Sakai et al. (2000) using the axis ratios from our isophotal fits and H I velocity widths extracted from LEDA.

[b]Calculated from the relations given in Appendix A of Bell et al. (2003).

[c]NGC 4605 colors were measured for $10'' \leq r \leq 140''$.

[d]NGC 5949 colors were measured for $6'' \leq r \leq 32''$.

[e]NGC 5963 colors were measured for $8'' \leq r \leq 32''$.

[f]NGC 6689 colors were measured for $16'' \leq r \leq 138''$.

[g]Note that this mass-to-light ratio is actually calculated for the Sloan r' band, not the Kron-Cousins R band.

Comparison of Hα and CO Data

For NGC 4605 and NGC 5963, we have resolved CO velocity fields in addition to the Hα observations. To check for agreement between these different data sets, we compared the Hα and CO velocities at every position where emission is visible from both species. In the case of NGC 5963, we find a mean offset of less than 1 km s^{-1}, with a scatter of 7.8 km s^{-1}, indicating excellent agreement between the Hα and CO velocities. For NGC 4605, only the westernmost molecular cloud has a velocity that agrees exactly with the velocity of the surrounding ionized gas. Elsewhere in the galaxy there is a small but consistent offset of 4.8 km s^{-1}, in the sense that the Hα velocities are smaller. The scatter between the two velocity fields is 8.4 km s^{-1}. Nevertheless, tilted-ring models based only on the CO velocity field match Hα-only tilted-ring models quite closely, so this velocity offset does not affect our results. Velocity differences of this magnitude are expected to arise from flows of the ionized gas away from molecular clouds (Fich et al. 1982, 1990). Since the Hα and CO data appear to be both reliable and consistent with each other, the velocity field fitting described in the following section was performed on the combined velocity data for these two galaxies.

Tilted-Ring Modeling and Error Analysis

We derived rotation curves for each galaxy in the same way as in Chapter 5. Using the geometric parameters measured from the photometry (and listed in Table 1), we ran the tilted-ring modeling routine RINGFIT to extract the rotational, radial, and systemic velocities as a function of radius from the velocity fields. As detailed in Appendix A, RINGFIT is similar to the standard ROTCUR algorithm (Begeman 1987) in that it includes both rotation and radial motions in its ring fits, but it does not allow the PA, inclination angle, or center to vary from ring to ring. Next, we applied a bootstrap technique to estimate the uncertainties in the PA, center position, and inclination angle. Typical bootstrap uncertainties were 1″ in RA and Dec, 4° in PA, and 2° in inclination. For all four galaxies, we found that the kinematic and photometric values of the PA, center, and inclination angle agreed within the errors.

After running the bootstrap, we constructed Gaussian distributions of each of the geometric parameters, assuming that the full width at half maximum of the Gaussian was equal to the bootstrap uncertainty. We then created 1000 Monte Carlo realizations of each

rotation curve by randomly selecting a PA, center position, and inclination angle from the Gaussian distributions and running RINGFIT with the selected parameters as inputs. This process resulted in 1000 Monte Carlo rotation velocities at each radius. We then defined our final rotation curves to be the means of the Monte Carlo rotation velocities and the uncertainties on the rotation curves to be the standard deviations of the Monte Carlo rotation velocities. The final radial velocity curves were derived in the same manner. By incorporating the uncertainties of the PA, inclination, and center position, this technique yields more realistic rotation curve error bars than simply propagating the very small velocity uncertainties from each spectrum through the analysis. The Monte Carlo uncertainties (which we refer to as systematic uncertainties for the remainder of this chapter) are always much larger than the statistical uncertainties calculated by standard error propagation. The uncertainties we use for the remainder of the chapter are the sum in quadrature of the systematic and statistical uncertainties.

Higher Order Harmonic Fits

In addition to the standard use of RINGFIT described in the previous section, the algorithm can also be used to decompose the velocity field into Fourier components up to third order ($\sin 3\theta$ and $\cos 3\theta$). If present, these higher order terms strongly suggest the existence of a bar or other non-axisymmetric perturbation to the gravitational potential. With enough S/N, the unique signatures of a bar, spiral arms, an elliptical potential, or lopsidedness can be detected (Schoenmakers, Franx, & de Zeeuw 1997). We find weak evidence for nonzero higher order components in the velocity fields of NGC 4605, NGC 5949, and NGC 5963. Each galaxy has several adjacent rings in which the fits deviate from zero by $\sim 2\,\sigma$ (all four higher-order terms for NGC 4605, $\cos 2\theta$ and $\sin 3\theta$ for NGC 5949, and $\cos 2\theta$ and $\sin 2\theta$ for NGC 5963). Typical amplitudes of the higher order components are $2 - 5$ km s^{-1}, which should not be large enough to affect our derivation of the density profiles in the following section. Although the significance of these components does not generally exceed 2.5 σ in a given ring, we argue that these detections are probably real because (1) a number of consecutive rings have consistent Fourier amplitudes, and (2) we have probably overestimated the rotation curve uncertainties (see §6.3.3). NGC 6689 does not have enough data points in most of its rings to obtain reliable higher order fits. For comparison, we find $3 - 5$ km s^{-1} $\cos 2\theta$, $\cos 3\theta$, and $\sin 3\theta$ components over small ranges of

radii in the NGC 2976 velocity field studied in Chapter 5. Including terms up to third order in the tilted-ring models (seven free RINGFIT parameters instead of three) does significantly improve the reduced χ^2 value of the fits in many cases, but this is often because the number of data points in the ring is not much larger than seven so that the fit can go through almost every point, leaving the physical meaning of these terms open to debate. More detailed descriptions of the higher order motions in each galaxy can be found in §6.3.5.

6.3 Results

In this section we fit the rotation curves with a variety of functional forms to ascertain the shapes of the density profiles. We first consider the likely contribution of the stellar disk to the rotation curve, and then remove it from the data to reveal the rotation curve of the dark matter halo.

The rotation curves produced by the tilted-ring models in §6.2.3 are displayed in Figures $6.4a$ - $6.7a$. Radial velocity curves and the uncertainties on both the rotation velocities and the radial velocities are also plotted in the same figures.

6.3.1 Removing the Baryons

What we are actually interested in are the rotation curves of the *dark matter halos* of these galaxies, which are only equivalent to the total rotation curves shown in Figures $6.4a$ - $6.7a$ in the minimum disk scenario ($M_*/L = 0$). We therefore need to account for the contribution of the baryons to the rotation curves. An *upper limit* on the dark matter rotation curve (and also the slope of the density profile) can be found if the disk mass is zero, and a *lower limit* to the dark matter rotation curve and density profile slope is obtained for a maximum disk. In general, for galaxies of normal surface brightness, the minimum disk solution is physically unrealistic and the actual mass distribution is likely to be closer to the maximum disk case.

We used the stellar disk rotation curves calculated in §6.2.2 to construct maximum disk models.[4] In order to avoid being unduly influenced by a single unrepresen-

---

[4]With the possible exception of NGC 6689, these galaxies do not appear to contain bulges, so the stellar disk is the only baryonic component that we model. Including the gas disk as well would increase the effective mass-to-light ratio of the disk somewhat but does not affect our results (see following paragraph).
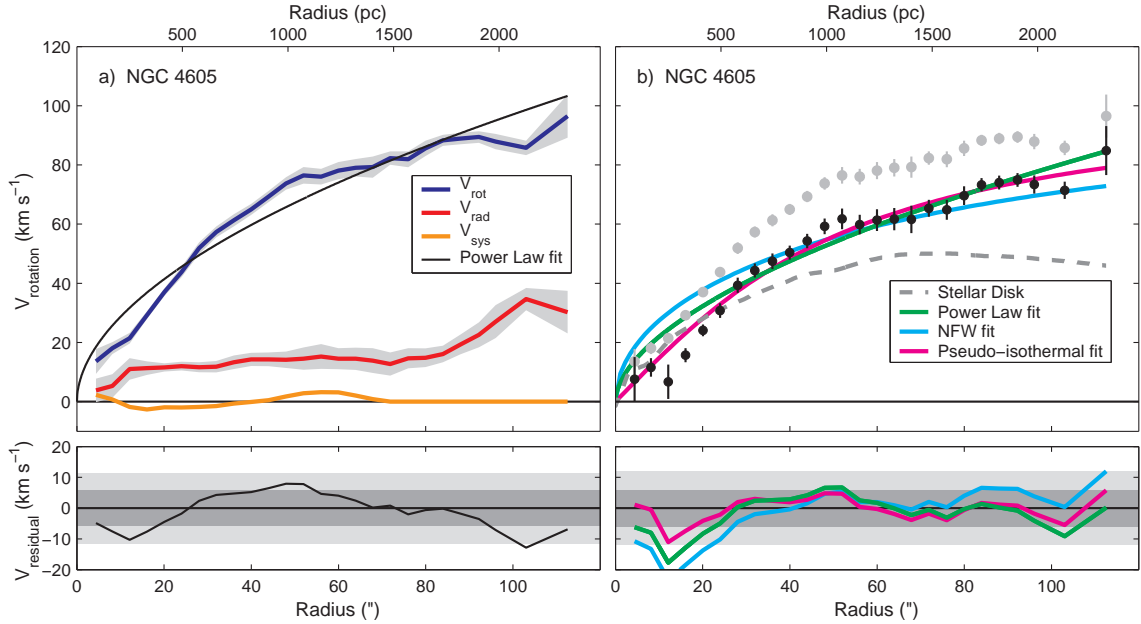
Figure 6.4 — (a) Tilted-ring model for NGC 4605. The thick blue curve represents the rotation curve, and the thick red and orange curves show the radial velocity curve and the systemic velocities, respectively. Starting at a radius of 72″ the systemic velocities were held fixed at zero. The shaded gray regions surrounding the rotation and radial velocity curves represent the combined systematic and statistical $1\,\sigma$ uncertainties from the bootstrap and Monte Carlo analysis. Note that for convenience we have plotted the radial velocities as positive; this choice does not indicate whether the radial motions are directed inwards or outwards. The thin black curve is a power law fit to the rotation curve. The residuals from this fit are plotted in the lower panel, and the $1\,\sigma$ and $2\,\sigma$ scatter of the data points around the fit is shown by the shaded gray areas. (b) Disk-subtracted rotation curve of NGC 4605. The gray points are the original rotation velocities from panel (a), and the black points are the dark matter halo rotation curve after subtracting the stellar disk ($M_*/L_R = 1.01\ \mathrm{M_\odot/L_{\odot,R}}$), which is shown as a gray dashed line. The thick green, cyan, and magenta curves show power law, NFW, and pseudo-isothermal fits to the halo rotation curve, respectively. The residuals from these fits are displayed in the lower panel, and the $1\,\sigma$ and $2\,\sigma$ scatter of the data points around the power law fit is shown by the shaded gray areas.
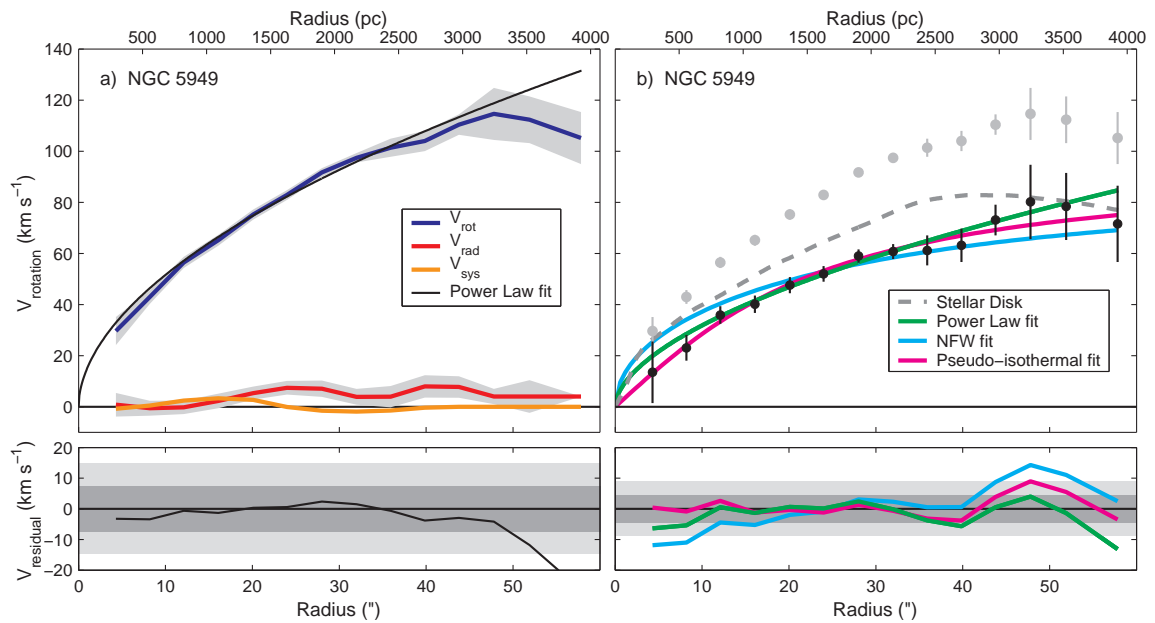
Figure 6.5 — (*a*) Tilted-ring model for NGC 5949. (*b*) Disk-subtracted rotation curve of NGC 5949 (for $M_*/L_R = 1.64$ $M_\odot/L_{\odot,R}$). Symbols, colors, and shading are as in Figure 6.4.
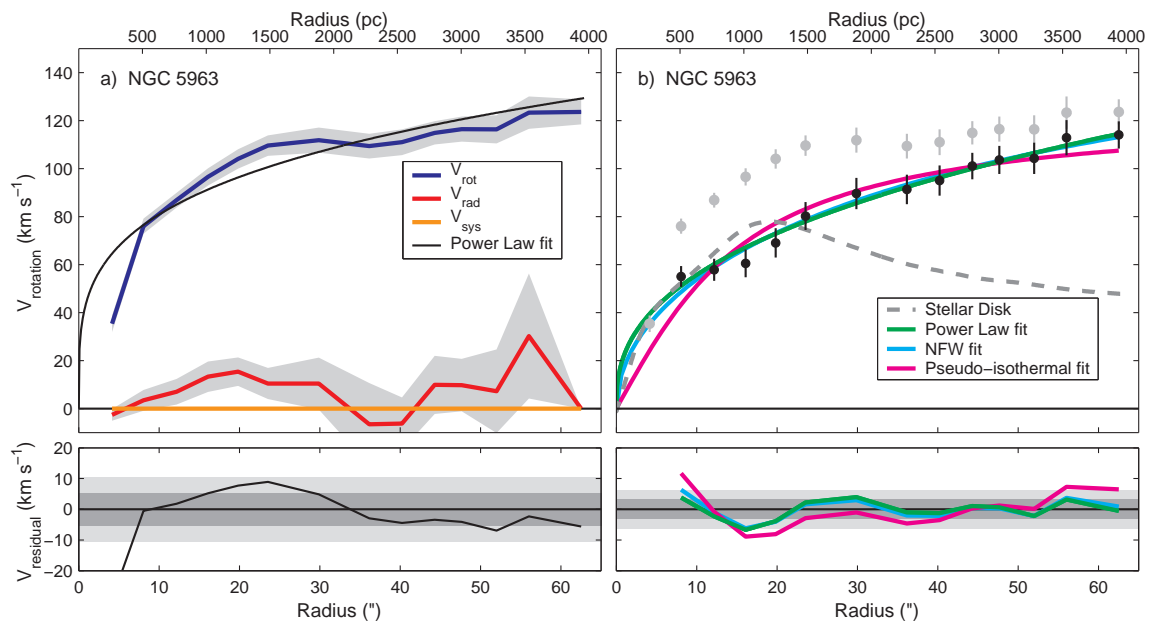
Figure 6.6 — (*a*) Tilted-ring model for NGC 5963. (*b*) Disk-subtracted rotation curve of NGC 5963 (for $M_*/L_R = 1.24$ $M_\odot/L_{\odot,R}$). Symbols, colors, and shading are as in Figure 6.4.

tative point in any of the observed rotation curves, we fit the inner five points of each rotation curve with a smooth function (a power law). We then incrementally increased the stellar mass-to-light ratio (the stellar rotation curve scales as $v_{*,rot} \propto \sqrt{M_*/L}$) until the stellar rotation curve exceeded the fit to the observed points. Because of the clear impact of the nucleus on the stellar rotation curve of NGC 4605, we ignored the innermost point of the fit to the observed rotation curve for that galaxy. With this procedure we defined the following maximum disk mass-to-light ratios: $M_*/L_R = 1.36$ M$_\odot$/L$_{\odot,R}$ (NGC 4605), $M_*/L_R = 2.07$ M$_\odot$/L$_{\odot,R}$ (NGC 5949), $M_*/L_R = 2.09$ M$_\odot$/L$_{\odot,R}$ (NGC 5963), and $M_*/L_{r'} = 3.14$ M$_\odot$/L$_{\odot,r'}$ (NGC 6689). Typical uncertainties on these values are $\sim 15\%$. For all of the galaxies, these kinematic mass-to-light ratios are significantly higher than the mass-to-light ratios predicted from the galaxy colors by the Bell et al. (2003) population synthesis models (see Table 6.2). We conclude that the disks of these galaxies are probably somewhat submaximal. For the remainder of this chapter, we adopt the following mass-to-light ratios (the average predicted from the $B - V$ and $B - R$ colors shown in Table 6.2): $M_*/L_R = 1.01$ M$_\odot$/L$_{\odot,R}$ (NGC 4605), $M_*/L_R = 1.64$ M$_\odot$/L$_{\odot,R}$ (NGC 5949), $M_*/L_R = 1.24$ M$_\odot$/L$_{\odot,R}$ (NGC 5963), and $M_*/L_{r'} = 1.96$ M$_\odot$/L$_{\odot,r'}$ (NGC 6689).

Note that since we do not have H I data, we are neglecting the contribution of the gas to the rotation curve in this analysis. In galaxies the size of our targets, however, the stellar disk almost always contributes significantly more mass at the center of the galaxy than the gas does, and the effect of including the gas is similar to a 20% change in the stellar mass-to-light ratio (Bolatto et al. 2002, Chapter 5). If we arbitrarily increase M_*/L to simulate this effect, the slope of the dark matter density profile decreases by $2 - 12\%$. Allowing the stellar disk to have a nonzero thickness (see §6.2.2) would offset this decrease.

6.3.2   Power Law Density Profile Fits

We can now consider the central density profile slopes of the dark matter halos of each galaxy. Following the notation of Chapter 5, we parameterize the rotation curve by $v_{rot} \propto r^{(2-\alpha_{\mathrm{DM}})/2}$, which corresponds to a power law density profile: $\rho_{\mathrm{DM}} \propto r^{-\alpha_{\mathrm{DM}}}$. Allowing the stellar mass-to-light ratios to vary from zero up to the maximum disk values determined in the previous paragraph, the limits we place on α_{DM} are given in Table 6.3. Obviously, the impact of changing the mass-to-light ratio on the density profiles is minimal for NGC 4605 and NGC 5949. These galaxies have very similar dark matter density

profiles in the maximum and minimum disk cases, so their density profile slopes are tightly constrained.

The rotation curve fits for these limiting cases are displayed in Figures 6.4 - 6.7. In the left panel of each figure, a minimum disk power law fit is displayed, with the residuals from the fit in the lower panel. The right panel of each figure contains a power law fit to the dark matter halo in the maximum disk case, again with residuals shown in the lower panel. In all cases, a power law provides a reasonable fit to the rotation curve at least out to the radius at which the rotation curve begins to flatten significantly (at which point the density profile slope is obviously changing with radius and a single power law cannot be expected to accurately represent the rotation curve). The numerical parameters of the power law fits for the disk-subtracted rotation curves are listed in Table 6.4 and those for the total rotation curves (with no disk subtraction) in Table 6.5. The dark matter density profile slopes we derive after subtracting the stellar disks are $\alpha_{\mathrm{DM}} = [0.78,\ 0.88,\ 1.20,\ 0.79]$ for NGC 4605, NGC 5949, NGC 5963, and NGC 6689, respectively. If we fit the velocity fields without allowing radial motions, we find density profile slopes of $\alpha_{\mathrm{DM}} = [0.64,\ 0.98,\ 1.19,\ 0.79]$. These changes are small (comparable to or less than the $1\ \sigma$ uncertainties) and go in different directions for different galaxies. We conclude that including radial motions in our tilted-ring models does not systematically affect the density profile slopes we derive.

Table 6.3.   Limits on Dark Matter Density Profile Slopes

Galaxy	maximum disk α_{DM}	minimum disk α_{DM}
NGC 2976	0.01 ± 0.13	0.27 ± 0.09
NGC 4605	0.71 ± 0.06	0.90 ± 0.02
NGC 5949	0.79 ± 0.17	0.93 ± 0.04
NGC 5963	0.75 ± 0.10	1.41 ± 0.03
NGC 6689	0.43 ± 0.18	1.07 ± 0.06
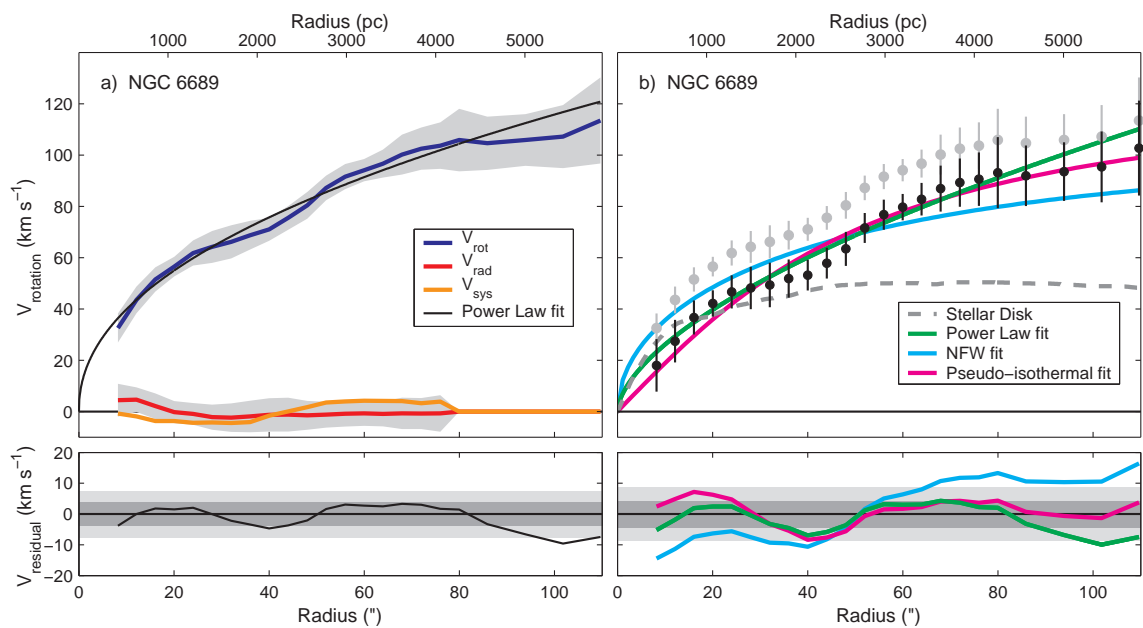
Figure 6.7 — (*a*) Tilted-ring model for NGC 6689. (*b*) Disk-subtracted rotation curve of NGC 6689 (for $M_*/L_{r'} = 1.96$ M$_\odot$/L$_{\odot,r'}$). Symbols, colors, and shading are as in Figure 6.4.

Table 6.4. Rotation Curve Fit Results After Disk Subtraction

Galaxy	Power law fit parameters		NFW fit parameters				Pseudo-isothermal fit parameters					
	V_0 [km s^{-1}]	α	r_s [kpc]	R_{200} [kpc]	c	V_{200} [km s^{-1}]	ρ_0 [g cm^{-3}]	R_c [kpc]	χ^2_{pl} [d]	χ^2_{NFW} [d]	χ^2_{iso} [d]	$\chi^2_{mod\_iso}$ [d]
NGC 2976[a]	43.0	0.01	... [b]	... [b]	... [b]	... [b]	7.7×10^{-24}	2.5	0.27	> 5.8	0.43	1.00
NGC 4605	51.4	0.78	> 5.00	> 91	< 18.3	> 65	2.0×10^{-23}	0.8	3.74	< 8.03	1.53	2.88
NGC 5949	39.3	0.88	> 6.40	> 87	< 13.6	> 62	7.8×10^{-24}	1.2	0.38	< 1.24	0.24	0.27
NGC 5963	66.4	1.20	10.8	160.9	14.9	114.3	3.4×10^{-23}	0.8	0.34	0.43	1.36	0.64
NGC 5963[c]	74.5	1.50	6.71	127.7	19.0	90.7	2.7×10^{-23}	0.9	2.19	0.42	0.98	0.57
NGC 6689	37.8	0.79	> 8.7	> 108.8	< 12.5	> 77	4.8×10^{-24}	2.1	0.30	< 1.31	0.46	0.30

[a]Using data from Chapter 5.

[b]No meaningful NFW fits could be made for NGC 2976, even with only one parameter free. The "best" fit had $\chi^2_{red} = 5.8$.

[c]Using the rotation curve presented in this chapter plus the rotation velocities measured by Bosma, Athanassoula, & van der Hulst (1988) at $55'' \leq r \leq 165''$.

[d]All χ^2 values listed here actually represent the reduced χ^2 (χ^2 per degree of freedom in the fits).

Table 6.5. Rotation Curve Fit Results With No Disk Subtraction

Galaxy	Power law fit parameters		NFW fit parameters				Pseudo-isothermal fit parameters					
	V_0 [km s^{-1}]	α	r_s [kpc]	R_{200} [kpc]	c	V_{200} [km s^{-1}]	ρ_0 [g cm^{-3}]	R_c [kpc]	χ^2_{pl}[d]	χ^2_{NFW}[d]	χ^2_{iso}[d]	$\chi^2_{mod\_iso}$[d]
NGC 2976[a]	52.1	0.27	... [b]	... [b]	... [b]	... [b]	1.3×10^{-23}	1.5	0.33	> 5.8	0.48	0.93
NGC 4605	65.0	0.89	> 42.0	> 347	< 8.3	> 246	4.0×10^{-23}	0.7	8.28	< 9.28	1.53	4.92
NGC 5949	63.3	0.93	> 38.0	> 325	< 8.6	> 231	2.2×10^{-23}	1.1	1.50	< 2.00	1.00	0.64
NGC 5963	87.8	1.41	2.86	102.7	35.9	72.9	1.3×10^{-22}	0.4	6.88	3.57	1.22	3.04
NGC 5963[c]	89.5	1.62	3.42	109.9	32.1	78.0	1.2×10^{-22}	0.4	6.52	2.64	1.07	1.82
NGC 6689	53.1	1.07	41.5	286.7	6.9	203.6	1.4×10^{-23}	1.1	0.32	0.31	0.95	0.42

[a]Using data from Chapter 5.

[b]No meaningful NFW fits could be made for NGC 2976, even with only one parameter free. The "best" fit had $\chi^2_{red} = 5.8$.

[c]Using the rotation curve presented in this chapter plus the rotation velocities measured by Bosma et al. (1988) at $55'' \leq r \leq 165''$.

[d]All χ^2 values listed here actually represent the reduced χ^2 (χ^2 per degree of freedom in the fits).

6.3.3 Alternative Density Profile Fits

In order to obtain a more complete understanding of the allowed shapes of the inner density profiles of the galaxies in our sample, we also fit the rotation curves with several other functional forms. The two most commonly used profiles in the literature are the pseudo-isothermal profile (an isothermal sphere with a central core) and the NFW profile.[5] The functional form for the pseudo-isothermal density profile is

$$\rho(r) = \frac{\rho_0}{1 + (r/r_c)^2}, \tag{6.1}$$

where ρ_0 is the central density and r_c is the core radius (e.g., Kent 1986).

Since pseudo-isothermal density profiles are not expected on theoretical grounds, and there is little observational support for NFW profiles, it is important not to limit ourselves to only these possibilities. Fitting the data with other density profiles can help to elucidate the physical meaning of the fits. We therefore also used a profile that we defined to have characteristics intermediate between those of the pseudo-isothermal and NFW profiles:

$$\rho(r) = \frac{\rho_c}{(r/r_c)^{1/2}(1 + r/r_c)^{3/2}} , \tag{6.2}$$

where r_c and ρ_c are the characteristic radius and density, respectively. The inner slope of this profile is $\alpha = 0.5$, giving it a shallow inner cusp. At large radii the slope is $\alpha = 2$ (corresponding to a flat rotation curve), so the fact that our observations only just reach the flat part of the rotation curve should not adversely affect the fits. Note that the χ^2 values for fits to this function are given in Tables 6.4 and 6.5 even though we do not list r_c and ρ_c for each galaxy.

We used a χ^2-minimization routine to find the best fit parameters for each of these functions. With the exception of NGC 4605, in which small-scale bumps and wiggles in the rotation curve inflate χ^2, typical reduced χ^2 values for the best fits were ≈ 0.3, suggesting that the systematic uncertainties on our rotation curves have been overestimated by a factor of about 1.7. A. Dutton (2003, private communication) similarly inferred that our rotation curve error bars for NGC 2976 were overestimated, indicating that the bootstrap and Monte Carlo analysis described in §6.2.3 may be excessively conservative.

The results of these fits after removing the contribution of the stellar disk of each galaxy are summarized in Table 6.4, and fits without removing the stellar disk rotation

---

[5]For our NFW fits, we chose the scale radius r_s and the virial radius r_{200} to be the two free parameters.

velocities are given in Table 6.5. The best power law, NFW, and pseudo-isothermal fits (after subtracting the stellar disk) are displayed in Figures 6.4b - 6.7b by the green, cyan, and magenta curves, respectively. Residuals from each fit are shown in the same colors in the lower right panels of each figure.

With the exception of NGC 5963 (and NGC 6689 in the minimum disk case), we were unable to obtain reasonable NFW fits to the rotation curves. Since our data generally do not extend well into the flat part of the rotation curve, r_s and r_{200} are highly covariant. To prevent both parameters from running away to unphysically large values for NGC 4605, NGC 5949, and NGC 6689, we held r_s fixed and only fit for r_{200}. An infinite number of such fits are possible, with χ^2 decreasing as r_s and r_{200} increase. The NFW fits listed in Tables 6.4 and 6.5 are for r_s values chosen to keep χ^2 low ($\Delta\chi^2 \approx 1$ relative to the best fitting power law) without allowing r_{200} to become completely unreasonable.

Fit Results

NGC 5963, strikingly, is best fit by a very steep ($\alpha_{\mathrm{DM}} > 1$) power law or an NFW profile unless its stellar mass-to-light ratio is unrealistically high. The formal best fit for NGC 4605 is a pseudo-isothermal profile, although none of the profiles have good χ^2 values. The best power law (which does not describe the full rotation curve very accurately) still has a relatively steep slope. NGC 5949 is also best fit by a pseudo-isothermal density profile, but power laws with slopes slightly shallower than NFW, and the modified pseudo-isothermal profile given in Equation 6.2, fit very well. NGC 6689 is better described by a power law than by a pseudo-isothermal profile and, in the case of a low stellar M/L, can even be fit by an NFW profile, although the scale radius and virial velocity suggested by the NFW fit are unrealistically large. For every galaxy except NGC 4605, Equation 6.2 (the modified pseudo-isothermal profile with a shallow central cusp) provides fits that are comparable to or better than the pseudo-isothermal profile.

Navarro et al. (2004) Density Profile

In addition to the profiles described above, we also fit the rotation curves (after removing the stellar disks) with the new density profile proposed by Navarro et al. (2004):

$$\rho_\eta(r) = \rho_{-2} e^{-\frac{2}{\eta}\left[\left(\frac{r}{r_{-2}}\right)^\eta - 1\right]}, \tag{6.3}$$

where ρ_{-2} and r_{-2} are the density and radius at which the logarithmic density profile slope

equals -2 and η is an additional free parameter[6] that controls how fast the density profile slope changes with radius. The rotation curve associated with this density profile is

$$V(R) = \left[\frac{4\pi G \rho_{-2} e^{\frac{2}{\eta}}}{R\eta} \left(\frac{2}{\eta r_{-2}^{\eta}} \right)^{-\frac{3}{\eta}} \Gamma\left(\frac{3}{\eta}\right) \gamma\left(\frac{3}{\eta}, \frac{2}{\eta}\left[\frac{R}{r_{-2}}\right]^{\eta}\right) \right]^{1/2}, \qquad (6.4)$$

where $\gamma(a, x)$ is the lower incomplete gamma function. With the extra free parameter afforded by this function, we are able to achieve very good fits to the rotation curves of all five of our targets. In Table 6.6 we present the results of these fits and compare them to the fits Navarro et al. (2004) performed to four simulated dwarf galaxies that have total masses similar to our targets. Only for NGC 5963 are the fit parameters we derive remotely close to those measured by Navarro et al. (2004) in their simulations.

6.3.4 Comparison to Previously Published Rotation Curve Data

In the remainder of this section, we discuss details of our analysis of each galaxy. Readers who are primarily interested in the more general results of our work may wish to skip to §6.4.

Each of the four galaxies we observed have existing Hα or H I rotation curve data in the literature. Our new data should improve on previous measurements in velocity resolution, control of systematics, angular resolution (in the case of H I measurements), and sensitivity, but it is useful as a first-order test of the accuracy of our data to compare the rotation curves we obtain with previous measurements.

NGC 4605 has been the subject of several rotation curve studies (Rubin, Thonnard, & Ford 1980; Sofue et al. 1998; Bolatto et al. 2002). All three of those studies derived very similar rotation curve shapes and amplitudes. While our methodology is different from that employed by the previous authors (we do not produce separate fits for the approaching and receding sides of the galaxy), our results are qualitatively in agreement. In particular, the break in the rotation curve at a radius of $40''$ is quite apparent in the two recent data sets (the Rubin et al. 1980 rotation curve does not have enough angular resolution), and the maximum rotation velocities match well. The primary quantitative discrepancy is the result of the incorrect plate scale assumed by Bolatto et al. (2002) for the Hα spectrum they obtained. In that paper, we used a value of 3.0 arcsec pixel^{-1}, but subsequent measurements

---

[6]Navarro et al. (2004) use α instead of η, but since we have defined α to be the slope of a power-law density profile, we adopt a different symbol here for clarity.

Table 6.6. Navarro et al. (2004) Profile Fit Results

Name	r_{-2} [kpc]	ρ_{-2} [g cm^{-3}]	η	χ^{2a}
		Galaxies		
NGC 2976[b]	1.65	5.6×10^{-24}	8.99	0.26
NGC 4605	1.34	5.8×10^{-24}	1.84	1.37
NGC 5949	3.85	7.5×10^{-25}	0.67	0.25
NGC 5963	6.44	6.0×10^{-25}	0.28	0.62[c]
NGC 5963[d]	6.04	6.4×10^{-25}	0.28	0.43
NGC 6689	3325[f]	1.3×10^{-28f}	0.12	0.31
		Simulated Halos		
D1[e]	4.55	1.1×10^{-25}	0.164	$\cdots$
D2[e]	4.28	1.5×10^{-25}	0.211	$\cdots$
D3[e]	3.62	1.5×10^{-25}	0.122	$\cdots$
D4[e]	3.62	2.1×10^{-25}	0.166	$\cdots$

[a]χ^2 values listed here actually represent the reduced χ^2 (χ^2 per degree of freedom in the fits)

[b]Using data from Chapter 5.

[c]The three-parameter fit using only our data for NGC 5963 is degenerate. Better χ^2 values than shown here can be achieved, but only when r_{-2} and ρ_{-2} run away to unrealistic values. We therefore fixed η to the value obtained when the Bosma et al. (1988) data are included as well (see the following line of this table) and ran the fit with only two free parameters.

[d]Using the rotation curve presented in this chapter plus the rotation velocities measured by Bosma et al. (1988) at $55'' \leq r \leq 165''$.

[e]Simulated dwarf galaxy halo from Navarro et al. (2004).

[f]The fit values for NC 6689 are clearly completely unrealistic, and are included as an illustration of the r_{-2} and ρ_{-2} values that are necessary to achieve a value of η that is similar to the simulations.

showed that the actual plate scale is 2.1 arcsec pixel^{-1}. Correcting this error reduces the extent of the Hα rotation curve by 30%, but should not substantially change the power law indices measured for the rotation curve and density profile. Indeed, our new rotation curve matches the old one near the center of the galaxy ($r < 10''$) and at large radii ($r > 65''$). From $10''$ to $30''$ our rotation curve is a few km s^{-1} lower than the old one, and from $30''$ to $65''$ our rotation curve exceeds the old one by $1 - 6$ km s^{-1}. The net effect of these changes[7] is to modestly steepen the maximum disk density profile from $\rho_{\mathrm{DM}} \propto r^{-0.65}$ (Bolatto et al. 2002) to $\rho_{\mathrm{DM}} \propto r^{-0.88}$. Given typical uncertainties on α_{DM} of 0.1 in our analysis (Chapter 5), these results are marginally consistent. The earlier study by Persic & Salucci (1990) found a density profile of $\rho \propto r^{-0.68}$, also consistent with our results. The best fitting power law rotation curve at large radii still overestimates the rotation velocities in the inner region of the galaxy, as seen in Bolatto et al. (2002) and Figure 6.4a.

The rotation curve of NGC 5949 has previously been measured by Karachentsev & Petit (1990) and Courteau (1997) with long-slit spectra. The Karachentsev & Petit data are consistent with the rotation curve we derive, although our rotation velocities are somewhat larger and our measurements extend to larger radii. Our rotation curve matches that of Courteau within the uncertainties of the data.

The kinematics of NGC 5963 have been investigated in detail in two previous papers (Romanishin, Strom, & Strom 1982; Bosma, Athanassoula, & van der Hulst 1988). The shape of the Hα rotation curve measured by Romanishin et al. (1982) is very similar to the shape of our rotation curve; the amplitude they derive is slightly larger (with an asymptotic rotation velocity of 131 km s^{-1}), but this appears to be the result of the smaller inclination angle they used. The H I rotation curve presented by Bosma et al. (1988) is perfectly consistent with our rotation curve over the common range of radii, except that the inner two points of their rotation curve are affected by beam smearing. For the fits presented in Tables 6.4 – 6.6, we give results for both our data alone, and our data with the Bosma et al. (1988) points at large radii added.

The Hα velocity field of NGC 6689 was observed by the GHASP survey (Garrido

---

[7]Note that the stellar disk we use is not the same as that of Bolatto et al. (2002). Bolatto et al. calculated the stellar rotation curve for an exponential disk and we use the actual surface brightness profile to determine the stellar rotation curve. Although the resulting stellar disks are not quite identical, the differences do not significantly affect the density profile results.

et al. 2003). Those authors found a decidedly asymmetric rotation curve, but the filter they used for the observations may have cut off the emission line profiles on the approaching side of the galaxy. The receding side of the rotation curve presented by Garrido et al. (2003) is consistent with the overall rotation curve we derive out to a radius of $45''$, but at larger radii our rotation curve shows significantly smaller rotation velocities.

6.3.5 Comments on Individual Galaxies

NGC 4605

Of our four target galaxies, NGC 4605 is the only one that appears to deviate significantly from axisymmetry. The non-axisymmetric structures are visible both photometrically and kinematically. In broadband optical images, the galaxy contains a pronounced elongated region that is offset from its nucleus to the east. This feature, which has a somewhat higher ellipticity and a different position angle than the rest of the galaxy, persists out to K-band although it weakens with increasing wavelength. In Figure 6.8, we plot the isophotal fit parameters as a function of radius (where we now allow the isophotal center, PA, and ellipticity to vary from ring to ring), and the impact of the asymmetry is easily visible out to a radius of $70''$. Since this lopsidedness is also apparent in our Hα image (the galaxy's Hα emission extends to twice as large a radius on its eastern side as on the western side) and CO map, it may be associated with recent star formation.

The kinematic effects of this asymmetry are twofold: (1) the kinematic center of the galaxy is offset from the nucleus, and (2) the galaxy contains relatively large (and significant) noncircular motions. Tilted-ring models of the galaxy centered on the nucleus result in a systematic trend of the systemic velocity with radius. Moving the center position around so as to remove this trend and simultaneously minimize the scatter of the systemic velocities about their mean value, we found that the preferred kinematic center is southeast of the nucleus by $10''$ (206 pc). Offsets of the kinematic center of this magnitude do not significantly change the slope of the density profile that we derive. Irrespective of the center position, the models also show a clear detection of radial motions in NGC 4605. The amplitude of these motions increases to 8 km s^{-1} at a radius of $20''$ and then stays constant out to $80''$. At larger radii (the outermost six rings) the radial motions begin to increase again, reaching 20 km s^{-1} at the edge of the galaxy ($r = 113''$). However, this increase is not very well constrained due to the poor angular coverage of the velocity data at large
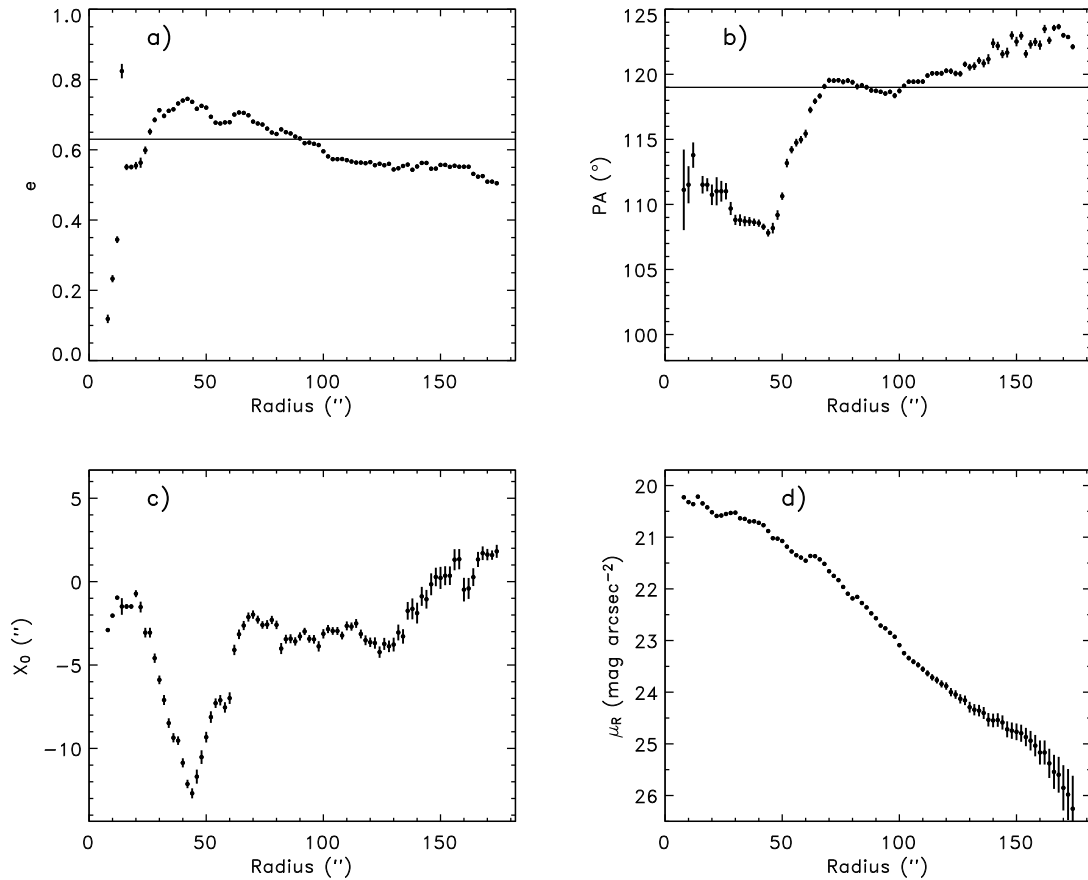
Figure 6.8 — R-band isophotal fit parameters for NGC 4605 with the ellipticity, PA, and center left free to vary. (a) Isophotal ellipticity as a function of radius. The peak at $r = 30 - 40''$ is due to the asymmetric structure of the galaxy. Note the corresponding features in panels (b) and (c). The horizontal line shows the mean value used in our analysis. (b) Isophotal position angle as a function of radius. The horizontal line shows the mean value used in our analysis. (c) Isophotal center position along the x (right ascension) axis of the image, in arcseconds. The position of the nucleus corresponds to $X_0 = 0$, which coincides with the center of the outermost isophotes. The center position along the y (declination) axis shows almost identical behavior, but with smaller amplitude because the asymmetric structure is located mostly east of the galaxy center. (d) Surface brightness as a function of radius, using the parameters shown in the other panels. Note that since our final isophotal fits did not allow the parameters to vary with radius, this surface brightness profile differs slightly from the one used to derive the stellar disk rotation curve (Figure 6.2a).

radii. Unsurprisingly, we find small $(2-6 \text{ km s}^{-1})$ but consistently nonzero $\cos 2\theta$, $\sin 2\theta$, $\cos 3\theta$, and $\sin 3\theta$ terms in the velocity field of NGC 4605 at various ranges of radii between $16''$ and $68''$.

The combination of photometric and kinematic lopsidedness suggests that the mass distribution of the galaxy indeed is lopsided, as opposed to the possibility of asymmetric star formation mentioned earlier. Despite the lopsidedness of NGC 4605, the stellar disk is described well by an exponential profile, as shown in Figure 6.2a.

In order to determine the potential impact of these asymmetries on our density profile analysis, we considered the maximum changes they could cause. The photometric structure makes it difficult to choose an ellipticity and position angle that are representative of the whole galaxy. In §6.2.2 we used a weighted mean of the ellipticity and PA at radii between the outer edge of the asymmetric structure (at $r = 70''$) and the edge of the galaxy. As an alternative, we tried setting the ellipticity to its maximum and minimum values over the whole galaxy and repeated the tilted-ring modeling and isophotal fitting. We found that the rotation curve and density profile shape are largely insensitive to changes in the inclination angle. Even for ellipticities as small as 0.56 ($i = 66°$) and as large as 0.73 ($i = 79°$), the largest change in the derived value of α_{DM} is -0.05. We therefore conclude that our analysis is robust to the uncertainties introduced by the asymmetry of NGC 4605.

NGC 5949

The surface brightness profiles of NGC 5949 are very similar to those of NGC 2976 (Chapter 5). Both galaxies contain a nucleus, a shallow (large scale length) inner disk, and a steep (small scale length) outer disk. Although other disk galaxies are known to have similar structures (e.g., Pohlen et al. 2002), the origin and physical significance of these two apparently distinct disks are not understood. Nevertheless, there is no reason to doubt that our thin-disk approximation is valid for this galaxy, so the shape of the stellar rotation curve we calculated should be accurate. Due to the high level of symmetry of NGC 5949 in all bands, the photometric inclination and PA are extremely well constrained, leading to very small systematic uncertainties on the rotation curve. It is worth noting that NGC 5949 is the only galaxy in our sample in which the shape of the stellar rotation curve is very similar to the shape of the observed rotation curve. Therefore, it is possible to model this galaxy with essentially only a stellar disk and barely any contribution from dark matter. The stellar mass-to-light ratio required to accomplish this is $M_*/L_R \approx 2.7 \text{ M}_\odot/\text{L}_{\odot,R}$, 30%

higher than the derived maximum disk value.

Our tilted-ring modeling of NGC 5949 reveals a small radial component to the velocity field with modest significance. These radial motions are detected beginning at a radius of $20''$, and remain present out to the edge of the galaxy. The maximum amplitude is 8 km s^{-1}, and there are a total of six consecutive rings that have radial motions deviating from zero by at least 1 σ. Since the radial motions are $\lesssim 10\%$ of the rotation speed at all radii, they should not affect our mass models of the galaxy. Note that because we do not know which side of the galaxy is closer to us, we cannot determine whether the detected radial motions correspond to inflowing or outflowing material. We also detect a ~ 2 km s^{-1} $\cos 2\theta$ term from $24''$ to $36''$ and a ~ 3 km s^{-1} $\sin 3\theta$ term from $12''$ to $32''$.

NGC 5963

Unlike the other three galaxies, the luminous component of NGC 5963 does not contain an easily identifiable exponential disk. At the center of the galaxy is a bright, elongated bar-like feature about $4''$ across. Outside this source is a small disk-like region (500 pc in radius) with four tightly wound spiral arms. At a radius of $15''$ (950 pc) the surface brightness profile begins a steep decline, falling by nearly 3 magnitudes over $18''$. Surrounding this region is an LSB, nearly exponential disk that extends out to a radius of at least $120''$ (see Figure 6.2c). The inner spiral arms can be traced out into this outer disk at very low surface brightness levels.

It is difficult to interpret this surface brightness profile in terms of the standard model of a disk galaxy. Ordinarily, one might assume that the bright central region of NGC 5963 is a bulge that just happens to be at the center of an unusually faint disk. The clear presence of spiral arms in this region, however, suggests that even here the galaxy is highly flattened. One possibility is that this structure is a pseudobulge that has formed via secular evolution of the galaxy (e.g., Kormendy & Kennicutt 2004). The central luminosity enhancement, nuclear spiral arms, and weak bar are all classic characteristics of pseudobulges. The most sensible way to derive the stellar rotation curve in this case is to apply our standard assumption that the disk can be treated as infinitesimally thin. The assumption that the stellar mass-to-light ratio remains constant throughout this galaxy may not be correct, but since the stars are far from dominating the gravitational potential for reasonable mass-to-light ratios this should not substantially change our results.

NGC 5963 also contains noncircular motions. The radial term in the tilted-ring

fits deviates from zero by more than 1 σ in five rings, from $12''$ to $30''$. The radial motions reach as high as 15 km s^{-1} in this region, before beginning to oscillate about zero (with large uncertainties) at larger radii. The second-order Fourier terms in this galaxy both have amplitudes of ~ 3 km s^{-1} from radii of $16'' - 24''$ ($\sin 2\theta$) and $12'' - 24''$ ($\cos 2\theta$).

NGC 6689

The high inclination of NGC 6689 makes our images and surface brightness profiles less revealing of details of its structure. Nevertheless, it is clear that this galaxy contains an exponential disk and a central light excess that could be attributable to a bulge or a bar. No bar is evident in our images, but as we noted in §6.2.1, some catalogs classify the galaxy as barred.

Despite the large inclination angle, the observed Hα emission lines from NGC 6689 are well represented by Gaussian fits. This implies that sightlines through NGC 6689 generally only intersect a single H ii region, which is consistent with the appearance of the galaxy in a narrow band Hα image. Therefore, it is not necessary to use an envelope-tracing method (e.g., Sofue 1996; Gentile et al. 2004) instead of Gaussian fits to extract rotation velocities from the spectra.

Neither our standard tilted-ring model nor the higher order harmonic fits detected any deviations from circular rotation in NGC 6689. To some degree, this is likely due to the inclination of the galaxy, which limits our resolving power along the minor axis where radial motions are most prominent. Nevertheless, a radial component of ~ 10 km s^{-1}, as we found in the other three galaxies, should have been detected if present.

6.4 Discussion

6.4.1 Is There a Universal Density Profile?

The primary goal of this study is to determine as accurately as possible the inner density profiles of the dark matter halos of the galaxies we observed. At radii of $\lesssim 1$ kpc, does the dark matter density continue to increase, as predicted by NFW and numerous other theoretical studies? Or are the density profiles flat, with constant density cores, as most previous observers have concluded? Are the variations in density profile shape from galaxy to galaxy as small as the simulations suggest?

Observational Results

For two of the galaxies in our sample (note that for the remainder of the chapter we include NGC 2976 in our analysis so that we have a total sample of five galaxies), these questions are easy to answer. NGC 2976, as we showed in Chapter 5, unambiguously contains a constant density core. An $\alpha_{\mathrm{DM}} = 0$ power law (constant density) provides an excellent fit to the rotation curve. A pseudo-isothermal profile with a core comparable to the optical size of the galaxy also produces a good fit. NGC 5963, on the other hand, quite clearly has a very steep central density profile. A power law with a slope of $\alpha_{\mathrm{DM}} = 1.20$ fits the rotation curve very well, and an NFW fit with $r_s \approx 11$ kpc and a concentration parameter of 14.9 is nearly as good. A pseudo-isothermal fit is significantly inferior.

For the remaining three galaxies, the interpretation of the fit results is not nearly as straightforward. NFW fits to the disk-subtracted rotation curves can be carried out, but the fit parameters are not meaningfully constrained. Power laws with slopes between $\alpha_{\mathrm{DM}} = 0.78$ (NGC 4605) and $\alpha_{\mathrm{DM}} = 0.88$ (NGC 5949) fit the rotation curves well, but they are matched in each case by pseudo-isothermal profile fits with comparable or better reduced χ^2 values.

How can a rotation curve be simultaneously consistent with both a pseudo-isothermal halo and an $\alpha \approx 0.8$ power law density profile? As shown by van den Bosch & Swaters (2001), the differences between the rotation curves associated with these density profiles tends to be smaller than typical observational uncertainties, even with the high velocity resolution of our data. The pseudo-isothermal profile has a slope that varies continuously from 0 (constant density) at its center to -2 (isothermal) at large radii. A power law, of course, has a constant slope that (for our fits) is intermediate between these two values. That both profiles fit the data suggests that (1) the mean density profile slope over the observed region is equal to the value preferred by the power law, but that (2) the slope changes with radius, which is better described by the pseudo-isothermal profile. Previous studies have often assumed that if a pseudo-isothermal rotation curve fits the data, then the galaxy in question must contain a constant-density core. Our successful fits with the modified pseudo-isothermal profile (Equation 6.2) show that this assumption is not correct. Even when a pseudo-isothermal profile fits well, other density profiles with steeper central slopes may provide equally good fits.

Taken together, these observational results argue against the proposition that all

galaxies share a universal density profile. Common two-parameter profiles other than a power law cannot fit all of the galaxies in our sample, and even for power law fits the solutions span the range from constant-density to very cuspy. If a universal density profile exists, the scatter from halo to halo is large.

Simulation Results

The idea of a universal dark matter density profile traces back to NFW, and the most recent simulations continue to support this picture (Navarro et al. 2004; Diemand, Moore, & Stadel 2004; Stoehr 2004). The favored functional form of the universal profile, however, has not been agreed upon. For several years the debate focused on the exact value of the central cusp slope, but with the increasing resolution of the simulations, it now seems that this question may be the wrong one to ask. The highest resolution ΛCDM simulations reveal that dark matter density profiles do not converge to an asymptotic central slope (Power et al. 2003; Navarro et al. 2004; Diemand et al. 2004). Instead, the logarithmic slope continues to get shallower at smaller radii, and the best procedure for extrapolating the profiles to radii below the resolution limits[8] of the simulations is not clear.

The new density profile proposed by Navarro et al. (Equation 6.3) fits simulated dark matter halos more accurately and over a wider radial range than does the original NFW profile. All of the halos presented by Navarro et al. (2004) are well described by the new profile. A key difference between this profile and the classic NFW or Moore et al. (1999b) profiles is that there is no well-defined central cusp. The density reaches a finite central value rather than diverging. On observationally relevant scales (100 to 1000 pc), though, the density profile remains rather steep. Observations like ours with a resolution of tens or hundreds of parsecs would be expected to find density cusps only marginally shallower than an NFW profile. Only on *sub-parsec* scales does the logarithmic slope of this profile reach even $\alpha = 0.5$ (Navarro et al. 2004).

When the fits to Equation 6.3 for various simulated halos are rescaled by the characteristic density (ρ_{-2}) and radius (r_{-2}) of each halo, they are all essentially identical, corroborating the hypothesis of a universal density profile. Diemand et al. (2004) confirm the ability of this functional form to fit their own independently simulated halos. However,

---

[8]Note that the highest-resolution simulations currently have a resolution limit of $500 - 1000$ pc, so another factor of ~ 5 improvement in the resolution is needed before the simulations reach the scales probed by observations.

Diemand et al. also show that a generalized three-parameter NFW profile with a formal central cusp is able to fit the halos nearly as well. Note that our observations still probe well below the scales that are resolved by the simulations, and it is unknown which, if any, of the profiles motivated by the simulations provides the most accurate extrapolation to smaller radii.

Comparison

Despite our lack of knowledge about the precise functional form of simulated density profiles at small radii, we can still compare our observational results with the profiles that fit the simulations best. In a general sense, it is obvious merely from inspection of Figures 6.4 to 6.7 (and Figure 5.10) that the five rotation curves have rather different shapes. This visual impression is confirmed by the fits we performed in §6.3. If we use power laws to describe the density profiles, the mean slope is $\alpha_{\mathrm{DM}} = 0.73$, with a dispersion of 0.44. By comparison, Diemand et al. (2004) find for the generalized NFW profile fits that the central power law index is $\alpha_{\mathrm{DM}} = 1.16 \pm 0.14$. A more dramatic (although less intuitive) illustration of the difference between the observed and simulated density profiles is provided by our fits with the new Navarro et al. (2004) density profile. Although this formula fits our data well, as shown in §6.3.3 and Table 6.6, we derive values of η ranging from 0.12 to 8.99. Even if we ignore the clearly absurd results for the flat density profile of NGC 2976, we find a mean value of $\eta = 0.73$, with a dispersion of 0.78. From the simulations, Navarro et al. (2004) measure $\eta = 0.172 \pm 0.032$ and Diemand et al. (2004) are in agreement, finding $\eta = 0.186 \pm 0.037$. With the exception of NGC 5963, our fits are seriously discrepant with these results. If we force η to lie within the range preferred for the simulated halos, the scale radius and scale density run away to unreasonable values (as can be seen in Table 6.6 for NGC 6689).

Thus, there are two notable differences between our results and the most recent CDM simulations: (1) the halo-to-halo scatter is $\gtrsim 3$ times larger than the simulations, and (2) the observed central slopes are on average shallower than the simulated ones. Both of these differences present challenges for future simulations.

Although the *shapes* of the central density profiles we derive disagree with the theoretical predictions, the actual *values* of the central densities are relatively consistent with the simulation results. In Table 6.7 we give measured values for the dimensionless quantity $\Delta_{V/2}$ introduced by Alam, Bullock, & Weinberg (2002) to parameterize halo central

densities. In a ΛCDM cosmology, the galaxies in our sample should have $\Delta_{V/2}$ values between 10^6 and 3×10^6 (assuming NFW density profiles), similar to the values we observe. The galaxies do have a tendency to lie somewhat below the predicted level, but the difference is within the $1 \, \sigma$ scatter expected for ΛCDM.

Table 6.7.   Are Galaxy Parameters Correlated With Density Profile Slope?

Galaxy	Distance [Mpc]	M_I [mag]	$\mu_{0,I}$[a] [mag arcsec^{-2}]	$V-I$ [mag]	M_{dyn}[b] [M$_\odot$]	M_*/L_R [M$_\odot$/L$_{\odot,R}$]	i [deg]	$V_{max,halo}$[c] [km s^{-1}]	$R_{V/2}$[d] [pc]	$\Delta_{V/2}$[e]	$\alpha_{\rm DM}$
NGC 2976[f]	3.45	-18.6	19.73	0.87	3.7×10^9	0.53	61.4	74	900	7.0×10^5	0.01
NGC 4605	4.26	-18.9	19.36	0.75	4.7×10^9	1.01	71.5	74	560	1.7×10^6	0.78
NGC 5949	14.0	-19.8	19.75	0.95	1.1×10^{10}	1.64	64.6	74	880	6.8×10^5	0.88
NGC 5963	13.0	-19.1	18.10	0.85	1.4×10^{10}	1.24	48.4	114	660	2.9×10^6	1.20
NGC 6689	11.0	-19.0	21.25	$\cdots$	1.5×10^{10}	1.96[g]	76.0	94	1330	4.8×10^5	0.79

[a]Extrapolated central surface brightness of the disk.

[b]We calculate the dynamical mass as $M_{dyn} = V_{max}^2 R_{max}/G$, where V_{max} is the maximum observed rotation velocity and R_{max} is the largest radius our observations reach. Since the galaxies extend to much larger radii, these numbers clearly represent lower limits to the actual masses of each galaxy.

[c]The maximum rotation velocity of the dark matter halo after removing the stellar disk.

[d]The radius at which the dark matter rotation curve reaches half of $V_{max,halo}$, as defined by Alam et al. (2002).

[e]The mean dark matter density within $R_{V/2}$, in units of the critical density.

[f]Using data from Chapter 5.

[g]This mass-to-light ratio is calculated for the Sloan r' band, not the Kron-Cousins R band.

6.4.2   The Significance of NGC 5963

Despite these differences from the simulations, the density profile of NGC 5963 appears to be in good agreement with the theoretical models. The rotation curve of this galaxy rises so rapidly than an NFW profile fits the data very well. A power law with a slope steeper than NFW provides an even better fit. To our knowledge, NGC 5963 is the only low-mass disk galaxy for which a CDM-like central density cusp is confirmed and shallow density profiles are ruled out.

Since NGC 5963 represents the exception rather than the rule, the question is, are all galaxies formed with cuspy density profiles and most lose them, or did an unusual event during the evolution of NGC 5963 cause its density profile to become so steep? The key to answering this question is identifying what about NGC 5963 makes it unique.

A number of galaxy properties from our sample are summarized in Table 6.7. Among these galaxies, NGC 5963 has the highest central surface brightness, despite the very low surface brightness of its outer disk. It also has the most unusual surface brightness profile (see §6.3.5), although the significance of this is not clear. NGC 5963 is in the middle of the luminosity range of our targets (and the total span between the five galaxies is only ~ 1 magnitude). It does have the largest rotation velocity, and therefore the highest mass, among our sample. Other than mass, the most obvious distinction between NGC 5963 and the other galaxies is the sharp transition between the inner and outer surface brightness profiles. This causes the derived stellar disk rotation curve to peak at small radii ($r = 20''$) and then drop steeply, making the outer parts of the galaxy highly dark matter dominated (see Figure 6.6b). Although this concentration of luminous material near the center of the galaxy may be related to the similar concentration we find for the dark matter, we do not know its physical origin. If the galaxy really does contain a pseudobulge, then the processes that have funneled baryons toward the center of the galaxy could have moved the dark matter inward as well.

It is also noteworthy that high-resolution two-dimensional velocity fields and deep multicolor imaging are not necessary to recognize the unique dark matter density profile of NGC 5963. Using lower resolution H I data, a long-slit Hα spectrum of modest resolution, and photographic U- and R- band imaging more than 15 years ago, Bosma, Athanassoula, & van der Hulst (1988) already concluded that this galaxy probably contains "an unusually centrally concentrated and massive halo." Since high-resolution CDM simulations of galaxy

structure had not yet been carried out Bosma et al. could not generalize this result into any broader implications for dark matter or galaxy formation.

6.4.3   NFW and Pseudo-Isothermal Fits to Rotation Curves

Our study is not alone in finding that pseudo-isothermal profiles fit many rotation curves better than do NFW profiles. A number of previous authors have reached similar conclusions (e.g., de Blok et al. 2001a; Borriello & Salucci 2001; de Blok et al. 2001b; de Blok & Bosma 2002; Salucci et al. 2003, Chapter 5). We emphasize, however, that the observation that pseudo-isothermal fits produce lower reduced χ^2 values than NFW or Moore profiles does not demonstrate the presence of a constant-density core. We showed in §6.3.3 that in many cases power law density profiles with intermediate ($0 < \alpha < 1$) slopes provide comparable fits. A modified pseudo-isothermal profile with a shallow $\alpha = 0.5$ central cusp (Equation 6.2) also fits these rotation curves as well as a true pseudo-isothermal profile with a constant-density core does. Since current theories of galaxy formation do not lead naturally to either cores or pseudo-isothermal density profiles, a preference for constant-density cores over shallow density cusps is not justified. Whether these galaxies actually contain a central region of constant density or if they have shallow ($\alpha < 1$) cusps cannot be determined from the present data, despite the high resolution of our measurements.

We do agree with past studies that for most galaxies the NFW form does not fit the inner density profile very effectively (see Figures 6.4b - 6.7b). When r_s and r_{200} are constrained to stay roughly in the range expected from simulations, the χ^2 values for NFW fits are generally rather high. We also point out, however, that the NFW fit parameters are quite poorly constrained unless the observations extend well into the flat part of the rotation curve. If there are only a few data points on the flat part of the rotation curve (especially when these data points have the largest uncertainties, as is often the case), they do not provide significant leverage on the fit. In such cases, the NFW scale radius and virial radius (or any other pair of parameters that can be used to describe an NFW profile) become completely degenerate. In order to obtain accurate estimates of the NFW fit parameters, our results suggest that $\gtrsim 50\%$ of the observed part of a galaxy must have a nearly flat rotation curve.

6.4.4 Implications for CDM

Combining this study with our previous analysis of NGC 2976, we have shown that the five galaxies in our sample have density profiles with a wide range of central slopes. If we fit the data with power laws, we find that three galaxies have central cusps of $\alpha_{\mathrm{DM}} \approx 0.8$, while the other two galaxies have very different central slopes ($\alpha_{\mathrm{DM}} = 0.01$ and $\alpha_{\mathrm{DM}} = 1.20$). Of the outliers, NGC 2976 is a satellite of M81, and thus may have been subject to tidal stripping. There are suggestions in the literature that tidal stripping acts to remove density cusps (Stoehr et al. 2002; Hayashi et al. 2003), but the most recent simulations find that the central density slope is not altered by tidal effects (Kazantzidis et al. 2004b). It is not clear why NGC 5963 differs so strongly from the other galaxies. These fits demonstrate that while galaxies with steep central density cusps do exist, they are not shared by all galaxies. Furthermore, no single value of the central slope can describe all five of the rotation curves in our sample.

On the other hand, if we consider the pseudo-isothermal fit results (as most previous observational studies have done), we find that good fits can be obtained for four of the five galaxies (see Table 6.4). It is interesting to note that these galaxies all have central densities within a factor of 7 of each other. Only for NGC 5963 is the quality of the pseudo-isothermal fit sufficiently poor that a constant-density core can be excluded. The rotation curves of the other four galaxies are consistent with cores, but all except NGC 2976 are also consistent with cusps. The implication of these findings is that some previous studies may have overestimated the disagreement between their data and the CDM simulations.

Based on these results, we reach the following conclusions:

- First, the observed variation in density profile slopes from halo to halo is much larger than expected from the simulations. We also find that none of the commonly used density profile functional forms can describe all five galaxies.

- Second, most galaxies have density profiles significantly shallower than the $\alpha_{\mathrm{DM}} = 1$ central cusps preferred by the simulations. Nevertheless, the difference between the central slopes we measure and the theoretical values is much smaller than suggested by most previous studies.

- And third, some galaxies do contain $\alpha_{\mathrm{DM}} \gtrsim 1$ cusps with an overall density profile that follows the NFW form, hinting that it may still be possible to reconcile the results of

the pure dark matter cosmological simulations with observations.

Do these differences between the observations and the simulations indicate a fundamental problem with the CDM paradigm? Probably not. A great many plausible theoretical explanations have been proposed in attempts to understand this problem, and a few of the recent ideas are mentioned below. Taylor & Navarro (2001) suggested based on phase-space arguments that CDM density profiles should have $\alpha = 0.75$ cusps, very similar to the average we measure. Ricotti (2003) found that the dark matter halos of simulated dwarf galaxies have shallower cusps than those of massive galaxies. In a similar experiment, however, Colín et al. (2004) reached the opposite conclusion, so the degree to which dwarf galaxy density profiles are expected to match those of large galaxies has not yet been settled. Boylan-Kolchin & Ma (2004) showed that major mergers leave cuspy remnants unless both precursors had cores, so at least in the case of pure dark matter halos, mergers cannot destroy cusps. Baryonic processes, however, probably can (e.g., Weinberg & Katz 2002). Even the dark matter itself may be able to flatten cuspy density profiles; Ma & Boylan-Kolchin (2004) argued that energy deposition by merging dark matter substructures can puff up central cusps into shallower density profiles. This effect might have escaped notice in previous simulations due to insufficient resolution or overmerging (unrealistic destruction of subhalos in dense regions). Finally, Hayashi et al. (2005) have shown that if dark matter halos are significantly triaxial (see §6.5), for some viewing angles the derived density profiles can appear much shallower than the actual density profiles.

Since we have shown that cuspy density profiles are consistent with a large fraction of our sample, and in light of the variety of potential effects not currently accounted for in the simulations that could change the predicted density profiles, there is little reason to conclude at this point that the density profile controversy represents a crisis for CDM.

6.5 The Effects of Halo Triaxiality

Almost every previous observational study of density profiles and rotation curves has assumed that dark matter halos are spherical. CDM simulations, however, suggest that dark matter halos are triaxial (Dubinski & Carlberg 1991; Warren et al. 1992; Cole & Lacey 1996; Jing & Suto 2002; Bailin & Steinmetz 2005). Unfortunately, very few observations of individual galaxies are available to test this prediction. Several polar-ring galaxies have been studied, with results ranging from axis ratios as small as 0.3–0.4 up to axis ratios of 1

(spherical halos) (Schweizer, Whitmore, & Rubin 1983; Whitmore, McElroy, & Schweizer 1987; Sackett & Sparke 1990; Sackett et al. 1994; Combes & Arnaboldi 1996; Iodice et al. 2003). A variety of techniques suggest that the gravitational potential of the dark matter halo of the Milky Way is close to spherical (Kuijken & Tremaine 1994; Olling & Merrifield 2000). Despite the scarcity of reliable constraints on individual halo ellipticities, statistical arguments provide a way to determine the average shape of galaxy halos. Franx & de Zeeuw (1992) showed that the observed scatter in the Tully-Fisher (TF) relation places a strong upper limit on the allowed ellipticities of spiral galaxy disks. Even if *all* of the TF scatter is caused by elongated disks, the mean disk ellipticity is required to be less than 0.1. More likely, the scatter is a result of a combination of effects, indicating that on average disk ellipticities must be $\lesssim 0.05$. In this section we consider the effects triaxial halos could have on the velocity fields we observe.

6.5.1 Halo Oblateness

Galaxy disks are expected to be oriented such that the disk lies in the plane described by the major and intermediate axes of the halo, with the z-direction pointing along the halo minor axis (Sharma & Steinmetz 2004; Bailin & Steinmetz 2005). We first consider the effect of this flattening of the halo, under the assumption that halo shape in the disk plane is circular.

The rotation velocity of a disk in such an oblate spheroidal halo is given by Equation 2-91 in Binney & Tremaine (1987):

$$v_{rot}^2(R) = 4\pi G\sqrt{1-e^2} \int_0^R \frac{\rho(m)m^2 dm}{\sqrt{R^2 - m^2 e^2}}, \tag{6.5}$$

where $\rho(m)$ is the density profile of the halo in the spheroidal coordinate m [defined by $m^2 = r^2 + z^2/(1-e^2)$] and e is the eccentricity of the spheroid. For any density profile, this integral can be evaluated numerically to give the rotation curve for various degrees of oblateness. We performed this calculation for spheroidal power laws [$\rho(m) = \rho_0(m/m_0)^{-\alpha}$] and NFW profiles [$\rho(m) = \rho_c\delta_c(m/m_s)^{-1}(1+m/m_s)^{-2}$]. The change from a spherical halo to an oblate one could affect both the shape of the rotation curve and its amplitude. We find that as the halo becomes flatter ($e \to 1$), the amplitude of the rotation curve increases (as expected, since the mass becomes concentrated closer to the disk). We also find that the shape of the rotation curve is completely independent of the halo flattening for a power law density profile; the same power law index for the rotation curve (and density profile)

is derived for any value of e. For an NFW density profile, the shape of the rotation curve changes very subtly with eccentricity (the peak of the rotation curve shifts to smaller radii as the halo becomes flatter), but the inner slope of the rotation curve is essentially unaffected.

6.5.2   Disk Ellipticity

In the previous subsection, we showed that the flattening of the halo does not alter the observed density profile for a circular disk. We now remove the assumption that the disk is circular and study the effects of disk ellipticity on the observed velocity field.

Are Noncircular Motions Common in Disk Galaxies?

Four of the five galaxies in our sample show evidence for a radial component to their velocity fields. In two of these, the radial motions are detected very strongly; for the other two the significance of the radial term is lower, although it is still confirmed at $\sim 95\%$ confidence. Other recent studies have also begun to find significant numbers of galaxies with noncircular motions (Schoenmakers, Franx, & de Zeeuw 1997; Swaters et al. 2003b; Coccato et al. 2004; Blais-Ouellette et al. 2004; Wong, Blitz, & Bosma 2004). A large majority of the galaxies studied by these authors (and us) are not barred. However, of the galaxies in which observations could have detected radial motions, nearly all indeed appear to contain them. Are radial components to the velocity fields ubiquitous in late-type spiral galaxies? What is the cause of these motions?

Measuring Disk Ellipticity With Noncircular Motions

Since there is no strong evidence for bars in the four galaxies where we detect noncircular motions, other sources of these motions should be considered. First, we note that the observed noncircular motions are dominated by the radial component. The simplest possibility is that the galaxies contain strong radial flows directed toward their centers. Given the observed magnitude of the radial motions at a radius of ~ 1 kpc and an assumed volume density for the gas (1 H atom cm^{-3}), if the radial motions actually represent a net inflow of gas we conservatively estimate that all of the gas would accumulate within a ~ 1 kpc radius of the galaxy centers in 1–3 Gyr. The star formation rate over the same region is at least an order of magnitude too small to consume the inflowing gas. We therefore conclude that this interpretation is not viable. The most intriguing remaining explanation

is that the gas is moving on elliptical orbits, which could result from the influence of a triaxial dark matter halo.

In a disk galaxy with a triaxial dark matter halo, the potential in the plane of the disk will in general be elliptical. The closed orbits in such a potential are also ellipses, which means that the observed line-of-sight velocities of an elliptical disk will differ from pure circular rotation. This problem has been considered in detail by Binney (1978), Teuben (1991), Franx, van Gorkom, & de Zeeuw (1994), Schoenmakers et al. (1997), and Schoenmakers (1998). Franx et al. (1994) showed that an elliptical potential induces components in the velocity field proportional to the ellipticity and the angle between the long axis of the ellipse and the observer's line of sight. Adopting their formalism (Franx et al. 1994, Equation A10), we have the following relations:

$$\hat{c}_1 = \left[1 - (\frac{3}{4} - a)\epsilon_R \cos 2\phi_{obs} \right] v_c \sin i \qquad (6.6)$$

$$\hat{s}_1 = \left[\left(\frac{5 - q^2}{4(1 - q^2)} - a \right) \epsilon_R \sin 2\phi_{obs} \right] v_c \sin i, \qquad (6.7)$$

where $\hat{c}_1$ and $\hat{s}_1$ are the $\cos\theta$ (rotation) and $\sin\theta$ (radial) components of the tilted-ring model, respectively. The hat symbols indicate that these quantities are derived under the assumption of circular orbits, and will therefore differ systematically from the true values if the potential is elliptical. These formulae are valid when the rotation curve, $v_c(r)$, can be represented as a power-law with index β, which we have shown is a reasonable assumption for these galaxies. β is related to a by $a = \frac{1}{2}\beta/(1 + \beta)$, q is the axis ratio of the galaxy (which we take from the photometry), ϕ_{obs} is the angle between the long axis of the potential and the line of sight, and ϵ_R is the ellipticity of the orbit. The relationship between the ellipticity of the potential, ϵ_{pot}, and that of the orbit, ϵ_R, is given by Franx et al. (1994):

$$\epsilon_{pot} = \frac{1 - \beta}{1 + \beta}\epsilon_R. \qquad (6.8)$$

In order for us to make the simplifying assumption that the apparent rotation velocities are equal to the true rotation velocities (i.e., that the orbits are nearly circular), the following condition must be met:

$$(\tfrac{3}{4} - a)\epsilon_R \cos 2\phi_{obs} \ll 1. \qquad (6.9)$$

In this case, Equation 6.6 reduces to $\hat{c}_1 = v_c \sin i$. Substituting this expression into Equation

6.7 and solving for the potential ellipticity yields

$$\epsilon_R \sin 2\phi_{obs} = \frac{1}{\left(\frac{5-q^2}{4(1-q^2)} - a\right)} \frac{\hat{s}_1}{\hat{c}_1}. \tag{6.10}$$

Thus, if the observed noncircular motions are indeed due to an elliptical potential in the plane of the disk, the relative amplitudes of the circular and radial motions put a direct constraint on the ellipticity. Note that since $\sin 2\phi_{obs} \leq 1$, this constraint is actually a *lower limit* on ϵ_R. Using the known values of q and a, and the results of our tilted-ring models for $\hat{c}_1$ and $\hat{s}_1$, we calculate $\epsilon_R \sin 2\phi_{obs}$ as a function of radius for each galaxy. The results are shown in Figure 6.9. NGC 4605, with its very strongly detected radial motions, has a large and nearly constant ellipticity that deviates significantly from zero beginning at a radius of $20''$. The mean value of $\epsilon_R \sin 2\phi_{obs}$ over the entire galaxy is 0.175 ± 0.016, making the orbits in the disk of this galaxy substantially elliptical. From Equation 6.8, we see that $\epsilon_{pot} = 0.18\epsilon_R$, so the ellipticity of the potential is at least 0.03. $\epsilon_R \sin 2\phi_{obs}$ differs from zero at the $\sim 3\,\sigma$ level in NGC 5949 and NGC 5963. We find that $\epsilon_R \sin 2\phi_{obs} = 0.043 \pm 0.014$ for NGC 5949 and $\epsilon_R \sin 2\phi_{obs} = 0.060 \pm 0.020$ for NGC 5963. We do not detect any evidence for elliptical orbits in NGC 6689: $\epsilon_R \sin 2\phi_{obs} = 0.007 \pm 0.014$. NGC 2976 is the only galaxy in which the ellipticity is not constant with radius. This could suggest that either the halo structure is more complicated in this galaxy (e.g., the axis ratios of the halo change with radius), or that its radial motions may be caused by something other than triaxiality. If the halo of NGC 2976 is triaxial, the mean ellipticity of the disk orbits is $\epsilon_R \sin 2\phi_{obs} = 0.116 \pm 0.013$.

Given the determination of $\epsilon_R \sin 2\phi_{obs}$, we can now go back and confirm that the assumption stated in Equation 6.9 (that the difference between the apparent and true rotation velocities is small) was justified. As long as the ellipticity is modest ($\epsilon_R \lesssim 0.2$, which requires that the viewing angle be larger than $\sim 9°$ for most of these galaxies), this condition will be satisfied. Note, however, that for NGC 4605, ϵ_R may be larger than this value.

These calculations show that, if the observed radial motions are indeed due to halo triaxiality, the lower limit on the mean potential ellipticity is of order a few percent. Since the scatter in the TF relation indicates that the average ellipticity of the potential has a strict upper limit of 0.1 (Franx & de Zeeuw 1992), the ellipticities are now constrained within a relatively narrow range. CDM simulations predict that the dark matter halos of galaxies similar in mass to our targets should have axis ratios of $c/a = 0.47$ and $b/a = 0.62$
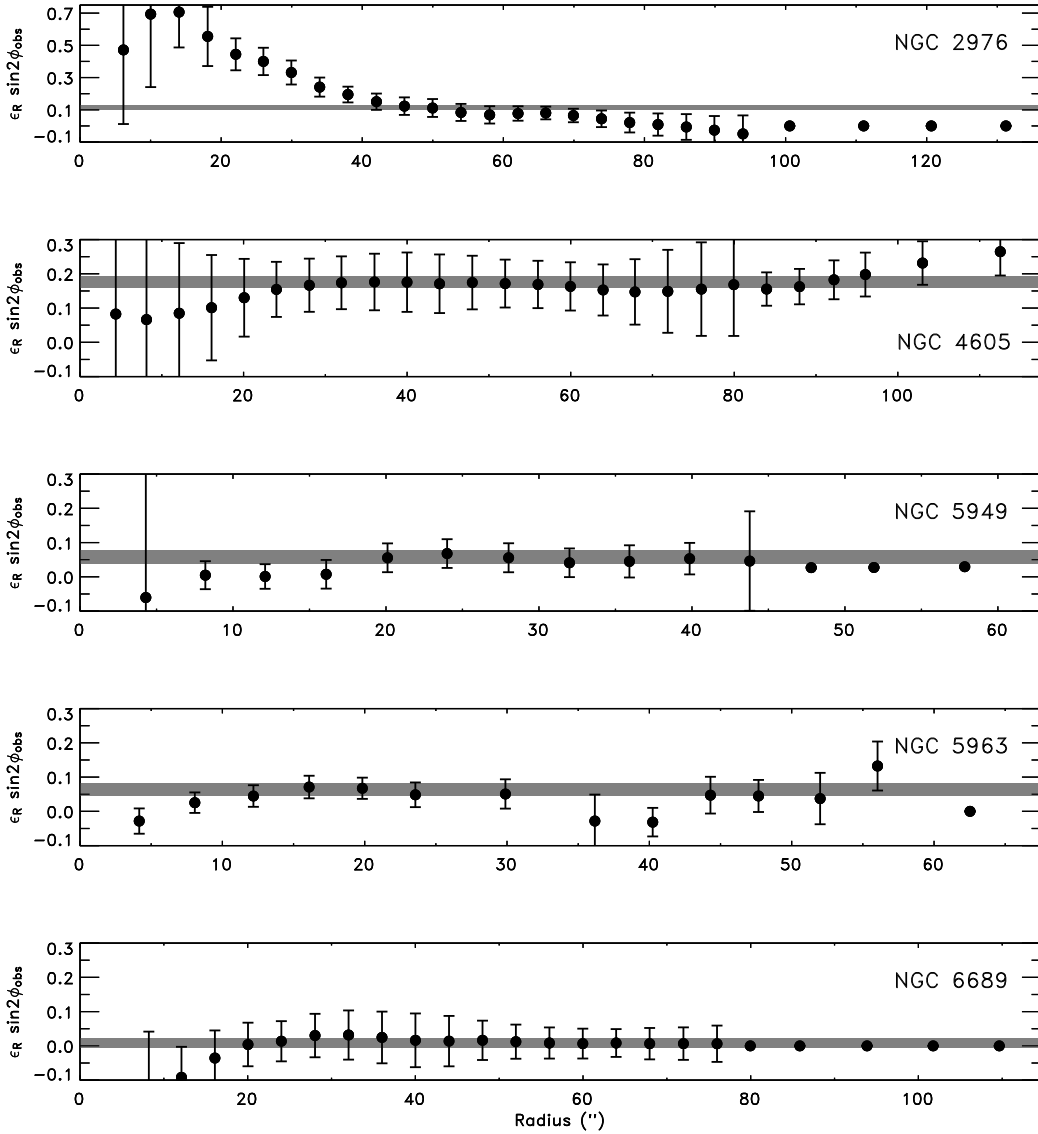
Figure 6.9 — $\epsilon_R \sin 2\phi_{obs}$ as a function of radius for (from top to bottom) NGC 2976, NGC 4605, NGC 5949, NGC 5963, and NGC 6689. The shaded gray bands across each panel represent the weighted mean value of $\epsilon_R \sin 2\phi_{obs}$. The points at large radii without error bars correspond to rings in which the radial velocity was held fixed because the ring contained too few data points or the angular coverage of the data was not sufficient to constrain the radial motions. These points do not contribute to the weighted average and should not be considered to contain significant information about the orbital ellipticity. Only in NGC 6689 does the gas appear to be traveling on circular orbits, although it is also possible that $\phi_{obs} \approx 0°$ or $90°$ for this galaxy. The ellipticity of the potential is a factor of a few smaller than the ellipticity of the orbits that is plotted here (see Equation 6.8). Note that these values are lower limits on the true ellipticity due to the unknown viewing angle.

(Jing & Suto 2002), which would suggest larger ellipticities than we measure. Bailin & Steinmetz (2005) find somewhat less triaxial halos with $c/a = 0.65$ and $b/a = 0.83$ for halos with masses of $\sim 3 \times 10^{10}$ M$_\odot$. Adding gas cooling to the simulations may make the inner regions of the halo even more spherical (Kazantzidis et al. 2004a), in agreement with the observational constraints. With observations of a larger sample of galaxies, it may be possible to obtain robust constraints on the three-dimensional shapes of galaxy halos, which would then provide another strong test of CDM simulations on small scales.

6.6 Summary and Conclusions

We have used two-dimensional CO and Hα velocity fields, sampled at high spatial resolution and high spectral resolution, to constrain the dark matter density profiles of four nearby, low-mass, late-type galaxies. We obtained rotation curves from the data cubes by constructing tilted-ring models, and found that three of the four galaxies contain radial motions in addition to rotation. Combining these data with the observations of NGC 2976 presented in Chapter 5 gave us a sample of five galaxies to study.

For each galaxy we constructed a model of the stellar disk and investigated the density profile of the dark matter halo under varying assumptions about the stellar mass-to-light ratio. In most cases, over the range of plausible mass-to-light ratios, the dark matter density profiles do not change significantly. For the mass-to-light ratios indicated by the galaxy colors, we found that the five galaxies span a range of central density profile slopes from $\alpha_{\mathrm{DM}} = 0$ to $\alpha_{\mathrm{DM}} = 1.20$. The mean slope is $\alpha_{\mathrm{DM}} = 0.73$, with a dispersion of 0.44. Neither of the standard density profile functional forms (pseudo-isothermal and NFW) is able to adequately fit all five galaxies. The scatter in slope that we observe is three times larger than that seen in the simulations, and the mean slope is smaller than predicted. We do note, however, that NGC 5963 is the first low-mass disk galaxy in which a cuspy density profile of the predicted form is confirmed, while shallower alternative profile shapes are ruled out.

Although these results still indicate significant disagreements between CDM simulations and the properties of real galaxies, there are also some differences between the findings of this chapter and those of previous observational analyses. Many authors have concluded that density profiles with constant-density cores fit the rotation curves of dwarf and LSB galaxies better than cuspy density profiles do (e.g., de Blok et al. 2001a; Borriello

& Salucci 2001; de Blok et al. 2001b; de Blok & Bosma 2002; Salucci et al. 2003, Chapter 5). Typical results from these studies are that the distribution of density profile slopes is $\alpha = 0.2 \pm 0.2$ (de Blok et al. 2001a; de Blok & Bosma 2002; de Blok et al. 2003). Some other studies agreed that cored profiles generally fit the data better, but argued that this effect is primarily the result of systematic uncertainties in the observations (van den Bosch et al. 2000; van den Bosch & Swaters 2001; Swaters et al. 2003a). When we fit power laws to the rotation curves we find significantly steeper density profile slopes on average than previous authors did, although both pseudo-isothermal density profiles (constant-density cores) and relatively cuspy profiles are consistent with our data. Despite our disagreement on the value of the mean slope, we agree with other recent studies that found that dark matter density profiles span a wide range of slopes (e.g., de Blok et al. 2003; Swaters et al. 2003a).

What is responsible for the steeper slope that we find? One important element of our study is that the two-dimensional velocity fields, high spatial resolution, and target selection we employed significantly reduce the impact of systematic uncertainties on our results (Chapter 5). As an illustration of this point, van den Bosch & Swaters (2001) showed that to obtain tight constraints on density profile slopes, at least one of the three following conditions must be met: (1) the uncertainties on the rotation curve must be $\lesssim 0.2$ km s^{-1}, (2) the rotation curve must extend out beyond 20% of the virial radius, and (3) the rotation curve must extend inward to radii less than $\sim 2\%$ of the virial radius. While we do not reach the velocity precision of criterion (1), we approach it as closely as feasible, with typical systematic uncertainties as small as ~ 2 km s^{-1}. Although higher velocity resolution spectroscopy is possible, our velocity measurements have already run into the limit imposed by the small-scale random motions of ~ 5 km s^{-1} that most galaxies appear to contain. Without H I observations at large radii, we also fail to meet criterion (2), but our high spatial resolution does allow us to satisfy criterion (3). Galaxies with masses similar to those studied here may have virial radii of 50–75 kpc (Bullock et al. 2001; Navarro et al. 2004), so even for our most distant targets our ~ 250 pc resolution probes well within 2% of the virial radius. In addition, we explored functional forms for the density profiles other than the standard NFW/pseudo-isothermal dichotomy, thereby demonstrating that good pseudo-isothermal fits in general do not rule out cuspy density profiles. Given these new results, we conclude that while the discrepancies between CDM and galaxy rotation curves may not be as severe as previously thought, improved simulations are needed in

order to determine whether the theoretical and observational findings can be brought into agreement.

Finally, we considered the origin of the noncircular motions that are now being detected regularly in disk galaxies. A number of previous authors have showed that a triaxial dark matter halo can produce exactly the observed effect on the gas orbits. Under the assumption that halo triaxiality is causing the noncircular motions, we measure lower limits to the orbital ellipticities of 0.02-0.17. These correspond to lower limits on the ellipticities in the potential between 0.005 and 0.03.

Chapter 7

Conclusions

In this thesis we have presented a variety of observations that test two of the small-scale problems with the Cold Dark Matter model, the substructure problem and the central density problem. While we have not yet succeeded in completely resolving either problem, we have made progress in understanding them, particularly with regard to the central density problem, and we can now point the way to future investigators. In §7.1, we summarize our results on the substructure problem and describe additional observational work that may help to elucidate the origin and significance of the problem. In §7.2, we discuss the current status of the central density problem in light of our work and conclude with some ideas for more detailed comparisons between observations and simulations that may finally isolate and reveal the processes responsible for the problem.

7.1 The Substructure Problem

Without observational confirmation of the presence of large numbers of low-mass dark matter halos, the possible explanations for the substructure problem are (1) the excess dark matter minihalos do not exist (i.e., the simulations are seriously in error), (2) the excess dark matter minihalos do exist and contain stars and/or gas in addition to dark matter (similar to other dwarf galaxies), but are faint enough in the optical to have escaped detection in previous surveys, or (3) the excess dark matter minihalos do exist, but star formation has been suppressed in them. With our extensive search for stars in compact high-velocity clouds (Chapter 2), we thoroughly investigated and falsified the hypothesis that HVCs represent a large population of normal low surface brightness dwarf galaxies. This result rules out scenario (2) unless none of the missing dwarfs managed to retain any

of their gas. Because the first scenario would require substantial modifications to CDM that do not appear warranted by other observations, and because there are numerous theoretical reasons to expect the third scenario to be plausible, we favor the latter possibility.

The other results from our HVC studies offer significant observational support for this idea. We identified two HVCs that are massive, dark matter-dominated (almost certainly in one case and probably in the other), and lack stars. Complex H (Chapter 3) is one of the four very extended HVC complexes that are known or thought to be located quite close to the Milky Way. Complexes A and M have upper distance limits based on absorption-line detections in the spectra of Galactic halo stars (Danly, Albert, & Kuntz 1993; Keenan et al. 1995; van Woerden et al. 1999), but Complex H appears to lie behind all of the available stellar absorption probes (Wakker et al. 1998). Nevertheless, Lockman (2003) succeeded in modeling Complex H as a cloud in an inclined, retrograde orbit around the Galaxy, suggesting a distance of 27 kpc. At this distance, Complex H has the largest H I mass of any of the Milky Way satellites except for the Magellanic Clouds, with 2×10^7 M$_\odot$ of neutral gas. Our infrared and radio observations place limits of 3×10^{-4} M$_\odot$ yr^{-1} on the current star formation rate in Complex H and rule out the presence of an old stellar population comprising more than $\sim 3 \times 10^5$ M$_\odot$. We therefore concluded that Complex H does not have a normal stellar counterpart (where by "normal" we mean one that is comparable to other known dwarf galaxies).

In a more serendipitous discovery, we found that the compact high-velocity cloud HVC $127-41-330$, which is located just $30'$ from the dwarf galaxy LGS 3, is also distant, massive, and starless (Chapter 4). By virtue of the apparent interaction between the HVC and LGS 3, we estimated that the HVC is ~ 700 kpc away from the Sun, implying an H I mass of 2.6×10^6 M$_\odot$. The most likely explanation for the velocity gradient across the HVC is that the cloud is rotating, which allows us to derive a dynamical mass of 2.0×10^7 M$_\odot$. The only assumptions needed to conclude that this object is dark matter-dominated are that (1) the velocity gradient really does indicate rotation, and (2) the HVC has a distance of less than 2 Mpc. It is visually obvious from examination of POSS-II data that HVC $127-41-330$ does not have an optical counterpart with a surface brightness or luminosity that is comparable to those of LGS 3 ($\mu_{\rm V} = 24.7$ mag arcsec^{-2}; $M_V = -10.1$ [Lee 1995]), which is easily visible on the same Palomar plate (Figure 4.4).

Based on these observational findings, we propose that both Complex H and HVC $127-41-330$ are *dark galaxies* in the Local Group. These objects probably have

dark matter halos with masses greater than 10^7 $M_\odot$ and have become detectable as a result of accreting some gas, but formed few if any stars. It is not yet clear whether their gaseous components could have been acquired at high redshift and maintained for a Hubble time, or if the accretion must have occurred recently. If CDM predictions of substructure are correct, then these two failed dwarf galaxies are the prototypes of a large population of such objects that surround the Milky Way, Andromeda, and other massive galaxies. Our continued inability to locate the expected hundreds of similar dark matter halos in the Local Group suggests that perhaps the bulk of this population lacks any baryonic component at all and thus remains completely invisible. Critical questions to address in this circumstance include (1) What is special about these two dark matter halos that allowed them to accumulate so much more neutral gas than other halos? and (2) Why has star formation not proceeded in these objects as it did in other low-mass galaxies?

One obvious answer to the first question is that both clouds are in close proximity to other galaxies; HVC 127$-$41$-$330 has a projected separation of 5.8 kpc from LGS 3 and Complex H is only 27 kpc away from the Milky Way. Perhaps they acquired their gas as a result of interactions with the neighboring galaxies, although in the case of HVC 127$-$41$-$330 it is hard to understand how the interaction could have left the HVC with 90% of the gas in the system (since the HVC and LGS 3 have similar total masses). This idea is also unsatisfactory because simulations indicate that large numbers of subhalos should be located quite close to the Milky Way and M 31, suggesting that Complex H should not be the only gas-rich satellite present. The second question is equally problematic. It seems reasonable to suppose that the internal pressure in these clouds is simply too low for self-shielded molecular clouds to form (especially given the low metallicities that are expected for such gas). On the other hand, the objects that became normal dwarf galaxies should have experienced the same difficulty, and yet they still managed to form $10^5 - 10^8$ $M_\odot$ of stars. So perhaps the better question to ask is, Why are there any dwarf galaxies at all? One of the few currently promising solutions to this problem is the idea that what we now see as dwarf galaxies were originally very massive objects, similar to the Magellanic Clouds, that have been tidally stripped down to their present-day sizes (Kravtsov, Gnedin, & Klypin 2004). The existence of very old, very low-mass, and very isolated dwarfs such as Cetus and Tucana would seem to pose a challenge for this model, since there is no nearby massive galaxy that could be responsible for the extensive stripping these galaxies must have undergone. However, Kravtsov et al. (2004) claim that the model can accommodate Cetus and Tucana

if they were once satellites of larger galaxies that have since been destroyed by the Milky Way or M 31.

Although the identification of *any* dark galaxies represents a significant success for CDM, since their existence may be regarded as a prediction from the numerical simulations, the two objects we have identified fall far short of the expected number. Furthermore, none of the few dozen other HVCs that have been observed at high spatial resolution show convincing evidence for massive dark matter halos, which argues against the possibility that HVCs could comprise the bulk of the missing subhalo population. In order to solve the substructure problem, either many additional dark galaxies must be discovered, or an explanation must be found for why these two halos alone are visible. Future studies that will be helpful include searches for extremely faint resolved dwarf galaxies in photometric databases such as the Sloan Digital Sky Survey (as Zucker et al. 2004 and Willman et al. 2005a,b have shown) and in-depth studies of the objects currently suspected to be dark galaxies to gain a better understanding of their nature. For example, we plan to model the interaction between HVC 127$-$41$-$330 and LGS 3 to determine whether the morphology and kinematics of the features that we are interpreting as tidal tails are indeed consistent with the interaction hypothesis. We have also acquired deep *V*- and *I*-band imaging of this region that we can use to place much tighter limits on the stellar content of the HVC, and we have obtained shallow *U*- and *g*-band imaging to search for a bright quasar located behind the HVC that we can use as a background source for an absorption-line abundance study of the cloud.

7.2   The Central Density Problem

Our velocity field studies of five nearby, dark matter-dominated galaxies showed that the central density problem cannot be entirely attributed to observational systematic effects (Chapters 5 and 6). The density profiles we derived differ from those seen in previous surveys in that they are not uniformly shallow profiles; instead, we found a wide range of density profile shapes. We identified at least one galaxy that is very well described by an NFW density profile, but another one of our targets contains a large constant-density core, and the sample as a whole does not provide a good match to the predictions from CDM simulations. The mean slope that we measure ($\alpha_{\mathrm{DM}} = 0.73$) is shallower than the simulations indicate, and the dispersion of the slope from galaxy to galaxy ($\Delta\alpha_{\mathrm{DM}} = 0.44$) is much larger

than expected. Thus, we confirm that the central density problem is real, although the problem is less severe than most previous studies suggested. The most important questions that we now face are (1) What is the observational distribution of density profile shapes? and (2) What causes the clear differences between many observed and simulated density profiles?

The answer to the first question awaits a systematic survey of high-resolution, two-dimensional velocity fields of a large sample of galaxies. The study of five galaxies that we presented in Chapter 6 represents an initial step in this direction, but a minimum of $15 - 20$ galaxies may be needed to begin to meaningfully constrain the density profile distribution. Similar work by Swaters et al. (2003b), Blais-Ouellette et al. (1999, 2004); Blais-Ouellette, Amram, & Carignan (2001), and the Gassendi Hα survey of SPirals (GHASP; Garrido et al. 2002, 2003; Garrido, Marcelin, & Amram 2004) can contribute to this effort, but uniform analysis techniques may be required to prevent systematic uncertainties from affecting the results.

I expect that the result from such a survey will be a broad distribution of density profile shapes, as seen previously by Swaters et al. (2003a), de Blok, Bosma, & McGaugh (2003), and in Chapter 6 of this thesis. Our current work suggests that the distribution will likely be centered between $\alpha_{\mathrm{DM}} = 0.5$ and $\alpha_{\mathrm{DM}} = 1$, with a dispersion from galaxy to galaxy that could easily be as large as $\Delta\alpha_{\mathrm{DM}} = 0.5$. In comparison, the most recent simulations find central slopes of $\alpha_{\mathrm{DM}} \gtrsim 1.2$ for galaxy-size halos and a scatter of $\Delta\alpha_{\mathrm{DM}} = 0.14$ for halos of a given mass (Navarro et al. 2004; Diemand, Moore, & Stadel 2004). If this conjecture is correct, the burden will then fall on the simulations to explain why real galaxies have density profiles that are shallower and vary much more between galaxies than current CDM models predict.

One new approach to the problem that seems likely to prove productive will be to increase the uniformity of the treatment of observed and simulated data. Currently, as described in Chapter 5 and Appendix A, observed two-dimensional velocity fields are converted into one-dimensional rotation curves via a tilted-ring model, and the rotation curves are then inverted to yield density profiles. On the other hand, simulated density profiles are derived by averaging the dark matter particles in spherical (or occasionally triaxial) shells around the halo center. Actual velocities are never measured in this process, and even worse, it is not clear how accurately the kinematics of a gaseous disk embedded in the halo reflect the density profile of the dark matter, particularly when the halo is not

spherical. Simulating halos that contain disks and then "observing" the velocity fields of those disks in a manner similar to that which an observer would use will provide a much better basis for comparison to the velocity fields of real galaxies. The preliminary results obtained by Hayashi et al. (2005) suggest that taking these differences into account may be able to explain the variety of observed density profiles without resorting to modifications of CDM itself, and we are actively working on testing this hypothesis more fully.

Because we have shown that the kinematics of many galaxies are consistent with relatively steep central density profiles ($\alpha_{\mathrm{DM}} \gtrsim 0.8$), even though the detailed profile shapes do not seem to match those seen in simulations, we argue that the central density problem should no longer be regarded as a crisis for CDM. We are currently studying the idea that the complications involved in putting a gaseous disk into a triaxial dark matter halo are responsible for some or all of the differences between simulated and observed density profiles. Numerous other theoretical explanations have been proposed, including the straightforward possibility that adding baryons to what are currently pure dark matter simulations will likely change the predicted density profile shapes. Although it is not yet clear which of the myriad explanations might prove correct, the variety of ideas, combined with our finding that the density profile differences are less dramatic than previously thought, suggests that the end of the central density problem may be in sight.

Bibliography

Alam, S. M. K., Bullock, J. S., & Weinberg, D. H. 2002, ApJ, 572, 34

Aparicio, A., Gallart, C., & Bertelli, G. 1997, AJ, 114, 669

Appleton, P. N., Davies, R. D., & Stephenson, R. J. 1981, MNRAS, 195, 327

Armandroff, T. E., Da Costa, G. S., Caldwell, N., & Seitzer, P. 1993, AJ, 106, 986

Armandroff, T. E., Davies, J. E., & Jacoby, G. H. 1998, AJ, 116, 2287

Armandroff, T. E., Jacoby, G. H., & Davies, J. E. 1999, AJ, 118, 1220

Bailin, J., & Steinmetz, M. 2005, ApJ, submitted (preprint: astro-ph/0408163)

Banks, G. D., et al. 1999, ApJ, 524, 612

Barden, S. C., Sawyer, D. G., & Honeycutt, R. K. 1998, in Proc. SPIE Vol. 3355, Optical
    Astronomical Instrumentation, ed. S. D'Odorico, 892

Barnes, J. E., & Hernquist, L. 1992, Nature, 360, 715

Beauchamp, D., Hardy, E., Suntzeff, N. B., & Zinn, R. 1995, AJ, 109, 1628

Begeman, K. G. 1987, Ph.D. Thesis, Kapteyn Inst.

Bell, E. F. & de Jong, R. S. 2001, ApJ, 550, 212

Bell, E. F., McIntosh, D. H., Katz, N., & Weinberg, M. D. 2003, ApJS, 149, 289

Binney, J. 1978, MNRAS, 183, 779

Binney, J., & Tremaine, S. 1987, Galactic Dynamics (Princeton: Princeton Univ. Press)

Birnboim, Y., & Dekel, A. 2003, MNRAS, 345, 349

Blais-Ouellette, S., Amram, P., & Carignan, C. 2001, AJ, 121, 1952

Blais-Ouellette, S., Amram, P., Carignan, C., & Swaters, R. 2004, A&A, 420, 147

Blais-Ouellette, S., Carignan, C., Amram, P., & Côté, S. 1999, AJ, 118, 2123

Bland-Hawthorn, J., & Maloney, P. R. 2002, in ASP Conf. Ser. 254, Extragalactic Gas at Low Redshift, ed. J. S. Mulchaey & J. Stocke (San Francisco: ASP), 267

Blitz, L., & Robishaw, T. 2000, ApJ, 541, 675

Blitz, L., & Rosolowsky, E. 2004, ApJ, 612, L29

Blitz, L., Spergel, D. N., Teuben, P. J., Hartmann, D., & Burton, W. B. 1999, ApJ, 514, 818

Blumenthal, G. R., Faber, S. M., Primack, J. R., & Rees, M. J. 1984, Nature, 311, 517

Blumenthal, G. R., Pagels, H., & Primack, J. R. 1982, Nature, 299, 37

Bode, P., Ostriker, J. P., & Turok, N. 2001, ApJ, 556, 93

Böker, T., Stanek, R., & van der Marel, R. P. 2003, AJ, 125, 1073

Böker, T., et al. 1999, ApJS, 124, 95

Bolatto, A. D., Leroy, A., Israel, F. P., & Jackson, J. M. 2003, ApJ, 595, 167

Bolatto, A. D., Simon, J. D., Leroy, A., & Blitz, L. 2002, ApJ, 565, 238

Bond, J. R., & Efstathiou, G. 1984, ApJ, 285, L45

Bond, J. R., & Szalay, A. S. 1983, ApJ, 274, 443

Borriello, A., & Salucci, P. 2001, MNRAS, 323, 285

Bosma, A. 1978, Ph.D. Thesis, Univ. Groningen

Bosma, A., Athanassoula, E., & van der Hulst, J. M. 1988, A&A, 198, 100

Boyce, P. J., et al. 2001, ApJ, 560, L127

Boylan-Kolchin, M., & Ma, C. 2004, MNRAS, 349, 1117

Braun, R., & Burton, W. B. 1999, A&A, 341, 437

Bregman, J. N. 1980, ApJ, 236, 577

Broeils, A. H. 1992, A&A, 256, 19

Bullock, J. S., Kolatt, T. S., Sigad, Y., Somerville, R. S., Kravtsov, A. V., Klypin, A. A., Primack, J. R., & Dekel, A. 2001, MNRAS, 321, 559

Bullock, J. S., Kravtsov, A. V., & Weinberg, D. H. 2000, ApJ, 539, 517

Burkert, A. 1995, ApJ, 447, L25

Caldwell, N. 1999, AJ, 118, 1230

Caldwell, N., Armandroff, T. E., Seitzer, P., & Da Costa, G. S. 1992, AJ, 103, 840

Carignan, C., & Beaulieu, S. 1989, ApJ, 347, 760

Carignan, C., & Freeman, K. C. 1988, ApJ, 332, L33

Carpenter, J. M., Heyer, M. H., & Snell, R. L. 2000, ApJS, 130, 381

Chiba, M. 2002, ApJ, 565, 17

Christian, C. A., & Tully, R. B. 1983, AJ, 88, 934

Coccato, L., Corsini, E. M., Pizzella, A., Morelli, L., Funes, J. G., & Bertola, F. 2004, A&A, 416, 507

Cole, A. A. 2001, ApJ, 559, L17

Cole, S., & Lacey, C. 1996, MNRAS, 281, 716

Colín, P., Avila-Reese, V., & Valenzuela, O. 2000, ApJ, 542, 622

Colín, P., Klypin, A., Valenzuela, O., & Gottlöber, S. 2004, ApJ, 612, 50

Combes, F., & Arnaboldi, M. 1996, A&A, 305, 763

Cook, K. H., Mateo, M., Olszewski, E. W., Vogt, S. S., Stubbs, C., & Diercks, A. 1999, PASP, 111, 306

Corwin, H. G., de Vaucouleurs, A., & de Vaucouleurs, G. 1985, University of Texas Monographs in Astronomy, 4, 1

Côté, S., Carignan, C., & Freeman, K. C. 2000, AJ, 120, 3027

Cotton, W. D., Condon, J. J., & Arbizzani, E. 1999, ApJS, 125, 409

Courteau, S. 1997, AJ, 114, 2402

Cowsik, R., & McClelland, J. 1972, Physical Review Letters, 29, 669

Cutri, R. M. et al. 2003, VizieR Online Data Catalog, 2246, 0

Dalal, N., & Kochanek, C. S. 2002, ApJ, 572, 25

Danly, L., Albert, C. E., & Kuntz, K. D. 1993, ApJ, 416, L29

Davies, J., Sabatini, S., Davies, L., Linder, S., Roberts, S., Smith, R., & Evans, R. 2002, MNRAS, 336, 155

Davies, J. I., Disney, M. J., Phillipps, S., Boyle, B. J., & Couch, W. J. 1994, MNRAS, 269, 349

Davies, R. D. 1975, MNRAS, 170, 45P

Davis, M., Efstathiou, G., Frenk, C. S., & White, S. D. M. 1985, ApJ, 292, 371

—. 1992, Nature, 356, 489

de Blok, W. J. G., & Bosma, A. 2002, A&A, 385, 816

de Blok, W. J. G., Bosma, A., & McGaugh, S. 2003, MNRAS, 340, 657

de Blok, W. J. G., & McGaugh, S. S. 1997, MNRAS, 290, 533

de Blok, W. J. G., McGaugh, S. S., Bosma, A., & Rubin, V. C. 2001a, ApJ, 552, L23

de Blok, W. J. G., McGaugh, S. S., & Rubin, V. C. 2001b, AJ, 122, 2396

de Heij, V., Braun, R., & Burton, W. B. 2002, A&A, 391, 159

de Vaucouleurs, G. 1959, Handbuch der Physik, 53, 311

de Vaucouleurs, G., de Vaucouleurs, A., Corwin, H. G., Buta, R. J., Paturel, G., & Fouque, P. 1991, Third Reference Catalogue of Bright Galaxies (Berlin: Springer)

Dekel, A., & Birnboim, Y. 2004, astro-ph/0412300

Dekel, A., & Woo, J. 2003, MNRAS, 344, 1131

Diemand, J., Moore, B., & Stadel, J. 2004, MNRAS, 353, 624

Dieter, N. H. 1971, A&A, 12, 59

Djorgovski, S. 1985, PASP, 97, 1119

Dolag, K., Bartelmann, M., Perrotta, F., Baccigalupi, C., Moscardini, L., Meneghetti, M., & Tormen, G. 2004, A&A, 416, 853

Dubinski, J., & Carlberg, R. G. 1991, ApJ, 378, 496

Efstathiou, G. 1992, MNRAS, 256, 43P

Egan, M. P., et al. 2003, AFRL Tech. Rep. No. AFRL-VS-TR-2003-1589

Einasto, J., Kaasik, A., & Saar, E. 1974, Nature, 250, 309

Faber, S. M., & Gallagher, J. S. 1979, ARA&A, 17, 135

Falco, E. E., et al. 1999, PASP, 111, 438

Feitzinger, J. V., & Galinski, T. 1985, A&AS, 61, 503

Fich, M., Dahl, G. P., & Treffers, R. R. 1990, AJ, 99, 622

Fich, M., & Terebey, S. 1996, ApJ, 472, 624

Fich, M., Treffers, R. R., & Blitz, L. 1982, in ASSL Vol. 93: Regions of Recent Star Formation, 201

Flores, R. A., & Primack, J. R. 1994, ApJ, 427, L1

Fouque, P., Durand, N., Bottinelli, L., Gouguenheim, L., & Paturel, G. 1990, A&AS, 86, 473

Fouque, P., Gourgoulhon, E., Chamaraux, P., & Paturel, G. 1992, A&AS, 93, 211

Franx, M., & de Zeeuw, T. 1992, ApJ, 392, L47

Franx, M., van Gorkom, J. H., & de Zeeuw, T. 1994, ApJ, 436, 642

Freedman, W. L., et al. 2001, ApJ, 553, 47

Freeman, K. C. 1970, ApJ, 160, 811

Frenk, C. S., White, S. D. M., Efstathiou, G., & Davis, M. 1985, Nature, 317, 595

Fukuda, Y., et al. 1998, Physical Review Letters, 81, 1562

Fukugita, M., Hogan, C. J., & Peebles, P. J. E. 1998, ApJ, 503, 518

Fukushige, T., Kawai, A., & Makino, J. 2004, ApJ, 606, 625

Fukushige, T., & Makino, J. 1997, ApJ, 477, L9

—. 2001, ApJ, 557, 533

—. 2003, ApJ, 588, 674

Gal, R. R., de Carvalho, R. R., Brunner, R., Odewahn, S. C., & Djorgovski, S. G. 2000, AJ, 120, 540

Garrido, O., Marcelin, M., & Amram, P. 2004, MNRAS, 349, 225

Garrido, O., Marcelin, M., Amram, P., & Boissin, O. 2003, A&A, 399, 51

Garrido, O., Marcelin, M., Amram, P., & Boulesteix, J. 2002, A&A, 387, 821

Gentile, G., Salucci, P., Klein, U., Vergani, D., & Kalberla, P. 2004, MNRAS, 351, 903

Genzel, R., Baker, A. J., Tacconi, L. J., Lutz, D., Cox, P., Guilloteau, S., & Omont, A. 2003, ApJ, 584, 633

Ghigna, S., Moore, B., Governato, F., Lake, G., Quinn, T., & Stadel, J. 2000, ApJ, 544, 616

Gibson, B. K., Giroux, M. L., Penton, S. V., Stocke, J. T., Shull, J. M., & Tumlinson, J. 2001, AJ, 122, 3280

Giovanelli, R., Haynes, M. P., Herter, T., Vogt, N. P., da Costa, L. N., Freudling, W., Salzer, J. J., & Wegner, G. 1997, AJ, 113, 53

Girardi, L., Bressan, A., Bertelli, G., & Chiosi, C. 2000, A&AS, 141, 371

Glazebrook, K., et al. 2004, Nature, 430, 181

Gnedin, O. Y., & Zhao, H. 2002, MNRAS, 333, 299

Gott, J. R. I., & Turner, E. L. 1977, ApJ, 213, 309

Governato, F., et al. 2004, ApJ, 607, 688

Grebel, E. K., & Guhathakurta, P. 1999, ApJ, 511, L101

Gunn, J. E., Lee, B. W., Lerche, I., Schramm, D. N., & Steigman, G. 1978, ApJ, 223, 1015

Harrison, E. R. 1970, Phys. Rev. D, 1, 2726

Hartmann, D., & Burton, W. B. 1997, Atlas of Galactic Neutral Hydrogen (New York: Cambridge Univ. Press)

Hayashi, E., Navarro, J. F., Taylor, J. E., Stadel, J., & Quinn, T. 2003, ApJ, 584, 541

Hayashi, E., et al. 2005, ApJ, submitted (preprint: astro-ph/0408132)

Haynes, M. P., Giovanelli, R., Chamaraux, P., da Costa, L. N., Freudling, W., Salzer, J. J., & Wegner, G. 1999a, AJ, 117, 2039

Haynes, M. P., Giovanelli, R., Salzer, J. J., Wegner, G., Freudling, W., da Costa, L. N., Herter, T., & Vogt, N. P. 1999b, AJ, 117, 1668

Hegyi, D. J., & Olive, K. A. 1983, Physics Letters B, 126, 28

—. 1986, ApJ, 303, 56

Heiles, C. 2000, Arecibo Technical & Operations Memo Series ATOMS 2000-04

Held, E. V., Saviane, I., & Momany, Y. 1999, A&A, 345, 747

Helfer, T. T., & Blitz, L. 1995, ApJ, 450, 90

Hopp, U., Schulte-Ladbeck, R. E., & Kerp, J. 2003, MNRAS, 339, 33

Hulsbosch, A. N. M. 1971, A&A, 14, 489

Hulsbosch, A. N. M., & Wakker, B. P. 1988, A&AS, 75, 191

Hut, P., & White, S. D. M. 1984, Nature, 310, 637

Ibata, R. A., Gilmore, G., & Irwin, M. J. 1995, MNRAS, 277, 781

Iodice, E., Arnaboldi, M., Bournaud, F., Combes, F., Sparke, L. S., van Driel, W., & Capaccioli, M. 2003, ApJ, 585, 730

Ivezić, Ž., & Christodoulou, D. M. 1997, ApJ, 486, 818

Jaffe, A. H., et al. 2001, Phys. Rev. Lett., 86, 3475

Jing, Y. P., & Suto, Y. 2000, ApJ, 529, L69

—. 2002, ApJ, 574, 538

Jobin, M., & Carignan, C. 1990, AJ, 100, 648

Joncas, G., Durand, D., & Roger, R. S. 1992, ApJ, 387, 591

Kamionkowski, M., & Liddle, A. R. 2000, Physical Review Letters, 84, 4525

Kaplinghat, M., Knox, L., & Turner, M. S. 2000, Physical Review Letters, 85, 3335

Karachentsev, I., & Petit, M. 1990, A&AS, 86, 1

Karachentsev, I. D., & Karachentseva, V. E. 1999, A&A, 341, 355

Karachentsev, I. D., et al. 2002, A&A, 383, 125

Kauffmann, G., White, S. D. M., & Guiderdoni, B. 1993, MNRAS, 264, 201

Kazantzidis, S., Kravtsov, A. V., Zentner, A. R., Allgood, B., Nagai, D., & Moore, B. 2004a, ApJ, 611, L73

Kazantzidis, S., Mayer, L., Mastropietro, C., Diemand, J., Stadel, J., & Moore, B. 2004b, ApJ, 608, 663

Keenan, F. P., Shaw, C. R., Bates, B., Dufton, P. L., & Kemp, S. N. 1995, MNRAS, 272, 599

Kent, S. M. 1986, AJ, 91, 1301

Keres, D., Katz, N., Weinberg, D. H., & Davé, R. 2004, MNRAS, submitted (preprint: astro-ph/0407095)

Kerr, F. J., & Sullivan, W. T., I. 1969, ApJ, 158, 115

Klypin, A., Kravtsov, A. V., Bullock, J. S., & Primack, J. R. 2001, ApJ, 554, 903

Klypin, A., Kravtsov, A. V., Valenzuela, O., & Prada, F. 1999, ApJ, 522, 82

Knapp, G. R., Kerr, F. J., & Williams, B. A. 1978, ApJ, 222, 800

Kochanek, C. S., & Dalal, N. 2004, ApJ, 610, 69

Kormendy, J., & Kennicutt, R. C. 2004, ARA&A, 42, 603

Kraan-Korteweg, R. C., van Driel, W., Briggs, F., Binggeli, B., & Mostefaoui, T. I. 1999, A&AS, 135, 255

Kravtsov, A. V., Gnedin, O. Y., & Klypin, A. A. 2004, ApJ, 609, 482

Kroupa, P. 2001, MNRAS, 322, 231

Kuijken, K., & Tremaine, S. 1994, ApJ, 421, 178

Kutyrev, A. S., & Reynolds, R. J. 1989, ApJ, 344, L9

Landolt, A. U. 1992, AJ, 104, 340

Lange, A. E., et al. 2001, Phys. Rev. D, 63, 042001

Lee, M. G. 1995, AJ, 110, 1129

Lee, M. G., Aparicio, A., Tikonov, N., Byun, Y., & Kim, E. 1999, AJ, 118, 853

Lee, M. G., Freedman, W. L., & Madore, B. F. 1993, ApJ, 417, 553

Leitherer, C., et al. 1999, ApJS, 123, 3

Leroy, A., Bolatto, A. D., Simon, J. D., & Blitz, L. 2005, ApJ, in press

Lin, D. N. C., & Faber, S. M. 1983, ApJ, 266, L21

Lockman, F. J. 2003, ApJ, 591, L33

Lu, L., Savage, B. D., & Sembach, K. R. 1994a, ApJ, 426, 563

—. 1994b, ApJ, 437, L119

Lupton, R., Blanton, M. R., Fekete, G., Hogg, D. W., O'Mullane, W., Szalay, A., & Wherry, N. 2004, PASP, 116, 133

Ma, C., & Boylan-Kolchin, M. 2004, Physical Review Letters, 93, 021301

Maller, A. H., & Bullock, J. S. 2005, MNRAS, in press

Mao, S., & Schneider, P. 1998, MNRAS, 295, 587

Marchesini, D., D'Onghia, E., Chincarini, G., Firmani, C., Conconi, P., Molinari, E., & Zacchei, A. 2002, ApJ, 575, 801

Martimbeau, N., Carignan, C., & Roy, J.-R. 1994, AJ, 107, 543

Mateo, M. L. 1998, ARA&A, 36, 435

Matthews, L. D., & Gallagher, J. S. 2002, ApJS, 141, 429

Mayall, N. U. 1960, Annales d'Astrophysique, 23, 344

McGaugh, S. S., & de Blok, W. J. G. 1998, ApJ, 499, 41

McGaugh, S. S., Rubin, V. C., & de Blok, W. J. G. 2001, AJ, 122, 2381

Méndez, B., Davis, M., Moustakas, J., Newman, J., Madore, B. F., & Freedman, W. L. 2002, AJ, 124, 213

Méndez, B. J. 2002, Ph.D. Thesis, Univ. California, Berkeley

Metcalf, R. B., & Madau, P. 2001, ApJ, 563, 9

Metcalf, R. B., Moustakas, L. A., Bunker, A. J., & Parry, I. R. 2004, ApJ, 607, 43

Metcalf, R. B., & Zhao, H. 2002, ApJ, 567, L5

Milgrom, M. 1983a, ApJ, 270, 371

—. 1983b, ApJ, 270, 384

—. 1983c, ApJ, 270, 365

Mill, J. D., et al. 1994, Journal of Spacecraft and Rockets, 31, 900

Miller, B. W., Dolphin, A. E., Lee, M. G., Kim, S. C., & Hodge, P. 2001, ApJ, 562, 713

Minchin, R., et al. 2005, ApJ, in press (preprint: astro-ph/0502312)

Moore, B. 1994, Nature, 370, 629

Moore, B., Ghigna, S., Governato, F., Lake, G., Quinn, T., Stadel, J., & Tozzi, P. 1999a, ApJ, 524, L19

Moore, B., Quinn, T., Governato, F., Stadel, J., & Lake, G. 1999b, MNRAS, 310, 1147

Mould, J. 1997, PASP, 109, 125

Murphy, E. M., et al. 2000, ApJ, 538, L35

Näslund, M., & Jörsäter, S. 1997, A&A, 325, 915

Navarro, J. F., Frenk, C. S., & White, S. D. M. 1995a, MNRAS, 275, 720

—. 1995b, MNRAS, 275, 56

—. 1996, ApJ, 462, 563

—. 1997, ApJ, 490, 493

Navarro, J. F., et al. 2004, MNRAS, 349, 1039

Newberg, H. J., et al. 2002, ApJ, 569, 245

Newton, I. 1687, Philosophiae Naturalis Principia Mathematica (London: Royal Society)

Nikolaev, S., & Weinberg, M. D. 2000, ApJ, 542, 804

Nilson, P. 1973, Uppsala General Catalogue of Galaxies (Uppsala: Uppsala Astron. Obs.)

Oke, J. B., et al. 1995, PASP, 107, 375

Olling, R. P., & Merrifield, M. R. 2000, MNRAS, 311, 361

—. 2001, MNRAS, 326, 164

Oort, J. H. 1966, Bull. Astron. Inst. Netherlands, 18, 421

—. 1970, A&A, 7, 381

Osterbrock, D. E., Fulbright, J. P., Martel, A. R., Keane, M. J., Trager, S. C., & Basri, G. 1996, PASP, 108, 277

Ostriker, J. P. 1993, ARA&A, 31, 689

Ostriker, J. P., Peebles, P. J. E., & Yahil, A. 1974, ApJ, 193, L1

Padmanabhan, T. 1993, Structure Formation in the Universe (Cambridge: Cambridge Univ. Press)

Page, T. 1962, ApJ, 136, 685

Peacock, J. A. 1999, Cosmological Physics (Cambridge: Cambridge Univ. Press)

Peebles, P. J. E. 1982, ApJ, 263, L1

—. 1993, Principles of Physical Cosmology (Princeton: Princeton Univ. Press)

Peebles, P. J. E., & Yu, J. T. 1970, ApJ, 162, 815

Peng, Q., Peng, F., Chou, C., & Lin, Y. 2002, Ap&SS, 282, 499

Perlmutter, S., et al. 1999, ApJ, 517, 565

Persic, M., & Salucci, P. 1990, MNRAS, 245, 577

Persic, M., Salucci, P., & Stel, F. 1996, MNRAS, 281, 27

Peterson, S. D. 1978, Ph.D. Thesis, Cornell Univ.

Pisano, D. J., & Wilcots, E. M. 1999, AJ, 117, 2168

Pohlen, M. 2002, Ph.D. Thesis, Ruhr-Univ.

Pohlen, M., Dettmar, R.-J., Lütticke, R., & Aronica, G. 2002, A&A, 392, 807

Power, C., Navarro, J. F., Jenkins, A., Frenk, C. S., White, S. D. M., Springel, V., Stadel, J., & Quinn, T. 2003, MNRAS, 338, 14

Preskill, J., Wise, M. B., & Wilczek, F. 1983, Physics Letters B, 120, 127

Price, S. D., Egan, M. P., Carey, S. J., Mizuno, D. R., & Kuchar, T. A. 2001, AJ, 121, 2819

Pryke, C., Halverson, N. W., Leitch, E. M., Kovac, J., Carlstrom, J. E., Holzapfel, W. L., & Dragovan, M. 2002, ApJ, 568, 46

Puche, D., Carignan, C., & Wainscoat, R. J. 1991, AJ, 101, 447

Putman, M. E., et al. 2002, AJ, 123, 873

Reed, D., Governato, F., Verde, L., Gardner, J., Quinn, T., Stadel, J., Merritt, D., & Lake, G. 2005, MNRAS, 357, 82

Richter, P., et al. 2001, ApJ, 559, 318

Ricotti, M. 2003, MNRAS, 344, 1237

Riess, A. G., et al. 1998, AJ, 116, 1009

Roberts, M. S. 1976, Comments on Astrophysics, 6, 105

Roberts, M. S., & Whitehurst, R. N. 1975, ApJ, 201, 327

Robertson, B., Yoshida, N., Springel, V., & Hernquist, L. 2004, ApJ, 606, 32

Robishaw, T., Simon, J. D., & Blitz, L. 2002, ApJ, 580, L129

Rocha-Pinto, H. J., Majewski, S. R., Skrutskie, M. F., Crane, J. D., & Patterson, R. J. 2004, ApJ, 615, 732

Romanishin, W., Strom, S. E., & Strom, K. M. 1982, ApJ, 258, 77

Rood, H. J., & Dickel, J. R. 1978, ApJ, 224, 724

Rood, H. J., Page, T. L., Kintner, E. C., & King, I. R. 1972, ApJ, 175, 627

Rosenberg, J. L., & Schneider, S. E. 2000, ApJS, 130, 177

Rosolowsky, E., Engargiola, G., Plambeck, R., & Blitz, L. 2003, ApJ, 599, 258

Rubin, V. C., & Ford, W. K. J. 1970, ApJ, 159, 379

Rubin, V. C., Thonnard, N., & Ford, W. K. 1978, ApJ, 225, L107

—. 1980, ApJ, 238, 471

Sackett, P. D., Rix, H., Jarvis, B. J., & Freeman, K. C. 1994, ApJ, 436, 629

Sackett, P. D., & Sparke, L. S. 1990, ApJ, 361, 408

Sakai, S., et al. 2000, ApJ, 529, 698

Salpeter, E. E. 1955, ApJ, 121, 161

Salucci, P., Walter, F., & Borriello, A. 2003, A&A, 409, 53

Saviane, I., Held, E. V., & Bertelli, G. 2000, A&A, 355, 56

Saviane, I., Held, E. V., & Piotto, G. 1996, A&A, 315, 40

Scannapieco, E., Ferrara, A., & Broadhurst, T. 2000, ApJ, 536, L11

Scannapieco, E., Thacker, R. J., & Davis, M. 2001, ApJ, 557, 605

Schlegel, D. J., Finkbeiner, D. P., & Davis, M. 1998, ApJ, 500, 525

Schoenmakers, R. H. M. 1998, in ASP Conf. Ser. 136, Galactic Halos, ed. D. Zaritsky (San Francisco: ASP), 240

Schoenmakers, R. H. M., Franx, M., & de Zeeuw, P. T. 1997, MNRAS, 292, 349

Schramm, D. N., & Steigman, G. 1981, ApJ, 243, 1

Schweizer, F., Whitmore, B. C., & Rubin, V. C. 1983, AJ, 88, 909

Scott, D., White, M., Cohn, J. D., & Pierpaoli, E. 2001, astro-ph/0104435

Sembach, K. R., Gibson, B. K., Fenner, Y., & Putman, M. E. 2002, ApJ, 572, 178

Sembach, K. R., Savage, B. D., Lu, L., & Murphy, E. M. 1999, ApJ, 515, 108

Shapiro, P. R., & Field, G. B. 1976, ApJ, 205, 762

Sharma, S., & Steinmetz, M. 2004, astro-ph/0406533

Sharpless, S. 1959, ApJS, 4, 257

Siegel, M. H., et al. 2005, ApJ, in press (preprint: astro-ph/0412699)

Simon, J. D., & Blitz, L. 2002, ApJ, 574, 726

Simon, J. D., Bolatto, A. D., Leroy, A., & Blitz, L. 2003a, ApJ, 596, 957

Simon, J. D., Robishaw, T., & Blitz, L. 2003b, in ASP Conf. Ser. 327, Satellites and Tidal Streams, ed. F. Prada, D. Mártinez-Delgado, & T. J. Mahoney (San Francisco: ASP), 32

Smith, S. 1936, ApJ, 83, 23

Sofue, Y. 1996, ApJ, 458, 120

Sofue, Y., Tomita, A., Tutui, Y., Honma, M., & Takeda, Y. 1998, PASJ, 50, 427

Somerville, R. S. 2002, ApJ, 572, L23

Spekkens, K., Giovanelli, R., & Haynes, M. P. 2005, AJ, in press (preprint: astro-ph/0502166)

Spergel, D. N., & Steinhardt, P. J. 2000, Physical Review Letters, 84, 3760

Spergel, D. N., et al. 2003, ApJS, 148, 175

Sternberg, A., McKee, C. F., & Wolfire, M. G. 2002, ApJS, 143, 419

Stetson, P. B. 1987, PASP, 99, 191

—. 2000, PASP, 112, 925

Stetson, P. B., Hesser, J. E., & Smecker-Hane, T. A. 1998, PASP, 110, 533

Stil, J. M., & Israel, F. P. 2002a, A&A, 389, 29

—. 2002b, A&A, 389, 42

Stoehr, F. 2004, MNRAS, submitted (preprint: astro-ph/0403077)

Stoehr, F., White, S. D. M., Tormen, G., & Springel, V. 2002, MNRAS, 335, L84

Swaters, R. A. 1999, Ph.D. Thesis, Univ. Groningen

Swaters, R. A., & Balcells, M. 2002, A&A, 390, 863

Swaters, R. A., Madore, B. F., & Trewhella, M. 2000, ApJ, 531, L107

Swaters, R. A., Madore, B. F., van den Bosch, F. C., & Balcells, M. 2003a, ApJ, 583, 732

Swaters, R. A., Verheijen, M. A. W., Bershady, M. A., & Andersen, D. R. 2003b, ApJ, 587, L19

Szalay, A. S., & Marx, G. 1976, A&A, 49, 437

Taylor, E. N., & Webster, R. L. 2005, ApJ, submitted (preprint: astro-ph/0412699)

Taylor, J. E., & Navarro, J. F. 2001, ApJ, 563, 483

Teuben, P. J. 1991, in Warped Disks and Inclined Rings Around Galaxies, ed. S. Casertano, P. D. Sackett, & F. H. Briggs (Cambridge: Cambridge Univ. Press), 40

Teuben, P. J. 1995, in ASP Conf. Ser. 77, Astronomical Data Analysis Software and Systems IV, ed. R. Shaw, H. E. Payne, & J. J. E. Hayes (San Francisco: ASP), 398

Thuan, T. X., & Martin, G. E. 1979, ApJ, 232, L11

Tripp, T. M., et al. 2003, AJ, 125, 3122

Tufte, S. L., Reynolds, R. J., & Haffner, L. M. 1998, ApJ, 504, 773

Turner, E. L. 1976, ApJ, 208, 304

Vallejo, O., Braine, J., & Baudry, A. 2002, A&A, 387, 429

van den Bergh, S. 1960a, ApJ, 131, 558

—. 1960b, MNRAS, 121, 387

—. 1961, AJ, 66, 566

—. 1999, A&A Rev., 9, 273

—. 2000, PASP, 112, 529

van den Bosch, F. C., Robertson, B. E., Dalcanton, J. J., & de Blok, W. J. G. 2000, AJ, 119, 1579

van den Bosch, F. C., & Swaters, R. A. 2001, MNRAS, 325, 1017

van Woerden, H., Schwarz, U. J., Peletier, R. F., Wakker, B. P., & Kalberla, P. M. W.
    1999, Nature, 400, 138

Verde, L., Oh, S. P., & Jimenez, R. 2002, MNRAS, 336, 541

Verschuur, G. L. 1969, ApJ, 156, 771

Wagoner, R. V., Fowler, W. A., & Hoyle, F. 1967, ApJ, 148, 3

Wakker, B., van Woerden, H., de Boer, K. S., & Kalberla, P. 1998, ApJ, 493, 762

Wakker, B. P. 2001, ApJS, 136, 463

Wakker, B. P., & Schwarz, U. J. 1991, A&A, 250, 484

Wakker, B. P., & van Woerden, H. 1991, A&A, 250, 509

Wakker, B. P., Vijfschaft, B., & Schwarz, U. J. 1991, A&A, 249, 233

Wakker, B. P., et al. 1999, Nature, 402, 388

Walter, F., Taylor, C. L., Hüttemeister, S., Scoville, N., & McIntyre, V. 2001, AJ, 121, 727

Walter, F., Weiss, A., Martin, C., & Scoville, N. 2002, AJ, 123, 225

Warren, M. S., Quinn, P. J., Salmon, J. K., & Zurek, W. H. 1992, ApJ, 399, 405

Weinberg, M. D., & Katz, N. 2002, ApJ, 580, 627

Weinberg, S. 1978, Physical Review Letters, 40, 223

Weiner, B. J., Sellwood, J. A., & Williams, T. B. 2001a, ApJ, 546, 931

Weiner, B. J., Vogel, S. N., & Williams, T. B. 2002, in ASP Conf. Ser. 254, Extragalactic
    Gas at Low Redshift, ed. J. S. Mulchaey & J. Stocke (San Francisco: ASP), 256

Weiner, B. J., & Williams, T. B. 1996, AJ, 111, 1156

Weiner, B. J., Williams, T. B., van Gorkom, J. H., & Sellwood, J. A. 2001b, ApJ, 546, 916

Welch, W. J., et al. 1996, PASP, 108, 93

Weldrake, D. T. F., de Blok, W. J. G., & Walter, F. 2003, MNRAS, 340, 12

White, S. D. M., Davis, M., & Frenk, C. S. 1984, MNRAS, 209, 27P

White, S. D. M., Frenk, C. S., & Davis, M. 1983, ApJ, 274, L1

Whiting, A. B., Hau, G. K. T., & Irwin, M. 1999, AJ, 118, 2767

Whiting, A. B., Irwin, M. J., & Hau, G. K. T. 1997, AJ, 114, 996

Whitmore, B. C., McElroy, D. B., & Schweizer, F. 1987, ApJ, 314, 439

Wilczek, F. 1978, Physical Review Letters, 40, 279

Willman, B., Dalcanton, J., Ivezić, Ž., Schneider, D. P., & York, D. G. 2002, AJ, 124, 2600

Willman, B., et al. 2005a, AJ, in press (preprint: astro-ph/0410416)

—. 2005b, ApJ, submitted (preprint: astro-ph/0503552)

Wong, T. 2000, Ph.D. Thesis, Univ. California, Berkeley

Wong, T., Blitz, L., & Bosma, A. 2004, ApJ, 605, 183

Worthey, G. 1994, ApJS, 95, 107

Wright, M. C. H. 1974, A&A, 31, 317

—. 1979, ApJ, 233, 35

Yi, S., Demarque, P., Kim, Y., Lee, Y., Ree, C. H., Lejeune, T., & Barnes, S. 2001, ApJS, 136, 417

Young, J. S., et al. 1995, ApJS, 98, 219

Young, L. M., & Lo, K. Y. 1997, ApJ, 490, 710

Yun, M. S., Ho, P. T. P., & Lo, K. Y. 1994, Nature, 372, 530

Yun, M. S., Ho, P. T. P., & Lo, K. Y. 2000, in ASP Conf. Ser. 217, Imaging at Radio through Submillimeter Wavelengths, ed. J. G. Mangum & S. J. E. Radford (San Francisco: ASP), 374

Zeldovich, Y. B. 1972, MNRAS, 160, 1P

Zucker, D. B., et al. 2004, ApJ, 612, L121

Zwicky, F. 1933, Helvetica Phys. Acta, 6, 110

—. 1937, ApJ, 86, 217

Appendix A

Rotation Curve Fitting Algorithms

When dealing with long-slit kinematic data it is relatively straightforward to transform the reduced observations into a rotation curve. For a full velocity field, the process is more complicated because it involves converting two-dimensional data to one dimension while retaining as much of the information as possible. In this appendix, we describe the various techniques we use to make this conversion. Note that some details of this discussion are particular to NGC 2976 (Chapter 5), even though the techniques we use are general.

A.1 Rotcur

ROTCUR (Begeman 1987) is a standard algorithm to fit galaxy kinematics with a tilted-ring model. We used the implementation of ROTCUR in the NEMO package (Teuben 1995). ROTCUR divides the galaxy into a set of narrow, concentric rings, and in each ring performs a nonlinear least squares fit to the function

$$
\begin{aligned}
v_{model}(x,y) = \\
v_0 + v_{rot}\sin i \frac{-(x-x_0)\sin PA + (y-y_0)\cos PA}{\sqrt{(x-x_0)^2 + (y-y_0)^2/\cos^2 i}},
\end{aligned}
\tag{A.1}
$$

where v_0 is the systemic velocity, v_{rot} is the rotation velocity, i is the inclination angle, PA is the angle between north and the receding side of the galaxy's major axis, and (x_0, y_0) is the galaxy's center. Each ring can thus contain up to six free parameters (the central position requires two), and ROTCUR finds the best fit by minimizing $\sum_i (v_{obs,i} - v_{model,i})^2/w_i^2$, where w_i is the weight ascribed to each point. We weight each point by the cosine of the angle between the point and the major axis, automatically deemphasizing points near the minor

axis, so it is not necessary to discard points within some angle of the minor axis. ROTCUR's most serious weakness is that it can only model circular motions.

To create the ROTCUR rotation curve, we used the best-fit center and systemic velocity that we determined with RINGFIT. Because the position angle must be a function of radius if the galaxy is modeled with purely rotational motions, we first ran ROTCUR with both the rotation velocities and the position angle free to vary to determine $PA(r)$. We then used this description of the position angle as an input to ROTCUR, and ran it again with only the rotation velocities as free parameters. The rotation curve produced in this way is displayed in Figure 5.7b. We did not allow ROTCUR to fit for the inclination angle because it was apparent early on that the rotation curve of NGC 2976 is essentially solid-body, which means that dv_{rot}/dr is small. Therefore, the inclination angle and the rotation velocities are degenerate in Equation A.1, making the kinematic inclination angle poorly determined. We judged that the inclination angle was unlikely to differ significantly from the photometric value anyway, so the safest course was to leave the inclination fixed at $61°\!.5$.

A.2   Ringfit

In addition to ROTCUR we constructed tilted-ring models with our own routine, RINGFIT. The purpose of this exercise was twofold: first, to compare the results from ROTCUR with those from a completely independent program and make sure that the answers agreed, and second, to fit for radial motions in the plane of the galaxy (inflow or outflow) instead of just assuming that the observed velocities are due only to rotation. The RINGFIT fitting function is similar to Equation A.1, except that we add an extra term to allow for radial velocities, and we do not fit for the PA, inclination, or the center. Thus, we can drop the explicit mention of the PA, x_0, and y_0, and write

$$v_{model} = v_0 + v_{rot} \sin i \cos \theta + v_{rad} \sin i \sin \theta, \qquad (A.2)$$

where $\cos \theta$ is equal to the fractional expression that follows $v_{rot} \sin i$ in the second term on the right hand side of Equation A.1, and the free parameters in each ring are v_0, v_{rot}, and v_{rad}. The solution is then determined with a linear least squares fit. The inclination, PA, and central position must be specified as inputs, but they can also be solved for by running RINGFIT with a grid of input parameters and finding the minimum χ^2. We have verified that ROTCUR and RINGFIT give indistinguishable results when the same input parameters

and weighting function are used.

A.3   Rotcurshape

We also employed the NEMO routine ROTCURSHAPE, which is closely related to (and based on) ROTCUR. ROTCURSHAPE dispenses with dividing the galaxy into rings and instead fits the whole velocity field at once. In addition to calculating the best-fit values for the PA, inclination, systemic velocity, and center, ROTCURSHAPE also assumes a functional form for the rotation curve/density profile (e.g., power law, NFW, pseudoisothermal, etc.) and solves for the free parameters of that function. One advantage of this approach is that near the center of the galaxy, where the velocities may be changing rapidly with radius, all of the data points are not artificially placed at the same radius (as was necessary with ROTCUR, where every point with $r < 8''$ was in the same ring). Another is that the kinematic parameters of the galaxy and the parameters of the fitting function are determined in a single step. This makes it straightforward to measure the global agreement between the model and the data. For a power law rotation curve, the results from ROTCURSHAPE are nearly identical to the ones we derive by running ROTCUR or RINGFIT and then fitting a power law to the resulting rotation velocities.

Appendix B

NFW and Power Law Density Profiles

Navarro, Frenk, & White (1996) showed that CDM halos have density profiles of the form

$$\frac{\rho(r)}{\rho_{crit}} = \frac{\delta_c}{(r/r_s)(1 + r/r_s)^2} \ , \tag{B.1}$$

where $\rho_{crit} = 3H^2/8\pi G = 1.88 \times 10^{-29} \ h^2 \ \mathrm{g \ cm^{-3}}$ is the critical density, δ_c is the halo overdensity, and r_s is the scale radius (simulations suggest $r_s \sim 2.5$ kpc for a galaxy the size of NGC 2976). For $r \ll r_s$, Equation B.1 clearly reduces to $\rho \propto r^{-1}$. The commonly-discussed concentration parameter c is the ratio of the virial radius of the halo (r_{200}, the radius enclosing a mean density of 200 times the background density) to the scale radius. In the simulations analyzed by NFW the concentration parameter varied from ~ 7 for galaxy clusters up to ~ 16 for large galaxies. Later studies at lower masses found a median concentration of $c = 19.5$ for $3 \times 10^{10} \ \mathrm{M_\odot}$ halos (Bullock et al. 2001; Dolag et al. 2004). Other numerical simulations have resulted in slightly different profile shapes. For example, Moore et al. (1999b) argued that CDM halos exhibit steeper central cusps when simulated at higher resolution; their best-fitting functional form is similar to that of NFW, except that both terms in the denominator of the right hand side of Equation B.1 are raised to the 1.5 power, resulting in a $\rho \propto r^{-1.5}$ central density profile. Most subsequent numerical studies in the literature have found central slopes that are bracketed by the NFW and Moore profiles (e.g., Jing & Suto 2000; Ghigna et al. 2000; Klypin et al. 2001; Power et al. 2003; Navarro et al. 2004; Diemand et al. 2004; Reed et al. 2005). It is noteworthy that no set of simulations has found central density profiles that are shallower than $\rho \propto r^{-1}$,

although Taylor & Navarro (2001) presented analytical arguments for a $\rho \propto r^{-0.75}$ central slope.

Since we are primarily interested in power law fits to the rotation curve, we also note that for a spherical mass distribution, a density profile $\rho = \rho_0(r/r_0)^{-\alpha}$ implies that

$$v_{rot} = \sqrt{\frac{4\pi G \rho_0 r_0^2}{3-\alpha}} \left(\frac{r}{r_0}\right)^{(2-\alpha)/2} \quad , \tag{B.2}$$

and correspondingly, a rotation curve that can be fit by a power law $v_{rot} = v_0(r/r_0)^\beta$ yields a density profile

$$\rho = \frac{(2\beta+1)v_0^2}{4\pi G r_0^2} \left(\frac{r}{r_0}\right)^{2\beta-2} \quad . \tag{B.3}$$

A galaxy with a constant density halo thus has a linear ($v_{rot} \propto r$) rotation curve, while the rotation curve associated with an NFW $\rho \propto r^{-1}$ central density profile is $v_{rot} \propto r^{1/2}$.